Imperial College London

Department of Digestion, Metabolism and Reproduction

Improving spatially resolved MSI analysis of tissue sections for DMPK and toxicity studies

---

Doctor of Philosophy

Andreas Dannhorn

2020

Declaration of Originality

I hereby declare that the work presented in this thesis is based on my original research or the original work is referenced.

Copyright Declaration

Acknowledgements

I would like to thank Imperial College London, the BBSRC and AstraZeneca for the award of my industrial CASE PhD studentship. I would like to thank my supervisors Prof Zoltan Takats and Dr Richard A.J. Goodwin for the guidance throughout my studies. It was an interesting experience to work within the research group at Imperial College and I would like to thank the MSI group at AstraZeneca for welcoming me to spent significant amounts of my studies within their labs. In particular, I would like to single out Dr John G Swales who was always available when professional guidance, moral support or simply a motivating hug was required.

I would also like to thank my family and friends for being supportive despite having to listen through long complaints or when I was out of touch for some time. I would particularly like to thank my grandparents Horst and Ingrid Rydzek who supported every step of my academic development, and without whom I would have not been able to take the path I did.

Abstract:

The aim of the work presented herein was to re-evaluate the sample preparation pipeline for mass spectrometry imaging (MSI) experiments focusing on metabolite distributions and drug disposition. The work evaluated the steps from sample collection to quantitative interpretation of the results. A major focus of the work was set on the integration of the evaluated and newly developed workflows with orthogonal tissue imaging techniques. The work evaluated the effects of sample collection in formalin and subsequent preparation into formalin-fixed, paraffin embedded tissues. Overall, these treatments were found to substantially alter the tissue metabolome and distort metabolite and drug distributions, validating the current 'gold standard' of fresh-frozen tissues for metabolite and drug disposition focused MSI studies. These high-quality tissues require commonly cryo-sectioning to enable MSI analysis. Sample embedding strategies were explored to allow simultaneous preparation and analysis of several tissue specimens at once to increase technical reproducibility. To achieve highest preservation of the specimens, a novel embedding medium based on a hydroxypropyl-methylcellulose and polyvinylpyrrolidone hydrogel was developed. Within the frame of this work, strategies to decontaminate prepared tissue sections prior to MSI analysis will be reviewed, to minimize the infection risk when handling human tissues or specimen from infection models. Irradiation with UV-C light was found to be a suited decontamination as it enables accurate elucidation of endogenous biodistributions whilst only inflicting minor alterations to the tissue metabolome. The utility of a novel DESI setup based on a triple-quadrupole mass spectrometer was described and its application to elucidate drug disposition within tissues. The quantitative relationship of DESI- and MALDI-MSI were explored and some of the newly developed and established workflows were utilized in a multi-omics approach to elucidate the toxicokinetic effects of polymyxin B1 in a model of drug induced nephrotoxicity.

Table of Figures:

Table of Tables

Chapter 1: Introduction

Scope of the Project

Mass spectrometric imaging (MSI) allows spatially resolved, qualitative and quantitative determination of numerous molecular classes, including endogenous metabolites, lipids and proteins[1-5]. With the ability to detect a wide chemical scope in a single experiment, MSI techniques are the method of choice for tissue-based metabolomics, proteomics, drug distribution and toxicity studies[6-9].These new molecular imaging technologies allow researchers to get a comprehensive view on the molecular content of tissue specimens and generate metabolic maps of the same sample. The integration of this novel type of information with established imaging modalities drives recent insights gained across fundamental research, drug discovery and clinical disciplines. For this reason that MSI is regularly combined with orthogonal analysis modalities such as morphological assessment through histological staining, autofluorescence[10], or immunofluorescence[11] immunohistochemistry (IHC)[12, 13], imaging mass cytometry (IMC) as well as transcriptomics or genomics. These so called 'multi-omics' studies performed at systems biology level are increasingly important to better understand the pathomechanism of diseases such as auto-immune diseases[14] and cancer[15]. The greater understanding of the driving disease pathways can subsequently be leveraged to identify 'druggable' targets in the drug development process[16, 17].

The existence of numerous established sample preparation protocols for each of the assays limit the feasibility to integrate these protocols into a single sample preparation workflow for the different analytical techniques. Integration attempts often result in either an inability to acquire the full range on molecular and morphological information from a given sample or a compromise in data quality. This is particularly pertinent when utilizing new molecular imaging technologies that require methods to capture morphology yet also stabilize a rapidly changing tissue metabolome[18]. The aim of this project was a systematic re-evaluation of sample preparation procedures and the needs and requirements of the different techniques to work

towards accurate and reproducible acquisition and interpretation of MSI data whilst offering uncompromised adaption of the preparation workflows for orthogonal techniques.

Mass spectrometry

Mass spectrometry describes a set of techniques that take a given sample and analyze its chemical composition based on the mass to charge ratio (*m/z*). Basically, all mass spectrometers are combinations of an ion source that generates gas-phase ions, a mass analyser that separates the formed ions based on their *m/z* values and a detector. The fundamentals of the most commonly used ion sources and mass analyser relevant to this work are described below.

Ion sources

The ion source is the functional part of a mass spectrometer that liberates ions from the sample which is usually introduced as liquid or in solid state depending on the nature of the ion source.

Secondary ion mass spectrometry (SIMS)

First described[19] in 1949 SIMS is one of the oldest ion sources which is still in use today. For SIMS experiments a primary ion beam, which is generated in ion guns, is directed onto a solid sample. The kinetic impact ablates the sample surface, liberating secondary analyte ions into the vacuum chamber. These secondary ions get transferred into a mass analyser to determine their *m/z* values. The ability to focus and pulse the primary ion beam allows to raster across the sample surface and acquire spectral information whilst recording the coordinates of the origin makes SIMS a suited setup for MSI experiments. As the primary ion beam constantly ablates the sample surface it exposes deeper layers of the sample. Repeated analysis of the newly exposed layers allows reconstruction of 3D chemical distribution maps[20]. The introduction of instruments using large ion-cluster such as C_{60}^+ as primary ion beam reduce fragmentation of organic compounds through distribution of the impact energy on a larger surface area, but it remains a draw-back for the application of SIMS in biomedical research and life sciences. A similar drawback is the low mass resolving power of most commercially available SIMS instruments utilizing a time-of-flight mass analyser, but recent instrumental

advancements allowed integration of SIMS with a higher resolution mass analyser[21]. The schematics of SIMS are displayed in Figure 1.1a.

Matrix assisted laser desorption/ionization (MALDI)

First reported[22] in 1985, MALDI is one of the most commonly used ionization techniques for analysis of large molecules such as intact peptides, proteins and synthetic polymers. The soft ionization is promoted by an organic matrix which is either mixed with the analyte solution or applied onto the sample surface and re-crystalized through evaporation of the solvent. Irradiation of the matrix with ultra-violet light emitted by a pulsed laser and results in spontaneous ablation, liberating matrix and analyte molecules into the vacuum chamber. The analyte molecules undergo protonation or deprotonation in the ablation plume forming molecular ion species that can be accelerated and introduced into a mass analyser. The choice of the organic matrix compound and the wavelength of the laser enables selective ionization of target analytes[23]. As first described[24] in 1997, MALDI is well suited for MSI as it allows collection of mass spectral information whilst recording the coordinates for the origin of the spectra and has since emerged to be the most commonly used ionization technique for MSI. The schematics of MALDI are displayed in Figure 1.1b.

Electrospray ionization (ESI)

ESI was first reported in 1984 as an ionization source for the continuous introduction of liquid samples into a mass spectrometer[25]. An aerosol is formed from the liquid sample through emission of a charged droplet jet at the end of a capillary. High voltage applied between the capillary and the collector plate of the mass spectrometer results in formation of a liquid cone (Taylor cone) which emits the droplets. The droplets undergo desolvation to the extent that the number of charges exceeds the Rayleigh limit resulting in Coulomb fission when the charge repulsion exceeds the surface tension. The smaller droplets undergo further desolvation until small molecular species ionize through ion evaporation mechanisms whilst large molecules such as peptides and proteins form multiply charged gas phase ions through charge residue mechanism upon full evaporation of the solvent.

Desorption electrospray ionization (DESI)

First reported[26] in 2004 DESI builds on the mechanisms of ESI and shares similar ionization mechanisms. In contrast to ESI the beam of primarily charged solvent droplets is directed onto the sample surface where it extracts analyte molecules which are desorbed in secondary droplets that are aspirated into the mass spectrometer where they undergo desolvation and formation of gas phase molecular ion species. As DESI is an ambient ionization technique, the source is mounted onto the front plate of a mass spectrometer and operated under atmospheric conditions. As DESI is fundamentally a surface sampling technique, if operated in a continuous scanning mode with fixed scan times and lateral sample stage movements a methodology for producing surface images can be derived. This operation mode allows reconstruction of analyte distribution maps for MSI as first reported in[27]. The schematics of DESI are displayed in Figure 1.1c.

Inductively coupled plasma (ICP)

Inductively coupled plasma usually utilizes a stable argon plasma torch to atomize analytes forming elemental cations. The plasma is confined by a coil generating an electromagnetic field in which electrons are accelerated to initiate the plasma. The accelerated electrons ionize argon through electron impact ionization thus further promoting the plasma generation until it stabilizes into a steady state. ICP is commonly used for elemental analysis and determination of heavy metals in samples which are introduced as liquid or aerosol. Organic components disintegrate within the plasma, which normally has a temperature of approximately 10,000°K, liberating even covalently bound elements. The schematics of ICP are displayed in Figure1.1d. Recent advances in instrumentation allow the use of antibodies tagged with heavy metals to perform affinity-based labelling of recognizable targets such as peptides and proteins. The presence of the heavy metal tags and thus the abundance of the target can be analyzed in cell suspensions through mass cytometric analysis or within tissues as described under laser ablation - inductively coupled plasma – mass spectrometry (LA-ICP-MS).

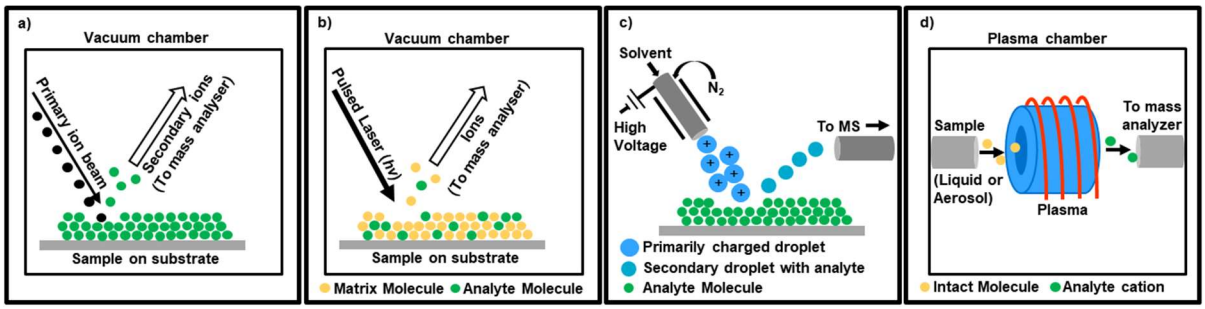

Figure 1.1, Basic schematics of the described ion sources: a) SIMS, b) MALDI, c) DESI and d) ICP.

Mass analysers

Once gas phase ions are formed, they are injected into a mass analyser to determine their *m/z* ratio. A variety of different mass analyte technologies emerged over time with the most relevant to this study, quadrupole, time of flight and Fourier transformation-based technologies, *i.e.* Orbitraps and Fourier transformation ion cyclotron resonance (FT-ICR) mass analysers being described in more detail in below.

Quadrupole

A quadrupole mass analyser consists of four cylindrical rods set parallel to each other. The opposing rod pairs are electrically coupled and a radio frequency (RF) with an offset DC voltage is applied between the pairs. Technically, quadrupoles are pure mass filter as they filter the target ions bases on their *m/z* values from the bulk of ions entering the quadrupole. The target ions are isolated through modulation of the applied voltages to create stable ion trajectories through the quadrupole. The schematics of a quadrupole mass filter are displayed in Figure 1-2 a. As a quadrupole is only a mass filter, a detector is required to 'count' the isolated ions. Commonly an electron multiplier is used as a detector in purely quadrupole-based instruments.

Time of Flight (ToF)

ToF mass analyser separate ions based on their *m/z* value by measuring their flight time through a field-free region. The mass measurement is initiated by acceleration of the ions through an electric field of known strength. The acceleration field supplies all ions of the same charge state with the same kinetic energy resulting in differential acceleration of the ions dependent on their *m/z* value. Ions with small *m/z* values will travel with higher velocity through

the field free region than those with higher *m/z* values. Differences in velocity separate the ions in space, thus allowing detection of the individual ion packages traveling through the flight tube. As the resolution of ions with different *m/z* values is dependent on the length of the flight pass many modern instruments utilize a reflectron to re-focus the traveling ion packages and invert their flight pass to allow for a second pass through the flight tube. As for quadrupoles, ToF-based mass analysers only separate ions based on their *m/z* values and an electron multiplier, usually in form of a multi-channel plate (MCP) is used as a detector to 'count' the arriving ions.

Fourier transformation (FT) based mass analysers

FT- based mass analysers differ from the previously described ones in that ions are trapped in a cell and the cell will act as mass analyser and detect all ion species simultaneously. In Orbitrap-based instruments, the ions injected into the trap are attracted to the static voltage applied to the spindle-shaped inner electrode. The trapped ions are stabilized in their *m/z* specific orbit by their inertia opposing the electrostatic attraction of the inner electrode. The formed ion packages travel along the axis of the inner electrode and the axial frequency is detected as free induction decay at the grounded outer electrodes. The schematics of an Orbitrap mass analyser are displayed in Figure 1.2 c. Fourier transformation - ion cyclotrons resonance (FT-ICR) instruments detect ions in a similar way. The ions are injected into the trapping cell with an externally applied electromagnetic field. The ions are excited by excitation plates within the cell and stabilized on axial rotational orbits. During the rotations the traveling ion packages pass detection plates on which the FID can be detected. The schematics of an FT-ICR are displayed in Figure 1.2 d. The FIDs detected by Orbitraps or FT-ICRs can be decoded into a frequency distribution through Fourier transformation and subsequently be translated into *m/z* values. The resulting mass spectrum is created based on the oscillation frequency which translates to *m/z* value and the amplitude of the FID which correlates with the number of ions traveling in the trap. As in FT-based mass analyser the spectral resolution of the peaks correlates with the number of oscillations inherently peaks in the small *m/z* range

are detected with higher resolution than peaks in higher mass ranges. Equally, as the mass resolution is based on the number of detected oscillations, the mass resolution of FT based mass analyser increases the longer the FIDs are recorded.

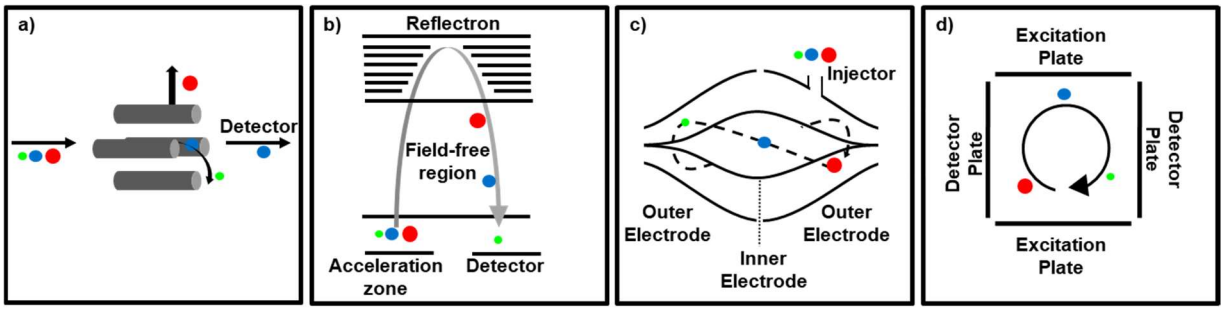

Figure 1.2, Schematics of different mass analysers: a) quadrupole, b) time-of-flight (ToF), c) orbitrap and d) Fourier transformation – ion cyclotron resonance (FT-ICR)

Combinations of mass analyser – Hybrid mass spectrometer

Mass analyser are often combined in so called 'hybrid mass spectrometer' to further study molecular ion species in tandem-mass spectrometry (tandem-MS or MS/MS) experiments. Usually a quadrupole is utilized to select an ion of interest and further characterize it. The ion of interest, the precursor ion, is subsequently accelerated into a second quadrupole which is filled with a gas, commonly argon or nitrogen. The quadrupole is operated in RF mode only guiding the ions during the collision events between the ions and the gas. When colliding with the gas, the kinetic energy of the ions is partly converted into elastic deformation of the molecular orbitals, resulting in separation of bonds when the impact energy exceeds the binding energy of the molecular orbitals. This principal of collision induced dissociation (CID) is used to generate a spectrum of the product ions obtained from the selected precursor ion (MS^2 spectrum) when analyzed in a research grade mass spectrometer with a high-resolution secondary mass analyser, *i.e.* ToF, orbitrap or FT-ICR. The generated product ion spectra can be interpreted to elucidate the molecular structure or be used as a molecular fingerprint and matched with a product ion spectrum of a reference standard. Though product ion spectra can be recorded with mass spectrometers where the secondary mass analyser is a quadrupole (triple quadrupole or TQ), but the low mass resolution of the quadruple and limited sensitivity of these instruments when operated in multiple-reaction-monitoring (MRM) mode, make this application obsolete. Today, TQs are mostly operated in static modes where Q1 is statically

set to a specific precursor, Q2 is used as a collision cell and Q3 is statically set to a previously identified product ion. Such static operation modes allow monitoring of one or more ions of interest with high specificity based on the fragmentation and high sensitivity as most of the chemical background noise will be removed by the dual mass filtering of Q1 and Q3. The high sensitivity of these instruments over a wide dynamic range is commonly used for targeted quantification of analytes.

Hyphenated mass spectrometry based technologies

The wide scope of applications and the wealth of information that provided by mass spectrometers drives the combination of mass spectrometers with orthogonal techniques. The aim of these orthogonal techniques is often to make samples accessible to mass spectrometric analysis or to separate sample components from one another through chromatographic separation techniques such as gas chromatography (GC) or liquid chromatography (LC) as examples of mass spectrometer couplings relevant to the here presented work. The principles of liquid chromatography – mass spectrometry (LC-MS) and laser ablation – inductively coupled plasma – mass spectrometry (LA-ICP-MS) will be explained below.

Liquid Chromatography – Mass Spectrometry (LC-MS)

To reduce ion suppression effects arising from the sample matrix liquid chromatography uses the principle of retention of analytes on a stationary phase to separate analytes in complex mixtures. For the separation, liquid samples are loaded onto a column filled with a stationary phase and the analytes are eluted with a mobile phase. In classical column chromatography the mobile phase runs through the column driven by gravity. To increase the separation efficiency and decrease the time demanded for full chromatographic separation, the mobile phase is usually delivered with elevated pressures in (ultra) high performance liquid chromatography (HPLC and UHPLC) setups. The chromatographic separation is based on differential affinity of the analytes to the stationary phase and analytes will ideally elute fully separated from one another under optimized chromatographic conditions. The stationary phase usually consists of porous silica spheres with or without chemical surface modifications.

Silica particles without surface modifications are commonly used in combination with aprotic hydrocarbon based mobile phases such as chloroform or hexane in what is defined as normal-phase chromatography to separate analytes soluble in non-aqueous solvents. The separation mechanism in normal-phase chromatography is largely based on adsorption effects of analytes on the stationary phase. Analytes usually elute from a normal-phase column in the order of polarity, with lipophilic compounds eluting first and the most polar compounds last. More commonly used for experimental procedures in life science and pharmaceutical research is reversed-phase (RP) chromatography, which uses silica spheres with modified surface-chemistry. The RP modifications include lipophilic groups such as octyl (C-8), octadecyl (C-18), phenyl-hexyl or pentafluorophenyl (PFP) groups (Figure 1.3). The mobile phases in RP chromatography usually consist of aqueous mixtures of polar-protic solvents such as methanol, 2-propanol, acetonitrile which can contain modifiers such as formic, acetic and trifluoroacetic acid or ammonium formate and acetate. The main mode of separation in reversed-phased chromatography is surface interactions between non-polar residues of the analytes and the stationary phase, retaining analytes with larger non-polar residues longer than those with large polarized surface areas. This mechanism allows separation of analytes over a wide chemical scope, covering biologically relevant analyte classes such as organic acids, lipids, proteins and peptides.

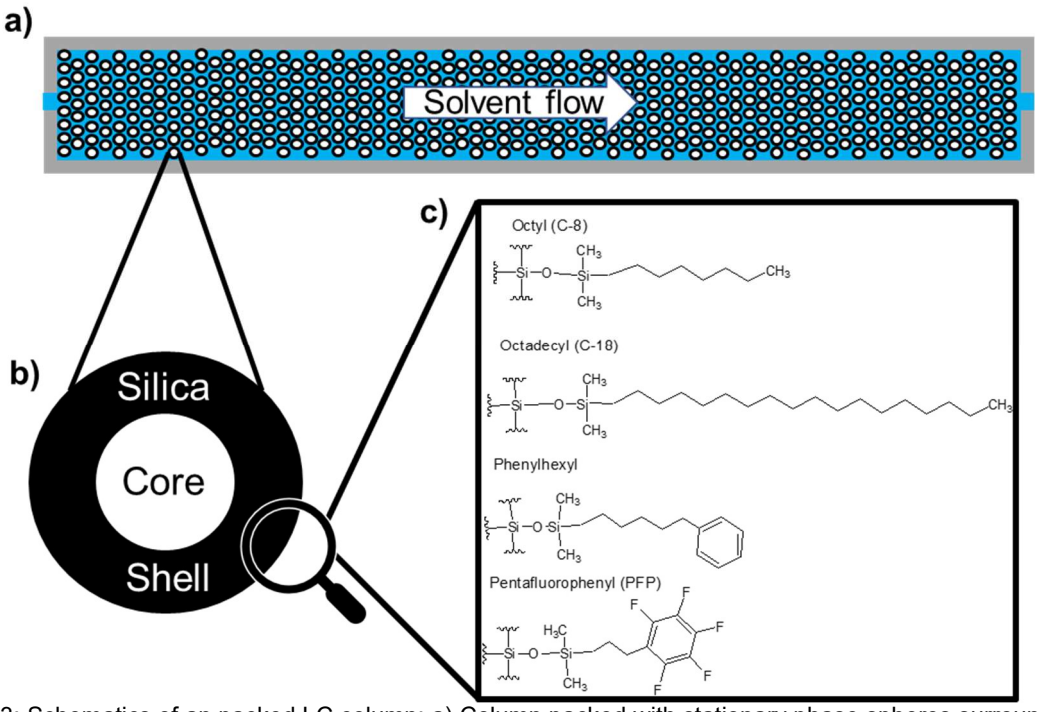

Figure 1.3: Schematics of an packed LC column: a) Column packed with stationary phase spheres surrounded by the flowing mobile phas. b) Zoom on a stationary phase sphere composed of the polymer core surrounded by the silica shell. c) Selection of common surface modifications used for reversed-phase liquid chromatography.

Laser ablation – inductively coupled plasma - mass spectrometry (LA-ICP-MS)

LA-ICP-MS is commonly used for direct elemental analysis of solid samples such as glass, soil, car paints or bones and teeth without complicated sample preparation. In short, a laser is used to ablate material from the sample surface and the ablation plume is introduced into the ICP torch where elemental ions are formed and analyzed by a mass spectrometer to detect and quantify elemental species within the sample. Recent advances in speed and sensitivity of LA-ICP-MS instrumentation allow high spatial resolution analysis of tissue sections. Commercially available LA-ICP-MS instruments, intended for the analysis of tissues, use heavy metal tagged antibodies, as those used for mass cytometry, and stain the targets *in situ*. Based on the principles of mass cytometry, this technique was adapted as imaging mass cytometry (IMC). The tissues are analyzed by ablating the tissues pixel-wise with a laser. The ablation plume is introduced into the ICP torch to remove organic molecules and ionize the heavy metal tags, allowing for detection with a fast scanning ToF-based mass spectrometer. The abundances of the detected metals for each pixel can then be reconstructed into ion density maps visualizing the distributions of the reporter ions and thus the target of the used antibody. Numerous antibodies against cellular targets are available and can be individually

tagged and multiple targets can be detected in the same experiment. These highly multiplexed experiments recode a wealth of information about tissue architecture and cellular populations can be recorded at once. This information is often used to segment tissues based on different cell and subtype population within the tissue. This segmentation approach, which was adapted as phenotyping, refines the segmentations through continuous addition of defining cellular marker thus continuously refining cellular and subtype annotations.

Histological techniques

Evaluation of tissues is commonly performed via histological analysis of stained sections of frozen or fixed tissues. The tissue sections are commonly stained with dyes to assess tissue morphology. Other approaches with higher information content are built around affinity-based reactions to stain for specific proteins or ribonucleic acids (RNA).

Dye-based stains

Dye-based stains are commonly utilized to allow for morphological assessment of a given tissue. Differences in the affinity of the dyes reveal the tissue structure. The tissues are often counterstained to highlight nuclei to identify individual cells. Probably the most commonly used dye-based stain uses hematoxylin and eosin (H&E). Eosin is a lipophilic red dye which accumulates in lipid membranes whilst hematoxylin stains predominantly chromatin but also the rough endoplasmic reticulum, ribosomes, collagen, myelin, elastic fibers, and acid mucins. Combined both dyes allow assessment of the cellular tissue composition and overall morphology. The stained tissue sections are evaluated with a brightfield microscope.

Affinity based stains

Affinity-based stains are commonly utilized to stain for specific peptides, proteins or RNA strains with selective probes and are commonly counterstained by nuclear marker such as hematoxylin, DAPI or Hoechst stain to visualize the underlying tissue morphology.

Immunohistochemistry (IHC)

IHC utilized antibodies to selectively bind to peptides or proteins in the tissue section, thus visualizing its expression. Usually a combination of a primary and a secondary antibody is used for IHC - the primary antibody binds to the target structure within the tissue whilst the secondary antibody, which is conjugated with alkaline phosphatase (AP) or horseradish peroxidase (HRP), detects species specific epitopes on the primary antibody. The reporter enzymes AP and HRP catalyze reactions forming a water insoluble dye which, depending on the reporter molecule used, usually precipitate as brown or red-pink spots where the target and thus the enzyme is present. The stained tissue sections are evaluated with a brightfield microscope.

Immunofluorescence (IF)

In principle the basics of IF are the same as described in IHC with the difference that the reporter molecule is a fluorescent dye which is conjugated to either the secondary antibody or less commonly to the primary antibody. If the label is attached to the primary antibody no secondary antibody is required. The stained tissue sections are evaluated with a fluorescence microscope.

In-situ hybridization (ISH)

In contrast to IHC ISH is utilized to visualize the distribution of deoxyribonucleic acid (DNA) and RNA. The probes are normally based on oligonucleotides that complementary hybridize with the target DNA or RNA at elevated temperatures. Excess probes can be removed using washing solutions. To only leave behind probes with full sequence binding to the target pH, detergent addition, temperature and osmolarity of the solutions can be adjusted. The probes can either be directly labelled or to increase specificity secondary reporter probes can be used. This dual-probe approach increases sensitivity when multiple reporter probes can bind to the primary probe. For detection of the target fluorescent dyes, alkaline phosphatase or less commonly radionucleotides can be conjugated to the labeled probe. The distribution of the

target DNA or RNA is determined via fluorescence microscopy, brightfield microscopy or autoradiography.

Transmission Electron Microscopy (TEM)

TEM is commonly used to evaluate the subcellular structures of cells and tissues. To prepare the specimens for analysis, the tissue's ultrastructure needs to be preserved through fixation in aqueous glutaraldehyde and osmium tetroxide solutions. Osmium tetroxides takes a dual function in TEM as it efficiently crosslinks lipid membranes and contrasts them by acting as an electron dense material. Tissue specimens are commonly further contrasted with agents such as uranyl acetate and lead citrate to allow visualization of the ultrastructure in greater detail. The specimens are then dehydrated, resin embedded, sections are collected at around 100 nm, placed on copper grits and analyzed. Electron microscopy shares the basic principles with light microscopy. Where for light microscopy the achievable magnification is limited by the wavelength of the photons, in electron microscopy the resolution is limited by the wavelength of the emitted electrons. The wavelength of electrons traveling with high velocity is orders of magnitude smaller that the wavelength of photons, allowing imaging down to atomic resolution. The image acquisition in TEM is initiated by emitting electrons form a tungsten filament or lanthanum hexaboride single crystal. The traveling electrons are focused and pass through the specimen. The electrons travel nearly unimpaired through electron light areas in the tissue, whilst they get slowed down or deflected in areas with accumulation of the contrast agents, shading these electron dense areas. In cells and tissues, these contrasts allow visualization of subcellular structures including visualization and differentiation of organelles such as mitochondria, lysosomes, vacuoles, nuclei and even lipid single and bi-layers.

Mass spectrometry imaging (MSI)

MSI as a collective of techniques bridges advanced chemical surface analysis with classical histology providing metabolite distribution maps for the different morphological features of a tissue. The ability to directly link metabolomic and proteomic profiles to the underlying tissue morphology makes MSI one of the most versatile tools in recent life science and

pharmaceutical research settings. However, MSI inherits the sample requirements and persisting problems from the bridged techniques. For example, mass spectrometry or nuclear magnetic resonance (NMR) spectroscopy based chemical analysis is commonly performed on tissue extracts to elucidate metabolomic and proteomic composition of the tissues or to identify xenobiotics within. However, the analyzed extracts lack any information regarding the spatial arrangement of the analytes within the tissue. The preparation protocols for these applications usually focus on the integrity of the analytes from sample collection until analysis. On the other hand, the main goal in sample preparation for histological analysis usually focus on preservation of the tissue morphology. Preparation protocols often include fixation of the tissues and cleansing of the tissues to increase optical transparency without any considerations to preserve the integrity of endogenous metabolites. For MSI, the stability of endogenous species is as important as the preservation of the tissue morphology to accurately link the bioaccumulation of metabolites, proteins and xenobiotics to the underlying morphological compartment. Impeccable histological preservation is of the essence when attempting to link these profiles to the underlying individual cellular phenotypes. To study spatial interaction maps on a wholistic level from small molecular species and metabolites over peptides to the underlying cellular and tissue interactions requires careful selection of the right sample specimens, processing protocols and MSI technique. The following paragraphs will focus on reviewing the current standards of instrumentation, considerations for the selections of sample specimens, processing protocols and the achievable data quality.

Selection of the ion source

The choice of the right ion source is dependent of the research question. Of the techniques described above, SIMS has the highest achievable spatial resolution. It enables visualization of elemental distributions on a nm scale and biomolecular distributions on a low µm scale. With respect to imaging of biological samples, commercial SIMS instruments are the only MSI platforms allowing analysis of single cells and elucidation of sub-cellular analyte distributions. However, the high energy ionization process induces severe fragmentation of molecular

species. Whilst this inherent fragmentation is leveraged in material sciences for instance in the analysis of synthetic polymers, it is a limitation to the chemical scope of biomolecules which can be detected from tissues. Whilst detection of elements and small molecular species are widely reported in the literature[28, 29], applying SIMS to image the distributions of intact larger molecular species such as lipids, peptides and proteins is possible[30, 31], but it has proven difficult. The spatial resolution of commercially available MALDI sources is around 10 to 100 µm and considerably lower than those achievable by SIMS. However, the chemical scope of accessible analytes is much wider spanning from small molecular species such as endogenous metabolites and lipids to intact peptides, proteins and other biological and synthetic polymers. The detection rates of target analytes can be influenced by the choice of the MALDI matrix as analytes incorporate differently into the crystal lattices of the matrices, resulting in differences in desorption/ionization efficacy. Whilst these phenomena can be leveraged to improve the detection of target analytes it can raise the need for time-consuming protocol optimization procedures. This is especially the case for analytes of low molecular mass analytes as their signals might be dwarfed or shaded by abundant matrix peaks. Selection of a different matrix or use of a deuterated matrix[32] compound might be necessary. Though imaging resolutions of down to 20 µm were reported for DESI-MSI[33], experiments are most commonly performed with spatial resolutions of 50 to 200 µm. The genuinely lower spatial resolution compared to MALDI and SIMS and the limited ability to detect peptides and proteins in DESI experiments is balanced by the wide accessible chemical scope of small molecular metabolites such as lactate, amino acids, organic acids, lipids without the spectral overlap commonly observed in MALDI experiments. Though commercial MALDI instruments can reach near single cellular resolution, the majority of MALDI and DESI experiments focus on the elucidation of analyte distribution on a tissue level aiming to differentiate the biodistributions across morphological features.

Selection of samples for MSI

Fresh frozen tissues are the current gold standard for MSI applications. However, recent reports focused on the analysis of archived tissue specimens such as formalin-fixed and formalin fixed paraffin embedded (FFPE) samples[34, 35]. These archived tissues are commonly used for histological evaluation of the specimens, leveraging the high preservation of the tissue morphology and easy sample storage at room temperature. The possibility to apply the same sample collection and preparation protocols or even use of the same samples for MSI as for histological evaluation would be beneficial. Streamlining of sample collection would reduce the workload during sample collection and the easy storage of formalin-fixed samples at room temperature eliminates the need to store samples in a -80°C or -150°C freezer for long-term archival.

However, histological preparation protocols are optimized to increase the clarity of optical images through removal of endogenous metabolites. Recent reports highlight the suitability of FFPE tissues for MSI-based tissue classification[36], proteomics[37] and N-glycan[38] studies. The sensitivity of the later applications is often limited in fresh-frozen tissue and tissue washes are commonly utilized. The washes aim to overcome ion suppression effects arising from the tissue metabolome and in particular from structural lipids[39, 40]. Comparable increase in sensitivity can be achieved through the preparation process for FFPE tissues, as the preparation is optimized to remove small molecular species, in particular lipids[41], from the tissue. This will ultimately alter analyte concentrations and potentially distorting the detectable distributions. The reproducibility of the preparation and evaluation of the general effects on the tissue metabolome is often insufficiently evaluated in the existing reports.

Fixed tissues are generally considered as chemically stable, and it is often neglected that the fixation in formalin is not an instantaneous step but progresses over time. Many enzymes show remnant post-mortem activity for several hours. During the fixation process the formaldehyde cross-linking disrupts enzyme activity, but only in fixed tissue compartments. Enzymes with reported post-mortem activity include choline acetyltransferase (ChAT), glutamine synthetase

(GS), glutamic acid decarboxylase (GAD), lactate (LDH) and glycerol-3-phosphate dehydrogenase (GPDH), tyrosine- and dopamine-β-hydroxylase, monoamine oxidase (MAO) and phospholipases[42-45]. Remnant enzyme activity in unfixed tissue compartments during the slow fixation could be a contributing factor in the established degradation of proteins and long DNA/RNA strands[46, 47] and lipids[48, 49] in FFPE tissues and is likely to similarly impact metabolites of the rapidly changing tissue metabolome.

Overall, the benefits of fixed tissues make them attractive substrates for MSI. The reduced workload during sample collection and possibility to store collected samples at room temperature would be beneficial for large scale MSI studies and creation of sample archives, analogous to clinical sample archives. Additional benefits arise from the effective inactivation of pathogens that might inherently be present in clinical samples and models for pathogen infection. These benefits raised the question if samples collected in formalin are generally suitable for MSI based drug metabolism and pharmacokinetic (DMPK) and metabolomics studies. The scope of the here presented work includes this evaluation and the experimental procedures and results can be found in Chapter 2.

Sample embedding strategies for MSI

Various embedding strategies have been reported in literature to improve the sample preparation for diverse imaging techniques, especially for the preparation of small or fragile samples as well as for whole animals[50, 51]. These strategies are commonly based on embedding in Optimal Cutting Temperature medium (OCT)[52, 53], sodium-carboxy-methyl cellulose (Na-CMC)[54, 55], gelatin[56], agarose[57] or poly(N-(2-hydroxypropyl)-methacrylamide) (HPMA)[58]. HPMA provides tissue support but also allows cold embedding (-8˚C) reducing the temperature difference between the frozen tissue specimens and the embedding medium thus limiting thawing of the specimens during preparation. It is imperative for any embedding protocol not to alter or thaw the samples to preserve the tissue morphology for histological evaluation. Additionally, the embedding should not alter the distribution of analytes within the tissue in order to allow accurate MSI results. Furthermore, the embedding medium should not

leak polymers which would alter the mass spectrometric signal or contaminate the instrument. Finally, the embedding should allow uncompromised integration of the sample preparation workflow with orthogonal tissue-based imaging techniques such as IHC, imaging mass-cytometry (IMC), fluorescence in-situ hybridization (FISH) or RNA-in-situ hybridization (RNA-ISH). These affinity-based techniques rely on hybridization of the probe with the target antigen or ribonucleic acid (RNA) and the ideal embedding medium does not show unspecific binding of probes or interferes adversely with the binding to their targets. Regarding mechanical requirements, the embedding medium must have sufficient viscosity and an adequate adherence to specimens to enable precise positioning of specimens and to allow easy sectioning without shifting or curling of sections. A systematic evaluation of the previously reported media was performed based on the criteria set above, but none met the requirements. For this reason, a new embedding medium was developed and evaluated as part of the here presented work. The experimental procedures and results can be found in Chapter 3.

Decontamination of clinical samples

MSI analysis of human specimens is gaining increasing importance in basic research into human tissue homeostasis in health and disease[6, 59, 60] as well as for drug disposition studies during clinical drug trials[61]. Clinically relevant material is often collected without further screening for the presence of potentially infectious pathogens though it is inherently likely to carry them due to the nature of the material. Clinical material can carry high viral loads which might experience aerosolization of the pathogens during the preparation or the analysis of the specimens. Whilst potentially infectious material needs to be handled in an air-flow controlled environment, preparation for MSI analysis involves steps which often require handling outside of such confinements. Sample preparation, especially cryo-sectioning and spray-deposition of ultraviolet light (UV) reactive MALDI matrices as well as analysis by ambient ionization techniques such as DESI or rapid evaporation ionization mass spectrometry (REIMS) may result in formation of airborne particles and aerosols which might carry an infectious load. Of particular interest for any chosen decontamination procedure is effective reduction of

potentially present viruses with human pathogenicity. Most troubling in this context are blood borne viruses and those with specific disease associations, such as Human Papilloma Virus (HPV) 16 and 18 in cervical[62], rectal and oropharyngeal[63, 64] cancer or Herpes viruses associated with Burkitt's and Hodgkin lymphoma, Kaposi's sarcoma, brain tumors, breast and cervical cancer respectively[65, 66]. To minimize health risks for the operator which are associated with the potentially infectious nature of the material part of the here presented work was to find and evaluate a reliable decontamination procedure compatible with downstream MSI analysis.

A wide variety of chemical, thermal or radiation-based decontamination strategies can be applied to decontaminate solid surfaces and biological materials for optical analysis. However, many of these strategies will impair subsequent MSI analysis as they might alter the chemical composition of the material or alter their biodistributions. Chemical agents such as *para*-formaldehyde (PFA), hypochlorite, hydrogen peroxide and organic solvents are highly effective, but they are commonly used in liquid form and as such likely to alter the metabolite distributions during the decontamination procedure. Heat treatment was previously reported as an efficient decontamination procedure[67] and downstream compatibility was shown for MSI analysis, but at cost of the integrity of the tissue morphology[68]. UV-C radiation has proven to be an effective germicide reducing viral, bacterial and fungal load. With a demonstrated reduction of clinically relevant viruses[69] and an active depth penetration of up to 40 µm into biological tissues[70], UV-C radiation is suited to decontaminate tissue slices for MSI analysis post cryo-sectioning whilst preserving the tissue morphology and biodistributions of metabolites within. The impact of the UV-C decontamination on the stability of endogenous metabolites and xenobiotics as well as other impacts on MSI analysis was evaluated as part of the here presented work. The experimental procedures and results can be found in Chapter 4.

Chapter 2 – Effects of sample collection protocols:

Aim/objective:

In this chapter MALDI- and DESI-MSI were used to evaluate the effects of formalin-fixation and. Formalin-fixed liver specimens were additionally paraffin embedded to create a multi-tissue FFPE block to evaluate the effects of downstream processing of the fixed tissues. The effects of the different collection and preparation procedures on the endogenous and xenobiotic tissue metabolome, including changes attributed to post-mortem enzyme activity, were evaluated.

Material and Methods:

Chemicals.

2,5-dihydroxybenzoic acid (DHB), 9-Aminiacridin hydrochloride (9-AA), trifluoroacetic acid (TFA), histology grade paraffin, terfenadine, dextromethorphan hydrobromide and diphenhydramine hydrochloride were purchased from Merck (Darmstadt, Germany). Methanol, water, iso-pentane, ethanol, xylene, 2-propanol and acetonitrile (ACN) were obtained from Fisher Scientific (Waltham, MA, USA). Losartan-potassium salt was obtained from Cambridge Bioscience (Cambridge, UK). All solvents used were of analytical grade or higher.

Animals and dosing.

Adult male Hans Wistar rats (approximate weight 260 g) were obtained from Charles River Laboratories (Margate, Kent, UK) and were acclimatized on site for a minimum of 3 days prior to dosing. Compounds were administered by oral gavage as a cassette of terfenadine, losartan, diphenhydramine and dextromethorphan, formulated in 5% dimethyl sulfoxide/95% (30% w/v) Captisol in water. Animals were dosed with 25 mg/kg/drug and euthanized 2 h post-dosing. Controls dosed with drug-free vehicle preparation were included in the study. Liver and Kidneys of the animals were dissected and separated. One half of the left kidney and one liver lobe were collected and stored in neutrally buffered formalin (Leica Biosystems, Nussloch, Germany). The remaining liver was immediately snap frozen in dry ice chilled 2-methylbutane.

To prevent fracturing of the kidney specimens, kidneys were snap frozen in dry ice chilled 2-propanol followed by a wash in dry ice chilled 2-methylbutane to wash off excess 2-propanol. The frozen tissue samples were stored at -80˚C until further processing. All tissue dissection was performed by trained AstraZeneca staff (project license 40/3484, procedure number 10). To evaluate the effects of short-term fixation, vehicle dosed rat liver specimens were fixed in formalin for 24 h and immediately prepared as described below. A total of n = 6 fresh-frozen kidneys (3 dosed, 3 vehicle controls) and n = 5 formalin-fixed kidneys (3 dosed, 2 vehicle controls) and n = 5 frozen liver specimen (2 dosed, 3 vehicle controls), n = 6 formalin-fixed specimens (3 dosed, 3 vehicle controls), and n = 6 FFPE liver specimens (3 dosed, 3 vehicle controls) were used to evaluate the effects of fixation and storage on the ENDOGENOUS AND xenobiotic tissue metabolome. The effects of 24 h formalin fixation were evaluated on frozen (n = 3) and formalin-fixed (n = 3) liver specimens collected from the vehicle control group.

Tissue preparation.

To enable cryo-sectioning of the formalin-fixed samples, the specimens were gradually washed for 1 min in 70% ethanol followed by 1 min in 100% ethanol to remove the adherent fixation buffer and subsequently snap frozen in dry ice chilled iso-pentane. Liver specimens selected for formalin-fixation, paraffin embedding were dehydrated and cleansed as described in Table 2.1 and subsequently co-embedded in a multi-tissue FFPE block.

Table 2.1: Preparation procedure for FFPE tissues

Treatment	Duration [h]	Temperature [˚C]
10% Formalin	1	40
70% EtOH	1	40
EtOH	1	40
EtOH	1	40
Xylene	0.5	40
Xylene	0.5	40
Paraffin	1	63

Tissue sectioning

Sectioning of frozen specimens was performed on a CM3050 S cryostat (Leica Biosystems, Nussloch, Germany) at a section thickness of 10 µm. The specimens were mounted with milli-Q water on the sample holder. The chamber temperature was set to -20˚C whilst the sample was held at -16˚C. For each animal, all matched tissue sections of formalin-fixed and fresh frozen tissues were mounted adjacent on one slide to achieve highest comparability of the results. Formalin-fixed, paraffin embedded tissues were sectioned to a thickness of 10 µm at room temperature on a Microtome (Finesse ME+, Thermo Scientific, Waltham, Massachusetts, USA) and straightened on a water bath held at 40˚C. The sections were fixed onto the slides by backing them for 1 h at 63˚C. To enable MSI analysis of FFPE treated samples the paraffin was removed by washing the slides for 1 min in xylene[71] followed by immediate drying under nitrogen. Samples were prepared on non-conductive SuperFrost microscope slides (Thermo Scientific, Waltham, Massachusetts, USA) for DESI experiments and optical stains whilst samples prepared for MALDI experiments were mounted onto conductive ITO slides (Bruker Daltonik, Bremen, Germany).

DESI-MSI.

Untargeted analysis was performed on a Q-Exactive plus mass spectrometer (Thermo Scientific, Bremen, Germany) equipped with an automated DESI ion source (Prosolia Inc., Zionsville, IN, USA). Data was acquired in positive detection mode between *m/z* 100 to 1000 and between *m/z* 80-1000 in negative ion mode. The nominal mass resolution was set to 70,000. The injection time was fixed to 150 ms resulting in a scan rate of 3.8 pixel/s. A home-built DESI sprayer[26] was operated with a mixture of 95 % methanol, 5 % water delivered with a flow rate of 1.5 µL/min and nebulized with nitrogen at a backpressure of 6 bar. The spatial resolution was set to 100 µm. The acquired .raw files were converted into .mzML files using ProteoWizard msConvert[72] (version 3.0.4043) and subsequently compiled to an .imzML file (imzML converter[73] version 1.3). All subsequent data processing was performed in SCiLS Lab (version 2019c, Bruker Daltonik, Bremen, Germany). All ion images are displayed normalized

to the total ion current (TIC) and with a weak denoising filter applied to compensate for pixel-to-pixel variability of the data.

MS/MS experiments were performed with the same instrument parameters as listed above. The data was acquired by running line scans across the tissue and collecting data with an increasing collision energy to acquire a variety of product ions. Applicable spectra were subsequently averaged and the resulting information rich product ion spectra were used for structural elucidation of the precursor ions. The injection time was fixed to 250 ms for all tandem-MS experiments. All precursor ions were isolated with an accuracy of ± 0.2 Da.

MALDI-MSI

To enable MALDI analysis, DHB was spray-deposited following a previously optimized protocol[74, 75]. A TM-Sprayer sample preparation system (HTX Technologies, LCC, Carrboro, NC, USA) was used to apply the matrix. DHB was dissolved in 50:50 v/v acetonitrile/water containing 0.1% TFA giving a final concentration of 37.5 mg/mL. The matrix solution was delivered with a flow rate of 80 µL/min and nebulized with a gas pressure of 10 psi. The nozzle temperature was set to 75 °C. A total of 8 passes of matrix application were performed in "criss-cross" pattern.

MALDI analysis was performed on a RapifleX Tissuetyper instrument (Bruker Daltonik, Bremen, Germany). MALDI experiments were performed with a spatial resolution of 10 µm. All MALDI experiments were performed in the mass range between *m/z* 100 and 1000 in positive ion mode. A total of 100 laser shots were summed up per pixel to give the final spectra. For all experiments the laser was operated with a repetition rate of 10 kHz. The acquired raw data was directly uploaded and processed in FlexImaging (Bruker Daltonik, Bremen, Germany) or SCiLS lab (Version 2019c) software packages. All MALDI data and images were normalized to the total ion current (TIC) to compensate for spectra-to-spectra variation of the data. In brief, TIC normalization is performed by dividing the abundance of each feature in a given spectrum to the sum of all features of the spectrum (or the TIC). Fundamentally, TIC normalization assumes that all spectra of a given experiment should have the same TIC and

if the experimental setup delivers spectra that in approximation have the same TIC It can efficiently compensate for variation in desorption/ionization efficiency. As in MALDI experiments the matrix itself generates ion cluster that generate analyte ions through charge competition it fundamentally fulfills the above criteria making TIC normalization particularly applicable for MALDI data[76].

Statistical analysis.

Features discriminating between the different treatments were identified using the receiver-operator-curve (ROC) function built-in in the SCiLS lab software. Features with a ROC-values above 0.75 were considered for further investigation. The results were manually filtered for massfilter representing chemical background detected on the slide and the remaining featured were annotated by accurate mass using databases such as METLIN (https://metlin.scripps.edu), human metabolome database (http://www.hmdb.ca) and LipidMaps (https://www.lipidmaps.org) were considered with a maximum error of 6 ppm difference between the mean measured and the theoretical mass. Overall, this approach is limited in its power for the identification of metabolites as it only relies on accurate mass measurement and usually further validation through tandem-MS, LC-MS or NMR experiments is required for full structure elucidation. However, it can still provide valuable information pointing towards overall effect levels when comparing different treatment groups and numerous metabolite annotations fall into the same group (*e.g.* oxy-lipids). Statistical significance for the annotated features was determined from all pixel of each treatment group and testing using the Kruskal-Wallis test followed by Dunn's test for multiple comparisons performed in GraphPad Prism (V. 8.0.1) (GraphPad Software, San Diego, CA, USA).

Results and Discussion

Formalin-fixation and formalin-fixation, paraffin embedding of fresh frozen specimens inflicts significant alteration of the detectable tissue metabolome. Figure 2.1 shows representative mean spectra of rat liver sections for the different treatment conditions. Fresh-frozen tissue sections show a typical DESI spectrum with small molecules such as amino acids, organic

amines, sugars and carnitine species in the low mass range between *m/z* 100-500, lysolipids and diglycerides in the mass range between *m/z 400-600* and glycerophospholipids such as phosphatidylcholines (PCs), phosphatidylethanolamines (PEs), phosphatidylserines (PSs), phosphatidylinositols (PIs), sterols and triglycerides in the mass range between *m/z* 600-1000. Whilst the spectrum of the formalin-fixed specimens is superficially comparable to the fresh frozen sample, the spectrum differs with overall reduced abundances and more visible peaks in the low mass range of the spectrum and a shift towards lower masses in the lipid range. The spectrum of the formalin-fixed, paraffin embedded sample was distinctively different with a prominent lack of signals in the lipid range and broad enveloped signals in the mass range between *m/z* 100-500.

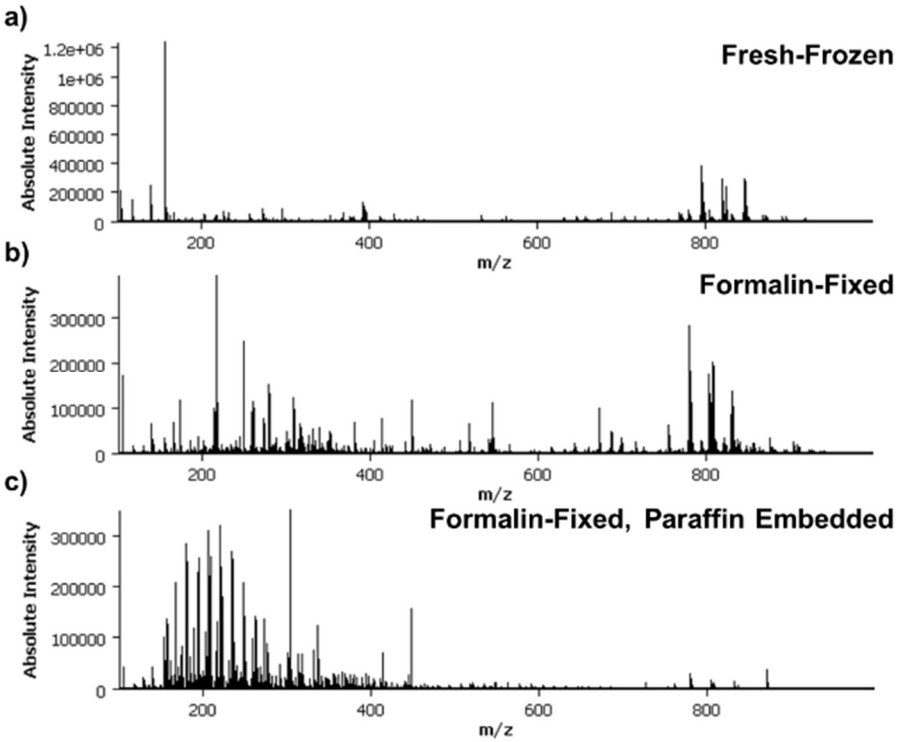

Figure 2.1, Representative mass spectra for the different sample collection conditions: a) fresh-frozen, b) formalin-fixed and c) formalin-fixed, paraffin embedded rat liver specimens analyzed by DESI-MSI in positive ion mode. All tissues were collected from the same animal.

The later are likely to be condensed formaldehyde oligomers[77]. Closer investigation revealed significant alterations of the endogenous tissue metabolome. The changes include washout of small molecular species such as amino acids, fatty acids and organic amines, oxidation of fatty acids (FAs) and lipids and reduced abundances of glycerophospholipids paired with increased

abundances of lyso-lipids, indicative of lipid hydrolysis (Figure 2.2). The washout of small molecular species was found to affect organic and inorganic species equally. The washout of potassium ions was most noticeable through the differences in adduct formation. In agreement with literature reports[78], highly abundant potassium adducts of PCs, PEs, di- and triglycerides observed in fresh-frozen tissues were significantly reduced leaving sodium adducts as the main molecular ion species for these analyte classes in formalin-fixed samples. These observations are consistent with the lower abundance of potassium chloride cluster in the fixed samples (Figure 2.2).

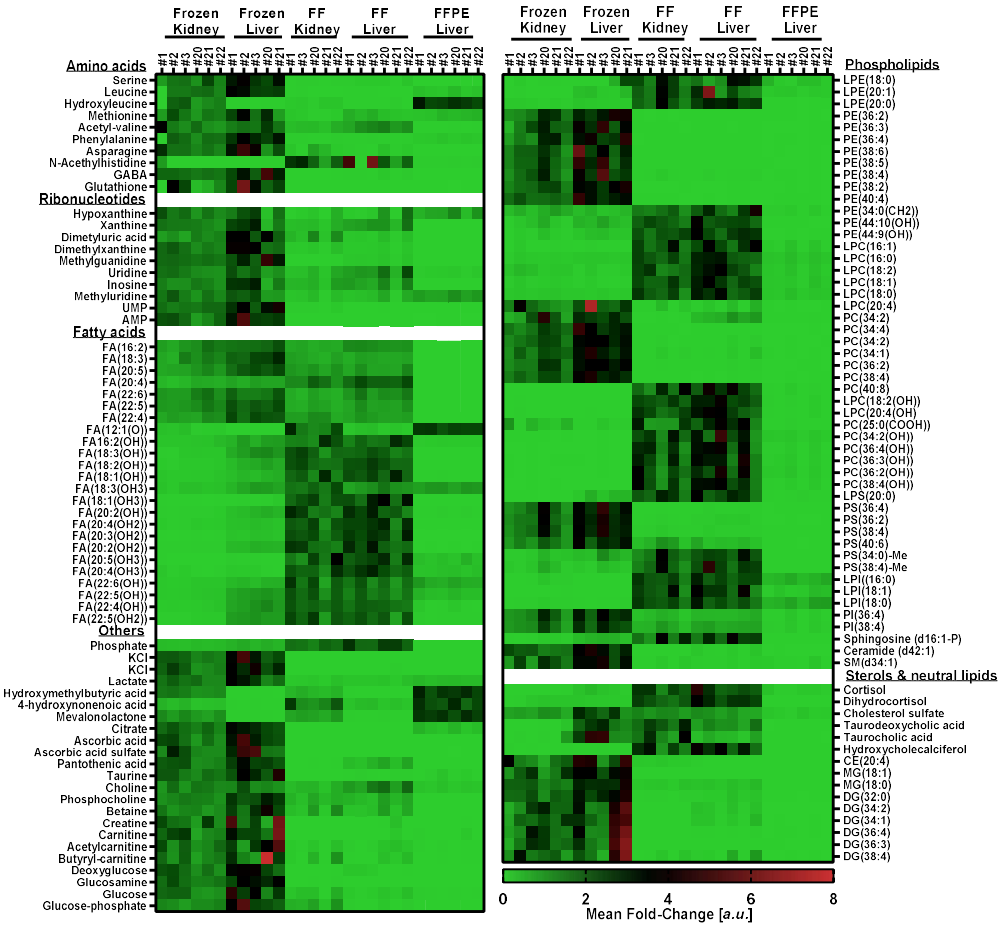

Figure 2.2, Effects of formalin fixation and formalin-fixation, paraffin embedding onto the tissue metabolome: Mean-Fold changes of metabolite abundances of fresh-frozen and formalin-fixed rat kidneys and fresh-frozen, formalin-fixed and formalin-fixed, paraffin embedded rat liver specimens respectively. Mean-fold changes were calculated to the average of all analyzed specimens in all treatment groups of one organ Detailed information for the annotations can be found in Table A1.1. Detailed information regarding statistical significance for the changes can be found in Table A1.2.

The lack in detection of analytes which primarily form potassium adducts might be misleading as it might be interpreted as absence of the analyte whilst it is likely that the predominant

adduct ion is missing and the analyte of interest is detected as a different molecular ion species. FFPE tissues showed overall a significant removal of a wide range of analytes from small polar analytes such as amino acids and organic amines to structural lipids. Class specific depletion of amine containing lipids upon formalin-fixation was previously reported[49] and has been linked to formylation of primary amine groups[48] present in lipid classes such as PEs and PSs. Tandem-MS experiments were performed to validate some of the annotations in Figure 2.2 and increase the understanding of the alterations formalin inflicts on the tissue metabolome.

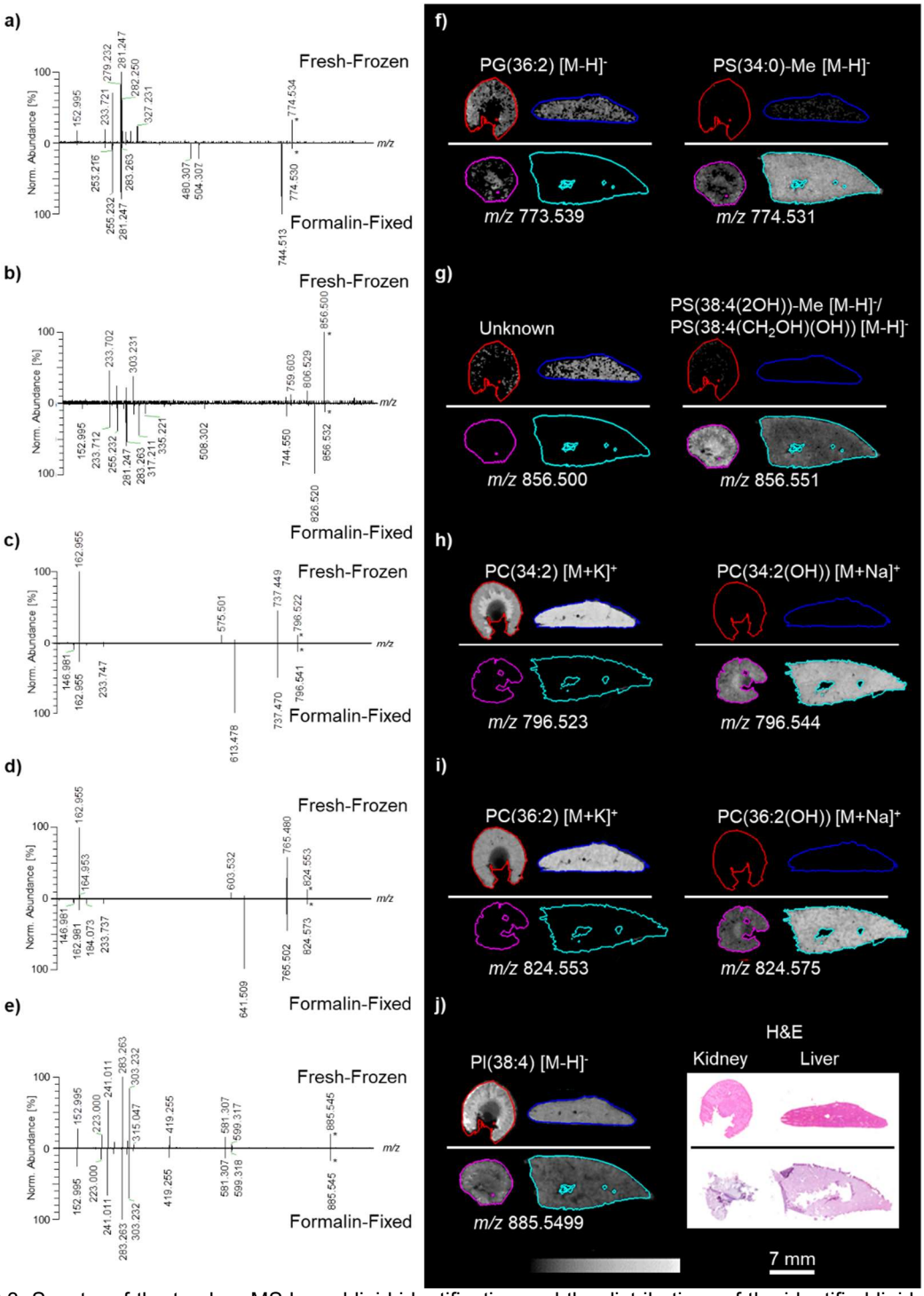

Figure 2.3, Spectra of the tandem-MS based lipid identification and the distributions of the identified lipid species in fresh-frozen and formalin-fixed tissues: MS/MS spectra of heatmap lipids in fresh-frozen (top) and formalin fixed liver (bottom) for a) m/z 774.5 (negative ion mode), 856.5 (negative ion mode), 796.5 (positive ion mode), 824 (positive ion mode) and 885.5. The * labels the precursor ions in each spectrum.

In fresh-frozen samples, the *m/z* 774.534 was found to correspond to the M+1 isotope of PG(36:2) detected as $[M-H]^-$ identifiable through the strong abundance of isotopes of the fatty acids *e.g. m/z* 282.250 as M+1 isotope of *m/z* 281.247 corresponding to FA(18:1). Isolation of the same precursor mass on formalin-fixed liver led to the identification of PS(34:0)-methyl

ester (Figure 2.3a,f). The methylation was elucidated from the neutral loss of 30 Da (*m/z* 774.530 to 744.513), which corresponds with the elimination of formaldehyde through comproportionation of the methanol and the carboxylic acid into the corresponding aldehydes. Isolation of *m/z* 856.500 from fresh-frozen tissue resulted in a product ion spectrum of a molecule that could not be elucidated solely from the product ions. The neutral loss of 50 Da (from *m/z* 856.500 to 806.529) indicates loss of CH_3Cl, which is indicative for phosphatidylcholines ionized as $[M+Cl]^-$, however, no reasonable structure could be elucidated matching the fatty acid chain composition (Figure 2.3Figure 2.3b). Isolated from formalin-fixed liver the product ion spectrum is dominated by the neutral loss of 30 Da indicating as above the formation of a methyl ester. The oxidation of the poly unsaturated FA(20:4), detected as shift of 2*16 Da from *m/z* 303.231 to *m/z* 335.221 for the double oxidized fatty acid and *m/z* 317.211 for the corresponding to the $[M-H_2O-H]^-$ of FA(20:4(2OH)). The oxidation complicates the determination of the exact molecular species as the spectrum does not allow exclusion of the possibility of the oxidized and N-formylated PS(38:4(CH_2OH)(OH)). Overall, the tandem-MS analysis validated putative lipid annotations confirming the presence of N-formylated PS species in formalin-fixed tissues (Figure 2.3a,b). In addition to formylation, methylation of the carboxylic acid moiety was observed. The methanol for the esterification is likely to originate from the commercially sourced formalin solution, in which it is commonly added to prevent spontaneous condensation reactions[79, 80] and oxidation of the formaldehyde. The majority of alterations in the lipidome were oxidation products of the unsaturated fatty acids in the lipids, validating the lipid annotations in the heatmap. It is notable that the potassium adducts of lipids in positive ion mode are close in mass to sodium adducts of the corresponding oxy lipid species, i.e. PC(36:2) as $[M+K]^+$ has a theoretical mass of 824.557 whilst PC(36:2(OH)) as $[M+Na]^+$ has a theoretical mass of 824.577. As these species are too close in mass to be resolved by a quadrupole in a tandem-MS approach, the resulting overlapping product ion spectra needed careful deconvolution (Figure 2.3c,d). Both precursor ions isolated from fresh-frozen tissue showed a neutral loss of 59 Da corresponding to the neutral loss of trimethylamine and a product ion detected at *m/z* 162.955 corresponding to ethylene-

cyclophosphane as $[M+K]^+$ ion[3] identifying the precursor as PC(34:2) and PC(36:2) detected as $[M+K]^+$ respectively. The product ion spectra acquired from formalin-fixed tissue share the same product ions as those from fresh-frozen tissue, but show an additional product ion at *m/z* 146.981 corresponding to the above described ethylene-cyclophosphane product ion detected as $[M+Na]^+$. The most reasonable explanation for the presence of the product ion is a shift from PC(34:2) and PC(36:2) detected as $[M+K]^+$ to PC(34:2(OH)) and PC(36:2(OH)) detected as $[M+Na]^+$ respectively. The annotation of the deconvoluted product ion spectra and their respective distributions in fresh-frozen and formalin-fixed kidney and liver are displayed in Figure 2.3c, d. With exception of product ion spectra obtained from PIs, the product ion spectra acquired from formalin-fixed samples were overall more complex than even the MS/MS spectra for the same masses obtained from fresh-frozen specimens. The significant alterations of the lipidome resulted in numerous additional peaks in the spectrally complex mass range between *m/z* 600-1000 which contains the structural lipids.

Pixel-wise Principal Component Analysis (PCA) performed on all samples found the largest variance in PC1 (variance explained by PC1 = 16.08% (positive ion mode and 9.49% negative ion mode) , for both positive and negative ion mode, to distinguish FFPE tissues from fresh-frozen and formalin-fixed samples. Subsequent principal components were found to largely account for the effects of the formalin-fixation (variance explained: positive ion mode: PC2 = 8.04%, PC3 = 6.07% and PC4 = 3.79%; negative ion mode: PC2 = 8.26%, PC3 = 4.63% and PC4 = 3.21%). Overall, even the difference between fresh-frozen liver and kidney specimens was lower than the variance introduced though the different sample treatments (Figure 2.4Figure 2.4). Little variance was found within the tissue sections by the spatial PCA maps.

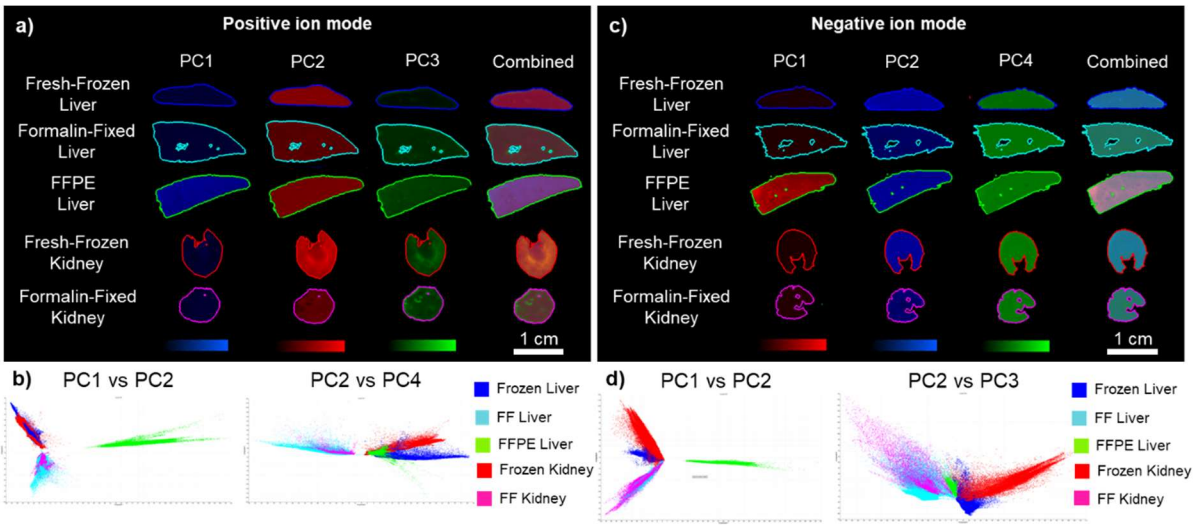

Figure 2.4: Pixel-wise PCA performed on tissue sections obtained from fresh-frozen, formalin-fixed and FFPE tissues: a) shows the representative spatial PCA maps for fresh-frozen, formalin-fixed (FF) and FFPE liver as well as fresh-frozen and formalin-fixed kidneys analyzed in positive ion mode. b) Corresponding scoring plots for all samples, the left-hand side shows PC1 vs PC2 and the right-hand side PC2 vs PC3, respectively. Each datapoint represents a single spectrum. c) Representative spatial PCA maps for fresh-frozen, formalin-fixed and FFPE liver as well as fresh-frozen and formalin-fixed kidneys analyzed in negative ion mode. b) Corresponding scoring plots for all samples, the left-hand side shows PC1 vs PC2 and the right-hand side PC2 vs PC3, respectively. All displayed tissue sections originate from the same animal.

To evaluate the suitability of fixed samples for drug distribution and spatially resolved pharmacokinetic studies the effects of the sample collection and processing were evaluated for the dosed drugs. The formalin-fixation did not significantly change the mean abundances of diphenhydramine, dextromethorphan or terfenadine in liver or kidney sections whilst losartan experienced significant washout from the liver specimens (Figure 2.5a, b). Elucidation of drug distributions from FFPE samples was not possible as the drug abundances were close to background levels.

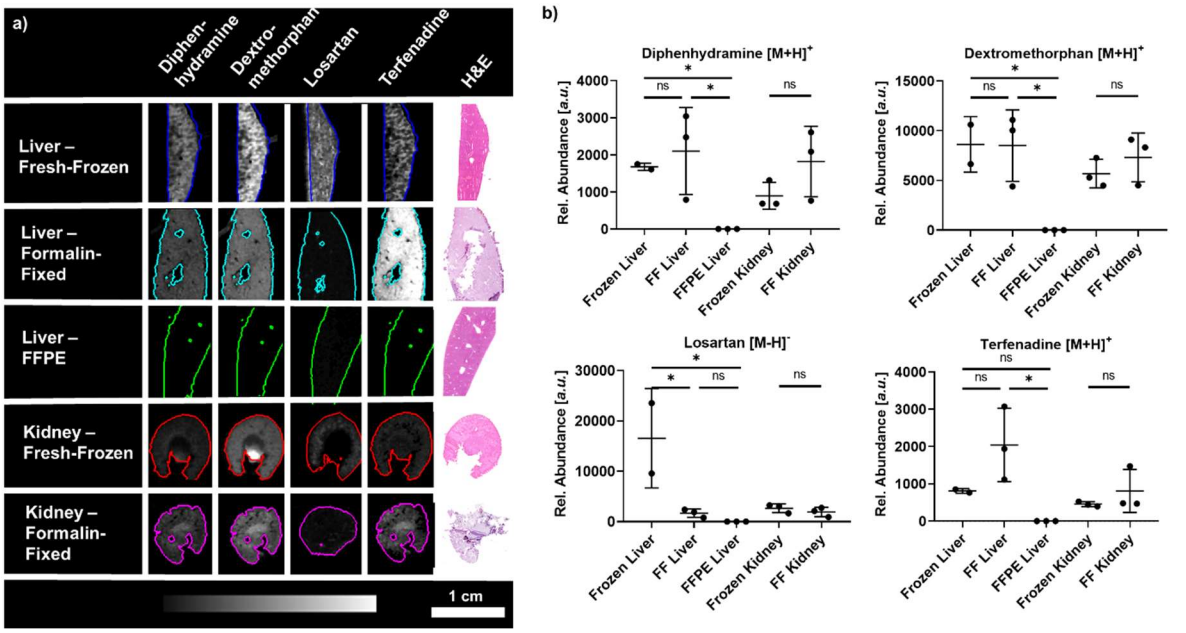

Figure 2.5: Effects of the sample collection and preparation on drug distribution and abundance: (a) representative distributions of the drugs and (b) mean abundance within the tissue sections for all biological replicates. Statistical significance one-way ANOVA for liver samples, two-tailed t-test for kidneys. ns = p(>0.05), * = p(<0.05), ** = p(<0.01), *** = p(<0.001)

Even though the mean abundances of the drugs were overall not significantly different, formalin-fixed samples showed higher variability between the biological replicates compared to the fresh-frozen samples. Whilst the mean abundances of diphenhydramine and terfenadine showed little variation between the fresh-frozen samples, the mean drug abundances in the formalin-fixed specimens were more variable with samples showing up to 3-fold higher abundances compared to unfixed samples. The higher abundances might be rooted in removal of organic and inorganic salts from the tissues reducing ion suppression effects[39, 81]. In addition to the altered abundances, distortion of the elucidated drug distributions was observed. The dosed drugs showed distinct zonation in the fresh frozen liver specimens, but the zonation of the drug distributions was lost within the formalin-fixed specimens. High resolution MSI experiments performed on fresh-frozen liver sections allowed elucidation of the distribution of terfenadine and its active metabolite fexofenadine on the morphological level of the liver (Figure 2.6). Terfenadine was detected in highest abundance in the periportal zone (hepatic zone 1), in contrast the endogenous lipid PC(36:2) which showed highest abundances in the centrilobular zone (hepatic zone 3) co-localizing with fexofenadine. Sections of the formalin-fixed counterpart were analyzed in the same experiments, but the dry tissue sections

were largely ablated during the data acquisition and no reasonable analyte distributions could be elucidated from these tissue sections.

Rapid freezing of the tissues post collection preserved the distribution of analytes within the specimens allowing accurate elucidation of rapidly changing analyte distributions. Formalin fixed samples did not preserve the endogenous analyte distributions resulting in loss and delocalization of analytes, making retrospective elucidation of accurate biodistributions impossible.

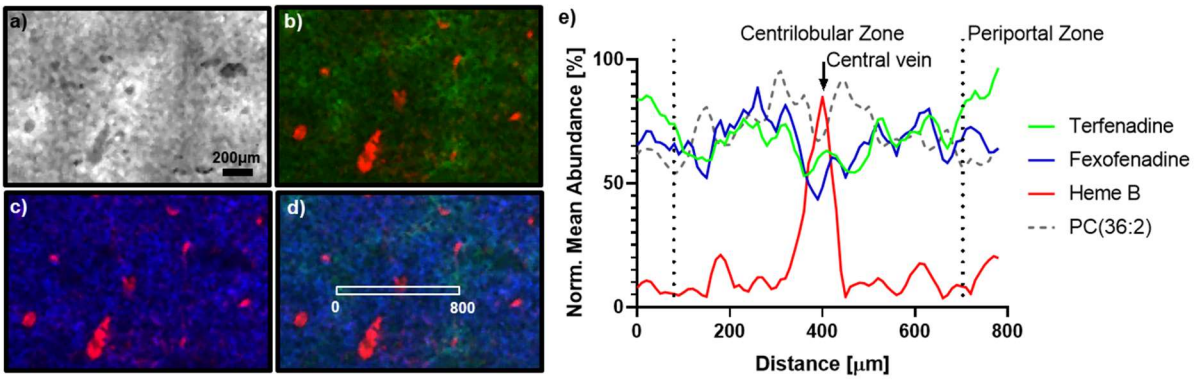

Figure 2.6, Distribution of terfenadine and its active metabolite fexofenadine in the rat liver: a) Hepatic lobule of a fresh frozen liver section outlined by PC(36:2) b) Terfenadine (green) in relative distribution to Heme B c) Distribution of Fexofenadine (active metabolite) compared to Heme B d) RGB overlay of Terfenadine, Fexofenadine and Heme B. The box highlights the pixel used for the profile plot. e) Profile plot of the normalized mean abundances of terfenadine, fexofenadine compared to PC(36:2) outlining the hepatic lobule and Heme B marking the central vein. Data is represented as mean of 3 separate lines, normalized to the highest pixel and cubically smoothed over 3 neighboring pixels to compensate for pixel-to-pixel variability.

The primary objective of this study was to evaluate the effects of prolonged storage of specimens in formalin solution at room temperature mimicking the treatment in a harmonized sample collection protocol for both MSI and histological studies. The magnitude of many of the observed alterations, especially of lipid hydrolysis, oxidation and washout are either reported to or are likely to correlate with the storage duration of the specimens in formalin[82]. The prolonged storage in formalin might lead to an overestimation of the effect level compared to the results of fixing for histological evaluation, which are with 24-72 h significantly shorter, but were not found to induce unprecedented effects observed in specimens fixed for 24 h. As the specimens stored in formalin showed significant delocalization and washout of small molecular species making elucidation of an analyte's origin within the tissue difficult, specimens fixed for 24 h were used to evaluate effects of remnant enzyme activity within the tissues. Even after

the shorter fixation, significant washout of low molecular weight analytes, especially around the tissue edges, made evaluation of standard tissue integrity benchmarks, such as the glutamine/glutamate ratios, difficult to evaluate. However, pixel-wise PCA revealed regional differences with the abundance PC2 increasing from the tissue edge towards the tissue core and PC3 fading from the tissue edge towards the core (Figure 2.7a). The gradual changes were found to spatially correlate with the increasing abundance of lyso-lipids towards the tissue core and the predominance of intact lipids at the tissue edges. The gradual differences within the formalin-fixed specimens point towards hydrolysis of PEs, PCs and PIs into the corresponding lyso-lipids and free fatty acids, as seen for PE(38:4) (detected as $[M-H]^-$ at *m/z 766.540)*, PC(38:4) (detected as $[M+Cl]^-$ at *m/z 844.564)*, and PI(38:4) (detected as $[M-H]^-$ at *m/z 885.550)* and the corresponding lyso-lipids LPE(18:0) (detected as $[M-H]^-$ at *m/z 480.310)*, LPC(18:0) (detected as $[M+Cl]^-$ at *m/z 558.334)*, and LPI(18:0) (detected as $[M-H]^-$ at *m/z 599.320)* and free fatty acid FA(20:4), which is most likely arachidonic acid. Both, lyso-lipids and free fatty acid were predominantly found in the center core of the fixed specimens and less in proximity to exposed edges and areas around larger blood vessels (Figure 2.7b).

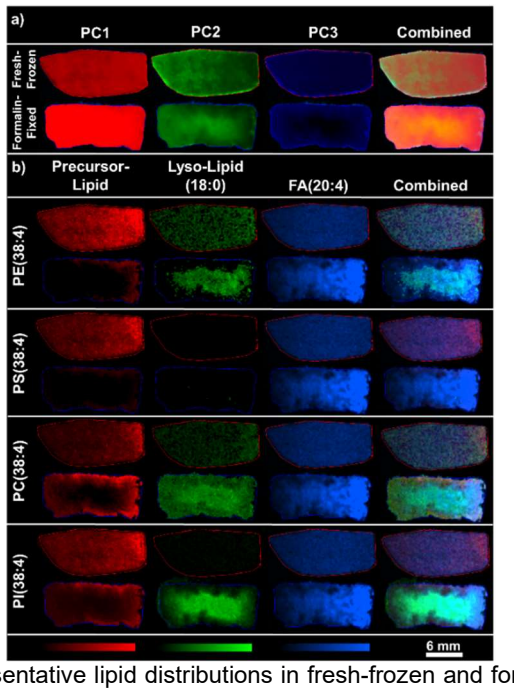

Figure 2.7, Comparison of representative lipid distributions in fresh-frozen and formalin-fixed rat liver specimens: a) Pixel-wise PCA of the tissue sections. PC1 (red) contributed 16.65 % PC2 (green) 9.38 % and PC3 (blue) 5.52% of the total observed variance. b) The regional differences found within the PC1-3 were found to correlate with the degradation of phospholipids in the tissue core and occurrence of the hydrolysis products lyso-lipids (18:0) and FA(20:4).

The localization of the lyso-lipids could be indicative of washout of the hydrolysis products from the tissue edges or chemical hydrolysis, however, lower abundance of the originating phospholipids and limited degradation of PS(38:4) (detected as $[M-H]^-$ at *m/z 810.528)* into LPS(18:0) (detected as $[M-H]^-$ at *m/z* 524.299) point towards remnant activity of phospholipases. In particular phospholipase A2 (PLA_2) could be accountable for the degradation, as it has been demonstrated to broadly accept PEs, PCs and PIs as substrates and to lesser extend PSs[83, 84]. The increased hydrolysis of lipids in the tissue core can be explained through the fixation kinetics of formaldehyde, which penetrates the tissue fast as the methanediol and reacts relatively slow as free aldehyde with amine and thiol groups within the tissue. Whilst fixed tissues are generally considered as stable, the actual fixation is a slow progressing process that can last several hours to fully fix the entire tissue as demonstrated in Figure 2.8.

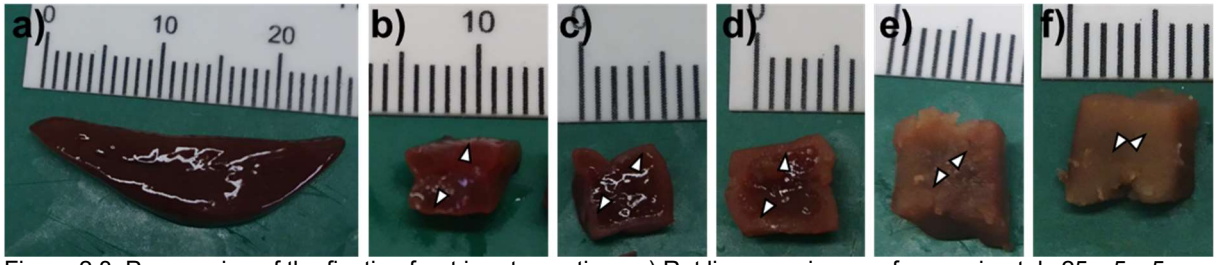

Figure 2.8, Progression of the fixation front in rat over time: a) Rat liver specimens of approximately 25 x 5 x 5 mm before fixation. The specimen was cut to expose the fixation front after b) 15 min, c) 30 min, d) 60 min, e) 120 min and f) 240 min in formalin. Arrowheads indicate the edge of the fixation front at the appropriate timepoints.

Analogue post-mortem alteration of the tissue metabolome and proteome through remnant enzyme activity can be assumed for a variety of analytes in unfixed tissue compartments. However, these changes might occur unnoticed even in controlled time-course experiments when the affected metabolites are washed out of the tissue during the fixation or subsequent sample treatments and were so far only reported for peptides[8]. If analyte distributions can be elucidated from fixed tissues, post-mortem alterations should be considered, and analyte distribution pattern should be thoroughly validated to avoid reporting of preparation artefacts.

Similar effects might arise from varying histological preparation protocols for the creation of FFPE tissue blocks. The used protocols might be adapted for different tissue types or vary

between automated platforms and laboratories. Varying preparation protocols are a source of variability on the level of proteomic, genomic, transcriptomic and histological investigation of tissues[85] and have to be assumed for investigation on a metabolomic level. These variations are difficult to control or retrospectively account for, especially in archived samples where the meta-data for the preparation might be missing. Furthermore, varying shapes, sizes and compositions of tissues introduce another source of variability which is difficult to control and even more difficult to standardize, thus limiting reproducibility. FFPE tissue specific preparation artefacts can arise from the cleansing steps to reducing endogenous metabolites and increase optical transparency of the tissue. These steps involve gradual dehydration in ethanol and rigorous washing in xylene and paraffin to remove endogenous lipids. Incomplete removal of lipids due to shape, size or different tissue composition of samples can falsify elucidated distribution patterns (Figure 2.9).

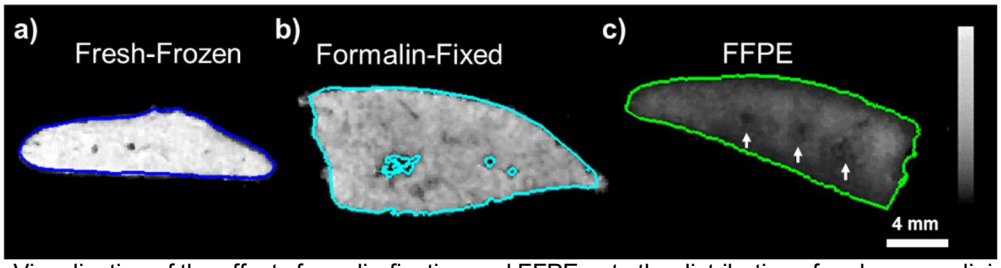

Figure 2.9, Visualization of the effects formalin-fixation and FFPE onto the distribution of endogenous lipid species: Distribution of PI(38:4) in a) fresh-frozen, b) formalin-fixed and c) formalin-fixed, paraffin embedded rat liver of the same animal. Arrows indicate areas of altered abundance of the lipid around larger blood vessel in the FFPE specimen.

Overall, the fresh-frozen samples were relatively easy to prepare with reasonable preservation of the tissue morphology, whilst formalin-fixed samples were brittle and difficult to cryo-section. Most formalin-fixed tissue sections were fragile and had low adherence to the glass slide resulting in partial ablation during DESI and MALDI analysis. Most analyzed slides had no relevant tissue remains suitable for histological evaluation. Even sections not analyzed by MSI were virtually impossible to H&E stain and most tissue sections were severely damaged or were removed from the slide during the staining procedure. However, the power of spatially resolved analysis is the ability to directly correlate the metabolic information obtained by MSI with the underlying morphology to draw conclusions about the underlying biological processes.

Without the morphological information, interpretation of MSI data may at best inform about high-level changes of the metabolome without enabling to link the metabolic information to the underlying cellular phenotypes. Paraffin embedding of formalin-fixed tissues was found to significantly improve tissue morphology, but at cost of analyte removal from the tissues. Taking advantage of the superior morphological preservation, the use of FFPE tissues for optical evaluation is well justified, however the use of such tissues for metabolomics and drug distribution studies remains questionable. To reduce workload during sample collection for prospective studies involving use of fresh-frozen and FFPE tissues, snap freezing of all tissues during collection and subsequent branching of the tissue preparation workflows should be considered.

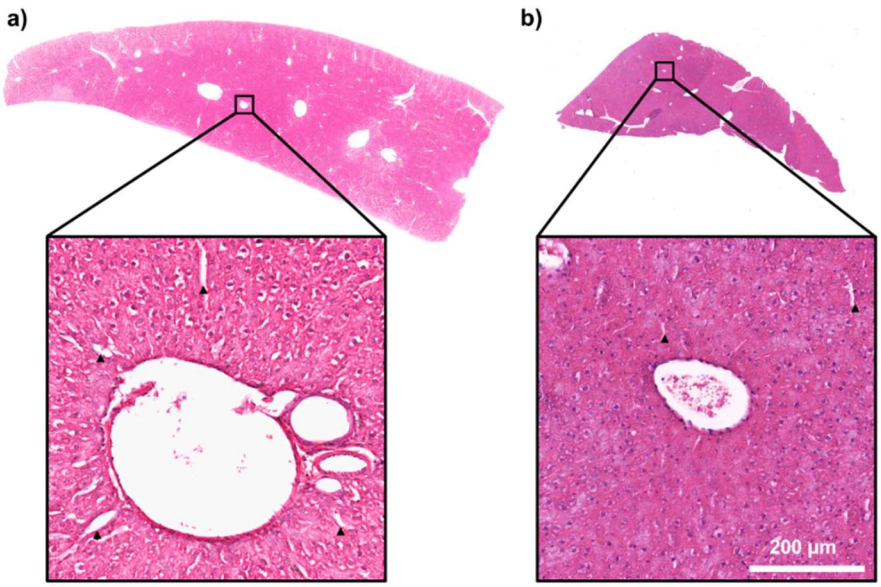

Figure 2.10, Effects of freezing and storage onto tissue morphology: H&E stained FFPE sections prepared from tissue a) collected and stored in 10% formalin or b) snap-frozen upon collection and subsequently fixed in 10% formalin for 24 h before paraffin embedding. Sections were cut at 10 µm thickness, analogous to the sections analyzed by MSI. The arrowheads indicate processing artefacts within the tissue sections.

Snap freezing offers unparalleled preservation of endogenous biodistributions of analytes without hampering the tissue morphology when freezing and storage are done correctly[85, 86]. Snap frozen samples can subsequently be processed into FFPE blocks through direct fixation of the frozen tissues in formalin and subsequent embedding in paraffin. Although this approach suffers the disadvantage that increased numbers of samples require storage at ultra-low temperatures, it does benefit from the ability to decouple sample collection and processing. Frozen samples can be stored at ultra-low temperatures without compromising quality[85]. This

allows one to schedule processing of tissues when capacity is available rather than having to process the tissues as dictated by the sample collection and the subsequent timings of the treatment protocols. Liver specimens collected and stored in formalin showed substantial impairment of the tissue morphology whilst FFPE tissues prepared from frozen specimens showed little hampering of the morphology by light microscopy (Figure 2.10) or on the ultrastructure evaluated by transmission electron microscopy (TEM) as described in chapter 7. The current and adapted workflows are depicted in Figure 2.11.

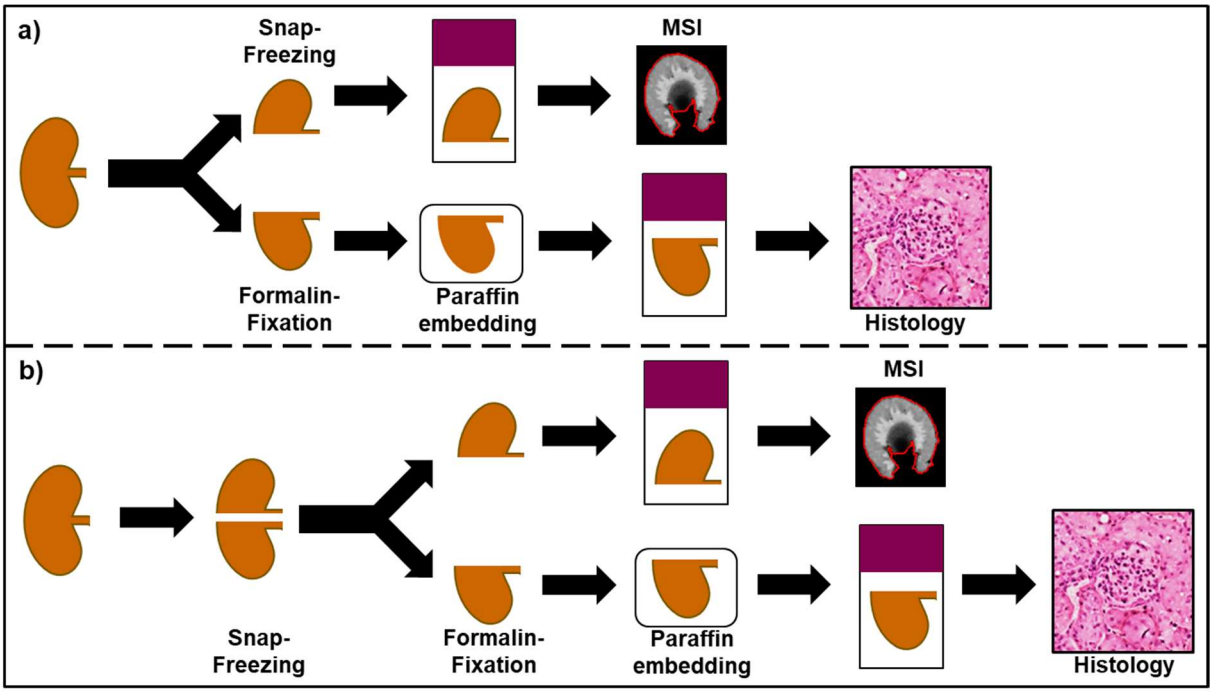

Figure 2.11, Comparison of current vs the adapted sample collection workflow. a) The current workflow in which the samples are divided, and the pieces processed according to the different protocols at the point of sample collection compared to b) the adapted workflow in which all samples are snap-frozen upon collection and subsequently processed for the different applications.

The observed decrease in tissue morphology of specimens stored in formalin is likely to arise from osmotic damage due to the formalin[80]. However, the liver is a fairly homogenous organ and the suitability of the suggested sample collection workflow for tissues comprised of a more complex mixture of morphological features may require further validation.

Conclusions:

Existing reports outline the possibility to use archived tissues for tissue classification studies and the availability of large tissue archives builds a basis for creation of background databases for MSI guided histological determination of tumor margins. FFPE tissues are widely available

in form of tissue micro arrays (TMAs), often containing 96 or more tissue cores. Analysis of slides prepared from TMAs allow for analysis to scale and could be a powerful tool to generate the underlying databases allowing robust tissue classification. However, potential loss of small molecular metabolites, xenobiotics and lipids biases the biochemical information that can be obtained from fixed tissues. Their use to probe molecular interaction networks responsible for tissue function in health and disease should be carefully considered. Selective loss and alteration of the tissue metabolome as well as potential introduction of artefacts during fixation and subsequent preparation might bias results. Overall, fresh frozen samples should be preferred substrates for MSI-based metabolomics and drug distribution studies to allow accurate elucidation of biodistributions. However, if for whatever reason prospective studies cannot source sufficient amounts of high quality fresh-frozen tissues for the entire study, careful validation of preparation effects onto the specific tissues and target analytes should be considered to limit the likelihood of drawing biased conclusions.

Chapter 3 – Sample embedding and processing

Scope:

Once high-quality sample material is sourced it needs to be processed and sectioned to enable analysis by MSI. Tissue sectioning of small, delicate specimens as well as preparation of samples for large-scale studies can be challenging and time consuming. For the latter, degradation of analytes during the time-course of the sectioning procedure can pose another difficulty to when samples are individually processed and mounted on the same slide[18]. To reduce the time-requirements for such large-scale studies simultaneous processing of multiple samples would be desirable. An alternative would be the use of TMAs in full first analogously to their use in histological analysis of FFPE tissues. Any such multiplexed preparation approach requires a scaffold that holds the samples in place during the preparation. Though the paraffin in FFPE blocks and TMAs fulfills this requirement, the disadvantages of FFPE tissues for use in metabolomics and DMPK studies is discussed in Chapter 2. For the reasons discussed there, this chapter focusses on the development of embedding and processing strategies for fresh-frozen samples to enable unimpaired MSI analysis. The mechanical properties of such an embedding medium should include a viscosity which is high enough to allow precise positioning of multiple tissue specimens. It is imperative for any embedding protocol not to alter or thaw the samples, thus hampering the tissue morphology and causing delocalization of analytes within the tissues. To enable unimpaired MSI analysis, the embedding medium is expected not to contain polymers which could alter the resulting mass spectra or contaminate the instrument. To maintain the ability to study tissues at a systems biology level, directly linking metabolic results to tissue morphology and cellular phenotypes, samples prepared for MSI should be compatible with probe or label-based techniques like IHC, imaging mass-cytometry (IMC), fluorescence in-situ hybridization (FISH) or RNA-in-situ hybridization (RNA-ISH) without interfering with the hybridization of the probes and the target or through unspecific background stains.

Aim/objective:

The work presented herin focused on the development of a sample embedding and processing protocol that provides downstream compatibility with numerous different histological and analytical techniques. The methodology is based on low temperature embedding of fresh frozen tissue specimens into a hydrogel composed of hydroxypropyl methylcellulose (HPMC) and polyvinylpyrrolidone (PVP) and subsequent processing on a standard cryo-microtome. The newly developed protocol was assessed for its compatibility with various analytical methods including MALDI- and DESI-MSI, IMC, IHC, RNA-ISH and standard histology.

Methods

Chemicals

Gelatin, poly N-(hydroxypropyl)-methacrylate, polyvinylpyrrolidone (PVP) (MW 360 kDa), (Hydroxypropyl)-methylcellulose (HPMC) (viscosity 40-60 cP, 2 % in H_2O (20 C), low and medium viscosity Na-Carboxymethyl cellulose, 2,5-dihydroxybenzoic acid (DHB), 9-aminoacridine hydrochloride (9-AA), (trifluoroacetic acid (TFA) and Triton-X 100 were purchased from Merck (Darmstadt, Germany). Optimal Cutting Temperature medium, methanol, water, 2-methylbutane, 2-propanol and acetonitrile (ACN) were obtained from Fisher Scientific (Waltham, MA, USA).

Animals

Adult male Hans Wistar rats (approximate weight 260 g) were obtained from Charles River Laboratories (Margate, Kent, UK) and were acclimatized on site for a minimum of 3 days. All dissected organs were snap frozen free-floating in dry ice chilled 2-methylbutane except for kidneys which were, to avoid fracturing of the samples, snap frozen in dry ice chilled 2-propanol followed by a wash in dry ice chilled 2-methylbutane to remove excess 2-propanol. All tissue dissection was performed by trained AstraZeneca staff and in agreement with the procedures approved by institutional review board (AstraZeneca Project license 40/3484, procedure number 10).

Tissue sectioning

Sectioning was performed on a CM3050 S cryostat (Leica Biosystems, Nussloch, Germany) at a section thickness of 10 µm. The specimen blocks were mounted with Milli-Q (Merck, Darmstadt, Germany) water on the sample holder. For all sectioning, the chamber temperature was set to -20˚C whilst the sample was held at -18˚C. Prior to sectioning for experiments analysing RNA, the cryostat chamber and all consumables were thoroughly cleaned to remove RNases using a commercially available cleaning agent (RNase away, Molecular BioProducts, San Diego, CA, USA). Tissue sections for DESI-MSI, IMC, RNA-ISH and IHC were thaw-mounted onto Superfrost microscope slides (Thermo Scientific Waltham, MA, USA), whilst sections prepared form MALDI-MSI were thaw mounted onto conductive ITO coated slides (Bruker Daltonik, Bremen, Germany).

Optimization of the tissue embedding protocol

Tissue embedding was performed using aqueous solutions of the investigated polymers. All cellulose derivatives and PVP were carefully stirred into Milli-Q water (Merck, Darmstadt, Germany) and stored at 4˚C overnight to allow full dissolution. HPMA was dissolved at room temperature and immediately used. Prior to tissue embedding, all gels were pre-conditioned on ice for 30 min. Gelatin solution was prepared by dissolving 10% (w/w) gelatin in water at 70˚C under constant stirring until gelatin was fully dissolved. The hot solution was immediately used for the tissue embedding.

All tissue embedding was performed on ice to prevent warming up of the embedding medium with exception of embedding experiments in gelatin. Embedding molds were filled with the medium before tissue specimens were added.

For the evaluation of the embedding media, liver, spleen and kidney specimens were co-embedded in one mold and frozen. The molds were either snap-frozen in dry ice chilled 2-methylbutane or stored in the -80˚C freezer as indicated until fully frozen. All blocks were subsequently cryo-sectioned and corresponding sections of snap-frozen and freezer frozen samples were mounted adjacently onto the same slide. Immediately after thaw mounting, the

sections were dried under a stream of nitrogen, vacuum packed, and stored in the -80˚C freezer until evaluation by MSI.

DESI-MSI

DESI analysis was performed on a Q-Exactive mass spectrometer (Thermo Scientific, Bremen, Germany) equipped with an automated 2D-DESI ion source (Prosolia Inc., Indianapolis, IN, USA). Data was acquired in positive and negative ion mode between *m/z* 100 and 1000 with a nominal mass resolution of 70,000. The injection time was fixed to 150 ms resulting in a scan rate of 3.8 pixel/s. A home-built DESI sprayer[26] was operated with a mixture of 95% methanol, 5% water delivered with a flow rate of 1.5 µL/min and nebulized with nitrogen at a backpressure of 6 bar. The spatial resolution was set to 100 µm. The resulting .raw files were converted into .mzML files using ProteoWizard msConvert[72] (version 3.0.4043) and subsequently compiled to an .imzML file (imzML converter[73] version 1.3). All subsequent data processing was performed in SCiLS Lab (version 2019b, Bruker Daltonik, Bremen, Germany).

MALDI-MSI

DHB was applied as MALDI matrix as described in Chapter 2. 9-AA was dissolved in 80% methanol and spray-deposited following an adaption of the methodology used for DHB with the difference that only 6 instead of 8 passes of matrix application were performed. analysis was performed on a RapifleX Tissuetyper instrument (Bruker Daltonik, Bremen, Germany) MALDI experiments in positive ion mode were performed with a spatial resolution of 50 or 10 µm in the mass range between *m/z* 200 and 2500. A total of 400 laser shots were summed up per pixel to give the final spectra for experiments performed with a spatial resolution of 50 µm, whilst 125 spectra were summed up for experiments performed with a spatial resolution of 10 µm. MALDI experiments in negative ion mode were performed with a spatial resolution of 10 µm in the mass range between *m/z* 200 and 1500. A total of 125 shots were averaged to give the final spectrum for each pixel. For all experiments the laser was operated with a repetition rate of 10 kHz. All raw data was directly uploaded and processed in FlexImaging (Bruker Daltonik, Bremen, Germany) or SCiLS lab (Version 2019b) software packages. All MALDI data

and images were normalized to the total ion current (TIC) to compensate for signal variation based on inhomogeneities in the applied MALDI matrix layer.

Imaging mass cytometry (IMC)

Tissue sections mounted on Superfrost slides were prepared manually according to a standard protocol adapted from the manufacturer. In brief, the tissue sections were fixed for 10 min in 4% PFA solution (AstraZeneca Media Prep Lab, Macclesfield, UK) followed by 3 washes of 5 min each in PBS/A buffer. A blocking/permeabilization step was performed by treating the tissue sections with 0.01% Triton-X100 in casein enriched PBS/A buffer for 10 min. The tissue sections were washed 3 times for 5 min in PBS/A followed by blocking of unspecific binding sites by incubation with a 1x casein-based blocking solution (prepared from 10x casein solution (SP-5020, Vector Laboratories, Burlingame, CA, USA) diluted in PBS/A) for 30 min. A heavy metal conjugated antibody panel, staining tissue architecture marker was used. Pre-labeled anti-Vimentin (D21H3), Anti-Pan-CK (C11) and Collagen-1 (Polyclonal) (Fluidigm, San Francisco, CA, USA) and anti-non-phospho-β-catenin antibody (D13A1) (purchased from Cell Signaling Technology, Danvers, MA, USA and labelled in house) were pre-mixed in diluent, spotted onto the tissue sections and incubated overnight at 4˚C in a water filled incubation chamber. The antibodies were used in the following dilutions: anti-Vimentin (1:100), anti-Non-phospho-β-Catenin (1:50), anti-Pan-CK (1:100) and anti-Collagen-1 (1:200). After the overnight incubation, the tissues were washed 3 times for 5 min in PBS/A and incubated for 30 min with an iridium-based intercalating agent. Excess of the intercalator was removed by 3 washing cycles in PBS/A for 5 min each, followed by a desalting step in milli-Q water for 1 minute. Tissue sections were analyzed by IMC once the tissues were fully dried. IMC analysis was performed on a Hyperion Laser ablation module coupled to an inductively coupled plasma (ICP)-TOF-MS analyser (Helios, Fluidigm, San Francisco, CA, USA). The laser ablation was performed with a repetition rate of 200 Hz and a pixel size of 1 µm.

Immunohistochemistry (IHC)

10 µm frozen sections were fixed in 4% PFA (AstraZeneca Media Prep Lab, Macclesfield, UK) for 10 min at room temperature and washed in PBS. Primary antibody Collagen I (AB758) (Merck, Darmstadt, Germany) was manually applied at a concentration of 1:200 in Antibody diluent (Roche Tissue Diagnostics, Tucson, Arizona, USA) and incubated for 1 h at room temperature. IHC was performed on the automated Ventana Discovery Ultra, using DISCOVERY ChromoMap DAB Kit (RUO) (Roche Tissue Diagnostics, Tucson, Arizona, USA) and counterstained with Hematoxylin and Bluing Reagent (Roche Tissue Diagnostics, Tucson, Arizona, USA). The stained slides were cover slipped and images were acquired with the Nanozoomer scanner (Hamamatsu Photonics, Hamamatsu, Japan) at 20x magnification. Negative controls without the primary antibody were performed for all samples to evaluate for unspecific stains.

RNA-In Situ Hybridisation (RNA-ISH)

ISH for Rn-Gapdh (ACDbio, Newark, CA, USA) expression were performed on the automated LeicaBond staining platform, using the RNAscope 2.5 LSx DAB kit (ACDbio, Newark, CA, USA), according to the manufacturer's instructions. Briefly, 10 µm slides were fixed in 10% NBF, washed in PBS and subsequently dehydrated in 50%, 70% and 100% ethanol. Once fully dry, the slides were loaded onto a Leica Bond automated staining system. The probes PPIB and DapB (ACDbio, Newark, CA, USA) were run in parallel as positive and negative control. Once stained, slides were cover slipped and images were analyzed with the Nanozoomer (Hamamatsu Photonics, Hamamatsu, Japan) at 40x magnification. Negative controls without the RNA probes were performed for all samples to evaluate for unspecific stains.

Results

Evaluation of physical properties of different embedding media

OCT medium is widely used for histological purposes as it was developed for cryo-sectioning of biological specimens. Designed for this purpose, it performed well during sample

preparation and cryo-sectioning. Similarly, gelatin prepared as 10% (w/v) solution is commonly used for sample embedding in histological workflows but was found to be suboptimal as it requires elevated temperatures for the embedding process. In addition, volume contraction of the medium during the freezing process resulted in poor adherence to the tissues and detachment of entire specimen during sectioning (Figure 3.1a). Sodium-carboxymethyl cellulose (Na-CMC) is commonly used to enable cryo-sectioning of fragile specimens in histology labs. Typically, 2-3% (w/w) of a 'medium viscosity' Na-CMC are used for histological applications, as it provides a sufficiently viscos solution for precise positioning of specimens. However, the medium crumbled during cryo-sectioning and the medium separated from the embedded tissues. This sectioning behavior is not desirable, especially when multiple specimens are embedded in one mold. It was found that a minimum concentration of 10% (w/w) Na-CMC was necessary as it allows sectioning of the medium as a single intact sheet. The minimum required concentration of 10% was found to be translatable to other polymers and was used as a starting point for concentration optimization of subsequently evaluated polymers. The 10% solutions of 'medium viscosity' Na-CMC were very viscous and difficult to handle, but solutions of 'low viscosity' Na-CMC were found to have excellent handling and sectioning properties. HPMA was found to have acceptable sectioning properties. Though frozen HPMA blocks were found to be brittle and sometimes difficult to section. The most important advantages of HPMA include the quick preparation comprising the single step of mixing with water and the reported possibility of cold embedding which was adapted in the evaluation of all other potential embedding media. The main drawbacks of using this medium are its price, limited availability and low viscosity. HPMA has a low capacity to bind water and 10% solution still has a low viscosity, making precise positioning of specimens challenging. PVP prepared as 15% (w/w) aqueous solutions has a viscosity that allows precise positioning of specimens in the medium. However, cutting temperatures as low as -30˚C were required to section the resulting blocks. The low temperatures resulted in fracturing of the tissue sections during cryo-sectioning. Temperatures optimal for tissue sectioning were clearly above the freezing point of the embedding medium. HPMC showed overall good sectioning performance

except for its poor adherence to the tissue. During the development of the embedding protocol this polymer was favored as no interference with mass spectrometry-based analysis was found. The viscosity of a 10% solution was sufficiently high to allow precise positioning of specimens in the hydrogel. To improve the poor tissue adherence of HPMC, mixtures of HPMC and PVP were evaluated. A 7.5% HPMC + 2.5% PVP mixture was found to give the desired viscosity and had the desired handling properties. The mechanical properties and sectioning behavior of the evaluated media are summarized in Table 3.1.

Table 3.1 Summary of sectioning properties for the evaluated embedding media.

Embedding medium	Preparation	Viscosity[a]	Possible to section	Adherence to tissue[a]
OCT medium	Ready to use	Acceptable	Yes	Very good
10% Gelatin	Fast preparation	Acceptable	Yes	Poor
10% HPMA	Fast preparation	Too low for precise sample positioning	Yes	Acceptable
12.5% Na-CMC	Swelling of polymer overnight	Very Good	Yes	Very Good
10% HPMC	Swelling of polymer overnight	Very Good	Yes	Acceptable
15% PVP	Swelling of polymer overnight	Good	No	Very Good
7.5% HPMC + 2.5% PVP	Swelling of polymer overnight	Very Good	Yes	Very Good

[a] *Attributes for viscosity and tissue adherence were rated subjectively given lack of objective measuring criteria. The classification categories were poor, acceptable, good, very good*

Evaluation of the media for MSI purposes

OCT was frequently reported to be unsuitable for MSI purposes as both polyvinyl alcohol and polyethylene glycol undergo ionization, resulting in polymer envelopes detected in positive ion mode. During sectioning, these polymers tend to additionally spread across the tissue sections, in a layer of varying thickness, dominating the resulting spectra, causing ion suppression and instrument contamination. Due to this effect reported in multiple publications[50, 52], the medium was not evaluated here for MSI applications. For the remaining

media, DESI-MSI analysis was performed to evaluate chemical background of the media and analyte delocalization.

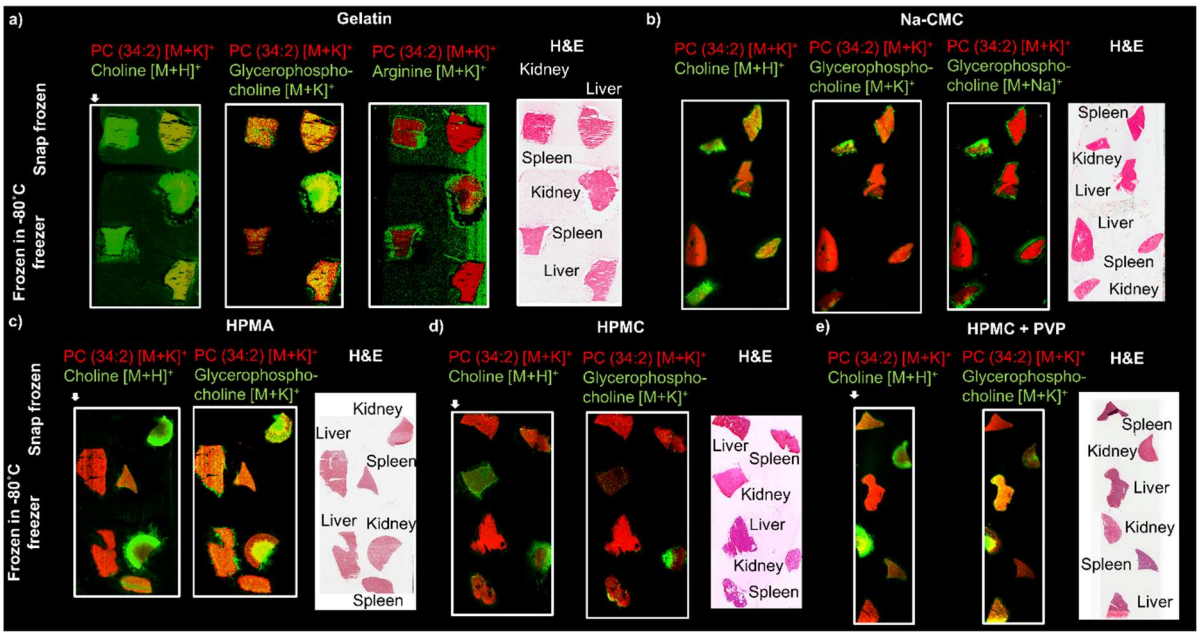

Figure 3.1, Evaluation of the embedding media by DESI-MSI in positive ion mode: Sections from snap frozen (top) and freezer frozen embedding blocks (bottom). The distribution of polar analytes (green) were compared to structural lipids (red) and post MSI H&E stained sections to evaluate for analyte delocalization for a) gelatin, b) Na-CMC, c) HPMA, d) HPMC and e) HPMC + PVP.

The evaluation of the background interference focused on chemical background interference through ionizing polymers and content of endogenous metabolites. In positive ion mode Gelatin showed chemical background and delocalization for choline, glycerophosphocholine and arginine (Figure 3.1a). Samples embedded in Na-CMC showed no delocalization for glycerophosphocholine detected as potassium adduct. The high sodium content of the medium promoted formation of the sodium adduct which showed significant delocalization in the freezer frozen samples (Figure 3.1b). Only limited delocalization of choline and glycerophosphocholine as potassium adducts were observed when the samples were snap frozen. The low viscosity of HPMA was found to promote delocalization of polar analytes into the medium in both freezer and snap frozen samples (Figure 3.1c). Embedding in HPMC and HPMC+PVP was found to result in significantly less analyte delocalization when the samples were snap frozen whilst significant amounts of analytes leaked into the embedding medium when the samples were frozen in the freezer (Figure 3.1d, e). Due to the well documented appearance of the OCT compound in mass spectra all embedding media were evaluated for

ionizing polymers. No obvious polymer signals could be detected in positive ion mode for gelatin, Na-CMC, HPMA, HPMC or HPMC+PVP (Figure 3.2a).

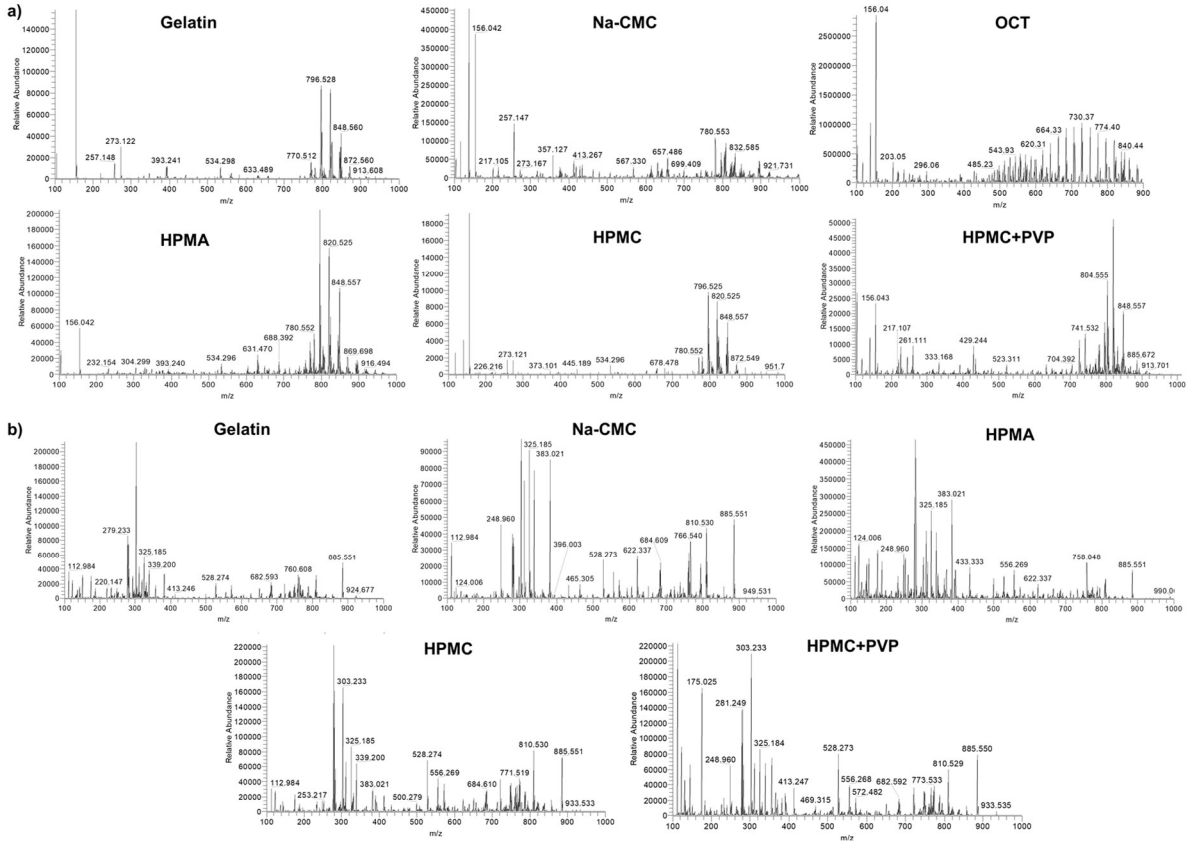

Figure 3.2, Representative mass spectra obtained from embedded rat liver sections: Spectra were acquired in a) positive and b) negative ion mode from liver sections embedded in the respective embedding medium as indicated.

Overall, little analyte delocalization was observed for snap frozen blocks whilst the freezer frozen samples showed substantial leakage of polar analytes into the embedding medium in negative ion mode. Gelatin showed substantial delocalization of polar metabolites as well as structural lipids regardless of the freezing method (Figure 3.3a). Na-CMC showed comparable analyte delocalization as observed for HPMC and HPMC+PVP, but deposition of the Na-CMC on the sample surface resulted in partial ion suppression visible as darker shadows on the ion images (Figure 3.3b, d and e). Additionally, strong background staining of the embedding medium was observed on the H&E stained sections. HPMA was found to promote delocalization of polar analytes which agrees with the findings in positive ion mode (Figure 3.3c). No obvious polymer signals could be detected for any of the embedding media (Figure 3.2b).

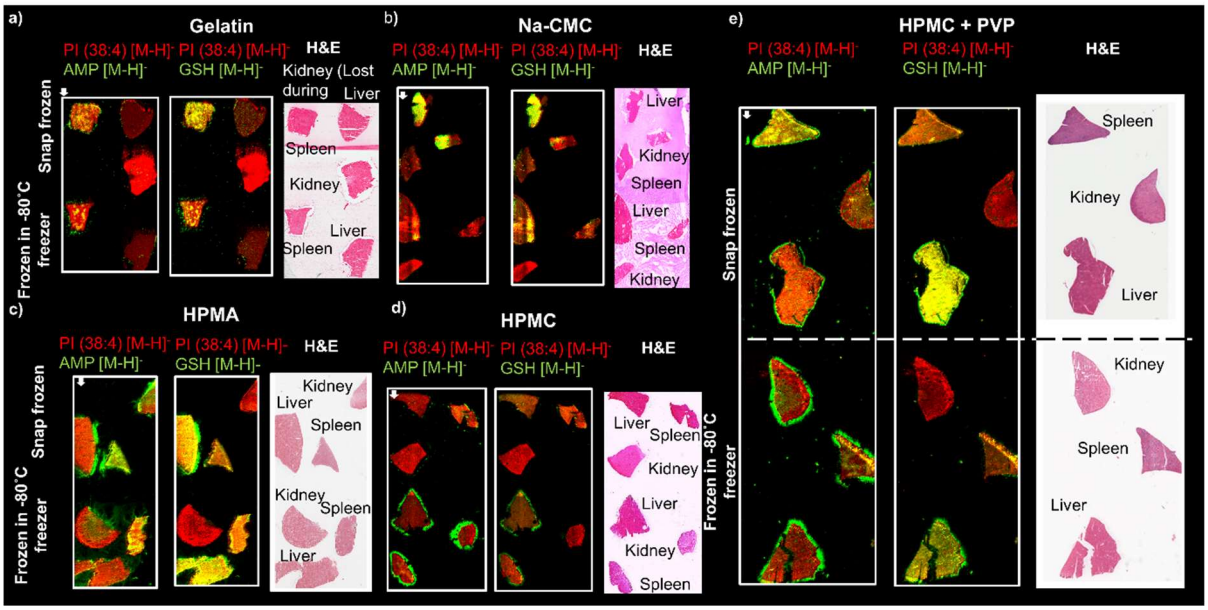

Figure 3.3, Evaluation of different embedding media by DESI-MSI in negative ion mode: Sections from snap frozen (top) and freezer frozen embedding blocks (bottom). The distributions of AMP (m/z 346.043) and glutathione (m/z 306.079) (GSH) (green) were compared to that of the structural lipid PI (38:4) (m/z 885.849) (red) and post MSI H&E stained sections embedded in a) gelatin, b) Na-CMC, c) HPMA and d) HPMC and e)HPMC + PVP. The sprayer direction for all DESI-MSI experiments is indicated by the white arrow.

For all media the delocalization of small polar analytes such as choline, glycerophosphocholine, adenosine-monophosphate (AMP), glutathione (GSH), through diffusion out of the tissue, was found to be reduced when the specimen blocks were snap frozen compared to slow freezing in the -80˚C freezer. Phospholipid species such as Phosphatidylinositol (PI) and phosphatidylcholine (PC) showed overall little delocalization and the outlines of the ion images matched up with the stained tissue sections. Figure 3.4 illustrates the concerning delocalization effects of the two different freezing approaches for the HPMC + PVP based embedding medium. The relative amount of analyte delocalization and the diffusion distance of AMP (m/z 346.053) and GSH (*m/z* 306.079) into the embedding medium were evaluated by plotting the mean abundance over the distance to the tissue edge. The tissue edges were defined as the outermost pixel of the ion images obtained for the structural lipid PI (38:4) (m/z 885.549) overlaying with the H&E stained tissue section and were attributed the distance 0. The plots were created by extracting the abundance of the analytes through pixel-by-pixel radial expansion from the tissue edge for 10 pixels into the tissue section (negative values) and up to 15 pixels out of the tissue (positive values).

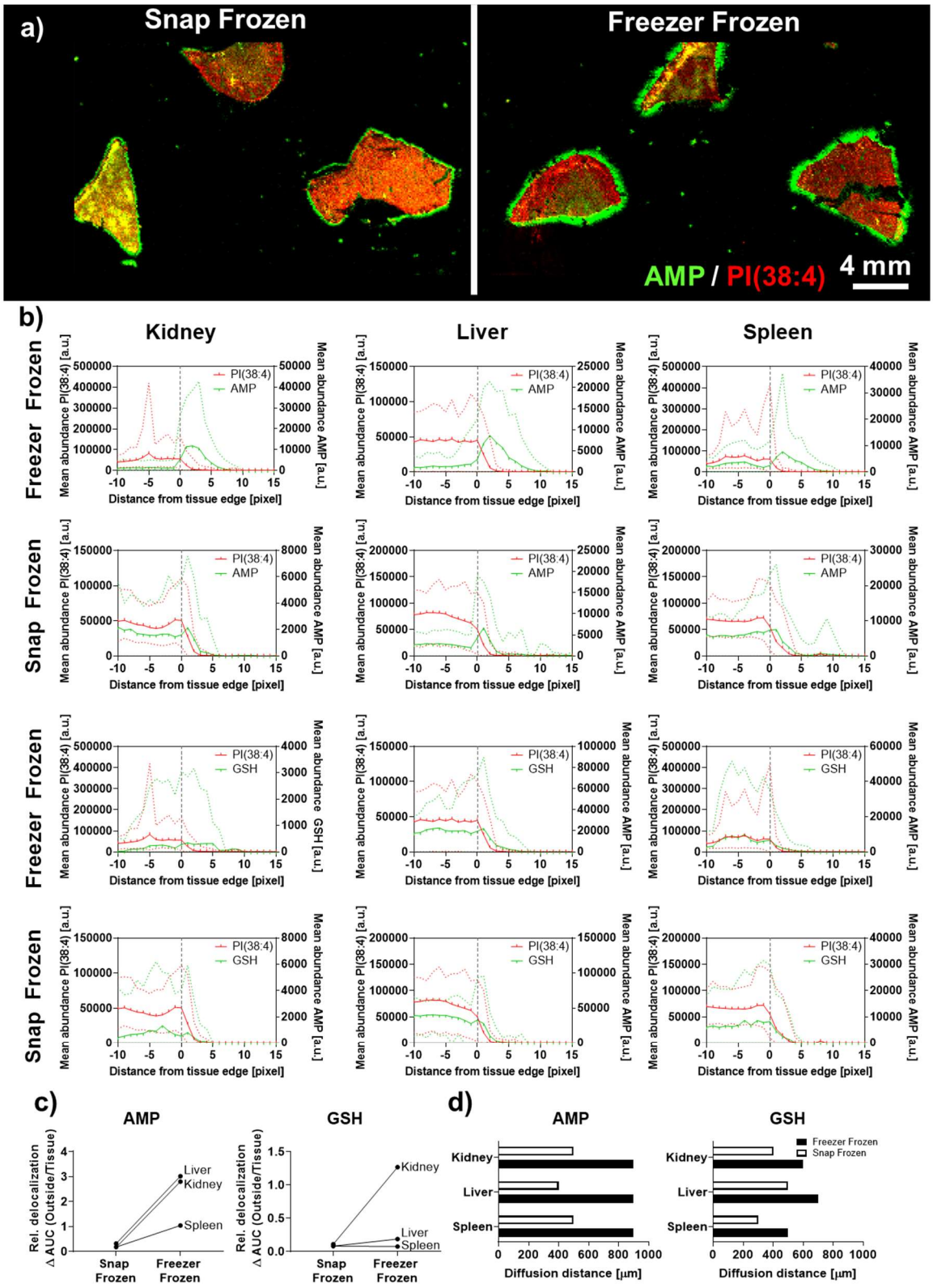

Figure 3.4, Evaluation of analyte delocalization in HPMC+PVP embedded tissue sections: (a) PI (38:4) outlines the tissue sections (red) visualizing the leakage of AMP into the tissue environment (green). b) The amount and diffusion distance of AMP and GSH into the embedding medium were evaluated by plotting the mean abundance over the distance to the tissue edge. The data is represented as mean of the tissue section and the error graphed as 95% CI (red dots for PI (38:4), green dots for AMP or GSH respectively). c) The relative delocalization for each tissue was estimated through the quotient of the analyte's area under the abundance-distance-curve (AUC). d). Diffusion distances into the medium for snap frozen and freezer frozen specimens.

The relative delocalization for each tissue was estimated through the quotient of the analyte's area under the abundance-distance-curve (AUC) within the tissue (pixel -10 to 0) and outside of the tissue (pixel 1 to maximum diffusion distance). Both analytes showed organ dependent differences in the extend of the analyte delocalization with higher effects on the delocalization of AMP from liver and kidney specimens compared to spleen, whilst kidneys showed a higher leakage of GSH into the tissue environment than liver and spleen. The pooled relative analyte delocalization for all organs was used to estimate the effect size of the freezing conditions using Cohen's d estimate. For both, AMP and GSH a large difference was found between the means of snap frozen and freezer frozen samples (AMP d = 2.69, 95% CI -0.44 to 5.81; GSH d = 0.90, 95% CI -1.48 to 3.28, n = 3 organs per group). The calculations of the AUCs from the plots were additionally used to define the maximum diffusion distance of the analytes from the tissue edge into the embedding medium. All freezer frozen specimens showed longer diffusion distances into the medium compared to the snap frozen specimens. The increased delocalization of AMP and GSH and the increased diffusion distance were attributed to the prolonged time until full freeze of the embedding medium. In addition to the DESI analysis, MALDI-MSI analysis was performed in positive ion mode to further evaluate chemical background for ionizing polymers taking advantage of its capability to desorb/ionize abundant large molecules such as peptides[24, 87], proteins[88, 89] and synthetic polymers [90-92]. The evaluation was performed in positive ion mode on the mass range up to *m/z* 2500 as it is commonly used for small molecule and peptide focused studies. No obvious polymer signals that would interfere with the analysis were observed on the tissue sections.

Though OCT medium and gelatin did not fulfill the requirements set for an ideal embedding medium, however, both are standard embedding media for fresh frozen samples in histological workflows, and as such they were included in the evaluation of other tissue-based techniques serving as a reference quality standard.

Effect of embedding and freezing procedure on tissue morphology

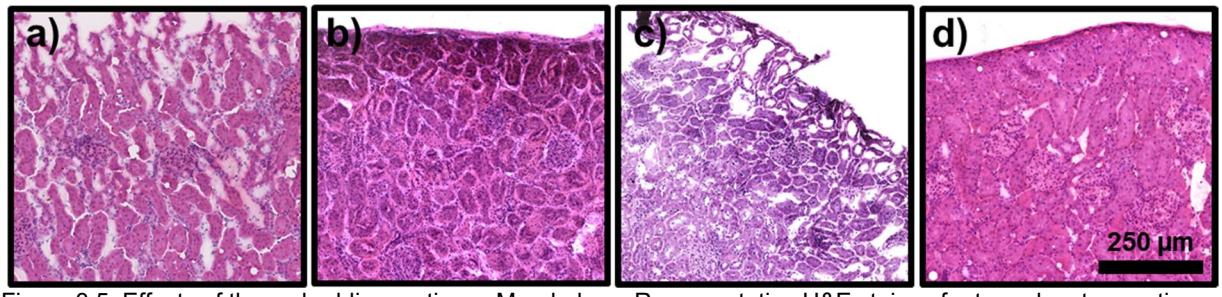

Figure 3.5, Effects of the embedding on tissue Morphology: Representative H&E stains of rat renal cortex sections a) without embedding or embedded in b) OCT, c) gelatin or d) the newly developed HPMC+PVP hydrogel.

MSI techniques are powerful tools to record molecular distributions of metabolites, lipids and proteins. These molecular maps, however, can only be properly interpreted if they are co-registered with morphological information through histological evaluation of stained tissue sections. Preservation of small morphological features such as small blood vessels or renal tubules is crucial to accurately annotate tissues and link the metabolite information to the right tissue compartments. Cold embedding in the presented HPMC+PVP hydrogel combined with snap freezing was found to improve section morphology compared to specimens that were sectioned without embedding. Similar to the section quality achieved through conventional embedding in OCT, the HPMC+PVP medium showed sufficiently good preservation of the tissue morphology and staining characteristics when the prepared sample molds were snap frozen (Figure 3.5). Embedding followed by freezing in the -80˚C freezer compromised section morphology. The H&E stained sections showed significant freezing artefacts with fracturing of the tissue and formation of large clefts by ice crystals hampering microscopic analysis of the tissue structure. As the -80˚C freezing of an embedding block takes about 15-20 min until full freeze, compared to 1-2 min when snap frozen. The compromised tissue quality likely arises from thawing of the samples followed by slow re-freezing resulting in formation of large ice crystals which is damaging the embedded tissues. Snap frozen gelatin molds showed mixed results regarding tissue morphology. Whilst the tissue cores showed good morphological preservation (bottom part of the gelatin embedded H&E stain in Figure 3.5), the outer layers showed substantial tissue damage induced by the hot embedding medium (top part of the tissue section). Additionally, when gelatin embedded samples were subjected to H&E staining,

the proteins and peptides in the medium were stained by eosin, resulting in masked tissue edges (Figure 3.1b and Figure 3.3). Similar to gelatin, the Na-CMC matrix was stained by eosin interfering with histological evaluation due to the masking of tissue contours.

Effect of the embedding media on affinity-based stains

Linking metabolite distribution maps elucidated by MSI with the underlying tissue morphology is often the first step when probing the biology of healthy and diseased tissue specimens. In multi-omics studies the next step is often to validate these metabolic phenotypes against changes at the transcriptome and proteome level. Determination and validation of protein expression patterns through single-plex IHC and more recently through multiplexed IMC analysis are standard tools in histological workflows. An antibody panel targeting basic tissue architecture was compiled for the evaluation of the effects the embedding media have on antibody-based stains. The panel was tested using IMC and certain findings were subsequently validated by traditional chromogenic IHC. No interference with antibody binding was found for either HPMC+PVP or OCT embedded samples compared to an unembedded control (Figure 3.6).

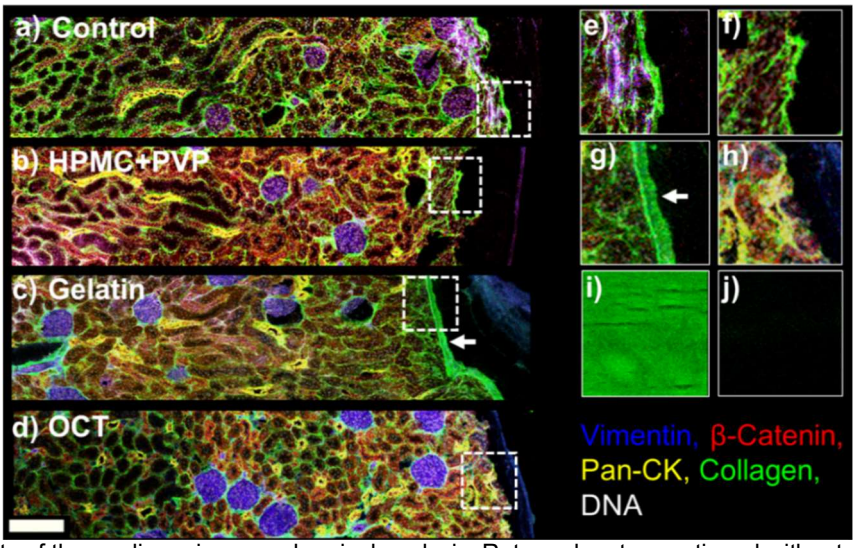

Figure 3.6, Effects of the media on immunochemical analysis. Rat renal cortex sectioned without embedding (a) or after embedding in HPMC+PVP (a), gelatin (b) or OCT (c) and corresponding zoomed sections of the tissue edges in the same order (d-f) analyzed by IMC. Arrows in c and g indicate remaining gelatin stained for collagen-1. Data acquired on pure gelatin confirms staining of the gelatin for collagen-1 (i) compared to the slide background (j). Scale bar 200 µm

The extensive fixation and washing steps prior to antibody labelling removed the embedding media in an analogous way reported for the proteomic analysis of OCT embedded samples

by MSI[93]. Gelatin did not directly interfere with the antibody binding, but it is formed of hydrolyzed protein fragments and was found to contain active protein epitopes for collagen-1 visible as staining of the medium. This background masked tissue edges where gelatin adhered to the tissues (Figure 3.6c, g). The background staining problem was confirmed using conventional chromogenic anti-collagen-1 IHC, although it was found to be less significant than in case of IMC. This difference was associated with the different sample preparation workflows. Overall, the manual staining procedures are quite gentle, whilst the harsher sample preparation conditions on the automated IHC staining platform removed most gelatin from the tissue edges and the glass slide. Those stained gelatin sheets occasionally covered the tissue section, masking the optical scans (Figure 3.7). In agreement with the histological evaluation of tissue sections obtained from embedded tissue specimens, the tissues embedded in OCT and HPMC + PVP showed highest morphological preservation. The section obtained from specimen which were processed without embedding as well as those obtained from gelatin embedded specimens showed hampering of the morphology.

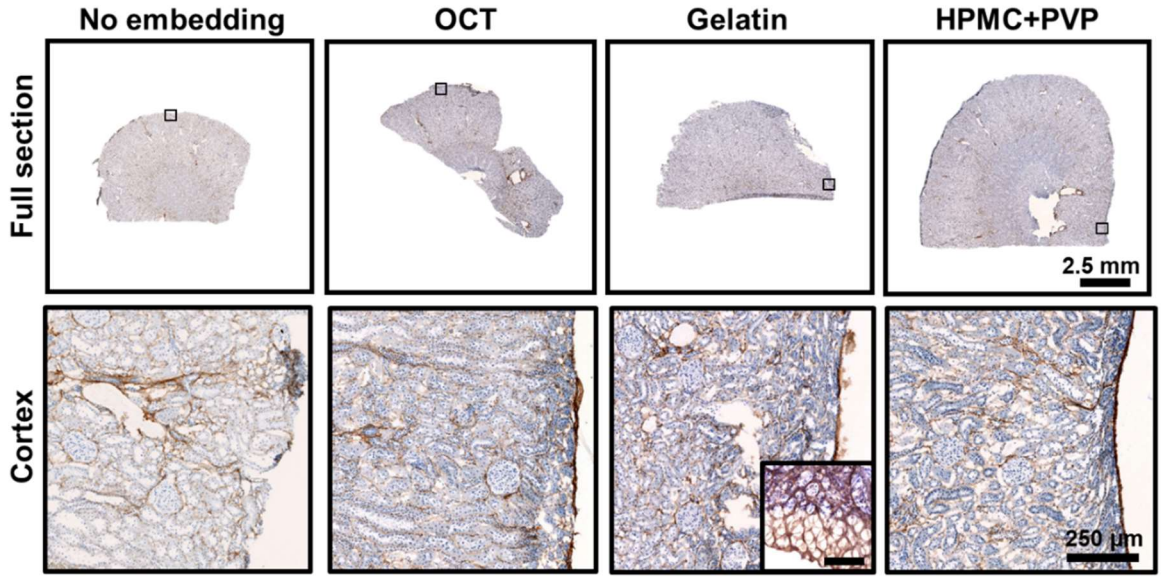

Figure 3.7, IHC staining for collagen-1: Tissue section prepared in the newly developed HPMC+PVP medium compared to OCT, gelatin and unembedded control samples. The top panel shows the entire tissue section whilst the bottom panel displays a zoom on the cortical region indicated by the square on the full section. The collagen stain (brown) is visualized within the tissue morphology which is outlined by a hematoxylin counter stain (blue). The single panel for gelatin shows gelatin stained for collagen-1 which delocalized throughout the staining and ended up on the tissue edge masking parts of the tissue. Scale bar zoom on gelatin = 100 µm

The integrity of mRNA in embedded tissues and any interference of the medium with in-situ analysis via probe-based stains was evaluated via chromogenic RNA-ISH. The analysis was

performed to elucidate the expression pattern of Glyceraldehyde 3-phosphate dehydrogenase (*Gapdh*) and peptidyl-prolyl cis/trans isomerase B (*Ppib*) in kidney tissue sections (Figure 3.8). These housekeeping genes are expressed in most tissues and are commonly included in assays as positive controls. Overall, no striking difference was found between specimens that were embedded in OCT, HPMC + PVP medium or sectioned without embedding. Only specimens embedded in gelatin showed lower amounts of *Ppib* and *Gapdh* mRNA across the kidney sections. The reduced abundances are likely to be an artefact due to RNA degradation during the embedding at elevated temperatures.

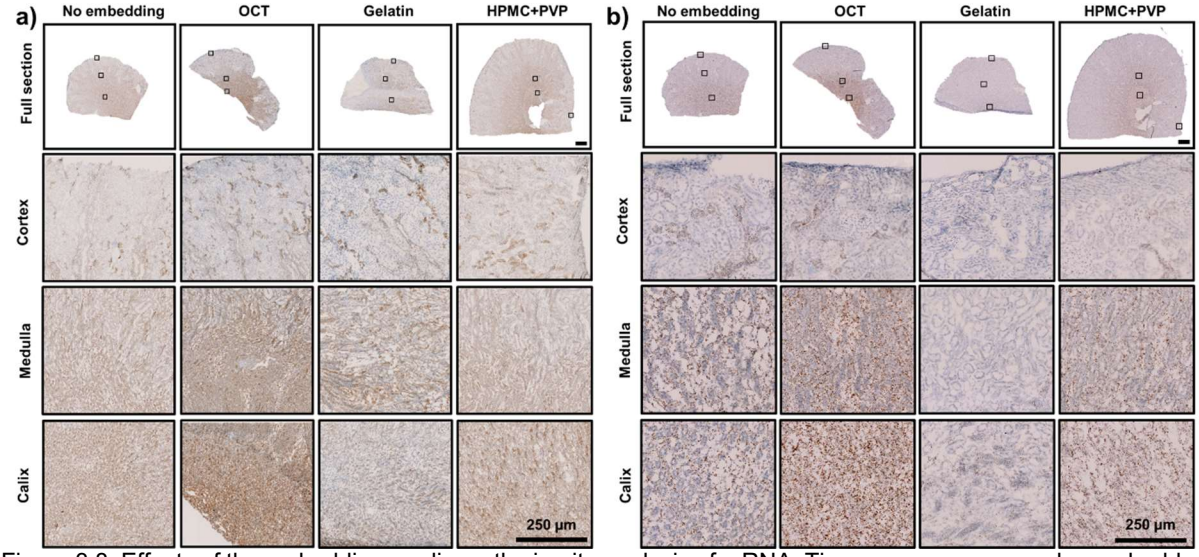

Figure 3.8, Effects of the embedding media on the in-situ analysis of mRNA: Tissues were processed unembedded or embedded in OCT, gelatin or HPMC+PVP and analyzed for a) Gapdh and b) Ppib. RNA-ISH showing the distribution of expressed mRNA (brown) against the counterstained nuclei (blue). The squares in the full section indicate the regions chosen for the zoomed panels. The scale bar for the full section view is 1 mm

The optimized processing protocol

Preparation of the HPMC+PVP hydrogel requires little effort. Both polymers are weighed out and dissolved in deionized water to a final concentration of 2.5% (w/w) PVP and 7.5% (w/w) HPMC. The mixture is kept at 4 ˚C overnight to allow complete dissolution of both polymers and settling of any foam formed. Prior to tissue embedding, the medium is pre-conditioned on ice for approximately 30 minutes. The ice-cold medium is transferred into conventional tissue embedding molds and kept on ice. The prepared tissue specimens are positioned one by one at the base of the mold, aligned by the intended sectioning plane. This step is time-critical and should be performed as quickly as possible to keep the tissues frozen and prevent tissue

damage and analyte delocalization. Blocks tend to fracture when directly snap frozen in dry ice chilled 2-methylbutane due to the fast expansion of the hydrogel bound water. Snap freezing in dry ice chilled 2-propanol was found to freeze the blocks at a slightly slower rate (approx. 2 min instead of 1 min in dry ice chilled 2-methylbutane) and enable snap freezing without fracturing the resulting blocks. Subsequent transfer into dry ice chilled 2-methylbutane for approximately 30 seconds was found to be beneficial to wash off excess 2-propanol and allow further rapid cooling to -80˚C. The snap freezing creates substantial amounts of aerosol due to escaping carbon dioxide and should be performed in a fume hood or if using biologically hazardous samples an airflow-controlled bio-safety cabinet. Once the sample blocks are fully frozen, they can be transferred onto dry ice to allow evaporation of the 2-methylbutane. The frozen sample blocks can be sectioned on a conventional cryo-microtome. Immediately after the sections are thaw-mounted on the target substrate they are dried under a stream of nitrogen or compressed air, vacuum sealed in slide mailers and transferred into a -80˚ C freezer for storage. Drying and vacuum-packing of the slides minimizes the risk of analyte delocalization and allows for accurate elucidation of biodistributions.

The reproducibility of the achievable results were evaluated for samples embedded according to the optimized protocol. Kidney, liver and spleen specimens were co-embedded and the prepared molds snap-frozen. The variation between the individual preparations was evaluated using DESI-MSI experiments performed with a spatial resolution of 100 µm allowing global evaluation of analyte distributions and delocalization of polar analytes into the tissue environment. (Figure 3a). Consistent with the initial evaluation described above, only limited delocalization of polar analytes such as glutathione and FA(18:2) (detected at *m/z* 279.234) was detected outside of the tissues as indicated by PI(38:4) as non-diffusing lipid marker. To minimize the likelihood of analyte delocalization into the tissue environment, the time between placing of the first specimen and snap-freezing of the prepared mold should be kept as short as possible, ideally below 1 min. For reference, the embedding procedures for the specimens in Figure 3 took approximately 15 s per mold.

Imaging experiments performed with a higher spatial resolution of 25 µm performed on an adjacent sections confirmed the limited diffusion of polar analytes such as GSH or FA(18:2) into the tissue environment whilst allowing clear identification of larger morphological features such as the hepatic zonation of the red and white pulp of the spleen (Figure 3b).

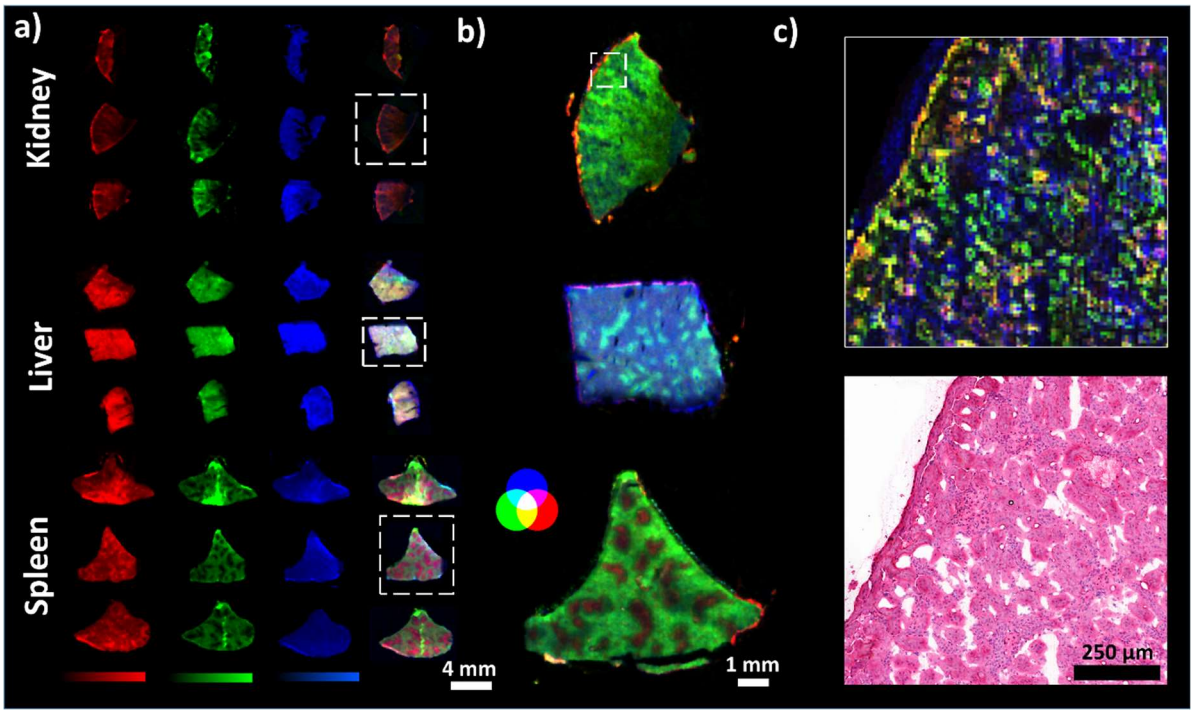

Figure 3.9, Reproducibility evaluation of the optimized embedding protocol and achievable imaging resolution: Replicates of co-embedded kidney, liver and spleen specimens analyzed using DESI-MSI at a spatial resolution of a) 100 µm and b) 25 µm. The presented images show the distributions of PI(38:4) (red), FA(18:2) (green) and Glutathione (blue). c) High-resolution MALDI-MSI experiments allowed elucidation of the analyte distributions at a spatial resolution of 10 µm compared to the post analysis H&E stained tissue section.

More complex tissues such as the renal cortex required higher imaging resolutions to identify clear tissue structures. MALDI-MSI experiments performed with a spatial resolution of 10 µm allowed clear delineation of analyte distributions even into small morphological features such as the tubular system of the renal cortex (Figure 3c) highlighting the excellent morphological preservation of tissues and of the molecular distribution maps within. The impact of condensation on the slide surface and strategies to overcome such phenomena are described in the literature[94].

Conclusions

The presented embedding and sample processing protocol allows alignment of sample preparation steps for histological and immunochemical analysis of frozen tissue specimens. The use of the same sample for MSI as well as histology practice used in research, industrial applications and clinical diagnostics allows for unparalleled data integration between modalities. The significance of MSI is rooted in its untargeted nature allowing determination of the biodistributions of thousands of features in a single experiment. Beyond the recording of molecular distribution maps, this data carries invaluable information on metabolism. However, these untargeted findings often require confirmation by orthogonal techniques such as immunohistochemistry, immunofluorescence or in-situ hybridization to determine proteomic and transcriptomic phenotypes and put the metabolic information into context of the underlying biochemical pathways. Integrating data from different modalities allows to transition from a descriptive approach to utilization of the data to gain mechanistic understanding of the structure of molecular interaction networks responsible for tissue function in health and disease. The feasibility of collecting these datasets in a co-registered manner is clearly demonstrated by the here presented work.

The developed method carries equal importance regarding the practical implementation of MSI studies. Currently most laboratories collect, store and analyze individual specimens. Not all steps from sample collection to the end of an imaging experiment can be properly controlled and reproduced. As a result, the individual imaging datasets often show pronounced batch effects, which may mask the biological effects studied. Also, dependent on the instrumentation used, imaging of a single tissue section may still require several hours (especially at high spatial resolution). Data collection for well-powered studies may require several weeks, further contributing to the introduced batch effects. In contrast, the proposed methodology enables the construction of fresh frozen tissue microarrays, which allows identical sample treatment and comparable analytical results across entire sample cohorts.

Chapter 4: Evaluation of UV-C decontamination procedures for clinical tissue sections

Aim/objective

Once tissue sections are prepared, they can usually be directly subjected to MSI analysis. However, clinical tissue specimens and tissues from infection models may contain pathogens. The preparation of such tissues for MSI analysis can cause aerosolization of particles potentially carrying an infectious load. This chapter focusses on a decontamination approach based on ultraviolet-C (UV-C) light to inactivate potential pathogens whilst preserving the biodistributions of the endogenous tissue metabolome and xenobiotics within the tissue.

Material and Methods

Chemicals

Terfenadine, dextromethorphan hydrobromide and diphenhydramine hydrochloride were purchased from Merck (Darmstadt, Germany). Methanol, 2-methylbutane and 2-porpanol were obtained from Fisher Scientific (Waltham, MA, USA). Losartan-potassium salt was obtained from Cambridge Bioscience (Cambridge, UK). All solvents used were of analytical grade or higher.

Animals

Adult male Han Wistar rats (approximate weight 260 g) were obtained from Charles River Laboratories (Margate, Kent, UK) and acclimatized on site for a minimum of 3 days prior to dosing. Dosing was performed as cassette of terfenadine, diphenhydramine, dextromethorphan and losartan at 25 mg/mg/drug. Compounds were formulated in 5% dimethyl sulfoxide/95% (30% w/v Captisol in water) and administered orally. Animals were euthanized 2 h post-dose. All tissue dissection was performed by trained AstraZeneca staff (project license 40/3484, procedure number 10). Brain, liver and spleen samples were snap-frozen in 2-methylbutane on dry ice, whilst kidneys were snap frozen in dry ice chilled 2-propanol, to avoid fracturing of the samples, followed by a wash in dry ice chilled 2-

methylbutane to wash off excess 2-propanol. All subsequent transfer of tissues was done on dry ice, and samples were stored at −80 °C until tissue processing.

Cryo-sectioning

Cryo-sectioning was performed with a section thickness of 10 µm on a CM1950 cryostat (Leica, Nussloch, Germany). Analogous to a previously reported drying approach using a stream of nitrogen to desiccate thaw-mounted tissue sections[18], each tissue was carefully dried using the vacuum suction of the instrument to suck air across the tissue thus minimizing formation of aerosols. All sections were either mounted onto conductive SuperFrost microscope slides (Thermo Scientific, Waltham, Massachusetts, USA) or polypropylene (PP) wafer which were cut from a larger PP sheet. All prepared slides were stored in vacuum-sealed slide mailer at -80˚C until further processing.

UV-C decontamination procedures

Decontamination experiments were performed using the built-in low pressure mercury arc lamp of the CM1950 cryostat. The germicidal emission maximum of the lamp is at wavelength 253.7 nm. The effects of the instrument's pre-programmed 30- and 180-min decontamination cycles on the tissue metabolome were evaluated as their use ensures controlled and reproducible irradiation experiments. For all experiments, samples were irradiated by placing them on the sectioning table in direct line of sight to the UV lamp avoiding shading of the slides. For the duration of the irradiation, the chamber temperature was kept at -20˚C. For initial evaluation of changes between irradiated samples and samples prepared according to a standard workflow, control samples were kept in vacuum sealed slide mailer inside the cryostat to mimic potential temperature effects. For all subsequent experiments control samples were kept inside the cryostat chamber with the UV lamp switched off to account for all effects inflicted by the storage in the cryostat chamber.

For experiments under inert atmosphere the cryostat was purged with approximately 50 L of argon gas to allow argon to replace air before the samples were placed in the cryostat and irradiated for 180 min. To prevent depletion of argon by seeping through openings in the

bottom of the cryostat chamber, the cryostat was constantly re-supplied with argon at a flow rate of 1 L/min delivered as laminar flow across the sample surface. Samples irradiated under inert atmosphere were compared to identically prepared slides openly stored in the cryostat for 180 min (controls) and samples irradiated for 180 min under normal conditions.

Kinetic experiments for photodegradation of the drugs were performed by spotting pooled drug standard solutions onto non-dosed rat liver sections and the spots were irradiated for 0, 15, 30, 60, 120 and 180 min respectively. Once the irradiation times for the spots were reached the respective tissue area was covered with a stainless steel MALDI target plate to avoid any further exposure to the UV-C radiation. A BioSpot workstation (BioFluidix GmbH, Freiburg, Germany) was used to deposit 50 nL droplets with a concentration of 4 µmol/L/drug. Each timepoint was carried out in triplicate on the same tissue section.

DESI-MSI

DESI experiments were performed on a Q-Exactive plus mass spectrometer (Thermo Scientific, Bremen, Germany) equipped with a 2D sampling stage (Prosolia Inc., Indianapolis, IN, USA) and a home-built DESI sprayer[26] operated with 95/5 (v/v%) methanol/water as electrospray solvent. The solvent was delivered with a flow rate of 1.5 µL/min and nebulized with a gas pressure of 7 bar. The mass spectrometer was operated in full scan mode between m/z 80 to 1000 with alternating line-to-line acquisition in positive and negative ion mode. The spatial resolution in the x dimension was fixed to 150 µm and the line-to-line offset was set to 75 µm, resulting in 150x150 µm interpolated pixel for each dataset. The resulting .raw files were separated based on polarity, converted into .mzML files using ProteoWizard msConvert[72] (V. 3.0.4043), subsequently compiled to .imzML files (imzML converter[73] V. 1.3) and uploaded into SCiLS lab (V. 2019c) (Bruker Daltonics, Bremen, Germany).

Tandem-MS experiments were performed with the same instrument parameters as listed above. The data was acquired by running line scans across the tissue and collecting data with an increasing collision energy to acquire a variety of product ions. Applicable spectra were subsequently averaged and the resulting in information rich MS/MS spectra were used for

structure elucidation of the precursor ions. The injection time was fixed to 250 ms for all tandem-MS experiments. All precursor ions were isolated with an accuracy of ± 0.2 Da.

Data analysis

Features discriminating between the different UV-C treatments were identified using the receiver-operator-curve (ROC) function built-in in the SCiLS lab software. Features with a ROC-value above 0.75 were considered for further investigation. The results were manually filtered for ions representing chemical background detected outside of the tissue sections and the remaining features were annotated based on their accurate mass using established databases (METLIN, human metabolome database (HMDB), LipidMaps) with a maximum error of 5 ppm between the mean measured mass and the theoretical mass. Statistical analysis for the features identified by the untargeted investigation as well as all subsequent comparisons between the treatment groups were determined by comparing the abundances of all pixels of each treatment group. Statistical significances were determined using the Kruskal-Wallis test followed by Dunn's test for multiple comparisons in GraphPad Prism (V. 8.0.1) (GraphPad Software, San Diego, CA, USA). All information regarding the metabolite annotations and the statistical significance identified in the untargeted approach are summarized in Table A2.1.

Pixel-wise principal component analysis (PCA) was always performed including all pixels from all tissues and treatment groups. The data was analyzed without normalization but including unit-variance scaling to compensate for bias based on the overall abundance of the features.

Results and discussion

To evaluate the impact of the proposed UV-C decontamination has on endogenous metabolites and xenobiotics in prepared tissue sections, various rat organs were prepared on microscope slides, irradiated using the 30- or 180-min decontamination cycle and analyzed side-by-side to control samples in a single DESI-MSI experiment. The results of the untargeted analysis revealed numerous changes in the tissue metabolome which are displayed in Figure 4.1.

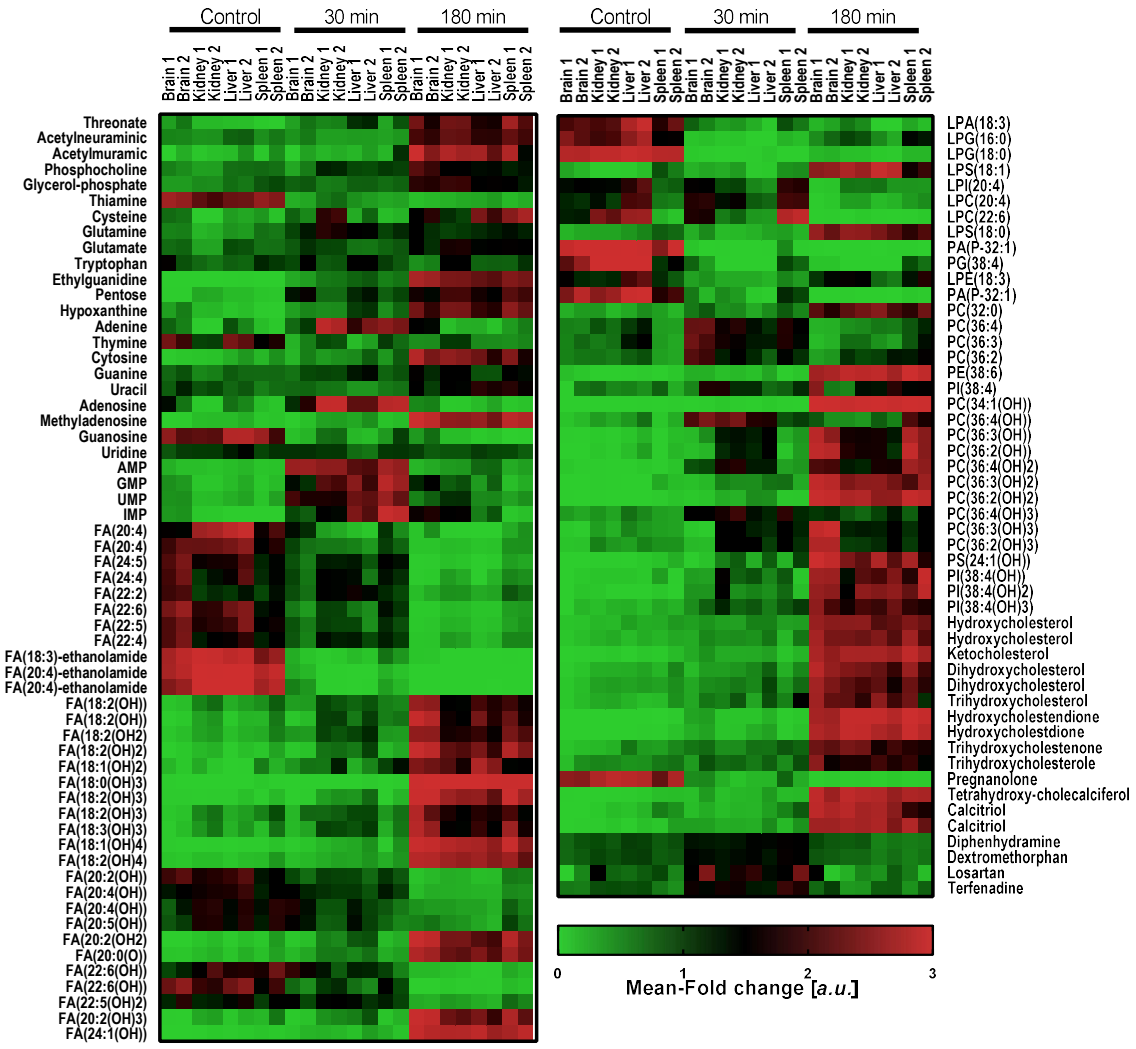

Figure 4.1, Alterations of the tissue metabolome inflicted by the UV-C irradiation: Mean-Fold changes of metabolite abundances after 30 and 180 min respectively compared to unirradiated controls. The mean-fold change for each organ was calculated for the mean of each simultaneously analyzed set or organs, i.e. Brain 1, brain 2, etc. AMP = Adenosine monophosphate, GMP = Guanosine monophosphate, UMP = Uridine monophosphate, IMP = Inosine monophosphate

The alterations of the tissue metabolome included, but were not limited to, decrease of (poly-unsaturated) free fatty acids (FAs) and glycerophospholipids, increase of glycerophospholipid and ribonucleotide fragments such as phosphocholine, glycerol-phosphate, ribose and methyladenine. Furthermore, oxidation of FAs, glycerophospholipids and sterols was observed. Whilst the decrease of FAs and glycerophospholipids and the appearance of oxidized lipids increase with the irradiation duration. Some analytes in Figure 4.1 appear to have increased abundances after 30 min of irradiation and decrease after irradiation for 180 min. These analytes include nucleotides adenosine monophosphate (AMP), guanosine monophosphate (GMP), uridine monophosphate (UMP) and inosine monophosphate (IMP) as

well as the dosed drugs. However, this increase was not reproducible in subsequent experiments and were attributed to non-reproducible drying effects of the tissues. These effects likely depend on the overall residence time of the samples in the cryostat chamber during sectioning and decontamination.

Pixel-wise PCA visualizes the discriminating alterations into spatial context of the analyzed specimens, revealing distinct tissue-type specific impacts of the UV-C irradiation. Figure 4.2a displays the RGB overlay of the first three principal components of the samples analyzed by DESI-MSI in negative ion mode. Whilst the brain and spleen sections showed only moderate deviation from the predominant PCs in the control sections, kidney and liver sections showed gradual transition of the predominant PCs over the treatment conditions. The monochromatic images for the principal components and the scoring plots can be found in Figure A2.1. The map of the metabolome alterations drawn by the spatial PCA analysis closely resembles the distributions of single metabolites such as the oxy-lipids PI(18:0/20:4(OH)) and PI(18:0/20:4(OH)3) which most likely originate from PI(18:0/20:4) formed in an oxidative environment. The Corresponding product ion spectra can be found in Figure A2.2.

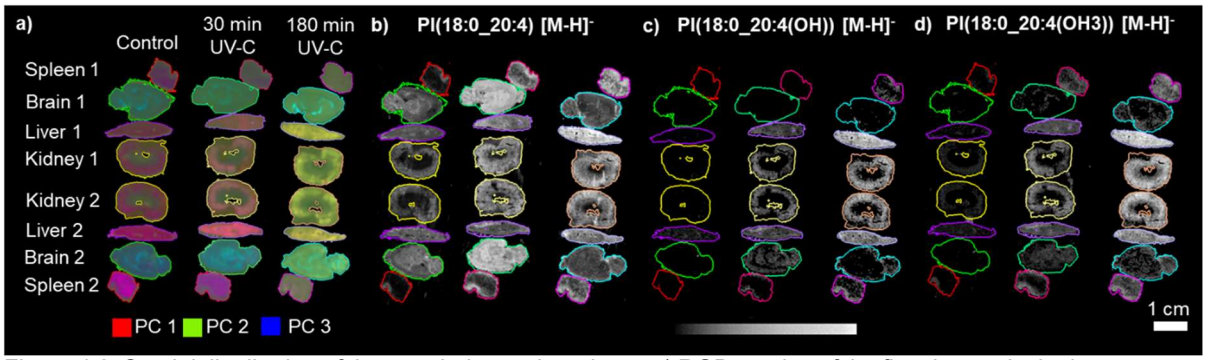

Figure 4.2, Spatial distribution of the metabolome alterations: a) RGB overlay of the first three principal components of the pixel-wise (PCA) of all sections analyzed by DESI-MSI in negative ion mode. b) Distribution of the PI(18:0/20:4) compared to the oxy-lipids c) PI(18:0/20:4(OH)) and d) PI(18:0/20:4(OH)3).

A strong scent of ozone emerged from the working chamber of the cryo-microtome after decontamination of the samples, particularly after the 180 min UV-C cycle. UV light is known to dissociate molecular oxygen (O_2) into oxygen atoms, which can react with molecular O_2 producing ozone (O_3). Ozone in turn can react with olefins under formation of ozonides, which hydrolyze into aldehydes, hydroxy-hydroperoxides and hydrogenperoxide[95] resulting in the

subsequent formation of additional reactive oxygen species (ROS). To investigate the role of atmospheric oxygen, and potentially identify a way to limit formation of oxy-species irradiation experiments were performed under inert argon atmosphere. As UV-C light had the most significant impact on liver and kidney sections, these samples were mounted onto standard glass microscope slides and irradiated under an inert atmosphere. These samples showed overall a significant formation of oxy-species which was for many molecular species comparable to samples irradiated under normal atmospheric conditions (Figure 4.3 and Table A2.2). The observed formation of oxy-species formation under inert atmosphere is a strong indicator that atmospheric oxygen plays only a minor role in the underlying mechanism. When these experiments were repeated with samples mounted on PP wafers, overall a significant formation of oxy-species under inert and normal atmosphere was detected. Interestingly, both irradiated samples showed only marginal formation of many oxy-species in kidney whilst larger amounts could be detected in liver sections (Figure 4.3 and Table A2.3).

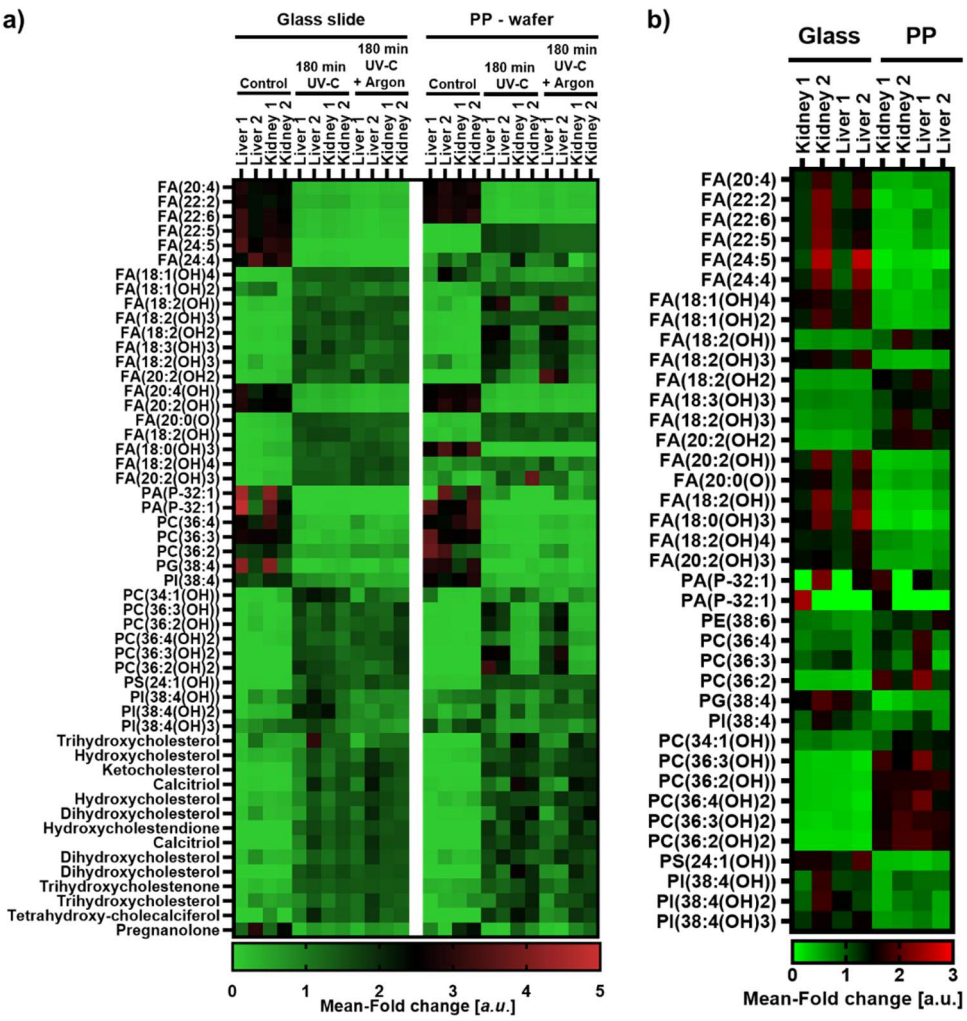

Figure 4.3, Effects of the mounting substrate on lipid oxidation: Heatmap with Mean-Fold changes in abundance of oxy-species and potential precursors after 180 min of irradiation and 180 min irradiation under inert atmosphere compared to unirradiated controls. The samples were either mounted on standard microscope slides (left) or polypropylene (PP) wafer (right and acquired in individual experiments and analyzed separately or b) analyzed and processed simultaneously). The mean-fold change for each organ was calculated for the mean of each simultaneously analyzed set or organs, i.e. Liver 1, Kidney 2, etc.

The reduced formation of oxy-species and the ability to observe these tissue-type dependent differences on PP wafers indicated that the carrier material the samples were mounted on was one of the main contributing factor for the formation of oxy-species. Liberation of reactive oxygen species from the amorphous crystal lattice of the glass appeared to be a dominating source of oxygen for the formation of oxy-species. However, side-by-side analysis of irradiated samples prepared on standard glass slides and PP wafer showed significant differences in abundance for many species. Interestingly, the differences were driven by the detection polarity and not by the formation of oxy-species due to the mounting substrate. Overall, analytes detected in negative ion mode showed higher abundances in samples mounted on

glass slides whilst analytes detected in positive ion mode showed higher abundances in samples mounted on PP wafers (Figure 4.3 and Table A2.4). These polarity-based effects are likely driven by differences in surface charging and electrical capacitation of the substrates during the desorption electrospray based ionization process[96], thus limiting the ability to directly compare the magnitude of oxy-species formation based on the substrate.

Secondary mechanisms of the oxidation could involve photo-activation of endogenous metabolites or remnant tissue bound water still present after the desiccation of the tissues. The underlying reactions can be as manifold as the complexity of the tissue metabolome itself and full elucidation of the mechanisms would exceed the scope of this study. Potential mechanisms could include indirect photo-degradation via photo-induced charge-transfer-based formation of radicals which can subsequently react with either tissue-bound water or oxygen-rich endogenous metabolites as it was reported indirect photodegradation of pharmaceuticals in waste water[97] or those reported for the oxidation of ethylenediaminetetraacetic acid (EDTA) and methionine by riboflavin in anaerobic solutions[98]. The tissue dependent effects between kidney and liver, which is rich in enzyme bound iron, may point towards potential involvement of iron catalyzed photo-generation of reactive oxygen species[99, 100]. Overall, the presence of atmospheric oxygen was found to be a minor factor in the formation of oxy-species. Due to the strong promotion of oxy-species formation the use of non-glass carrier materials such as stainless-steel targets for analysis by MALDI-MSI and non-conductive plastic microscope slides for analysis by DESI-MSI could be of advantage. The use of such non-glass materials additionally benefits from the sturdiness of these substrates and the reduced risk of injury inherently associated with the use of glass consumables. However, the drawback of these substrates is the incompatibility with optical microscopy imaging techniques due to the lack in transparency or incompatibility with organic solvents such as xylene. The use of standard glass microscope slides might be inevitable for classical histological staining approaches such as evaluation of H&E stained tissue sections.

Degradation of pharmaceuticals through photolysis under UV irradiation is widely reported and the basic underlying mechanisms are well understood[101-108]. Time-course experiments were performed to characterize the degradation kinetics of the dosed drugs, terfenadine, dextromethorphan, diphenhydramine and losartan. The mean relative abundances of the drugs plotted over the irradiation time resulted in well fitted first order decay kinetics for the four drugs (Figure 4.4). The coefficients of determination (R^2) ranged from 0.946 for losartan to 0.986 for terfenadine. Terfenadine and losartan had half-lifes of 22.2 min and 21.6 min whist dextromethorphan and diphenhydramine displayed faster degradation with half-lifes of 11.6 min and 13.4 min respectively (Figure 5). As the decay showed first order kinetics the degraded fraction of the drugs is proportional to the concentration of the drug and the exposure time and thus the UV-C fluency.

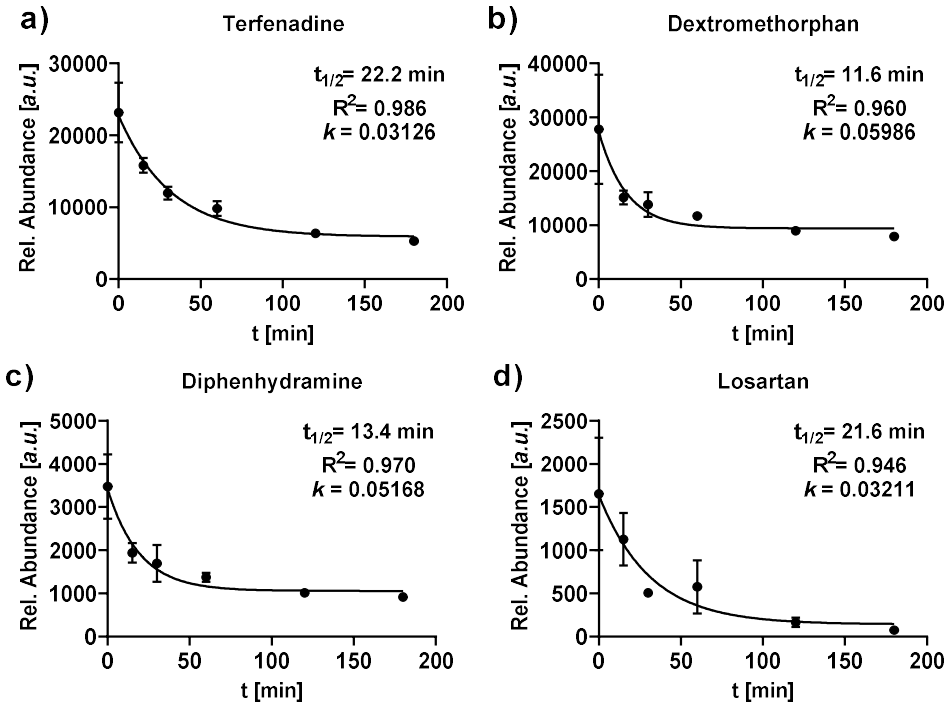

Figure 4.4, Decay of drugs under UV-C irradiation: a) terfenadine, b) dextromethorphan, c) diphenhydramine and d) losartan under UV-C irradiation over time. Curves were fitted as first order decay with R^2 as the measure for goodness of fit as well as the calculated half-life and decay constant k are given in each graph. Each datapoint is given as mean abundance ± SD of 3individual datapoints.

As in this relationship a drugs half-life is independent of the starting concentration it allows for accurate elucidation of the drug's biodistribution as the relative differences in concentration will be preserved across a given tissue section. The time-dependent decay of the drugs

resulted in decrease in abundances of 60.9% for terfenadine, 83.4% for dextromethorphan, 78.8% for diphenhydramine and 61.8% for losartan after 30 min of irradiation respectively. The relative abundances for all four drugs were reduced by >99% after 3 h of irradiation and the drugs effectively undetectable. The severe impact of the UV-C exposure onto the tissue metabolome and xenobiotics raises the need to limit exposure times to a required minimum and find a compromise that allows for safe handling of the samples outside an airflow-regulated biosafety cabinet whilst still allowing one to elucidate molecular distributions from the tissue sections.

The 3 h decontamination cycle of the instrument is certified for high level decontamination, effectively inactivating surface pathogens such as bacteria, fungi including spores and viruses[109]. As effective as the high-level decontamination is to reduce potential pathogen load, the decontamination cycle also leads to extensive degradation of the endogenous tissue metabolome and xenobiotics detectable by MSI. The intermediate decontamination cycle of 30 min was found to be less destructive but at cost of lower decontamination efficiency. UV-C resistant viruses such as adenovirus, hepatitis B virus and simian virus 40 are proven to show less than 4 $\log_{10}$ units of reduction[109] requested by official guidelines for testing of antiviral surface decontamination procedures[110]. Simian virus 40 (SV40) is a suited surrogate for eradication of papovaviridae[110] and is characterized by a particularly high resistance towards a variety of decontamination procedures[111]. Successful reduction of the resistant SV40 is a reliable surrogate for the reduction of the clinically more relevant Papovaviridae, including human papilloma virus (HPV) 16 and 18. However, incomplete reduction of SV40 does not necessarily reflect incomplete reduction of these clinically relevant strains, which explains why SV40 is only included in the German guidelines but not included in the European guidelines for surface disinfection[110-112]. The main safety concerns regarding the analysis of clinical samples by MSI arise from the risk of transmitting clinically relevant pathogens through aerosolization and the associated infection risk through contact with or inhalation of pathogen carrying particles. Pathogens identified as relevant to our current work are blood borne viruses

including HIV, Hepatitis B and C, and when examining cancer tissues, include high risk carcinogenic viruses such as HPV 16 and 18 for their high prevalence in cervical and head and neck cancer[113]. Other risk pathogens include Herpesviridae such as Human Herpes virus 6 (HHV6), Herpes simplex virus 2 (HSV2) and Epstein-Barr virus (EBV) which have a high prevalence in glioblastoma specimens[66]. Germicidal UV-C irradiation has proven to be an effective measure against these strains[69, 114, 115].

Germicidal UV-C decontamination is primarily a method suited for pathogen reduction on surfaces as the light has a limited penetration depth in organic matter[116]. However, UV-C induced DNA damage could be detected up to 40 µm in xenograft tumor models measured as 53BP1 foci formation[70]. With the additional observation of formation of reactive oxygen species from the glass substrate underneath the mounted tissue sections at least partial inactivation of potential pathogens can be assumed throughout the 10 µm thick tissue sections. The proposed methodology is a means to reduce pathogen load and increase operator safety when analyzing clinical samples by MSI but does not guarantee high level disinfection. The use of tissue sections exceeding 40 µm thickness are likely to limit the efficiency of the procedure and further validation of the efficiency would be required.

Conclusions

Analysis of clinical tissue specimen to elucidate biodistributions of drugs in clinical trial settings is gaining importance to build better understanding of the translational potential of pre-clinical findings into man. The ability to analyze a drugs distribution within the context of the tissue allows to differentially investigate the phenotypical differences of clinical outcomes, e.g. of responder vs non-responder in cancer treatment therapy. The here proposed UV-C based approach enables the pathogen load of clinical tissue specimens to be reduced prior to MSI analysis, increasing operator safety and reducing the risk of aerosolization of tumor promoting pathogens. The main drawback of the proposed procedure is the lack in control of the effective UV-C fluency imposed onto the tissues and the alterations of the metabolome and xenobiotics within treated tissues. The decontamination cycles of the cryostat used for the

decontamination involve large safety margins to compensate for fluctuations in the UV-C fluency across the chamber and are designed to allow for efficient irradiation of pathogens across the whole working chamber. The here presented work clearly established the feasibility to use UV-C radiation to treat clinical tissue specimens whilst still being able to subject these tissues to MSI analysis.

Chapter 5: Desorption electrospray ionization for targeted mass spectrometry imaging

Introduction

Once high quality tissue sections are prepared and if applicable decontaminated, they are ready for analysis by MSI. The majority of MSI studies employ expensive and complex mass spectrometer, using TOF[117, 118], Orbitrap[119, 120] or FT-ICR[121, 122] technology as mass analysers. These experiments produce large datasets containing comprehensive information about the spatial distribution of thousands of chemical constituents. The advantage of these large datasets is that they carry broad information about the overall status of the tissue and this information can further be interrogated to understand the undelying biochemical interactions. However, for many purposes the vast majority of the obtained information is not needed and monitoring of relevant features would be sufficient. Triple quadrupoles (TQs) operated in multiple reaction monitoring (MRM) mode are widely used for quantification purposes, taking advantage of their stable signal over a broad dynamic range. At the same time TQs operated in MRM mode show superior sensitivity and comparable specificity compared to other mass analysers. These advantages make TQs highly suitable and robust for MSI analysis. Furthermore, MRM based data acquired on a TQ mass spectrometer can increase throughput whilst reducing the amount of data to the required minimum reducing costs for data analysis and storage.

MSI based drug metabolism and pharmacokinetics (DMPK) studies are part of the early drug development process and predominantly evaluate the distribution of drugs and their metabolites within distinct tissues or whole body sections. The ability to monitor only selected features by MSI for DMPK studies were previously demonstrated by coupling of a MALDI source with an Q-trap mass spectrometer operated in MRM mode. Among others, this setup was applied to map the distribution of moxifloxacin in tuberculosis-infected rabbit lungs [123]. Previous reports demonstrated the possibillity of urinary screening for illicit drugs and quantitation of pharmaceuticals in plasma by coupling a DESI ion source to a TQ operated in

MRM mode[124, 125]. A recent report also highlights the ability to use such an approach for MSI purposes[126].

Aim/objective

This chapter will demonstrate the suitability of DESI performed on a TQ for MSI analysis and explore its applications in DMPK studies. Targeted data acquisition was used to determine the desorption/ionization kinetics of the novel setup and demonstrate the use for elucidation of drug distribution in tissue sections. The use of the setup to map biochemical pathways to monitor toxicodynamic effects will be explored in Chapter 7.

Materials and Methods

Chemicals

Analytical grade acetonitrile and water were obtained from Fisher Scientific (Loughborough, Leicestershire, UK). 2-Methylbutane, methanol and acetic acid were obtained from Sigma-Aldrich (Poole, Dorset, UK). Test compounds for dosing were obtained in house from AstraZeneca compound management group (Macclesfield, Cheshire, UK) with the exception of moxifloxacin which was purchased from Sigma-Aldrich (Poole, Dorset, UK). MALDI-MS grade 2,5-dihydroxybenzoic acid (DHB) was purchased from Sigma-Aldrich (Poole, Dorset, UK).

Animals and dosing

Adult male Han Wistar rats (approximate weight 260 g) were obtained from Charles River Laboratories (Margate, Kent, UK) and were acclimatized on site for a minimum of 3 days prior to dosing. Compounds were formulated in 5% dimethyl sulfoxide/95% (30% w/v Captisol in water) and administered orally. Control animals were dosed with vehicle via the same administration route. The samples used were from a previously reported study exploring cassette-dosing as a tool to increase throughput in DMPK studies [74]. The animals were cassette-dosed with moxifloxacin, olanzapine, erlotinib, and terfenadine at 25, 10, 10, and 25 mg/kg, respectively. Animals were euthanized either 2 or 6 h post dose. All tissue dissection was performed by trained AstraZeneca staff (project license 40/3484, procedure number 10).

Tissues (brain, kidneys, and liver) were snap-frozen in 2-methylbutane on dry ice, all subsequent transfer of tissues was done on dry ice, and samples were stored at −80 °C until tissue processing.

Tissue Processing for MSI

Tissue sections were cut at a thickness of 10 µm and thaw-mounted onto SuperFrost Plus Glass slides (Thermo Fisher Scientific Inc., Waltham, MA, USA) for DESI-MSI experiments or indium tin oxide (ITO)-coated MALDI target slides (Bruker, Bremen, Germany). For the drug distribution and toxicity studies sections were taken where possible at approximately equal depth from all organs to allow visualization of similar structures between samples. Slides with mounted tissue sections were stored at −80 °C until analysis. Where applicable, organ tissue sections from -dosed and vehicle control animals were mounted adjacent on the same slide and were analyzed in one experiment to limit the risk of any observed variation in relative abundance as a result in loss of analyser sensitivity during the course of the experiment.

DESI-MSI

DESI-MSI experiments were performed either on a Xevo G2-XS Q-TOF or a Xevo TQ-S (Waters, Manchester, UK) equipped with a 2D sampling stage (Prosolia Inc., Indianapolis, IN, USA) and a custom-built inlet capillary heated to 500˚C. The nominal pixel size was set to 50x50 µm. The Q-TOF setup was equipped with a commercially available DESI spray head (Waters, Manchester, UK) operated with a mixture of 95%/5% (v/v) methanol/water, containing 1 µg/ml raffinose for lockmass correction. The solvent was delivered with a flow rate of 0.75 µl/min the nebulizer gas pressure was set to 4 bar. The regions for the imaging experiments were selected and the resulting data processed in the High Definition Imaging software (Waters, Manchester, UK). Data was acquired in positive ion mode over a mass range of *m/z* 50 to 1200 for TOF-MS mode and *m/z* 50 to 750 for TOF-MS/MS mode. The collision energies for MS/MS acquisitions were manually optimized on the Q-TOF. The acquisition speed was set to 1 scan/s.

The TQ-setup was equipped with a home-built sprayer[26] operated with the same methanol/water mixture as used for the Q-TOF but without the addition of raffinose. The solvent was delivered with a flow rate of 1.5 µl/min and nebulized with a gas pressure of 7 bar. The stage movement was controlled through Omni Spray 2D (Prosolia Inc., Indianapolis, IN, USA). The scan speed was set to 10 scans/s. Positive ion mode MRM transitions were optimized for the drugs, their metabolites and endogenous metabolites. The latter were used to establish the tissue outline. Drug standards were infused into the mass spectrometer through the commercial ESI source and MRM transitions were optimized by running the auto-optimization function in the operating MassLynx software. MRM transitions for the drug metabolites were created based on their product ion spectra obtained from the MS^e function of the LC-MS based metabolite identification whilst transitions for endogenous metabolites were established based on product ion spectra obtained by DESI-MS/MS analysis performed on a Q-TOF. The final transitions are given in Table 5.1. The collision energies were for both species were subsequently manually optimized on the TQ to achieve optimal MS response. Separate line scans were performed over the imaging area and the resulting data files were processed in an in-house developed tool box operating in MATLAB (Mathworks, Natick, MA, USA) environment. The different functions were relatively scaled and overlaid where applicable to allow visualization of the drugs and metabolites within the tissue section.

Table 5.1: MRM transition used for the targeted DESI-MSI experiments:

Compound	**Transition**
Olanzapine	313.15>256.9
Erlotinib	394.18>278.09
Moxifloxacin	402.18>261.10
Terfenadine	472.32>436.30
PC(34:1) $[M+K]^+$	798.54>739.47
PC (36:2) $[M+K]^+$	824.55>765.48
PC(38:4) $[M+K]^+$	844.53>785.46

Re-alignment of the individual line scans

The individual line scans acquired on the TQ setup showed an instrument dependent offset between start of the stage movement and the data acquisition. The offset results in horizontal shifts of the individual line scans in the compiled image. The offset is increasingly noticeable with increasing scan rates, resulting in significant distortion at 10 scans/s. To compensate for the shifts, the individual line scans were re-aligned to reduce the blurriness of the images. To perform the re-alignment, the tissues were identified by k-means clustering (2 cluster) performed on the whole dataset (Figure A3.1). The first line scan of the tissue was manually selected, and subsequent lines were re-arranged by average smoothing of the tissue edge over 15 neighbouring lines (Figure 5.1b). The smoothed TIC image of the tissue section is displayed in Figure 5.1d.

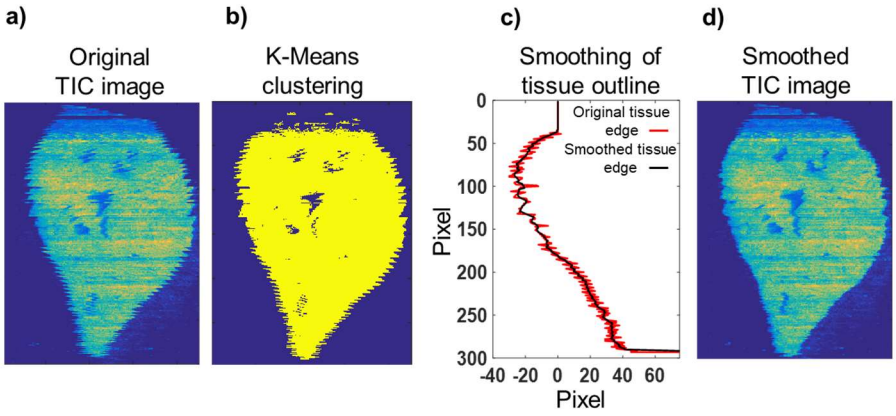

Figure 5.1**,** Re-alignment of the imaging data: a) Original total ion current (TIC) image of a rat liver section. b) K-means clustering (2 cluster) was used to distinguish between tissue (yellow) and background (blue). c) After manual selection of the first pixel, all subsequent lines were re-arranged by average smoothing over 15 adjacent line scans. d) The TIC image of the liver section after re-alignment.

MALDI-MSI

As the slides used in this chapter were not stored in a vacuum sealed slide mailer, they were immediately dried under a stream of nitrogen when removed from the -80˚C freezer to prevent water condensation on the sample surface. DHB was applied as MALDI matrix as described in Chapter 2. MALDI imaging was performed using a rapifleX MALDI Tissuetyper (Bruker Daltonics, Bremen, Germany) system equipped with a smartbeam 3D laser. Data acquisition was controlled through Bruker's Fleximaging software. The resulting data was converted into imzML files and processed in msIQuant [127]. The pixel size was set to 50 µm and 400 laser

shots were collected per pixel with a laser repetition rate of 5 kHz. The data was acquired in positive ion mode over a mass range from *m/z* 200 to 1000.

LC-MS based metabolite identification

Single tissue sections were transferred into extraction tubes and zirconia beads and 0.5 mL of ice-cold methanol were added. To break up the tissue structure tubes were vortexed for 1 min and subsequently transferred for 5 min in a sonic bath. The suspension was centrifuged for 10 min at 12000 rpm under refrigeration and the supernatant was transferred into a new extraction tube and stored on ice. The remains were twice re-suspended in 0.5 ml ice cold methanol, mixed in the vortex, centrifuged and the supernatant pooled with the previous supernatant of the sample. Pooled supernatants were dried under nitrogen and reconstituted in 150 µL 25/75% (v/v) methanol/water. The samples were again centrifuged under refrigeration for 20 min at 12000 rpm to ensure quantitative removal of all particles. The supernatant was transferred into 300 µL glass insert vials and stored at -80˚C until used. To identify the drug metabolites present in the different tissues, tissue extracts were analyzed by LC-MS. Separation of the drugs and their metabolites was carried out on an UPLC system (Waters Acquity System, Manchester, UK) equipped with a BEH C18 column with the following dimensions: 100 mm × 2.1 mm i.d., 1.7 µm particle size (Waters, Manchester, UK). The column was heated to 55˚C and operated with a mobile phase flow rate of 0.5 mL/min. Eluent A was 0.1% aqueous acetic acid and eluent B was 0.1% acetic acid in methanol. 5 µL were injected per sample and separated with the following linear gradient initially 5% B, T=0.5 min 5% B, T=8.00 min 90% B, T=8.01 min 100% B, T=8.50 min 100% B, T=8.51 min 5% B, T=9.00 min 5% B. The mass spectrometric analysis was performed with a Xevo G2-XS Q-TOF (Waters, Manchester, UK) operated in positive ToF-MS mode over a mass range from m/z 50 to 1200. Additionally, an MS^e function was acquired to obtain MS/MS spectra for the compounds eluting from the column. The collision energy for the MS^e acquisition was ramped from 25 to 40 V to obtain a broad variety of product ions.

Results and discussion

After the optimization of the MRM transitions for the drugs and endogenous lipid species, the effect of the dwell time was evaluated. Relative abundances of the 4 drugs and 3 endogenous lipids were compared at dwell times of 59, 27, 9 and 3 ms corresponding to acquisition rates of 1, 2, 5 and 10 pixel/s respectively (Figure 5.2a). For all experiments the stage movement was adapted to the scan speed and every spectrum represents 100 µm of scanned sample. For each dwell time 25 consecutive line scans were performed. The raw files were processed in Matlab environment. For each dwell time the spectral information was exported as the mean of 36 pixels. Interestingly, for the highly abundant endogenous lipids and terfenadine the relative abundances increased with shorter dwell times, whilst the abundances for erlotinib and olanzapine showed no direct dependence on the dwell time. With a maximum of 190 counts at a dwell time of 59 ms and no clear corresponding ion image for the drug moxifloxacin abundances are mainly below the limit of detection even on the longest dwell time tested. The ion abundance values reported by the instrument were normalized to the dwell time, thus the abundances of each analyte should be constant across all scan speeds. To explain the deviation from a linear relationship of signal-response to dwell time, the kinetics and dynamics of the DESI part were evaluated taking advantage of the fast scan rates of the setup. Desorption kinetics acquired under static conditions for the monitored drugs and lipids showed an initial delay in detection when the spray was directed onto a tissue section, followed by an increase in signal intensity, plateauing and subsequent decline (Figure 5.2c).

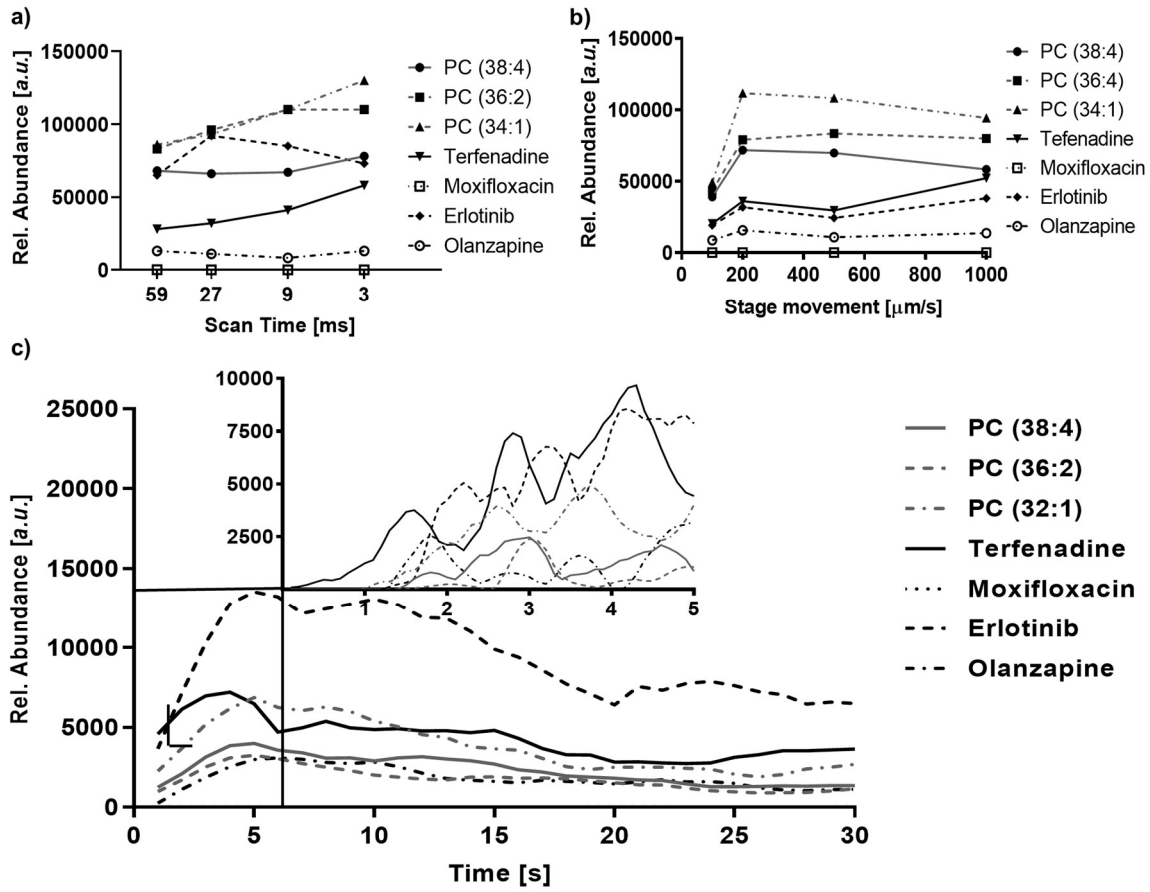

Figure 5.2, Evaluation of the desorption kinetics and dynamics of the DESI-TQ setup: a) Relative abundances of endogenous compounds and cassette-dosed drugs over dwell times of 59, 27, 9 and 3 ms/transition. PC-phosphatidylcholine. Data represents the mean of 3 randomly chosen ROIs per data-point. b) Desorption dynamics for the monitored compounds for stage movement of 100, 200, 500 and 1000 µm/s acquired at a constant dwell time of 9 ms resulting in a scan rate of 5 scans/s. Data represents the mean of 3 independent experiments. c) Kinetics experiment monitoring the same transitions were performed with a dwell time of 59 ms resulting in a scan rate of 1 scans/s. The zoomed panel shows the static kinetics of the first 5 seconds acquired with a dwell time of 3 ms resulting in a scan rate of 10 scans/s. All data represents the mean of 3 independent experiments.

The distinctive phases can be correlated with the steps of the desorption/ionization process depicted in Figure 5.3: The initial delay is based on the required re-hydration of the tissue section and dissolution of the compounds in the spray solvent. With increasing excess spray solvent present on the tissue surface, the desorption/ionization becomes more efficient as more of the analytes are dissolved at a given time resulting in signal increase with a slope defined by the dissolution kinetics of the compound in the spray solvent. The plateau marks the point for the process when the dissolution kinetics becomes the rate-limiting step for the process. The final decline of the signal demonstrates exhaustion of the tissue section and depletion of analytes that can be desorbed/ionized.

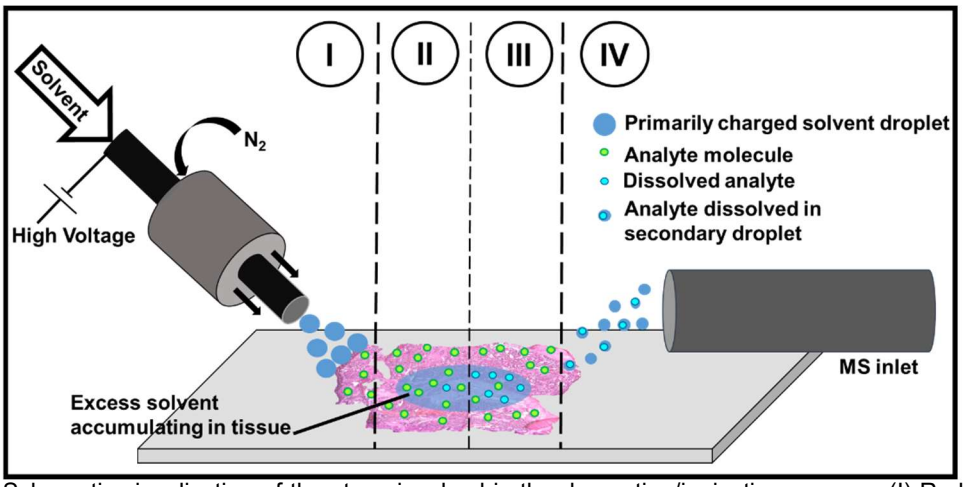

Figure 5.3, Schematic visualization of the steps involved in the desorption/ionization process: (I) Re-hydration of the tissue section through primarily charged electrospray solvent (II) Accumulation of excess spray solvent in the tissue section and dissolution of analytes (III) Analytes are increasingly dissolved in excess spray solvent and (IV) desorbed in secondary droplets which enter the mass spectrometer. For easier accessibility of the schematic not visualized is step (V) depletion of analytes from target tissue.

For an imaging application with a high scan rate the initial steps are particularly significant as they most closely represent the conditions in MSI experiments. The desorption dynamics for the initial seconds of spray solvent reaching the tissue were monitored with a scan rate of 10 scans/s (Figure 5.2c). The compounds showed different time onsets for the signal detection with terfenadine, erlotinib and olanzapine displaying the fastest desorption/ionization with first maxima observed between 1 to 2 s whilst the structural lipids display a slower desorption/ionization with maxima observed between 2 to 3 s. Interestingly, all compounds show an oscillating pattern. Terfenadine and olanzapine tend to show maxima at similar times whilst erlotinib anticorrelates and displays highest response when olanzapine and terfenadine valley, suggesting potential charge competition/suppression. The abundance of compounds observed in DESI-MSI experiments is not just dependent on the desorption kinetics but on the speed of stage movement. Additional experiments with constant scan rate and differential stage movement speed were performed to investigate the contribution of the dynamic stage movement to the detected signal. When increasing the stage movement speed from 100 µm/s to 200 µm/s the detected signal for all compounds doubles as expected, as twice the amount of tissue was analyzed. However, when the stage movement was increased to 500 µm/s the signal for most compounds dropped slightly,

most likely due to a shift of the detection from the exhaustion phase into the plateau phase observed in the kinetics experiments. Further increase of the stage movement results in a further decrease of the monitored lipids whilst the signal detected for the drugs increases to a maximum, consistent with a shift into the dynamic front region of the kinetics experiments, the phase in which the desorption/ionization is dependent on the dissolution speed of the target compound. This behavior allows careful optimization of the setup for target analytes, especially when they show differential dissolution kinetics than the main tissue components. As the shortest dwell time resulted in highest sensitivity for the xenobiotics, subsequent imaging experiments were performed with a dwell time of 3 ms corresponding to an acquisition rate of 10 scans/s. Figure 5.3 shows the distribution of terfenadine in rat liver sections 2 h post dose. The images obtained on the Q-TOF and TQ setup show comparable distributions of terfenadine within the organ. Terfenadine accumulates predominantly in the periportal zone (zone 1) with distinct separation from the endogenous lipid PC (36:2) highlighting centrilobular areas (zone 3).

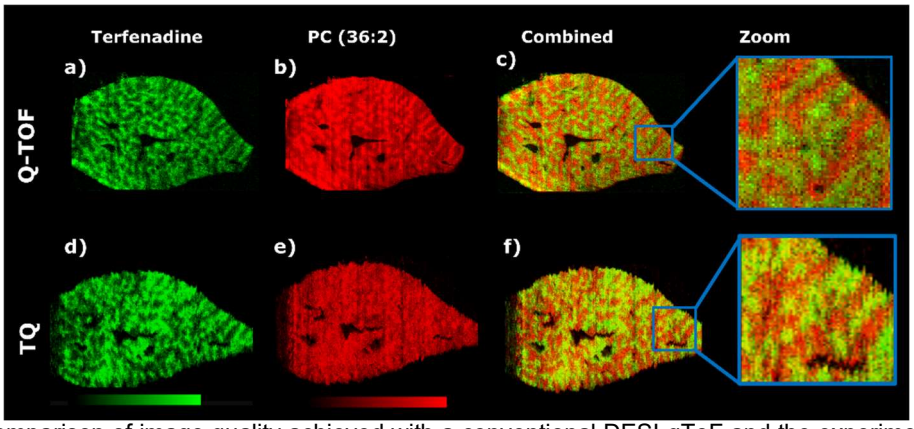

Figure 5.4, Comparison of image quality achieved with a conventional DESI-qToF and the experimental DESI-TQ setup: Ion images for terfenadine (a,d) and endogenous lipid PC (36:2) (b,e) obtained by DESI-MSI performed on a Xevo G2-XS or a Xevo TQ-S. Figures c and f show the combined ion images of the drug and the endogenous lipid. The zoomed view displays the tissue edges.

The feature resolution of the images obtained on the TQ appears lower even though both data sets were acquired with a spatial resolution of 50 µm. This distortion arises from an instrument dependent de-synchronization between stage movement and the start of the data acquisition. The de-synchronization results in line-to-line jitter by a few

pixels. The effect is more pronounced with increasing scan rates. The shifts were compensated in Figure 5.4 by re-aligning the individual line scans as described under "*Re-alignment of the individual line scans"* in the methods, the original images are displayed in Figure A3.1. Data on the biodistributions of olanzapine, erlotinib and terfenadine as well as selected endogenous species could be acquired with high sensitivity and specificity using the TQ setup. The resulting data file size, for a whole microscope slide holding 3 liver sections, was reduced from around 100 GB for the Q-TOF data to below 1 GB (873 MB) for the 16 acquired MRM transitions on the TQ. Additionally, the data acquisition rate could be increased from 1 scan/s on the Q-TOF to 10 scans/s on the TQ. To evaluate the sensitivity of the new setup, the detection level of olanzapine and its metabolite hydroxy-olanzapine in sagittal rat brain sections were compared between instrumental setups. The TQ setup was compared to a Q-TOF and a MALDI-TOF. As anticipated, the MALDI created images with high spatial resolution and sharp outlines of the tissue structures (Figure 5.5) but neither olanzapine nor the hydroxy-metabolites could be detected within brain tissue sections, even though the matrix and its application were previously optimized for the detection of the dosed drugs.

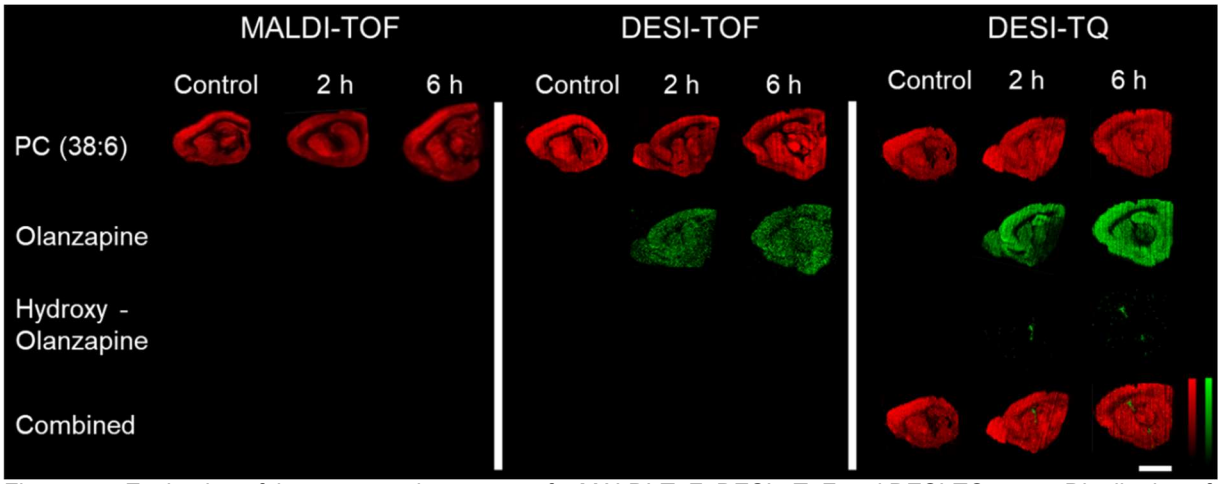

Figure 5.5**,** Evaluation of the compound coverage of a MALDI-ToF, DESI-qToF and DESI-TQ setup: Distribution of endogenous lipid PC(38:6), olanzapine and its metabolite hydroxy-olanzapine in sagittal rat brain sections collected 2 and 6 h post dosing compared to a vehicle control. Distributions were determined by MALDI and DESI-MSI. DESI-MSI experiments were performed on a standard Q-TOF or a TQ-setup respectively. All data was acquired with a spatial resolution of 50 µm. Scale bar = 4 mm CTX = frontal cortex, CC = corpus callosum, HP = hippocampus, V = ventricle

The DESI-Q-TOF setup delivered similar sharp ion images for endogenous compounds acquired in full scan mode. Through the reduction of chemical background, data acquired in MS/MS mode showed clearly the presence of olanzapine within the tissue section but based on the limited sensitivity a clear identification of areas with drug accumulation was not possible. The improved sensitivity of the DESI-TQ setup enabled to elucidate the biodistribution of the olanzapine and its hydroxy-metabolite. The TQ data revealed accumulation of olanzapine in the frontal cortex (CTX) and hippocampus (HP) whilst it could not be detected in the corpus callosum (CC). The overlay with the endogenous lipid PC(38:6) located the drug in the ventricle (V), where it most likely accumulates in the choroid plexus. The observed inability of hydroxy-olanzapine to penetrate the blood-brain barrier and accumulate in the brain tissue is consistent with previous reports[128].

Conclusions

The acquisition speed, instrumental robustness and the small size of the resulting data files make the presented DESI-TQ setup the perfect fit for large scale imaging studies with high sample throughput, allowing cost effective data acquisition, storage and processing. These advantages leave room to envision the potential of a semi- or fully automated setup - loading prepared slides, performing MSI analysis, staining the slides for histological evaluation and presenting the optical scans alongside the MSI results. Such an automated setup could equally be used for high-throughput elucidation of drug and drug metabolite distribution within biological samples. This could be advantageous as first line in vivo screening for candidate selection in the pharmaceutical development process to evaluate a compound's properties, e.g. target engagement or blood-brain-barrier penetration and help select the most promising candidates for further optimization. As described in Chapter 7, the ability of the setup to monitor the effects a drug causes within a tissue allows to directly link the drugs distribution to its toxicodynamic or pharmacodynamic effects. Creation and curation of biomarker libraries would allow to specifically evaluate the biodistribution of a drug alongside

readouts for efficacy and toxicity in early drug development pipelines. The channel-based structure of the TQ data would allow to handle the generated data as images and align the data processing pipelines with those already used for optical high throughput imaging approaches and present the combined datasets. Such an approach would allow for MSI analysis to scale supporting the early drug development process with high throughput drug distribution studies informing on efficacy and toxicity of the drug candidate on the molecular and histological level. Lower throughput imaging modalities based on high mass resolving analyser technology can then be utilized efficiently to study pharmacodynamic or toxicodynamic effects in-depth.

In clinical settings, high resolution mass analysers are well suited for investigative studies gathering a wealth of information in physiological, disease and fundamental research. Utilizing this knowledge combined with the availability of in vivo diagnostics (IVD) certified triple quadrupole mass spectrometers, TQs are routinely used for clinical screenings such as newborn screening (NBS). Integrated in an MSI approach, TQs could be utilized for MSI guided histopathological evaluation of tissues. The guidance of the MSI data would allow histopathologists to further characterize flagged regions of interest rather than having to annotate the whole slide, reducing workload and thus further increasing sample throughput.

Chapter 6: Correlating mass spectrometry imaging and liquid chromatography-tandem mass spectrometry for drug disposition studies

Scope

Quantification of drugs present in tissue samples by liquid chromatography followed by tandem mass spectrometry (LC-MS/MS) is a standard tool in pharmacokinetics and drug disposition studies[129-131]. The ability to use standardized sample preparation and analysis protocols make LC-MS/MS analysis highly quantitative and reproducible. However, the results always represent the average of the analyzed specimen and all spatial information is lost during sample preparation. In contrast, recent MSI studies demonstrate near cellular resolution imaging allowing resolution of small morphological tissue features[132-134]. The achievable high spatial resolution enables one to follow the distribution of endogenous metabolites and xenobiotics into small morphological tissue compartments. The impact of high spatial resolution imaging could be demonstrated in recent studies evaluating blood-brain barrier permeation in rodents[135] or studying the distribution of endogenous and xenobiotics along the villi-crypt axis in rat intestines[136].

Aim/objective

This chapter explores the use of LC-MS/MS and MSI to study the drug disposition of 4 orally co-administered off-the-shelf-drugs in the rat intestine. To facilitate rapid sample preparation, the sample embedding- and preparation-protocol described in Chapter 3 was used to prepare 15 intestine specimens at a time for MSI analysis.

Methods and materials

Chemicals

Polyvinylpyrrolidone (MW 360 kDa) (PVP), (Hydroxypropyl)-methylcellulose (viscosity 40-60 cP, 2 % in H_2O (20 C)) (HPMC), 2,5-dihydroxybenzoic acid (DHB), trifluoroacetic acid (TFA), terfenadine, terfenadine-*d3*, dextromethorphan hydrobromide, dextromethorphan-*d3*, diphenhydramine hydrochloride and diphenhydramine-d3 were purchased from Merck (Darmstadt, Germany). Methanol, water, 2-methylbutan, 2-propanol and acetonitrile (ACN)

were obtained from Fisher Scientific (Waltham, MA, USA). Losartan-potassium salt was obtained from Cambridge Bioscience (Cambridge, UK). Losartan-*d4* was purchased from Toronto Research Chemicals (Toronto, Canada). All solvents used were of analytical grade or higher.

Animals and dosing

Adult male Han Wistar rats (approximate weight 260 g) were obtained from Charles River Laboratories (Margate, Kent, UK) and were acclimatized on site for a minimum of 3 days prior to dosing. Compounds were administered by oral gavage as a cassette of terfenadine, losartan, diphenhydramine and dextromethorphan, formulated in 5% dimethyl sulfoxide/95% (30% w/v Captisol in water). Animals were dosed with 25 mg/kg/drug and euthanized at 1, 2, 4 or 6 h post-dosing. Vehicle control animals were euthanized at the latest sampling time at 6 h post dose. The first 20 cm of the small intestine were cut into four pieces each and snap frozen free-floating in dry ice chilled 2-methylbutane. For each animal, 3 intestine pieces were randomly selected for this study. The pieces were each split into half, one half was extracted for LC-MS/MS quantification, the other half was embedded and subjected to MSI analysis. All tissue dissection was performed by trained AstraZeneca staff in agreement with project license 40/3484, procedure number 10.

Preparation of intestine specimens for MSI analysis

The specimens were embedded and prepared according to the workflow described in chapter 3. In brief, the intestine specimens were co-embedded in a HPMC+PVP hydrogel to enable time efficient sectioning under comparable conditions for all specimens analyzed in one experiment. A total of 15 specimens was placed upright in peel-a-way molds (Thermo Scientific, Waltham, Massachusetts, USA) pre-filled with ice cold embedding medium. Snap freezing of the filled molds was performed in dry ice chilled 2-propanol followed by a wash in dry ice chilled iso-pentane to wash off the excess of 2-propanol. The frozen molds were kept on dry ice to allow evaporation of the adherent iso-pentane before they were sectioned on a cryostat. Sections of 10 µm thickness were cut at -18 ˚C and thaw mounted on either

SuperFrost slides (Thermo Scientific, Waltham, Massachusetts, USA) for DESI or ITO coated slides (Bruker Daltonik, Bremen, Germany) for MALDI experiments respectively. To preserve the analyte integrity, samples were desiccated under nitrogen immediately after the thaw mounting, packed in vacuum sealed slide mailer and stored in a -80 ˚C freezer until analysis[18].

DESI-MSI

DESI analysis was performed on a Q-Exactive mass spectrometer (Thermo Scientific, Bremen, Germany) equipped with an automated 2D-DESI ion source (Prosolia Inc., Zionsville, IN, USA) operated in positive ion mode between *m/z* 100 to 900 with a nominal mass resolution of 70,000. The injection time was fixed to 50 ms resulting in a scan rate of 3.7 pixel/s. A home-built DESI sprayer[26] was operated with a mixture of 95 % methanol, 5 % water delivered with a flow rate of 1.5 µL/min and nebulized with nitrogen at a backpressure of 6 bar. The spatial resolution was set to 75 µm. The resulting .raw files were converted into .mzML files using ProteoWizard msConvert[72] (version 3.0.4043) and subsequently compiled to an .imzML file (imzML converter[73] version 1.3). All subsequent data processing was performed in SCiLS Lab (version 2019b, Bruker Daltonik, Bremen, Germany).

MALDI-MSI

DHB was applied as MALDI matrix as described in Chapter 2. MALDI analysis was performed on a RapifleX Tissuetyper instrument (Bruker Daltonik, Bremen, Germany) operated in positive ion mode. Drug distribution studies on intestines were performed with a spatial resolution of 10 µm in the mass range between *m/z* 200 and 1000. A total of 100 laser shots were summed up per pixel to give the final spectra. For all experiments the laser was operated with a repetition rate of 10 kHz. All raw data was directly uploaded and processed in FlexImaging (Bruker Daltonik, Bremen, Germany) or SCiLS lab software packages (Version 2019b). All reported MALDI data and images were normalized to the total ion current (TIC) to compensate for spectrum-to-spectrum variation[76].

LC-MS/MS - sample preparation and analysis

Tissues were weighed into extraction tubes and 15 µL of mixed deuterium labeled drugs prepared in ACN (1 µmol/L/drug) were added as internal standards into each tube. After addition of zirconia beads and 0.75 mL ice cold ACN, the tissues were homogenized using a tissue homogenizer (Precelllys 24, Bertin Technologies SAS, Montigny-le-Bretonneux, France). The homogenization was performed in 3 cycles, each consisted of 45 s of shaking at 4600 rpm followed by 30 s of pause and another 45 s of shaking. To allow samples to cool down, tubes were stored on ice for 15 min in between cycles. Samples were centrifuged at 14,000 g for 20 min under refrigeration (PrismR, Labnet international Inc., Edison, NJ, USA) and the supernatant was transferred into a new extraction tube. The residue was reconstituted in 0.75 mL ice cold ACN followed by centrifugation for 20 min at 14,000 g under refrigeration. The supernatants for each sample were pooled. Aliquots of the supernatant were diluted 3-fold with HPLC-MS grade water and further diluted 1:10 in 25 % ACN in water. Calibration standards were prepared from vehicle dosed control specimens as described above. Appropriate concentration of the drug standards prepared in ACN were added to the extraction tube before homogenizing the tissues. The calibration curves used for the drug quantification can be found in Figure A4.1.

Chromatographic separation was performed on an UPLC system (Waters Corp., Milford, MA, USA) equipped with a BEH C18 column (Waters, Milford, MA, USA) with the following dimensions: 100 mm × 2.1 mm i.d. and a particle size of 1.7 µm. The column was operated at a temperature of 55 ˚C. 0.1% formic acid in water was used as aqueous mobile phase (A) whilst ACN was used as organic phase (B). The flow rate of the mobile phase was 0.5 mL/min throughout the gradient. 5 µL of each sample were injected and separated with the following gradient: T = 0 min 5% B, 0.5 min 5% B, 0.51 min 50% B, 4.5 min 80% B, 4.51 min 99% B till T = 5 min 99% B. The approximately 2 min lasting injection cycle of the LC system was used to re-equilibrate the column to 5% B for the next injection.

A Xevo TQ-XS (Waters, Wexford, IE) triple quadrupole instrument was used for mass spectrometric detection. MRM transitions for all compounds were optimized on standards using IntelliStart and used as provided by the software (Table 6.1). The other instrument settings were used as followed: capillary voltage: 3.5 kV (+ve), nebulizing gas 1200 L/h, desolvation temperature 350 ˚C, cone gas 150 L/h.

Table 6.1: MRM transitions for the drugs and respective internal standards. The peak area of the quantifier trace was used for the quantification whilst the qualifier trace was used to verify the identity of the integrated peak.

Compound	Quantifier transition	Qualifier transition
Diphenhydramine	256.3>167.0	256.3>165.0
Diphenhydramine-*d3*	259.3>167.0	259.3>165.1
Dextromethorphan	272.4>147.0	272.4>215.1
Dextromethorphan-*d3*	275.4>215.1	275.4>147.0
Losartan	423.5>207.0	423.5>179.9
Losartan-*d4*	427.5>211.1	427.5>184.0
Terfenadine	472.1>91.0	472.7>436.3
Terfenadine-*d3*	475.7>91.0	475.7>438.4

Results

The intestine is a complex organ consisting of multiple morphological compartments such as the muscularis, submucosa, the mucosa with the mucosal crypts and villi as well as the intestinal lumen (Figure 6.1). Whilst high resolution MSI allowed the determination of spatial distribution of analytes and correlation with small morphological features such as mucosal villi, homogenization and extraction of the drugs for LC-MS/MS analysis destroys the tissue morphology and retrospective linkage of the determined concentrations to distinct compartments is impossible.

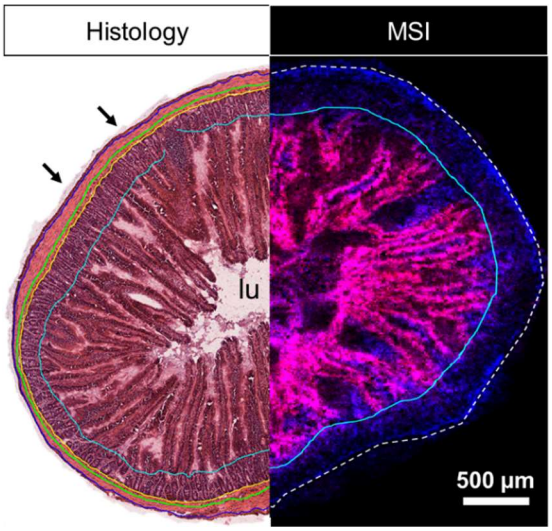

Figure 6.1, Visualization of the achievable high resolution in comparison to the underlying morphology of the intestine: Annotated H&E scan compared to combined ion image obtained from an adjacent tissue section analyzed by MALDI-MSI (endogenous lipids PC (34:2) $[M+K]^+$ (m/z 796.53) (red) and PC (34:1) $[M+K]^+$ (m/z 798.54) (blue). Histological annotation on the H&E stained tissue: arrows = serosa, outside blue line = outer muscularis, between blue and green line = inner muscularis, between green and yellow line = submucosa with mucosal crypts, between yellow and turquoise line = mucosal crypts, within turquoise line = mucosal villi and intestinal lumen (lu).

Even though the obtainable data is limited to absolute concentrations and lacks any spatial information, to date LC-MS/MS quantification of tissue extracts remains alongside quantitative whole-body autoradiography (qWBA) a standard tool in drug disposition studies[137-139]. The absolute drug concentration for all four drugs showed overall a rapid decline from the 1 h to the 2 h post dose samples and a slower decline for the later timepoints. Terfenadine shows a slower decline with no remaining drug 4 h post dose in two out of 3 animals (Figure 6.2a). For all four drugs the absolute intra and inter animal concentrations showed little variation with only single specimens showing higher concentrations. Compared to the later time-points, the inter animal variability 1 h post dose was much larger with around 5-fold higher for diphenhydramine concentrations for animal 1 compared to animal 3 (Figure 6.2d).

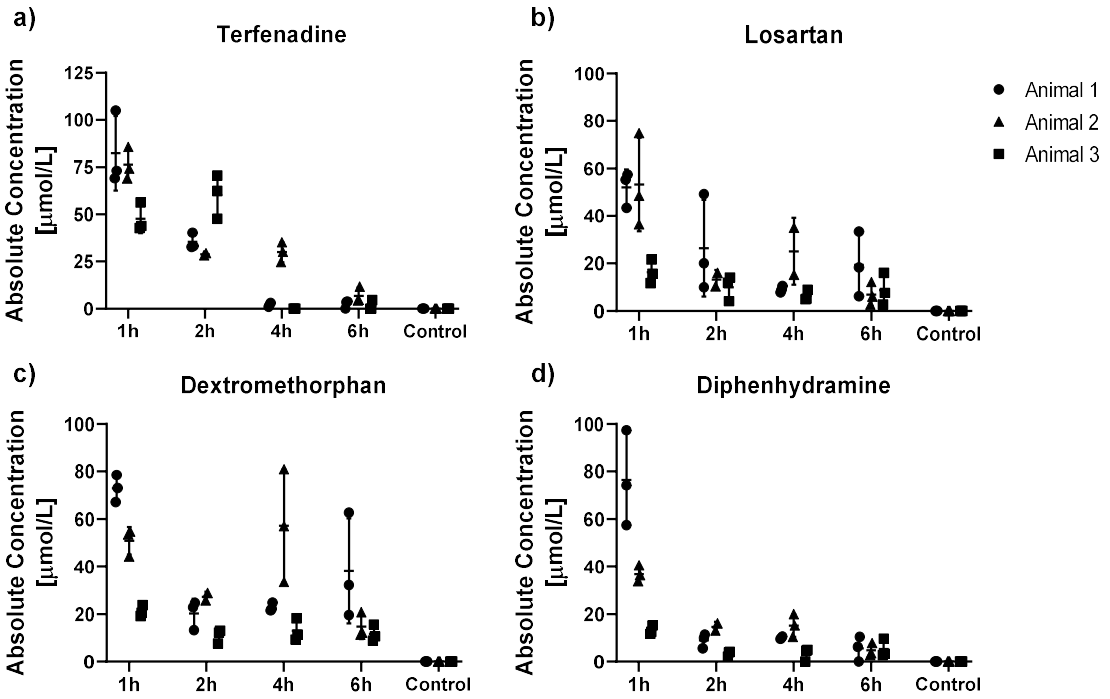

Figure 6.2, Tissue pharmacokinetics of the dosed drugs measured by LC-MS/MS: Pharmacokinetic profiles for drug tissue concentrations for a) terfenadine, b) losartan, c) dextromethorphan and d) diphenhydramine for the different time points post-dosing obtained by LC-MS/MS analysis. The data is presented as individual marker for the technical replicates and mean ± SD of the animal. As the sample collection was terminal, animals 1-3 represent individual animals for each timepoint. One specimen from Animal 2, 4 h post dose was excluded as it exceeded the upper limit of the calibration range.

In contrast to LC-MS/MS analysis, MSI allowed elucidation of the biodistribution of the dosed drugs. Both MSI techniques allowed detection of all 4 dosed drugs. Whilst terfenadine, diphenhydramine and dextromethorphan were detected as $[M+H]^+$ species (at *m/z* 472.32, 256.17 and 272.20 respectively) with either technique, losartan however, was detected as $[M+H]^+$ species at *m/z* 423.17 by MALDI-MSI and as $[M+K]^+$ species at *m/z* 461.129 by DESI-MSI. The drug abundances observed by MSI followed the trend observed for the absolute concentrations with highest concentrations in the early timepoints and a rapid decline over time. The control sections analyzed by DESI-MSI showed little interference through chemical background signals. Overall, the highest drug abundances were detected at 1 h post dose followed by a decline over time. The MALDI data followed the trend with the difference that Losartan had some chemical background for the selected mass window on none-dosed control sections. A relatively low spatial resolution of 75 µm was chosen for the performed DESI-MSI

experiments as it allowed analysis of each slide, holding 15 specimens, in an overnight experiment of approximately 12 h (Figure 6.3a).

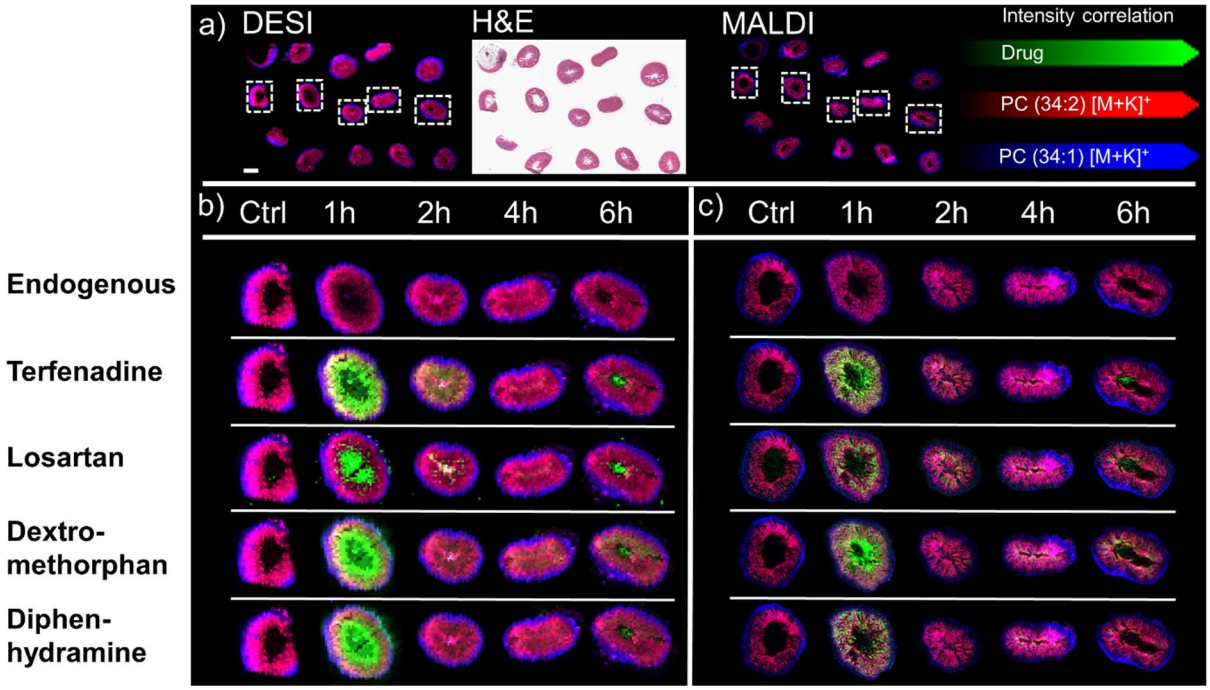

Figure 6.3, Tissue pharmacokinetics determined by MSI: Representative spatial distribution of the cassette dosed drugs determined by DESI- and MALDI-MSI: a) Panorama view on a whole slide as it was analyzed in one experiment by DESI- (left) and MALDI-MSI (right). The optical image in the middle is the post-DESI H&E stained slide. The scale bar is 2 mm. The spatial distribution of all 4 dosed drugs is shown in one representative replicate for all timepoints in relation to endogenous species outlining the tissues. The left-hand side of the figure shows the results of (b) DESI-MSI experiments performed with a spatial resolution of 75 µm whilst the right-hand side of the figure shows the results of (c) MADI-MSI experiments acquired with a spatial resolution of 10 µm.

The spatial resolution of the DESI-MSI experiments allowed localisation of the majority of the drugs in the mucosa/lumen and just small amounts in the submucosa/muscularis. However, it did not allow to greatly distinguish between mucosal villi and the intestinal lumen (Figure 6.3b). In the same time frame the slides could be analyzed by MALDI-MSI with a spatial resolution of 10 µm. The high spatial resolution of the experiments allowed differentiation between intestinal lumen and mucosal villi (Figure 6.3c).

To evaluate if the superficial agreement between the absolute concentrations and the ion images obtained by MSI were based on a quantitative nature of the MSI data, a “Gold standard” comparison was performed between the concentrations determined by LC-MS/MS and the mean tissue abundances determined by DESI- and MALDI-MSI respectively (Figure 6.4). For the linear regression, the concentration of each specimen was plotted against the

mean tissue abundance of the corresponding section analyzed by MSI. The data for all timepoints and replicates was pooled for the comparison.

Both techniques showed a comparably good correlation between the drug abundances determined by MSI and the absolute drug concentration across all samples. Both imaging techniques had a particularly good correlation for terfenadine (Figure 6.4a, e) and diphenhydramine (Figure 6.4d, h) with coefficients of determination (R^2) ranging between 0.886 and 0.945. Dextromethorphan showed a slightly lower correlation with R^2 values of 0.636 for MALDI and 0.789 for DESI-MSI respectively (Figure 6.4c, g). Only losartan showed just a moderate correlation (R^2 = 0.532 for MALDI and R^2 = 0.585 for DESI respectively) due to the low sensitivity for the drug with either imaging technique (Figure 6.4b, f). Overall, both MSI techniques showed a lower sensitivity for the drugs than LC-MS/MS analysis, manifesting in the offset on the x-axes in most graphs in Figure 6.4.

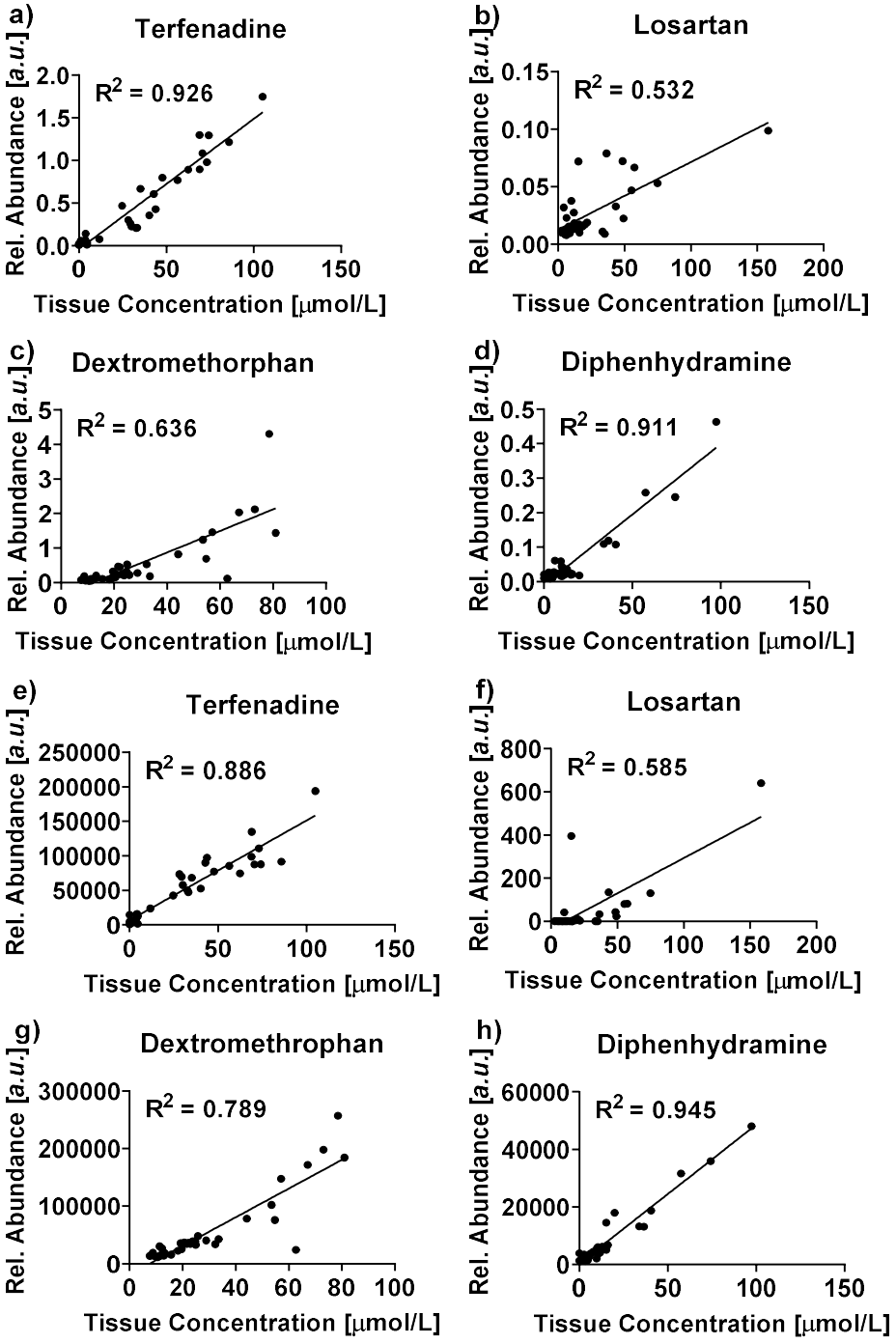

Figure 6.4, Gold standard comparison of drug tissue concentrations determined by LC-MS/MS and MSI: Correlation of drug tissue concentrations measured by LC-MS/MS and MALDI-MSI (a-d) and DESI-MSI (e-h) respectively. Relative abundances for MSI data are represented by the mean abundance of the whole tissue section.

However, the correlation proves a basis to use the MSI data for relative quantification of the drugs within and between specimens even without spray-depositing internal standard across the slide to compensate for local ion suppression effects. Spatial clustering of the MSI data (Figure 6.5) allowed extraction of the drug abundances in the resolved tissue compartments

and the intestinal lumen. This approach estimated the mean absorbed fraction of the drugs to range between 56% for terfenadine and 66% for Losartan (Figure 6.5e).

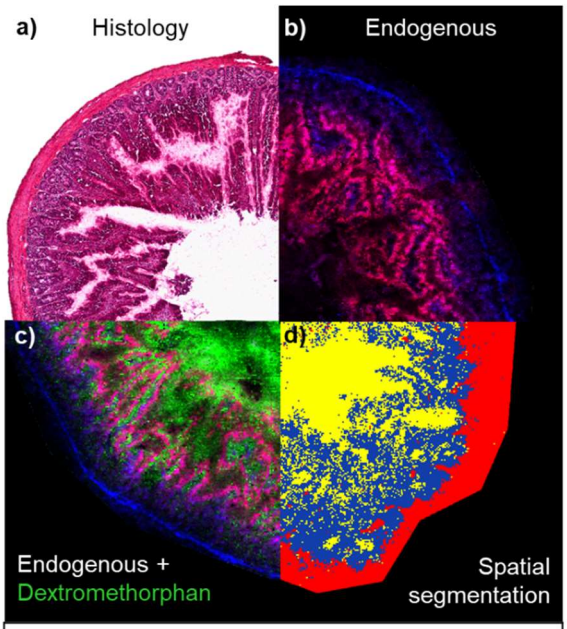

e)

Drug	Absorbed drug fraction [%] Mean ± STD	Min	Max
Terfenadine	56 ± 23	8	89
Losartan	66 ± 24	12	93
Dextromethorphan	57 ± 22	10	92
Diphenhydramine	64 ± 21	18	93

Figure 6.5, Segmentation of the MSI data into the morphological compartments: Extraction of the region-specific drug abundances in the different morphological features of the intestine: a) The H&E stained tissue shows the typical morphology of a representative intestine section. b) Shows the tissue outline determined by MALDI-MSI performed on an adjacent tissue section (endogenous lipids PC (34:2) $[M+K]^+$ (m/z 796.53) (red) and PC (34:1) $[M+K]^+$ (m/z 798.54) (blue). C) Shows the relative localization of dextromethorphan (green) within the tissue. d) Shows the result of the spatial segmentation bisecting K-means clustering of the tissue performed on features detected between m/z 750 to 850. Yellow = intestinal lumen, blue = mucosal villi and red = unresolved mix of mucosal crypts, submucosa and muscularis respectively. e) Displays the absorbed fraction of the 4 different drugs. The drug abundance of the tissue was extracted from the combined blue and red cluster seen in the spatial clustering. The data is presented as mean ± SD and range of all analyzed specimens. The individual values for each specimen can be found in Figure A4.2.

The high variability in the absorbed drug fraction was found to be largely based on differences in the amount of drug containing bowel content present in the specimens, depending on the thoroughness when removing the bowel content during necropsy. The here observed interference of the bowel content with LC-MS/MS analysis is commonly observed due to contamination of tissues with blood, measuring drugs from the circulation[140, 141] rather than pure tissue disposition. Such interferences highlight the value of spatially resolved MSI experiments to enable precise localization of the drugs within even small morphological

features of the tissue. The understanding of the drug distribution within the tissue can help to build better understanding of a compound's PK properties and draw the right conclusions from extract-based quantification approaches.

Conclusions

The here presented work successfully applied the in Chapter 3 described sample embedding and preparation protocol to co-embed and prepare multiple intestine specimens at a time. The used protocol allowed simultaneous preparation of up to 15 specimens per mold, significantly reducing the time required to section the samples. All samples analyzed in an experiment were prepared at the same time and under the same conditions, reducing the possibility of time-course effects due to analyte degradation/alteration observed when samples remain in the cryostat for extended periods of time. Preservation of the tissue morphology allowed to use the obtained tissue sections for high resolution MSI experiments and histological evaluation. The good correlation between MSI and absolute drug concentrations demonstrated minimal interference through the manipulation of the tissues during the embedding process and allowed determination of accurate, quantitative results. The correlation also proves the basis for mass spectrometry based spatial analysis of tissues and segmentation of the resulting distribution maps into the underlying morphological tissue compartments. Reasonably, the correlation holds up if the chemical composition of the different morphological compartments is not vastly different. Fundamental changes in the chemical composition are likely to result in drastic changes in local ion suppression effects, distorting the elucidated biodistributions.

Chapter 7: Spatially resolved profiling of Polymyxin B induced kidney injury

Introduction

The rise of multidrug resistant (MDR) pathogens pose a serious global health problem. Particularly Gram-negative bacteria such as P*seudomonas aeruginosa, Acinetobacter baumannii* and *Klebsiella pneumoniae* have become a serious problem as infections can result in sepsis with high mortality rates[142]. For life-threatening infections with MDR pathogens, *i.e.* carbapenem- and third generation cephalosporin-resistant *Enterobacteriaceae,* treatment with cationic polypeptide antibiotics of the polymyxin class are often used as a last-line therapy for combating Gram-negative sepsis caused by *P aeruginosa, A. baumannii, K. pneumoniae* and *Escherichia coli*[143, 144]. However, the efficacy of polymyxin B (PMB) and colistin (Polymyxin E) as the clinically used representatives of the class is linked to severe neuro- and nephrotoxicity. The clinical nephrotoxicity manifesting as acute kidney injury (AKI) often limits the treatment regime as therapy may be withdrawn when elevated kidney injury markers are observed, even when patients exhibited a clinical response to therapy.

The increasing understanding of novel urinary biomarkers for AKI offers better understanding for drug induced nephrotoxicity during treatment with polymyxin antibiotics compared to serum creatinine (Cr) as a traditional marker for renal function which has limited sensitivity for the direct evaluation of acute disease[145]. These novel biomarkers for AKI focus largely on functionality and damage of the proximal tubular epithelial cells (PTECs) and include Kidney Injury Molecule-1 (KIM-1), albumin, α-glutathione-S-transferase (α-GST), clusterin**,** osteopontin, renal papillary antigen-1 (RPA-1) and neutrophil gelatinase-associated lipocalin (NGAL) and less on marker for damage of the distal tubules such as glutathione S-transferase-yb1 (GSTYb1)[146, 147]. Particularly the phosphatidylserine receptor KIM-1 which confers a phagocytotic phenotype on PTECs[148] clearing cellular debris created by apoptotic and necrotic cell from the tubular lumen showed good predictive properties for AKI in preclinical models[146]. For the good predictive nature of these biomarkers, their translational value in the clinic was previously investigated[149]. However, even for a last-line therapy, reducing the risk associated

with the treatment through monitoring of biomarkers is only a temporary option which does not eliminate the need for novel treatment options with better therapeutic index. In attempts to develop safer derivatives to the currently used polymyxins, great efforts were made to understand the structure-activity based relationship between clinical efficacy and toxicity. Many derivatives with modifications of the cyclic peptide and reduced numbers of cationic charges as well as modification on the lipophilic N-terminal acyl-chain were synthesized and evaluated[150-154]. Though many of these derivatives were found to have decreased *in vitro* toxicity, they were often deprived of their antimicrobial properties, following the polymyxin B nonapeptide (PMBN) as precursor of many of these derivatives[155]. Even though these derivatives often lack antimicrobial activity they can increase potency when co-administered with other antibiotics[156, 157].

Due to the limited success developing novel polymyxins with a better therapeutic index than the ones currently used in the clinic, the focus shifted back to increase the understanding of the molecular mechanisms underlying the nephrotoxicity. The main focus of many of these studies was to understand the renal drug disposition through direct and indirect imaging approaches[75, 158, 159] and monitoring the toxicodynamic effects induced by polymyxin accumulation in PTECs[160]. The here presented work utilized a combination of clinical biomarker evaluation and a multimodal tissue analysis approach comprised of classical histopathological evaluation, mass spectrometry imaging (MSI) and transmission electron microscopy (TEM). This approach was aimed to understand the impact of renal drug disposition on the phenotypical and metabolic appearance of the tissues and to understand the influence of pathological findings onto urinary biomarkers. The integrated results build a better understanding of the toxicodynamic mechanisms that limit the clinical potential of such a fundamentally important class of antibiotics and will hopefully aid the development of novel polypeptide antibiotics.

Aim/objective

This chapter aims to demonstrate the benefits of using some of the working practices evaluated in this thesis to subject samples to multimodal tissue analysis. The samples used in this chapter were part of a toxicity study investigating Polymyxin B induced acute kidney injury in rats. The kidney specimens were snap frozen upon collection and either embedded and processed as described in chapter 3 and subjected to DESI- and MALDI-MSI analysis and histopathological evaluation. Independent pieces of the specimens were additionally prepared for histopathological evaluation of FFPE tissues and analysis by TEM.

Material and Methods

Chemicals

2,5-dihydroxybenzoic acid (DHB), Polyvinylpyrrolidone (PVP) (MW 360 kDa) and (Hydroxypropyl)-methylcellulose (HPMC) (viscosity 40-60 cP, 2 % in H2O (20 C) were purchased from Merck (Darmstadt, Germany). Methanol, 2-methylbutane and 2-porpanol were obtained from Fisher Scientific (Waltham, MA, USA). Polymyxin B1 sulfate and PMBN were supplied by AstraZeneca compound management group (Macclesfield, Cheshire, UK). All solvents used were of analytical grade or higher.

Animals and dosing

Adult male Han Wistar rats (approximately 10 weeks old, weight 300 to 325 g) were obtained from Charles River Laboratories (Raleigh, NC, USA) and were acclimatized on site for a minimum of 3 days prior to dosing. Compounds were administered through subcutaneous injection in the intrascapular region at 8 mg/kg/day (PMB Low dose), 25 mg/kg/day (PMB High Dose) or 22 mg/kg/day (PMBN). Total daily dosings were equally distributed over 4 injections per day (QID), approximately every 6 h, for 3 days. For animal sacrificed on treatment day 3, final doses were administered 1 to 3 h prior to necropsy. Recovery group animals for the PMB high dose and PMBN groups were dosed for 3 days and sacrificed, after a recovery period of 21 days, on treatment day 24. Control animals were dosed with saline vehicle via the same administration route and sacrificed at the appropriate time points on treatment day 3 or 24

respectively. All dosing was performed on 4 animals/group and timepoint. All tissue dissection was performed by trained AstraZeneca staff (project license 40/3484, procedure number 10). Tissues were snap-frozen in 2-methylbutane on dry ice, all subsequent transfer of tissues was done on dry ice, and samples were stored at −80 °C until tissue processing.

Processing of frozen tissues for MSI and histological evaluation

To achieve highest morphological preservation of the frozen tissue specimens whilst maintaining the ability to freely analyze the tissues with a broad range of analytical techniques, the samples were embedded and processed as described in Chapter 3. Cryo-sectioning of the frozen blocks was performed on a CM3050 S cryostat (Leica Biosystems, Nussloch, Germany) at a section thickness of 10 µm. The chamber temperature was set to -20˚C whilst the sample was held at -16˚C. Samples were prepared on non-conductive SuperFrost microscope slides (Thermo Scientific, Waltham, Massachusetts, USA) for DESI experiments and optical stains whilst samples for MALDI experiments were mounted onto conductive ITO slides (Bruker Daltonik, Bremen, Germany). All samples were immediately died under a stream of nitrogen and stored in vacuum sealed slide mailer at -80°C to avoid analyte delocalization and degradation[18].

MALDI-MSI

MALDI analysis was performed on a RapifleX Tissuetyper instrument (Bruker Daltonik, Bremen, Germany). DHB was used as the MALDI matrix and spray deposited as described in Chapter 2. MALDI experiments were performed with a spatial resolution of 10 or 50 µm respectively. All MALDI experiments were performed in the mass range between *m/z* 200 and 1500 in positive ion mode. To give the final spectra a total of 100 laser shots were summed up per pixel for experiments performed at 10 µm spatial resolution whilst 400 shots were summed up per pixel for experiments performed at 50 µm spatial resolution respectively. For all experiments the laser was operated with a repetition rate of 10 kHz. All raw data was directly uploaded and processed in FlexImaging (Bruker Daltonik, Bremen, Germany) or SCiLS lab

(Version 2019c) software packages. All MALDI data and images were TIC normalized to compensate for spectra-to-spectra variation of the data[76].

DESI-MSI

DESI-full scan experiments were performed on a Q-Exactive (Thermo Scientific, Bremen, Germany) mass spectrometer equipped with a home-built sprayer[26] operated with 95/5 (v/v%) methanol/water as spray solvent. The solvent was delivered with a flow rate of 1.5 µL/min and nebulized with a gas pressure of 7 bar. The mass spectrometer was operated in full scan mode between m/z 100 to 1000. The resulting .raw files were converted into .mzML files using ProteoWizard msConvert[72] (version 3.0.4043) and subsequently compiled to an .imzML file (imzML converter[73] version 1.3). The data was processed in MSiReader (v0.09)[161] where regions of interest (ROIs) were annotated for the renal cortex, the outer and inner stripe of the outer medulla and the inner medulla and mass spectral data was extracted with 0.1 Da binning. Univariate statistical analysis (two-tallied t-test, $p < 0.05$) were performed in GraphPad Prism (V. 8.0.1) (GraphPad Software, San Diego, CA, USA) to find the significant changes between control and treatment groups. Features with significantly different abundances were identified by DESI-MS/MS analysis performed on the Q-Exactive mass spectrometer with a nominal mass resolution of 70,000. To elucidate the biodistributions of identified metabolites, targeted DESI-MSI experiments were performed on the DESI-TQ setup described in chapter 5 where all details regarding the experimental setup, optimization of the experimental parameters and data handling can be found. Detailed information on the multiple-reaction-monitoring (MRM) transitions used can be found in Table A6.1. Experiments were performed with a dwell time of 4 ms/transition resulting in a total acquisition rate of 3 pixels/s. Targeted imaging experiments were performed with a spatial resolution of 75 µm.

Transmission Electron Microscopy (TEM)

The evaluation of the ultrastructure was performed by Dr Linda Moran at the EM Unit at the Charing Cross Hospital (NHS – Northwest London Pathology).

Snap frozen tissue specimens were directly thawed in cold 3% glutaraldehyde prepared in 0.1M sodium cacodylate buffer (EM fixative; pH 7.4) for 3 h in the fridge. Once fully thawed, the samples were trimmed to a maximum diameter of 1 mm and transferred into fresh EM fixative. Samples were then fixed for 24 hours at 4°C before further processing. Fixed tissue samples were processed and embedded in Spurr resin. In brief, the tissue samples were rinsed twice in 0.1M sodium cacodylate buffer (pH 7.4) before post-fixation in 1% aqueous osmium tetroxide, rinsing in distilled water and en bloc staining in 2% aqueous uranyl acetate. Samples were subsequently dehydrated through graded alcohols to absolute alcohol before immersion in propylene oxide. The samples were let to be infiltrated in 1:1 mixture of propylene oxide and Spurr resin and subsequently transferred into fresh Spurr resin. Samples were transferred into polypropylene embedding capsules containing fresh Spurr resin and polymerized at 100°C for 90 minutes.

Semi-thin sections of 1µm were cut and stained with toluidine blue-pyronin Y to select regions of interest. Ultrathin sections of approximately 120nm thickness were cut, mounted on Gilder 200 copper grids and contrasted in Reynolds lead citrate before imaging on a Hitachi H-7650 Transmission Electron Microscope.

Histopathology and clinical chemistry

The evaluation and interpretation of histopathological findings, urine and clinical chemistry as well as urinary biomarker was, if not specified otherwise, performed by Dr Kimberley Maratea (AstraZeneca) as the responsible study pathologist.

Urine collection

Animals were housed in metabolic cages for 6 h of a 24 h cycle. Though longer urine collection times can yield more accurate values, based on previous clinical observations with polymyxin analogues, a 6 h collection period was used in order to balance animal welfare concerns with data integrity considerations.

Clinical pathology, urine chemistry and urinary kidney injury biomarker.

Routine hematology, urine chemistry and urinary kidney injury biomarker were performed as previously reported[146]. All analytical methods were fully validated for rat samples. The reported mean changes were considered noteworthy because of the magnitude of change relative to vehicle controls. All other results were considered to fall within normal biological variation and any apparent differences were considered isolated or minor. Approximate % or fold changes were calculated against mean of the vehicle control group values.

Results and discussion

Pathological examination of fixed samples as per the case pathologists report:

Kidneys from all rats were examined histologically. The tissues were fixed in 10% neutrally-buffered formalin for approximately 48 h and subsequently processed, paraffin embedded and sectioned at 4 µm thickness. Sections were mounted onto glass slides, deparaffinized and stained with hematoxylin and eosin (H&E). Sections of kidney from rats treated with PMB or PMBN were evaluated by light microscopy on Day 3 and Day 24. Microscopic changes were graded semi-quantitatively as follows: 1 = minimal; 2 = mild; 3 = moderate; 4 = marked; 5 = severe. The histopathological grading scheme for degeneration was defined as follows: minimal: occasional degenerate (brightly eosinophilic) cells with pyknotic nuclei; mild: occasional degenerate cells with pyknotic to karyorrhectic nuclei and sloughed cells within tubular lumina (protein casts); moderate: small clusters of 2–4 degenerate cells with pyknotic nuclei and protein casts; marked: larger clusters and chains of degenerate cells, some with complete loss of chromatin, affecting numerous tubules; severe: majority of tubules affected by chains of degenerate cells, or entire tubular segments affected by degeneration.

Histological evaluation

Fixed kidney sections from all rats were examined histologically. Minimal tubular degeneration and necrosis was present in animals treated with PMB at 8 mg/kg/day on Day 3. Degenerative changes, particular single cell necrosis, were more pronounced in rats treated with PMB at 25 mg/kg/day. On Day 24, rats showed minimal to mild tubular degeneration consisting primarily

of vacuolated tubular epithelial cells. One of the vehicle control rats also had minimal tubular degeneration and interstitial fibrosis. In all affected rats, tubular changes were most prominent in the superficial cortex, and characterized by one or more of the following changes: vacuolated tubular epithelial cells, single cell necrosis, increased cell mitoses, and mononuclear cell infiltrates. Minimal tubular degeneration was present in PMBN treated rats on Day 3. Changes were resolved by the Day 24. A summary of the histopathological findings can be found in Table 7.1.

Table 7.1: Summary of histopathology findings showing incidence and median severity of salient changes.

	Incidence (Median score)			
Compound	Vehicle (saline)	PMB (Low Dose)	PMB (High Dose)	PMBN
Dose (mg/kg/day)	0	8	25	22
Day 3				
Cyst, cortex	1/4(2)	1/4(1)	0/4	0/4
Degeneration, tubular	0/4	1/4(1)	4/4(2.5)	2/4(1)
Fibrosis, interstitial	0/4	0/4	1/4(1)	0/4
Infiltrate, mononuclear cells	0/4	1/4(1)	1/4(2)	0/4
Mineralization, tubular	1/4(1)	0/4	1/4(1)	0/4
Day 24				
Degeneration, tubular	1/4(1)	-	2/4(1.5)	0/4
Fibrosis, interstitial	1/4(1)	-	0/4	0/4
Infiltrate, mononuclear cell	0/4	-	0/4	0/4
Incidence = number affected/number examined				

Clinical chemistry

Dose-related decreases in total protein (TP) (-12 to -24%), albumin (ALB) (-25 to -42%), and Albumin to Globulin (A/G) ratio (-30 to -44%) were observed upon PMB dosing on Day 3. The group dosed with 25 mg/kg/day also had increases in aspartate transaminase (AST) (3-fold), alanine transaminase (ALT) (+63%), urea (2.3-fold), and creatine (53%). All changes were resolved by Day 24. No meaningful changes were present on Day 3 or Day 24 in animals dosed with PMBN. Salient findings of the clinical chemistry are summarized in Figure 7.1.

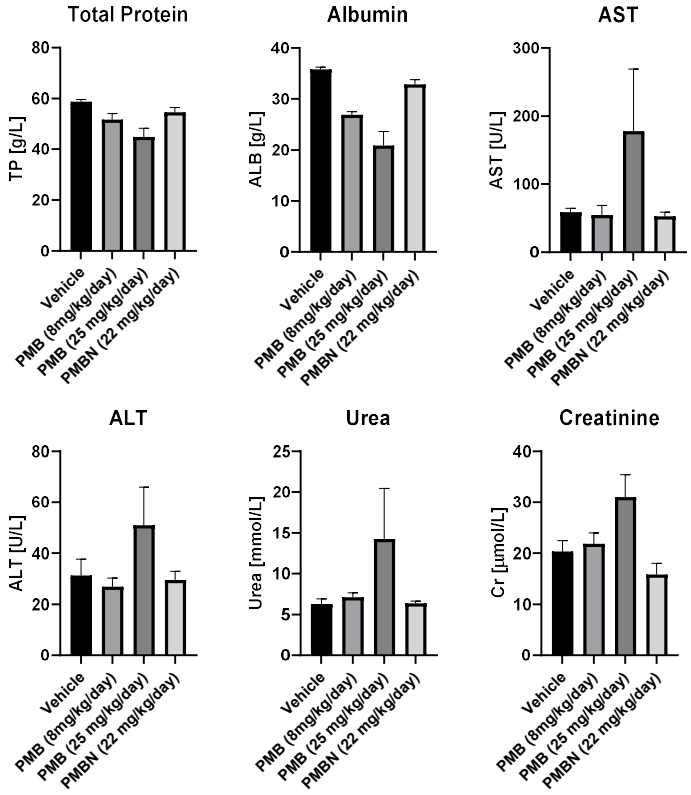

Figure 7.1: Summary of salient clinical chemistry parameters in rats on day 3. Data are expressed as Mean ± SD.

Urine Chemistry

On Day 1, animals of both PMB dosing groups had decreased urine volume (-63 to -73%) and increased urine creatinine (+21 to +40%), total protein/creatinine ratio (+69 to +120%), and glucose/creatinine ratio (~255-fold). Urine volume was variably increased on day 2, by approximately 3.5-fold in animals dosed with 8 mg/kg/day, and +21% in animals dosed with 25 mg/kg/day. Total protein/creatinine ratio was decreased (-34%) in the group dosed with 8 mg/kg/day and increased (2.5-fold) in the group dosed with 25 mg/kg/day. Glucose/creatinine ratios were increased up to 6.5-fold. On Day 23, urine volume remained somewhat elevated (+56%) in the group dosed with 25 mg/kg/day. Urine volume of PMBN dosed animals was increased on Days 1-2 (+36 to +38%), and mildly increased (+25%) on Day 23. Other changes included increased urine creatinine (+30 to +39%), and total protein/creatinine ratio

(+90 to +109%) on Days 1-2. These changes were reversed by Day 23. Salient findings of the urine chemistry are summarized in Figure 7.2

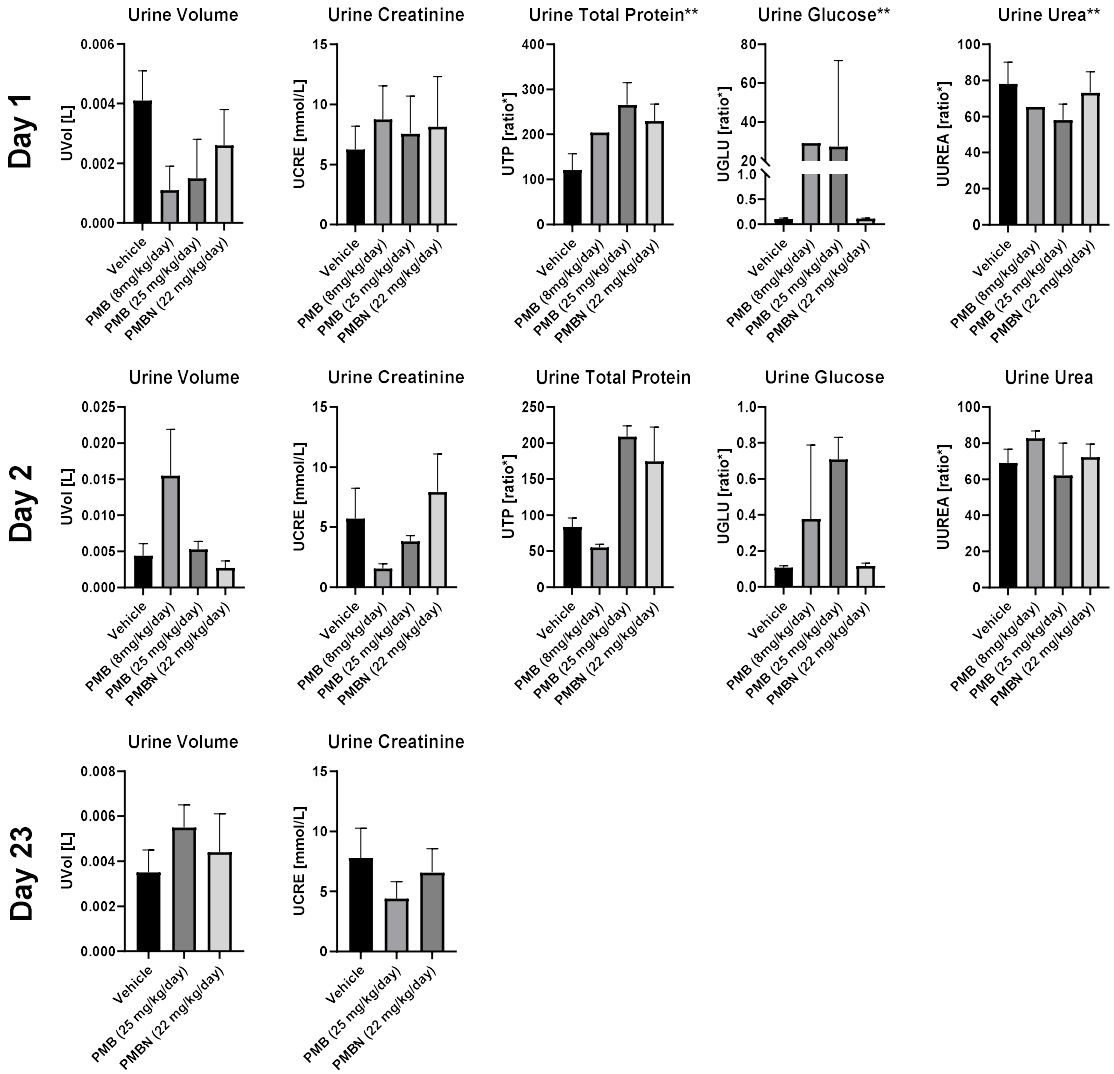

Figure 7.2: Summary of salient urine chemistry parameters in rats on Days 1, 2 and 23. Data are expressed as Mean ± SD. *Normalized to urine creatinine (UCRE); ** Repeated analysis was required due to instrument related issues. Only sufficient urine left from one animal to allow for repetition of the experimental procedures.

Acute Kidney Injury (AKI) Urine Biomarkers

The most notable elevations on day 1 in the PMB dosed animals relative to vehicle controls were noted in proximal tubule injury markers α -glutathione s-transferase (α-GST) (6-fold) and albumin (8-fold) in the 8 mg/kg/day dose group, and clusterin (15-fold) and albumin (4-fold) in the 25 mg/kg/day group. Lesser elevations (up to 3-fold) were also present in glutathione S-transferase-yb1 (GSTYb1) and clusterin in the 8 mg/kg/day group, α-GST, osteopontin, and kidney injury molecule-1 (Kim-1) in the 25 mg/kg/day group, and d renal papillary antigen-1 (RPA-1) and neutrophil gelatinase-associated lipocalin (NGAL) in both groups. On Day 2, the most significant elevations in both dose groups was the proximal tubule injury marker NGAL (380 to 1030-fold), with lesser elevations in α-GST (6 to 12-fold), RPA-1 (5-fold), clusterin (9 to 34-fold), albumin (<2 to 13-fold), osteopontin (5 to 14-fold), and Kim-1 (5 to 19-fold). On Day 23, slight increases (up to 2-fold) were present in RPA-1, clusterin, NGAL, and osteopontin. The most notable change upon dosing with PMBN was increased osteopontin on Day 1 (3-fold) and Day 2 (4.5-fold) in the 200 mg/kg/day group. Additional mild elevations (up to 3-fold) in α-GST, GSTYb1, RPA-1, albumin, and NGAL were present in one or both dose groups on Days 1 and 2. On Day 23, mild elevations (up to 2-fold) in GSTYb1 and osteopontin were present. Salient changes in urinary biomarkers are summarized in Figure 7.3.

Day 1

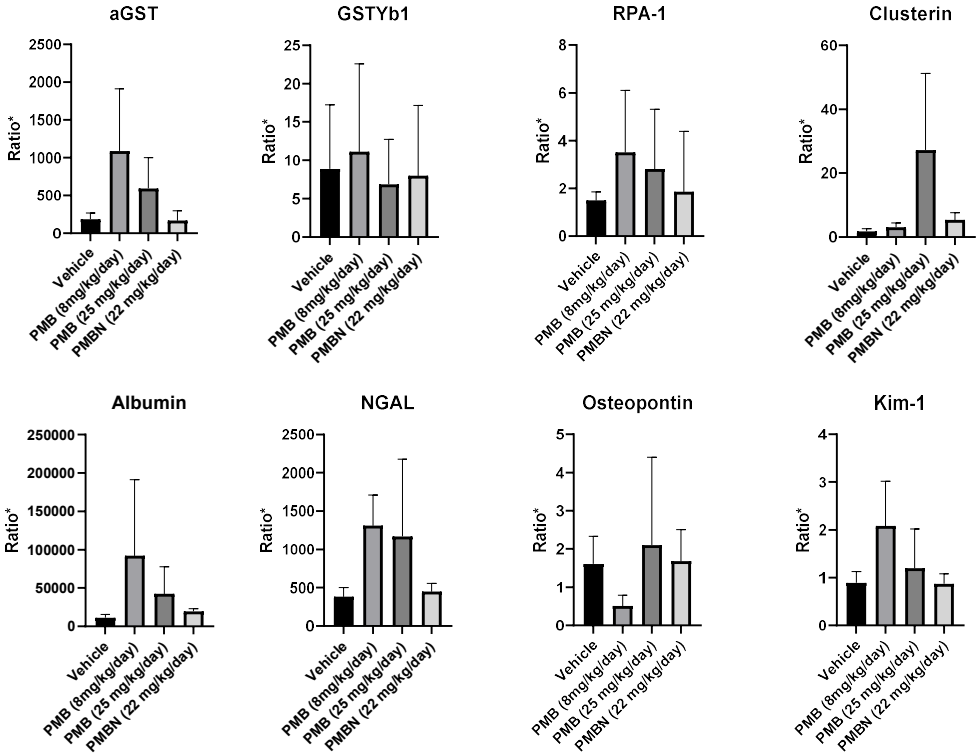
aGST
GSTYb1
RPA-1
Clusterin
Albumin
NGAL
Osteopontin
Kim-1
Ratio*
Vehicle
PMB (8mg/kg/day)
PMB (25 mg/kg/day)
PMBN (22 mg/kg/day)

Day 2

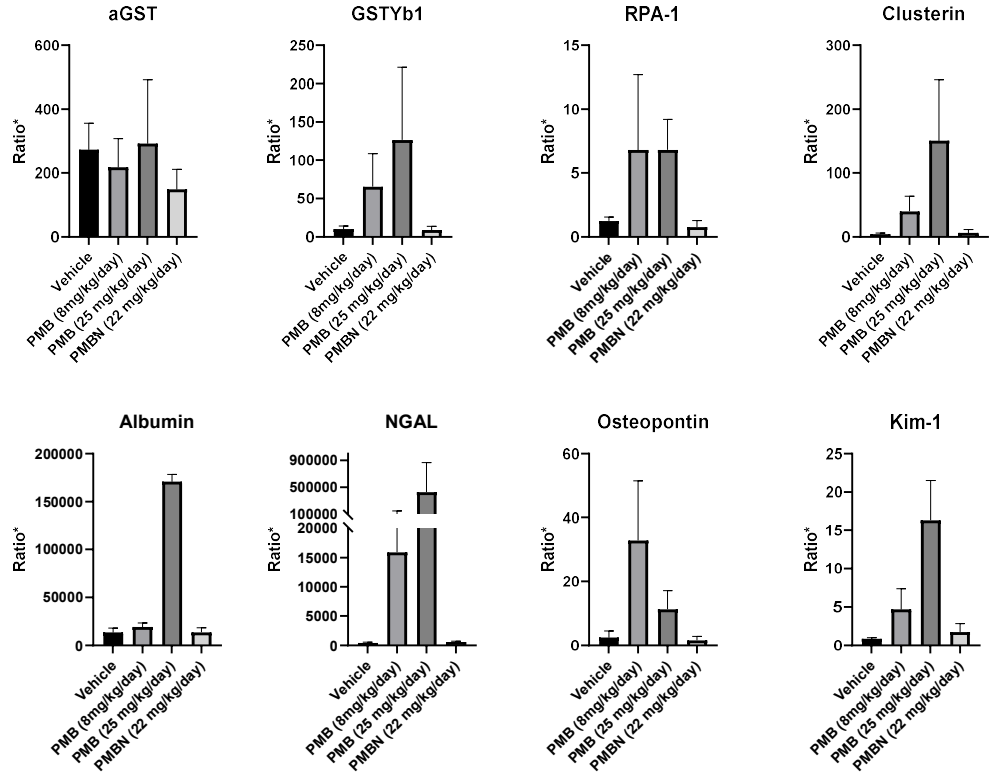
aGST
GSTYb1
RPA-1
Clusterin
Albumin
NGAL
Osteopontin
Kim-1
Ratio*
Vehicle
PMB (8mg/kg/day)
PMB (25 mg/kg/day)
PMBN (22 mg/kg/day)

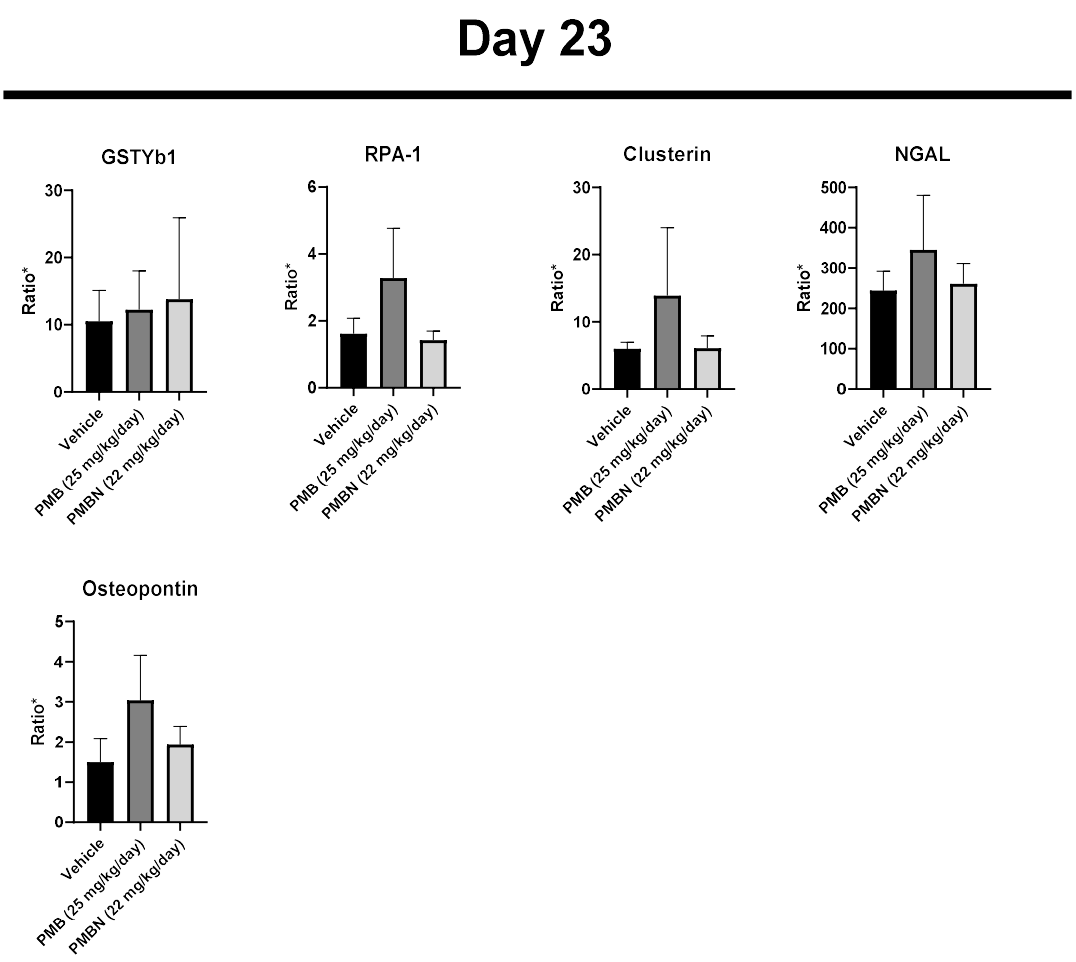

Figure 7.3: Summary of salient kidney injury biomarkers normalized to urinary creatinine on Days 1, 2 and 23. Data are expressed as Mean ± SD.

Conclusions of clinical and histopathological evaluation

In brief, clinical pathology abnormalities and microscopic lesions attributable to the dosing were present in animals treated with PMB. Collectively, these changes were consistent with acute kidney injury and were most pronounced in the group treated with 25 mg/kg/day. Consistent with histopathologic findings, the greatest changes in kidney biomarkers were noted in markers of proximal tubular injury, including NGAL, Kim-1, and albumin, and to a lesser extent the distal tubule marker GSTYb1. Transient glucosuria on Day 1 was also suggestive of proximal tubule damage. The most adverse change, single cell necrosis, was reversed following recovery on Day 24. Data to support PMBN-related changes in treated rats

were equivocal. Increases in kidney biomarkers were generally less than 2-fold, and histopathologic changes detected by light microscopy were absent or minimal.

Drug distribution – MALDI

Based on the histological findings and urinary biomarker the location of PMB induced kidney injury was assumed to be primarily located in the proximal tubules. To further validate the precise location, MALDI-MSI was employed to directly elucidate the biodistribution of PMB and PMBN within the kidney sections. The kidney has a complex morphology and can be superficially divided into cortex, the outer medulla which can be sub-divided into the inner and outer stripe and the inner medulla. The cortex largely comprises convoluted proximal and distal tubules interspersed with glomeruli, the outer stripe of the outer medulla largely comprises straight proximal and distal tubules, the inner stripe of the outer medulla is composed of collection ducts and the descending and ascending arms of the loop of Henle and the inner medulla which is composed of large collection ducts, interstitial tissue and vascular capillaries. Bisecting k-means clustering was applied to segment the MSI data to into the underlying morphological compartments.

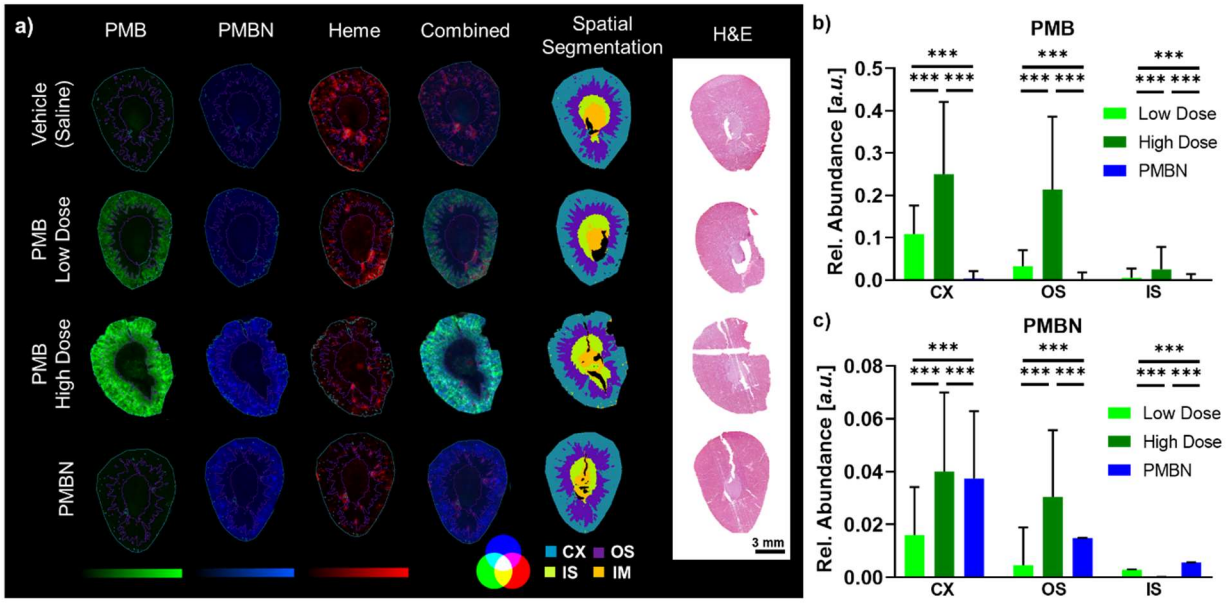

Figure 7.4, Distribution of PMB and PMBN in representative tissue sections in relation to the underlying tissue morphology: a) Global distribution of PMB, PMBN and heme in relation to each other and the spatial segmentation map (top to bottom) in whole kidney sections acquired at 50 µm resolution. b) Relative abundances of PMB and PMBN after background subtraction in the renal cortex (CX), the outer stripe (OS) and inner stripe (IS) of the outer medulla and the inner medulla (IM). Data are presented as mean ± SD. Statistical significance was determined by Kruskal-Wallis followed by Dunn's test considering all pixel for each region obtained from the spatial clustering, *P<0.05, **P<0.01, ***P<0.001

Even when the MSI experiments were performed with a spatial resolution of 50 µm, the segmentation maps allowed to distinguish between the different morphological zones and allowed the extraction of PMB and PMBN disposition within the organ (Figure 7.4a). PMB showed dose dependent differences in the drug disposition between the low and high dosed groups. Whist the low dosed group showed preferential drug disposition in the superficial cortex, the high dose group showed additionally drug disposition in the adjacent outer stripe of the outer medulla. Sections from both, vehicle controls and PMBN dosed animals show little background signals for the drug. In animals dosed with PMBN, it showed preferential accumulation in the renal cortex. PMBN has previously been identified as one of the main metabolites of PMB detectable in the kidney[75]. In animals dosed with PMB, the biodistribution of PMBN was found to correlate with the distribution of PMB. PMBN showed preferential disposition in the superficial cortex in the low dose group and significantly higher disposition in the cortex and outer stripe of the outer medulla in the high dose group (Figure 7.4). Overall both, PMB and PMBN showed in all dosing groups preferential disposition in tissue and low abundances were detected in correlation with heme as marker for blood suggesting accumulation and retention of the compounds in the renal tissue. These findings were supported by high resolution imaging experiments performed at 10 µm spatial resolution. Leveraging the increased detail of the images, it was possible to distinguish between renal tissues and small morphological features such as blood vessels or collection ducts which are clearly visible on the spatial segmentation maps. Only low abundance of PMB and PMBN were detected in blood vessels and collection ducts (Figure 7.5). Neither PMB or PMBN could be detected in specimens from animals of any of the recovery groups (data not shown).

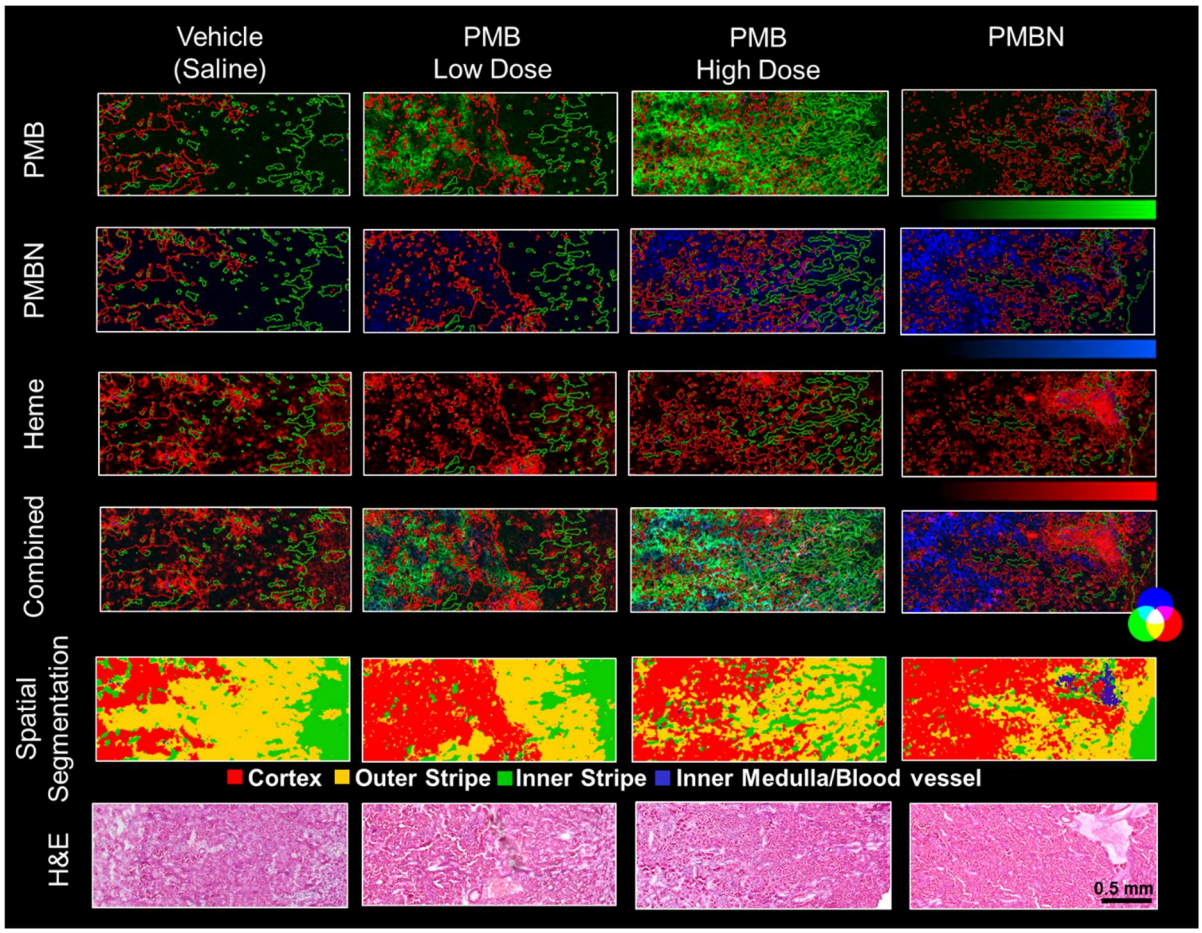

Figure 7.5, Disposition of PMB and PMBN in the kidney: Distribution of PMB, PMBN and heme in selected areas of sections from the same animals as in acquired at a spatial resolution of 10 µm.

Metabolic changes – DESI

Spatially resolved analysis of the tissue sections by DESI-MSI allowed to extract region-specific metabolic information. Consistent with the accumulation of PMB and PMBN, metabolic changes were overall most pronounced in the renal cortex and to a lesser extend in the outer stripe of the outer medulla. The inner stripe of the outer medulla and the inner medulla showed overall only minor changes and were excluded for the subsequent analysis to allow focusing on metabolic changes in the areas with drug accumulation. The most striking changes were found in the high dosed group. These alterations of the tissue metabolome included increased abundances of free poly-unsaturated fatty acids (PUFA) and changes in abundances of lipid species (Figure 7.6). The increase in free fatty acids such as FA(20:4) (Figure 7.6a) which is endogenously likely arachidonic acid (AA), and FA(22:6) (Figure 7.6b), which is endogenously likely docosahexaenoic acid (DHA) was most pronounced in the high PMB high dose group. The changes in the lipidome were more complex and showed dependency on class and acyl-

chain composition of the lipids. Phosphatidylcholine species (PCs) carrying predominantly unsaturated or monosaturated C16 and C18 fatty acids, resulting in an overall carbon-count of C32-C36, were significantly increased in the high dose group (Figure 7.6e-g). In turn, PCs with longer chains that are potentially carrying arachidonic acid showed a mild reduction (Figure 7.6h). Bridging lipid classes, this reduction was consistent with the reduced abundance of phosphatidylethanolamine (PE) PE(18:0_20:4) (Figure 7.6i) whilst phosphatidylserine (PS) and phosphatidylinositol (PI) species with comparable fatty acid substitution showed increased abundances (Figure 7.6k and p). In agreement with the histopathological evaluation, these changes describe an inflammation driven metabolomic phenotype characterized by tissue infiltration with mononuclear cells such as macrophages and leucocytes. Macrophages have reportedly a lipidome dominated by lipids composed of C16 and C18 fatty acids[162]. Upon activation cytosolic phospholipase A (PLA) is translocated onto the outer envelope of the asymmetrically distributed nuclear membrane, which are enriched with PCs and PEs but no PIs or PSs, mediating hydrolysis of the membrane lipids and release of free fatty acids. Released arachidonic acid is the precursor for biologically highly active pro-inflammatory lipid mediators, eicosanoids, of the prostaglandin-2-, tromboxan-2- and leukotriene-4-series. These eicosanoids are generated through oxidation of arachidonic acid by 5-Lipoxigenase (5-LO) for leukotrienes and cyclooxygenases (COX) for prostaglandins respectively. However, as these are highly active molecules, their generation and effect mediation are highly regulated to limit the likelihood of excessive immune reactions either through modulation of the primary stimuli or modulation of downstream effects such as the conversion of arachidonic acid into eicosanoids. DHA was found to suppress primary macrophage inflammation[163] and to attenuate immune responses from activation of Toll-like receptors (TLR)[164] through metabolism into anti-inflammatory eicosanoids of the prostaglandin-3-, thromboxane-3- and leukotriene-5-series[165]. Modulation of inflammatory responses was also reported for ionic cholesterol esters such as cholesterol phosphate and cholesterol sulfate which were found to limit the activity of 5-LO in polymorphonuclear leukocytes[166] and thus limit the production of chemotactic leukotrienes which would further promote inflammation. Together the observed

increased abundances of DHA and cholesterol sulfate (Figure 7.6d) and FA(20:6) (Figure 7.6b) could be part of the regulatory mechanisms leading to the accumulation of free FA(20:4). Accumulation of arachidonic acid was reported to lead to increased formation of arachidonoyl-CoA and subsequently to formation of PC and PE species containing adrenic acid (FA(22:4)) in lysophosphatidylcholine acyltransferase 3 (LPCAT3) deficient mice[167]. The lipids are likely synthesized after elongation of arachidonic acid to adrenic acid and incorporation into lipids such as PE(16:0_22:4) (Figure 7.6j). Increased formation of PCs with such a fatty acid composition is likely in the given in the samples, however differentiation of the acyl-chain substitution was not possible under the analytical conditions in positive ion mode due to a lack of product ions created through a loss of the acyl chains. As promising as these insights are to utilize MSI in future studies to investigate the spatial interaction networks of inflammation in tissues, they here only further confirmed the inflammatory phenotype characterized by apoptosis/necrosis and mononuclear cell infiltration already established through the histological examination. The depletion of anti-oxidants such as ascorbic acid (Figure 7.6c) further validate this phenotype as it is characterized by increased formation of reactive oxygen species (ROS).

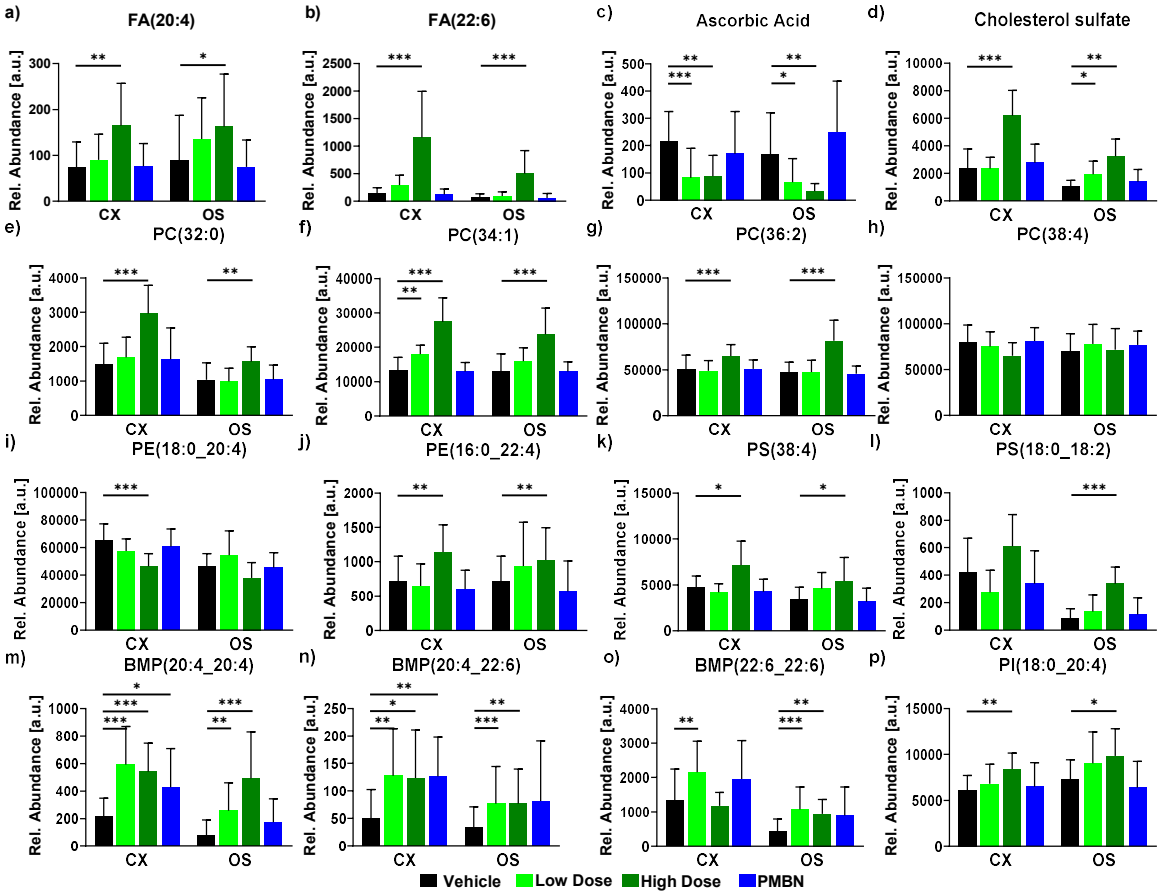

Figure 7.6, Toxicodynamic effects of PMB and PMBN in the kidney: CX = cortex, OS = outer stripe of the outer medulla. Data are expresses as mean ± SD, Statistical significance as determined by Kruskal-Wallis followed by Dunn's test testing all treatment groups against vehicle controls, n = 3-4 animals/group (5 ROI/animal), *P<0.05, **P<0.01, ***P<0.001

Mechanistically more insightful in the mechanisms underlying the PMB induced nephrotoxicity was the increase of bis-(monoacylglycerol)phosphates (BMPs) which are also known as lysobisphosphatic acid (LBPA). BMPs were previously associated with phospholipidosis (PLD) induced by cationic amphiphilic drugs (CADs) such as amiodarone or aminoglycoside antibiotics[168]. Though not previously associated, with a multi-basic headgroup and lipophilic terminus, PMB shares the characteristics of typical CADs. Interestingly all BMP species showed overall similar or higher abundances in the low dosed group except for BMP(20:4_20:4) which showed higher abundances in the outer stripe of the outer medulla in the high dosed group (Figure 7.6m-o). BMP(22:6_22:6) was described to be the major BMP species involved with the PLD defining formation of multi-lamellar bodies (myeloid bodies) in tissues[168], however it only showed a significant increase in the renal cortex of the low dosed group (Figure 7.6o). The differences in the abundances of BMP species could be linked to the

previously observed modulation of the lysosomal lipid profile and represent the gradual transition from phagosomes to phagolysosomes and subsequently late endosomes. Though the molecular mechanisms of these transitions are not well understood, evidence suggests that the accumulation of BMPs in lysosomal fractions arise from an inherent degradation resistance towards PLA_2, based on a *sn*-1/*sn*-1 configuration of the acyl chain substitution on the glycerol moieties with a lack of *sn*-2 substitution. With this inherent resistance towards degradation, BMPs are assumed to be required for the containment of the catabolic conditions in lysosomes and promote digestion of the acidified lysosomal contents through invagination of the lipid membranes.BMP containing lipid vesicles were found to spontaneously form multi-lamellar bodies when a physiological pH gradient is established between the inside and the surrounding medium[169].

Ultrastructural changes – TEM

The most reliable tool for the validation of drug induced PLD is through confirmation of the presence of multi-lamellar bodies in tissues by transmission electron microscopy (TEM). Specimens are commonly prepared for TEM by fixation with agents such as osmium tetroxide. These agents have a dual functionality by crosslinking lipid membranes stabilizing the cellular ultrastructure and by posing an electron-dense material thus contrasting crosslinked lipid layers and allowing differentiation between vacuoles with diffuse electron light lumen, lysosomes with an electron dense lumen and multi-lamellar late-endosomes. Evaluation of the ultrastructural changes of the PTECs upon dosing with PMB and PMBN revealed presence of multi-lamellar structures in all dosing groups (Figure 7.7). Whilst vehicle controls showed no multi-lamellar bodies (Figure 7.7a), PTECs from PMB dosed animals were characterized through the presence of multi-lamellar bodies indicative of PLD. However, the shape and number of the pathological alterations showed a dose-dependency. PTECs from the PMB low dose group showed presence of large bodies with well-defined parallel membrane invaginations which appear to be removed from the cells through ejection into the tubular lumen (Figure 7.7b). In contrast, PTECs from the PMB high dosed group were characterized

by vacuoles with diffuse lumen and numerous small lamellar bodies filled with electron-dense agglomerates Figure 7.7c). It has been postulated that these vesicle agglomerates commonly observed in PLD arise from lysosomal trapping of CADs where the cationic group interacts with negatively charged lipids, disrupting the lysosomal membrane. This disruption can result in leakage of lysosomal content into the cytosol triggering encapsulation of the affected areas in autophagosomes in which CADs interact with anionic lipids, resulting in perpetuating lysosomal leakage and encapsulation, manifesting in the observed agglomerates of multi-lamellar bodies. In contrast to most identified CADs, PMB has an intentional design allowing to bind negatively charged residues with its multiple cationic centers and a hydrophobic tail to disrupt lipid membranes. As such, it is easily imaginable that PMB can bind to BMPs enriched in the lysosomal membrane and disrupt membrane integrity when accumulating in sufficient concentrations. This concentration dependency would explain the maturation of the lysosomes into stable multi-lamellar late-endosomes in the low dose group whilst the lysosomes in the high dose group rupture, resulting in the observed pathological phenotype.

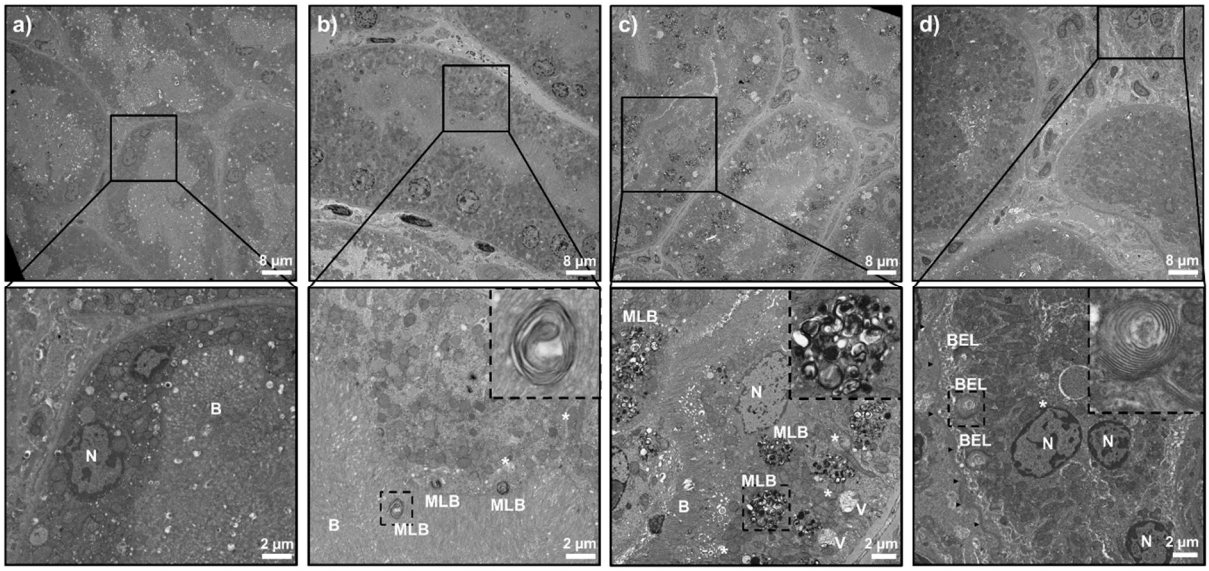

Figure 7.7, Ultrastructural changes of the renal cortex: Electron micrographs of renal tubules from a) vehicle control, b) PMB low dosed, c) PMB high dosed and d) PMBN treated animals in panorama view of whole tubules (top) and zoomed sections allowing clear visualization of subcellular organelles (bottom). N = nucleus, B = brush border, MLB = multi-lamellar bodies, V = vacuoles, BEL = basal extra-cellular labyrinth, * = swollen mitochondria, Arrow heads = tubular basal membrane

Tubules of PMBN treated animals showed pronounced multi-lamellar structures at the basal side of the cells that appear to be part of the extracellular basal labyrinth (BEL). These

structures penetrate further into the cellular space than observed in the vehicle controls (Figure 7.7Figure 7.7d). Swelling of the BEL was previously observed as a result of osmotic pressure inflicted onto labyrinth[170, 171]. These reports discussed the possibility that the content of endosomes might be ejected into the BEL through fusion of the endosomal and BEL membranes to allow for efficient recycling of the contents. Fusion of endosomal membranes with the BEL would explain the accumulation of BMPs in the PMBN dosed group without the presence of PLD indicating multi-lamellar bodies. In agreement with the histological evaluation of the tissues no major pathological findings on the ultrastructural level were found in the PMB dosed animals. All impairment was found to be reversed after the recovery period and no increased pathological findings were found compared to controls.

Overall, the presented results set the frame for the clinically observed toxicodynamic effects of PMB observed as dose-dependent impairment of the kidney function and acute kidney injury. After active uptake of the PMB into PTECs via receptor-mediated endocytosis promoted by cell-surface receptors such as megalin (also known as low-density-lipoprotein-related protein 2 [Lrp2])[172], PMB accumulates in endosomes which mature into phagolysosomes through merger with lysosomes which contain catabolic enzymes to digest the phago-lysosomal contents. Though the PMB can partly be degraded into PMBN by peptidases, the cyclic headgroup is vastly resistant towards degradation. The cationic cyclic peptides are likely to evade degradation through ionic interaction with anionic lipids which are enriched in lysosomal membranes. This close interaction and static attraction binds the PMB to the lysosomal membranes enabling the lipophilic tail to interact with the phospholipids of the membrane, increasing its permeability. Doses with subacute toxic effects can be compensated through increasing accumulation of lipids increasing the surface of the endosomes to facilitate the digestion of the contents and likely provide additional capacity to bind PMB and PMBN. These multilamellar bodies are then excreted into the tubular lumen and removed with the forming urine (Figure 7.8a).

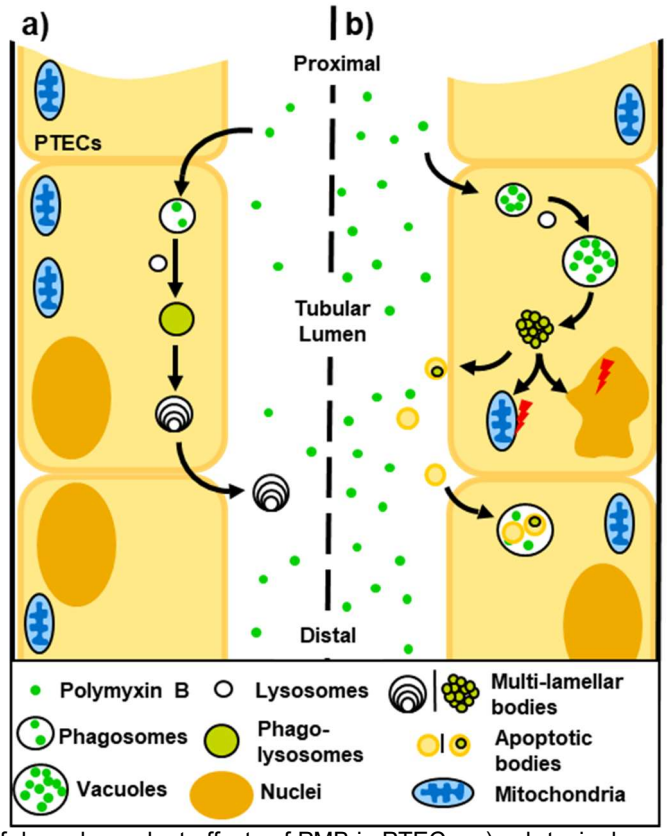

Figure 7.8, Schematics of dose dependent effects of PMB in PTECs: a) sub-toxic doses of PMB are taken up into epithelial cells and partly digested through fusion of the phagosomes through merger with lysosomes. These phagolysosomes mature to multi-lamellar bodies and are excreted into the tubule lumen. b) Acute-toxic exposure of PTECs to BMP results in uptake of critical amounts of PBM into phagosomes resulting in creation of vacuoles. The destabilization of the vacuole membrane by the PMB results in rupture or leakage of the content into the cytosol triggering encapsulation in autophagosomes. Exposure to vacuolar content and formation of ROS damages mitochondria and nuclei triggering apoptosis/necrosis of the affected cells and formation of apoptotic bodies/cellular debris. Receptor-mediated phagocytosis facilitates uptake into adjacent PTECs, exposing these to toxic amounts of PMB in a self-perpetuating progression along the tubules.

Uptake of acute toxic doses into PTECs manifest in acute kidney injury through endocytosis and trapping of osmotic active PMB concentrations manifesting in vacuolization of the epithelial cells. The amphiphilic nature of the PMB to destabilizes the vacuoles triggering auto-phagocytosis and formation of the small encapsulated MLBs observed in the electron micrographs of the high dosed rats. The leaking of lysosomal contents into the cytosol results in formation of ROS stressing the cells leading to mitochondrial swelling and nuclear degradation, triggering cell death manifesting in the observed single cell necrosis. The high abundance of PBMN in the renal cortex of PMB dosed animals indicates retention of the PMBN in the tissue which is unprecedented in PMBN dosed animals. The PMBN in the PMB dosed animals is likely formed in-situ through hydrolysis of the amide bond linking PMBN and the

lipophilic tail and is indicative of enzymatic degradation under conditions found in phagolysosomes.

When the cellular debris of the necrotic cells in the tubular lumen is recognized by scavenging receptors such as KIM-1 which recognize intracellular effectors such as phosphatidylserines, they promote a phagocyting phenotype in PTECs. Under physiological conditions this phenotype is assumed to facilitate the clearance of the cellular debris and promote regeneration of the affected tubular epithelium. Upon PMB dosing, the increased endocytosis of the cellular debris originating from dying PTECs results in a self-perpetuating feedback loop of increased internalization of PMB and PMB containing cellular debris into adjacent cells exposing these to acute-toxic concentrations of the polypeptide causing single cell necrosis. With excretion of toxic components into the tubular lumen, the flow of the primary urine transports the toxic components downstream causing progressive cell damage down the tubules from proximal to distal explaining the mild increase in GSTYb1 as biomarker for distal tubule damage (Figure 7.8b).

Conclusions

To date, the inherit link between toxicity and clinical efficacy observed for polymyxin antibiotics remains a treatment limitation for these last-resort treatment options. The possible necessity to withdraw treatment before the pathogens are successfully eradicated poses a direct health tread for the affected patients and increases the likelihood of adaption of additional antibiotic resistance mechanisms antagonizing the effects of polypeptide antibiotics. This acquisition of such resistance mechanisms, especially in MDR pathogens, further perpetuates the lack of treatment options. Understanding the root-cause of the treatment-limiting acute kidney injury caused by polymyxin antibiotics can help inform better treatment regimens for patients in critical condition until new polypeptide antibiotic with better therapeutic index are available. The active uptake of PMB into phagosomes initiates the chain of events leading towards the clinically observed acute kidney injury when spiking concentrations destabilize the endosomal membranes leading to single-cell necrosis, tubular degeneration, immune infiltration and

eventually organ failure. The active uptake can equally be considered as a target point to design new polypeptide antibiotics. The gradual pH changes of the phagosomes when merging with early/late endosomes and lysosomes could be leveraged to design compounds which change their 3D structure in acidic conditions in a way that the hydrophobic tail is immobilized and unable to destabilize lipid membranes. Another approach could be to design polypeptides which are degradable by lysosomal enzymes to allow detoxification and prevent accumulation of the lysing antibiotics in epithelial cells. Such digestible PMBs or variants without lysing properties under acidic conditions could be starting points for the development of new treatment options in the fight against MDR pathogens.

Chapter 8: Conclusions and future perspective

To generate accurate and reproducible results, any analytical technique relies on combination of optimized sample preparation protocols as well as extensive understanding of influences of analytical conditions onto the resulting data. As a combination of chemical surface analysis and tissue-based imaging, MSI inherits sample requirements of both fields. High-quality samples for MSI purposes require both, preservation of the integrity and distribution of chemical species as well of the tissue morphology. To meet these requirements, tissue specimens collected for MSI purposes are commonly snap frozen but other strategies were explored in the literature. These strategies are often based on fixation of the tissue specimens in formalin or formalin-fixing and paraffin embedding. Such tissues meet the requirement of morphological preservation as evident by their routine use for histological evaluation. However, the here presented work found severe alteration of the tissue metabolome through the fixation process, especially washout of analytes posing a severe problem. Subsequent processing such as paraffin embedding further alter the chemical scope detectable from the tissues as well as their biodistributions. For these reasons when fixed tissues are used for MSI purposes, the elucidated metabolite distribution maps should be interpreted carefully and evaluated for preparation artefacts. However, the presented work validates that snap frozen tissues should be the preferred starting material in MSI workflows wherever possible.

The collected high-quality specimens need to be prepared and cryo-sectioned to make them accessible for MSI analysis. To ensure highest preservation of the tissue morphology, embedding strategies are often utilized in classical histology workflows as well as in those for MSI. However, the choice of the embedding material is critical to ensure combability with MSI and other tissue-based analysis techniques. As discussed above, OCT as the benchmark embedding medium for histology is equally the prime example of an embedding medium which is incompatible with MSI analysis. The HPMC+PVP based embedding developed as part of the here presented work is compatible with a wide range of analytical techniques, enabling unhindered multimodal tissue analysis with the techniques of choice. At the same time, the

discussed workflow was optimized to achieve highest preservation of tissue morphology and analytes within. The presented work builds a strong framework to prepare samples for MSI purposes to scale, enabling fast turnaround of large-scale studies with numerous tissue samples whilst reaching the highest sample requirements. To further facilitate and adapt the methodology for large scale MSI studies, preparation protocols for the creation of tissue micro arrays, analogue to FFPE TMAs used in high-throughput histological analysis, should be explored in future studies. One existing problem the presented methodology does not address is the issue of potential analyte degradation and delocalization during the thawing of the cut tissue sections. Future work could investigate the possibility to keep sections frozen at all times from collection to and during analysis. Such strategies could involve cold mounting of tissue sections on adhesive substrates or the use of cryogenic sample stages comparable to those used in ToF-SIMS instruments.

Tissue sections prepared according to the discussed protocols are genuinely ready for MSI analysis, however, varying safety standards in different laboratories might require some level of decontamination to inactivate potential pathogens within the samples. The presented work clearly demonstrates the ability to use UV-C decontaminated tissues for MSI purposes as the procedures allow accurate elucidation of the biodistributions of endogenous metabolites and xenobiotics. Future work should focus on strategies to apply UV-C in a controlled manner. Utilizing sensor-based control of the applied UV-C fluency could allow the reliable and reproducible reduction of pathogens by at least 99% whilst limiting the degradation of analytes within treated tissues. Reducing the UV-C fluency to defined amounts required for increased operator safety will reduce photodegradation of xenobiotics and endogenous analytes, thus increasing sensitivity and accuracy of the achievable results. Further rigorous validation of the pathogen inactivation would allow determination of the exact UV-C fluencies required and would allow for better adaption of the values reported in the literature to the exact conditions used for decontamination.

Tissue sections prepared and analyzed in accordance with the developed workflows show unparalleled preservation of tissue morphology and analytes within. The compatibility of the sample preparation workflows with a wide range of analytical techniques allows to choose orthogonal tissue imaging techniques based on information needed for a project. Some analytical techniques remain still inaccessible for tissues prepared with the workflows described in this work. Analytical techniques such as TEM have vastly different sample preparation requirements such as fixation and are for these reasons incompatible with MSI. For compatible techniques, the ability to use adjacent sections for the different analytical techniques helps to reduce variation based on selection of specimens and allows for easier comparison and integration of the results. In the example investigation of polymyxin B induced nephrotoxicity, DESI- and MALDI-MSI could be used in conjunction with optical stains and IF fluorescence to elucidate the toxicodynamic effects of polymyxin B in the kidney. The multimodal integration of the sample preparation workflows enabled to use the initial results of the metabolomic profiling and follow-up with targeted analysis of protein distribution pattern in context of the tissue morphology. The gained insights into the toxicodynamic effects of polymyxin B will hopefully aid the development of novel antibiotics of this clinically crucial class of antibiotics and highlights the importance of unparalleled multimodal integration of imaging techniques.

References

1. Groseclose, M. R.; Castellino, S., A mimetic tissue model for the quantification of drug distributions by MALDI imaging mass spectrometry. *Anal Chem* **2013,** *85* (21), 10099-106.
2. Hamm, G.; Bonnel, D.; Legouffe, R.; Pamelard, F.; Delbos, J. M.; Bouzom, F.; Stauber, J., Quantitative mass spectrometry imaging of propranolol and olanzapine using tissue extinction calculation as normalization factor. *J Proteomics* **2012,** *75* (16), 4952-61.
3. Nilsson, A.; Fehniger, T. E.; Gustavsson, L.; Andersson, M.; Kenne, K.; Marko-Varga, G.; Andren, P. E., Fine mapping the spatial distribution and concentration of unlabeled drugs within tissue micro-compartments using imaging mass spectrometry. *PLoS One* **2010,** *5* (7), e11411.
4. Prentice, B. M.; Chumbley, C. W.; Caprioli, R. M., Absolute Quantification of Rifampicin by MALDI Imaging Mass Spectrometry Using Multiple TOF/TOF Events in a Single Laser Shot. *J Am Soc Mass Spectrom* **2017,** *28* (1), 136-144.
5. Pirman, D. A.; Reich, R. F.; Kiss, A.; Heeren, R. M.; Yost, R. A., Quantitative MALDI tandem mass spectrometric imaging of cocaine from brain tissue with a deuterated internal standard. *Anal Chem* **2013,** *85* (2), 1081-9.
6. Doria, M. L.; McKenzie, J. S.; Mroz, A.; Phelps, D. L.; Speller, A.; Rosini, F.; Strittmatter, N.; Golf, O.; Veselkov, K.; Brown, R.; Ghaem-Maghami, S.; Takats, Z., Epithelial ovarian carcinoma diagnosis by desorption electrospray ionization mass spectrometry imaging. *Sci Rep* **2016,** *6*, 39219.
7. Groseclose, M. R.; Laffan, S. B.; Frazier, K. S.; Hughes-Earle, A.; Castellino, S., Imaging MS in Toxicology: An Investigation of Juvenile Rat Nephrotoxicity Associated with Dabrafenib Administration. *J Am Soc Mass Spectrom* **2015,** *26* (6), 887-98.
8. Goodwin, R. J.; Pennington, S. R.; Pitt, A. R., Protein and peptides in pictures: imaging with MALDI mass spectrometry. *Proteomics* **2008,** *8* (18), 3785-800.
9. McDonnell, L. A.; Corthals, G. L.; Willems, S. M.; van Remoortere, A.; van Zeijl, R. J.; Deelder, A. M., Peptide and protein imaging mass spectrometry in cancer research. *J Proteomics* **2010,** *73* (10), 1921-44.
10. Patterson, N. H.; Tuck, M.; Van de Plas, R.; Caprioli, R. M., Advanced Registration and Analysis of MALDI Imaging Mass Spectrometry Measurements through Autofluorescence Microscopy. *Anal Chem* **2018**.
11. Sole-Domenech, S.; Sjovall, P.; Vukojevic, V.; Fernando, R.; Codita, A.; Salve, S.; Bogdanovic, N.; Mohammed, A. H.; Hammarstrom, P.; Nilsson, K. P.; LaFerla, F. M.; Jacob, S.; Berggren, P. O.; Gimenez-Llort, L.; Schalling, M.; Terenius, L.; Johansson, B., Localization of cholesterol, amyloid and glia in Alzheimer's disease transgenic mouse brain tissue using time-of-flight secondary ion mass spectrometry (ToF-SIMS) and immunofluorescence imaging. *Acta Neuropathol* **2013,** *125* (1), 145-57.
12. Michno, W.; Kaya, I.; Nystrom, S.; Guerard, L.; Nilsson, K. P. R.; Hammarstrom, P.; Blennow, K.; Zetterberg, H.; Hanrieder, J., Multimodal Chemical Imaging of Amyloid Plaque Polymorphism Reveals Abeta Aggregation Dependent Anionic Lipid Accumulations and Metabolism. *Anal Chem* **2018,** *90* (13), 8130-8138.
13. Seuma, J.; Bunch, J.; Cox, A.; McLeod, C.; Bell, J.; Murray, C., Combination of immunohistochemistry and laser ablation ICP mass spectrometry for imaging of cancer biomarkers. *Proteomics* **2008,** *8* (18), 3775-84.
14. Kantor, A. B.; Wang, W.; Lin, H.; Govindarajan, H.; Anderle, M.; Perrone, A.; Becker, C., Biomarker discovery by comprehensive phenotyping for autoimmune diseases. *Clin Immunol* **2004,** *111* (2), 186-95.
15. Hood, L.; Heath, J. R.; Phelps, M. E.; Lin, B., Systems biology and new technologies enable predictive and preventative medicine. *Science* **2004,** *306* (5696), 640-3.
16. Butcher, E. C.; Berg, E. L.; Kunkel, E. J., Systems biology in drug discovery. *Nat Biotechnol* **2004,** *22* (10), 1253-9.
17. Arrell, D. K.; Terzic, A., Network systems biology for drug discovery. *Clin Pharmacol Ther* **2010,** *88* (1), 120-5.

18. Swales, J. G.; Dexter, A.; Hamm, G.; Nilsson, A.; Strittmatter, N.; Michopoulos, F.; Hardy, C.; Morentin-Gutierrez, P.; Mellor, M.; Andren, P. E.; Clench, M. R.; Bunch, J.; Critchlow, S. E.; Goodwin, R. J. A., Quantitation of Endogenous Metabolites in Mouse Tumors Using Mass-Spectrometry Imaging. *Anal Chem* **2018,** *90* (10), 6051-6058.
19. Herzog, R. F. K.; Viehböck, F. P., Ion Source for Mass Spectrography. *Physical Review* **1949,** *76* (6), 855-856.
20. Fletcher, J. S.; Lockyer, N. P.; Vaidyanathan, S.; Vickerman, J. C., TOF-SIMS 3D biomolecular imaging of Xenopus laevis oocytes using buckminsterfullerene (C60) primary ions. *Analytical Chemistry* **2007,** *79* (6), 2199-2206.
21. Passarelli, M. K.; Pirkl, A.; Moellers, R.; Grinfeld, D.; Kollmer, F.; Havelund, R.; Newman, C. F.; Marshall, P. S.; Arlinghaus, H.; Alexander, M. R.; West, A.; Horning, S.; Niehuis, E.; Makarov, A.; Dollery, C. T.; Gilmore, I. S., The 3D OrbiSIMS—label-free metabolic imaging with subcellular lateral resolution and high mass-resolving power. *Nature Methods* **2017,** *14* (12), 1175-1183.
22. Karas, M.; Bachmann, D.; Hillenkamp, F., Influence of the wavelength in high-irradiance ultraviolet laser desorption mass spectrometry of organic molecules. *Analytical Chemistry* **1985,** *57* (14), 2935-2939.
23. Tanaka, K.; Waki, H.; Ido, Y.; Akita, S.; Yoshida, Y.; Yoshida, T.; Matsuo, T., Protein and polymer analyses up to m/z 100 000 by laser ionization time-of-flight mass spectrometry. *Rapid Communications in Mass Spectrometry* **1988,** *2* (8), 151-153.
24. Caprioli, R. M.; Farmer, T. B.; Gile, J., Molecular imaging of biological samples: localization of peptides and proteins using MALDI-TOF MS. *Anal Chem* **1997,** *69* (23), 4751-60.
25. Yamashita, M.; Fenn, J. B., Electrospray ion source. Another variation on the free-jet theme. *The Journal of Physical Chemistry* **1984,** *88* (20), 4451-4459.
26. Takats, Z.; Wiseman, J. M.; Gologan, B.; Cooks, R. G., Mass spectrometry sampling under ambient conditions with desorption electrospray ionization. *Science* **2004,** *306* (5695), 471-3.
27. Wiseman, J. M.; Ifa, D. R.; Song, Q.; Cooks, R. G., Tissue Imaging at Atmospheric Pressure Using Desorption Electrospray Ionization (DESI) Mass Spectrometry. *Angewandte Chemie International Edition* **2006,** *45* (43), 7188-7192.
28. Kempson, I. M.; Skinner, W. M., ToF-SIMS analysis of elemental distributions in human hair. *Science of The Total Environment* **2005,** *338* (3), 213-227.
29. Heard, P. J.; Feeney, K. A.; Allen, G. C.; Shewry, P. R., Determination of the elemental composition of mature wheat grain using a modified secondary ion mass spectrometer (SIMS). *The Plant Journal* **2002,** *30* (2), 237-245.
30. Thompson, C. E.; Jungnickel, H.; Lockyer, N. P.; Stephens, G. M.; Vickerman, J. C., ToF-SIMS studies as a tool to discriminate between spores and vegetative cells of bacteria. *Applied Surface Science* **2004,** *231-232*, 420-423.
31. Jungnickel, H.; Laux, P.; Luch, A., Time-of-Flight Secondary Ion Mass Spectrometry (ToF-SIMS): A New Tool for the Analysis of Toxicological Effects on Single Cell Level. *Toxics* **2016,** *4* (1).
32. Shariatgorji, M.; Nilsson, A.; Goodwin, R. J. A.; Svenningsson, P.; Schintu, N.; Banka, Z.; Kladni, L.; Hasko, T.; Szabo, A.; Andren, P. E., Deuterated Matrix-Assisted Laser Desorption Ionization Matrix Uncovers Masked Mass Spectrometry Imaging Signals of Small Molecules. *Analytical Chemistry* **2012,** *84* (16), 7152-7157.
33. Tillner, J.; Wu, V.; Jones, E. A.; Pringle, S. D.; Karancsi, T.; Dannhorn, A.; Veselkov, K.; McKenzie, J. S.; Takats, Z., Faster, More Reproducible DESI-MS for Biological Tissue Imaging. *Journal of the American Society for Mass Spectrometry* **2017,** *28* (10), 2090-2098.
34. Bruinen, A. L.; van Oevelen, C.; Eijkel, G. B.; Van Heerden, M.; Cuyckens, F.; Heeren, R. M., Mass Spectrometry Imaging of Drug Related Crystal-Like Structures in Formalin-Fixed Frozen and Paraffin-Embedded Rabbit Kidney Tissue Sections. *J Am Soc Mass Spectrom* **2016,** *27* (1), 117-23.
35. Buck, A.; Ly, A.; Balluff, B.; Sun, N.; Gorzolka, K.; Feuchtinger, A.; Janssen, K. P.; Kuppen, P. J.; van de Velde, C. J.; Weirich, G.; Erlmeier, F.; Langer, R.; Aubele, M.;

Zitzelsberger, H.; Aichler, M.; Walch, A., High-resolution MALDI-FT-ICR MS imaging for the analysis of metabolites from formalin-fixed, paraffin-embedded clinical tissue samples. *J Pathol* **2015,** *237* (1), 123-32.
36. Djidja, M. C.; Claude, E.; Snel, M. F.; Francese, S.; Scriven, P.; Carolan, V.; Clench, M. R., Novel molecular tumour classification using MALDI-mass spectrometry imaging of tissue micro-array. *Anal Bioanal Chem* **2010,** *397* (2), 587-601.
37. Bonnel, D.; Longuespee, R.; Franck, J.; Roudbaraki, M.; Gosset, P.; Day, R.; Salzet, M.; Fournier, I., Multivariate analyses for biomarkers hunting and validation through on-tissue bottom-up or in-source decay in MALDI-MSI: application to prostate cancer. *Anal Bioanal Chem* **2011,** *401* (1), 149-65.
38. Everest-Dass, A. V.; Briggs, M. T.; Kaur, G.; Oehler, M. K.; Hoffmann, P.; Packer, N. H., N-glycan MALDI Imaging Mass Spectrometry on Formalin-Fixed Paraffin-Embedded Tissue Enables the Delineation of Ovarian Cancer Tissues. *Mol Cell Proteomics* **2016,** *15* (9), 3003-16.
39. Lemaire, R.; Wisztorski, M.; Desmons, A.; Tabet, J. C.; Day, R.; Salzet, M.; Fournier, I., MALDI-MS direct tissue analysis of proteins: Improving signal sensitivity using organic treatments. *Anal Chem* **2006,** *78* (20), 7145-53.
40. Martin-Lorenzo, M.; Balluff, B.; Sanz-Maroto, A.; van Zeijl, R. J.; Vivanco, F.; Alvarez-Llamas, G.; McDonnell, L. A., 30mum spatial resolution protein MALDI MSI: In-depth comparison of five sample preparation protocols applied to human healthy and atherosclerotic arteries. *J Proteomics* **2014,** *108*, 465-8.
41. Cacciatore, S.; Zadra, G.; Bango, C.; Penney, K. L.; Tyekucheva, S.; Yanes, O.; Loda, M., Metabolic Profiling in Formalin-Fixed and Paraffin-Embedded Prostate Cancer Tissues. *Molecular Cancer Research* **2017,** *15* (4), 439-447.
42. Liguri, G.; Nassi, P.; Taddei, N.; Nediani, C.; Ramponi, G., Post-mortem modifications of the specific activity of some brain enzymes. *Neurosci Lett* **1988,** *85* (2), 244-8.
43. Fahn, S.; Cote, L. J., Stability of enzymes in post-mortem rat brain. *J Neurochem* **1976,** *26* (5), 1039-42.
44. Ritchie, T.; Scully, S. A.; de Vellis, J.; Noble, E. P., Stability of neuronal and glial marker enzymes in post-mortem rat brain. *Neurochem Res* **1986,** *11* (3), 383-92.
45. Gattaz, W. F.; Maras, A.; Cairns, N. J.; Levy, R.; Förstl, H., Decreased phospholipase A2 activity in Alzheimer brains. *Biological Psychiatry* **1995,** *37* (1), 13-17.
46. Vincek, V.; Nassiri, M.; Nadji, M.; Morales, A. R., A Tissue Fixative that Protects Macromolecules (DNA, RNA, and Protein) and Histomorphology in Clinical Samples. *Laboratory Investigation* **2003,** *83* (10), 1427-1435.
47. Williams, C.; Pontén, F.; Moberg, C.; Söderkvist, P.; Uhlén, M.; Pontén, J.; Sitbon, G.; Lundeberg, J., A High Frequency of Sequence Alterations Is Due to Formalin Fixation of Archival Specimens. *The American Journal of Pathology* **1999,** *155* (5), 1467-1471.
48. Gaudin, M.; Panchal, M.; Ayciriex, S.; Werner, E.; Brunelle, A.; Touboul, D.; Boursier-Neyret, C.; Auzeil, N.; Walther, B.; Duyckaerts, C.; Laprévote, O., Ultra performance liquid chromatography – mass spectrometry studies of formalin-induced alterations of human brain lipidome. *Journal of Mass Spectrometry* **2014,** *49* (10), 1035-1042.
49. Vos, D. R. N.; Bowman, A. P.; Heeren, R. M. A.; Balluff, B.; Ellis, S. R., Class-specific depletion of lipid ion signals in tissues upon formalin fixation. *International Journal of Mass Spectrometry* **2019,** *446*, 116212.
50. Goodwin, R. J., Sample preparation for mass spectrometry imaging: small mistakes can lead to big consequences. *J Proteomics* **2012,** *75* (16), 4893-911.
51. Zaima, N.; Hayasaka, T.; Goto-Inoue, N.; Setou, M., Matrix-assisted laser desorption/ionization imaging mass spectrometry. *Int J Mol Sci* **2010,** *11* (12), 5040-55.
52. Schwartz, S. A.; Reyzer, M. L.; Caprioli, R. M., Direct tissue analysis using matrix-assisted laser desorption/ionization mass spectrometry: practical aspects of sample preparation. *J Mass Spectrom* **2003,** *38* (7), 699-708.
53. Peukert, M.; Matros, A.; Lattanzio, G.; Kaspar, S.; Abadia, J.; Mock, H. P., Spatially resolved analysis of small molecules by matrix-assisted laser desorption/ionization mass spectrometric imaging (MALDI-MSI). *New Phytol* **2012,** *193* (3), 806-15.

54. Potchoiba, M. J.; Tensfeldt, T. G.; Nocerini, M. R.; Silber, B. M., A novel quantitative method for determining the biodistribution of radiolabeled xenobiotics using whole-body cryosectioning and autoradioluminography. *J Pharmacol Exp Ther* **1995,** *272* (2), 953-62.
55. Stoeckli, M.; Staab, D.; Schweitzer, A.; Gardiner, J.; Seebach, D., Imaging of a beta-peptide distribution in whole-body mice sections by MALDI mass spectrometry. *J Am Soc Mass Spectrom* **2007,** *18* (11), 1921-4.
56. Gill, E. L.; Yost, R. A.; Vedam-Mai, V.; Garrett, T. J., Precast Gelatin-Based Molds for Tissue Embedding Compatible with Mass Spectrometry Imaging. *Anal Chem* **2017,** *89* (1), 576-580.
57. Nelson, K. A.; Daniels, G. J.; Fournie, J. W.; Hemmer, M. J., Optimization of whole-body zebrafish sectioning methods for mass spectrometry imaging. *J Biomol Tech* **2013,** *24* (3), 119-27.
58. Strohalm, M.; Strohalm, J.; Kaftan, F.; Krasny, L.; Volny, M.; Novak, P.; Ulbrich, K.; Havlicek, V., Poly[N-(2-hydroxypropyl)methacrylamide]-based tissue-embedding medium compatible with MALDI mass spectrometry imaging experiments. *Anal Chem* **2011,** *83* (13), 5458-62.
59. Addie, R. D.; Balluff, B.; Bovée, J. V. M. G.; Morreau, H.; McDonnell, L. A., Current State and Future Challenges of Mass Spectrometry Imaging for Clinical Research. *Analytical Chemistry* **2015,** *87* (13), 6426-6433.
60. Mirnezami, R.; Spagou, K.; Vorkas, P. A.; Lewis, M. R.; Kinross, J.; Want, E.; Shion, H.; Goldin, R. D.; Darzi, A.; Takats, Z.; Holmes, E.; Cloarec, O.; Nicholson, J. K., Chemical mapping of the colorectal cancer microenvironment via MALDI imaging mass spectrometry (MALDI-MSI) reveals novel cancer-associated field effects. *Molecular Oncology* **2014,** *8* (1), 39-49.
61. Abu Sammour, D.; Marsching, C.; Geisel, A.; Erich, K.; Schulz, S.; Ramallo Guevara, C.; Rabe, J. H.; Marx, A.; Findeisen, P.; Hohenberger, P.; Hopf, C., Quantitative Mass Spectrometry Imaging Reveals Mutation Status-independent Lack of Imatinib in Liver Metastases of Gastrointestinal Stromal Tumors. *Sci Rep* **2019,** *9* (1), 10698.
62. Bosch, F. X.; Lorincz, A.; Muñoz, N.; Meijer, C. J. L. M.; Shah, K. V., The causal relation between human papillomavirus and cervical cancer. *Journal of Clinical Pathology* **2002,** *55* (4), 244-265.
63. D'Souza, G.; Kreimer, A. R.; Viscidi, R.; Pawlita, M.; Fakhry, C.; Koch, W. M.; Westra, W. H.; Gillison, M. L., Case–Control Study of Human Papillomavirus and Oropharyngeal Cancer. *New England Journal of Medicine* **2007,** *356* (19), 1944-1956.
64. Mehanna, H.; Beech, T.; Nicholson, T.; El-Hariry, I.; McConkey, C.; Paleri, V.; Roberts, S., Prevalence of human papillomavirus in oropharyngeal and nonoropharyngeal head and neck cancer—systematic review and meta-analysis of trends by time and region. *Head & Neck* **2013,** *35* (5), 747-755.
65. Kofman, A.; Marcinkiewicz, L.; Dupart, E.; Lyshchev, A.; Martynov, B.; Ryndin, A.; Kotelevskaya, E.; Brown, J.; Schiff, D.; Abounader, R., The roles of viruses in brain tumor initiation and oncomodulation. *J Neurooncol* **2011,** *105* (3), 451-66.
66. Strojnik, T.; Duh, D.; Lah, T. T., Prevalence of Neurotropic Viruses in Malignant Glioma and Their Onco-Modulatory Potential. *In Vivo* **2017,** *31* (2), 221-229.
67. Schroeder, M. R.; Loparev, V., Rapid Inactivation of Non-Endospore-Forming Bacterial Pathogens by Heat Stabilization is Compatible with Downstream Next-Generation Sequencing. *Applied Biosafety* **2019,** *24* (3), 129-133.
68. Cazares, L. H.; Van Tongeren, S. A.; Costantino, J.; Kenny, T.; Garza, N. L.; Donnelly, G.; Lane, D.; Panchal, R. G.; Bavari, S., Heat fixation inactivates viral and bacterial pathogens and is compatible with downstream MALDI mass spectrometry tissue imaging. *BMC Microbiol* **2015,** *15*, 101.
69. Meyers, C.; Milici, J.; Robison, R., UVC radiation as an effective disinfectant method to inactivate human papillomaviruses. *PLoS One* **2017,** *12* (10), e0187377.
70. Miwa, S.; Yano, S.; Hiroshima, Y.; Tome, Y.; Uehara, F.; Mii, S.; Efimova, E. V.; Kimura, H.; Hayashi, K.; Tsuchiya, H.; Hoffman, R. M., Imaging UVC-induced DNA damage response in models of minimal cancer. *J Cell Biochem* **2013,** *114* (11), 2493-9.

71. Ly, A.; Buck, A.; Balluff, B.; Sun, N.; Gorzolka, K.; Feuchtinger, A.; Janssen, K. P.; Kuppen, P. J.; van de Velde, C. J.; Weirich, G.; Erlmeier, F.; Langer, R.; Aubele, M.; Zitzelsberger, H.; McDonnell, L.; Aichler, M.; Walch, A., High-mass-resolution MALDI mass spectrometry imaging of metabolites from formalin-fixed paraffin-embedded tissue. *Nat Protoc* **2016,** *11* (8), 1428-43.
72. Adusumilli, R.; Mallick, P., Data Conversion with ProteoWizard msConvert. *Methods Mol Biol* **2017,** *1550*, 339-368.
73. Race, A. M.; Styles, I. B.; Bunch, J., Inclusive sharing of mass spectrometry imaging data requires a converter for all. *J Proteomics* **2012,** *75* (16), 5111-2.
74. Swales, J. G.; Tucker, J. W.; Strittmatter, N.; Nilsson, A.; Cobice, D.; Clench, M. R.; Mackay, C. L.; Andren, P. E.; Takats, Z.; Webborn, P. J.; Goodwin, R. J., Mass spectrometry imaging of cassette-dosed drugs for higher throughput pharmacokinetic and biodistribution analysis. *Anal Chem* **2014,** *86* (16), 8473-80.
75. Nilsson, A.; Goodwin, R. J.; Swales, J. G.; Gallagher, R.; Shankaran, H.; Sathe, A.; Pradeepan, S.; Xue, A.; Keirstead, N.; Sasaki, J. C.; Andren, P. E.; Gupta, A., Investigating nephrotoxicity of polymyxin derivatives by mapping renal distribution using mass spectrometry imaging. *Chem Res Toxicol* **2015,** *28* (9), 1823-30.
76. Norris, J. L.; Cornett, D. S.; Mobley, J. A.; Andersson, M.; Seeley, E. H.; Chaurand, P.; Caprioli, R. M., Processing MALDI Mass Spectra to Improve Mass Spectral Direct Tissue Analysis. *Int J Mass Spectrom* **2007,** *260* (2-3), 212-221.
77. Lyczko, J.; Beach, D. G.; Gabryelski, W., Commercial formaldehyde standard for mass calibration in mass spectrometry. *J Mass Spectrom* **2015,** *50* (3), 463-9.
78. Carter, C. L.; McLeod, C. W.; Bunch, J., Imaging of Phospholipids in Formalin Fixed Rat Brain Sections by Matrix Assisted Laser Desorption/Ionization Mass Spectrometry. *Journal of The American Society for Mass Spectrometry* **2011,** *22* (11), 1991.
79. Thavarajah, R.; Mudimbaimannar, V. K.; Elizabeth, J.; Rao, U. K.; Ranganathan, K., Chemical and physical basics of routine formaldehyde fixation. *J Oral Maxillofac Pathol* **2012,** *16* (3), 400-405.
80. Fox, C. H.; Johnson, F. B.; Whiting, J.; Roller, P. P., Formaldehyde fixation. *J Histochem Cytochem* **1985,** *33* (8), 845-53.
81. Song, X.; Luo, Z.; Li, X.; Li, T.; Wang, Z.; Sun, C.; Huang, L.; Xie, P.; Liu, X.; He, J.; Abliz, Z., In Situ Hydrogel Conditioning of Tissue Samples To Enhance the Drug's Sensitivity in Ambient Mass Spectrometry Imaging. *Anal Chem* **2017,** *89* (12), 6318-6323.
82. Heslinga, F. J.; Deierkauf, F. A., The action of histological fixatives on tissue lipids. Comparison of the action of several fixatives using paper chromatography. *J Histochem Cytochem* **1961,** *9*, 572-7.
83. Rordorf, G.; Uemura, Y.; Bonventre, J., Characterization of phospholipase A2 (PLA2) activity in gerbil brain: enhanced activities of cytosolic, mitochondrial, and microsomal forms after ischemia and reperfusion. *The Journal of Neuroscience* **1991,** *11* (6), 1829-1836.
84. Marion, J.; Wolfe, L. S., Origin of the arachidonic acid released post-mortem in rat forebrain. *Biochimica et Biophysica Acta (BBA) - Lipids and Lipid Metabolism* **1979,** *574* (1), 25-32.
85. Shabihkhani, M.; Lucey, G. M.; Wei, B.; Mareninov, S.; Lou, J. J.; Vinters, H. V.; Singer, E. J.; Cloughesy, T. F.; Yong, W. H., The procurement, storage, and quality assurance of frozen blood and tissue biospecimens in pathology, biorepository, and biobank settings. *Clinical Biochemistry* **2014,** *47* (4), 258-266.
86. Steu, S.; Baucamp, M.; von Dach, G.; Bawohl, M.; Dettwiler, S.; Storz, M.; Moch, H.; Schraml, P., A procedure for tissue freezing and processing applicable to both intra-operative frozen section diagnosis and tissue banking in surgical pathology. *Virchows Archiv* **2008,** *452* (3), 305-312.
87. Gobom, J.; Schuerenberg, M.; Mueller, M.; Theiss, D.; Lehrach, H.; Nordhoff, E., Alpha-cyano-4-hydroxycinnamic acid affinity sample preparation. A protocol for MALDI-MS peptide analysis in proteomics. *Anal Chem* **2001,** *73* (3), 434-8.

88. Lemaire, R.; Desmons, A.; Tabet, J. C.; Day, R.; Salzet, M.; Fournier, I., Direct analysis and MALDI imaging of formalin-fixed, paraffin-embedded tissue sections. *J Proteome Res* **2007,** *6* (4), 1295-305.
89. Chaurand, P.; Stoeckli, M.; Caprioli, R. M., Direct profiling of proteins in biological tissue sections by MALDI mass spectrometry. *Anal Chem* **1999,** *71* (23), 5263-70.
90. Payne, M. E.; Grayson, S. M., Characterization of Synthetic Polymers via Matrix Assisted Laser Desorption Ionization Time of Flight (MALDI-TOF) Mass Spectrometry. *J Vis Exp* **2018,** (136).
91. Peacock, P. M.; McEwen, C. N., Mass spectrometry of synthetic polymers. *Anal Chem* **2004,** *76* (12), 3417-27.
92. Marie, A.; Fournier, F.; Tabet, J. C., Characterization of synthetic polymers by MALDI-TOF/MS: investigation into new methods of sample target preparation and consequence on mass spectrum finger print. *Anal Chem* **2000,** *72* (20), 5106-14.
93. Cazares, L. H.; Troyer, D.; Mendrinos, S.; Lance, R. A.; Nyalwidhe, J. O.; Beydoun, H. A.; Clements, M. A.; Drake, R. R.; Semmes, O. J., Imaging mass spectrometry of a specific fragment of mitogen-activated protein kinase/extracellular signal-regulated kinase kinase kinase 2 discriminates cancer from uninvolved prostate tissue. *Clin Cancer Res* **2009,** *15* (17), 5541-51.
94. Dannhorn, A.; Kazanc, E.; Ling, S.; Nikula, C.; Karali, E.; Serra, M. P.; Vorng, J.-L.; Inglese, P.; Maglennon, G.; Hamm, G.; Swales, J.; Strittmatter, N.; Barry, S. T.; Sansom, O. J.; Poulogiannis, G.; Bunch, J.; Goodwin, R. J. A.; Takats, Z., Universal Sample Preparation Unlocking Multimodal Molecular Tissue Imaging. *Analytical Chemistry* **2020,** *92* (16), 11080-11088.
95. Pryor, W. A.; Squadrito, G. L.; Friedman, M., The cascade mechanism to explain ozone toxicity: the role of lipid ozonation products. *Free Radic Biol Med* **1995,** *19* (6), 935-41.
96. Volný, M.; Venter, A.; Smith, S. A.; Pazzi, M.; Cooks, R. G., Surface effects and electrochemical cell capacitance in desorption electrospray ionization. *Analyst* **2008,** *133* (4), 525-531.
97. Zhang, Y.; Zhang, J.; Xiao, Y.; Chang, V. W. C.; Lim, T.-T., Direct and indirect photodegradation pathways of cytostatic drugs under UV germicidal irradiation: Process kinetics and influences of water matrix species and oxidant dosing. *Journal of Hazardous Materials* **2017,** *324*, 481-488.
98. Enns, K.; Burgess, W. H., The Photochemical Oxidation of Ethylenediaminetetraacetic Acid and Methionine by Ribolflavin1. *Journal of the American Chemical Society* **1965,** *87* (24), 5766-5770.
99. Stasicka, Z., Chapter 7 - Transition metal complexes as solar photocatalysts in the environment: A short review of recent development. In *Advances in Inorganic Chemistry*, Eldik, R. v.; Stochel, G., Eds. Academic Press: 2011; Vol. 63, pp 291-343.
100. Gupta, P.; Lakes, A.; Dziubla, T., Chapter One - A Free Radical Primer. In *Oxidative Stress and Biomaterials*, Dziubla, T.; Butterfield, D. A., Eds. Academic Press: 2016; pp 1-33.
101. Albini, A.; Fasani, E., Photochemistry of drugs: An overview and practical problems. In *Drugs: Photochemistry and Photostability*, Albini, A.; Fasani, E., Eds. The Royal Society of Chemistry: 1998; pp 1-73.
102. Boreen, A. L.; Arnold, W. A.; McNeill, K., Photodegradation of pharmaceuticals in the aquatic environment: A review. *Aquatic Sciences* **2003,** *65* (4), 320-341.
103. Doll, T. E.; Frimmel, F. H., Fate of pharmaceuticals—photodegradation by simulated solar UV-light. *Chemosphere* **2003,** *52* (10), 1757-1769.
104. Kawabata, K.; Sugihara, K.; Sanoh, S.; Kitamura, S.; Ohta, S., Photodegradation of pharmaceuticals in the aquatic environment by sunlight and UV-A, -B and -C irradiation. *The Journal of Toxicological Sciences* **2013,** *38* (2), 215-223.
105. van Henegouwen, G. M. J. B.; van de Zijde, H. J.; van de Griend, J.; de Vries, H., Photochemical decomposition of diphenhydramine in water. *International Journal of Pharmaceutics* **1987,** *35* (3), 259-262.

106. Breier, A. R.; Nudelman, N. S.; Steppe, M.; Schapoval, E. E. S., Isolation and structure elucidation of photodegradation products of fexofenadine. *Journal of Pharmaceutical and Biomedical Analysis* **2008,** *46* (2), 250-257.
107. Tarozzi, A.; Andrisano, V.; Fiori, J.; Cavrini, V.; Forti, G. C.; Hrelia, P., Photomutagenic Properties of Terfenadine as Revealed by a Stepwise Photostability, Phototoxicity and Photomutagenicity Testing Approach ¶. *Photochemistry and Photobiology* **2003,** *77* (4), 356-361.
108. Andrisano, V.; Gotti, R.; Leoni, A.; Cavrini, V., Photodegradation studies on Atenolol by liquid chromatography. *Journal of Pharmaceutical and Biomedical Analysis* **1999,** *21* (4), 851-857.
109. Maier, P. D. D. I., Inactivation of bacteria, viruses and other pathogens by UV-C irradiation in the Leica cryostat product family. *ECOscope* **2007**, 1-17.
110. Rabenau, H. F.; Schwebke, I.; Blümel, J.; Eggers, M.; Glebe, D.; Rapp, I.; Sauerbrei, A.; Steinmann, E.; Steinmann, J.; Willkommen, H., Leitlinie der Deutschen Vereinigung zur Bekämpfung der Viruskrankheiten (DVV) e. V. und des Robert Koch-Instituts (RKI) zur Prüfung von chemischen Desinfektionsmitteln auf Wirksamkeit gegen Viren in der Humanmedizin. **2015**.
111. Exner, M.; Gebel, J.; GfV, W. G.; Goroncy-Bermes, P.; Kammler, H.-J.; DVV, H. R.; von Rheinbaben, F.; Steinmann, J.; Thraenhart, O.; Wolff, M., Prüfung und Deklaration der Wirksamkeit von Desinfektionsmitteln gegen Viren. *Bundesgesundheitsblatt-Gesundheitsforschung-Gesundheitsschutz* **2004,** *47* (1), 62-66.
112. EN 14476. Chemical disinfectants and antiseptics - Virucidal quantitative suspension test for chemical disinfectants and antiseptics used in human medicine. Test method and requirements (phase 2, step 1).
113. Van Dyne, E. A.; Henley, S. J.; Saraiya, M.; Thomas, C. C.; Markowitz, L. E.; Benard, V. B., Trends in human papillomavirus–associated cancers—United States, 1999–2015. *Morbidity and Mortality Weekly Report* **2018,** *67* (33), 918.
114. Henderson, E.; Heston, L.; Grogan, E.; Miller, G., Radiobiological inactivation of Epstein-Barr virus. *J Virol* **1978,** *25* (1), 51-59.
115. Lytle, C. D.; Sagripanti, J.-L., Predicted inactivation of viruses of relevance to biodefense by solar radiation. *J Virol* **2005,** *79* (22), 14244-14252.
116. Lindsley, W. G.; McClelland, T. L.; Neu, D. T.; Martin, S. B.; Mead, K. R.; Thewlis, R. E.; Noti, J. D., Ambulance Disinfection using Ultraviolet Germicidal Irradiation (UVGI): Effects of Fixture Location and Surface Reflectivity. *J Occup Environ Hyg. 15(1):1-12* **2018,** *15* (1).
117. Prentice, B. M.; Chumbley, C. W.; Caprioli, R. M., Absolute Quantification of Rifampicin by MALDI Imaging Mass Spectrometry Using Multiple TOF/TOF Events in a Single Laser Shot. *J Am Soc Mass Spectr* **2017,** *28* (1), 136-144.
118. Tata, A.; Perez, C. J.; Hamid, T. S.; Bayfield, M. A.; Ifa, D. R., Analysis of Metabolic Changes in Plant Pathosystems by Imprint Imaging DESI-MS. *J Am Soc Mass Spectr* **2015,** *26* (4), 641-648.
119. Manicke, N. E.; Dill, A. L.; Ifa, D. R.; Cooks, R. G., High-resolution tissue imaging on an orbitrap mass spectrometer by desorption electrospray ionization mass spectrometry. *J Mass Spectrom* **2010,** *45* (2), 223-6.
120. Rompp, A.; Guenther, S.; Takats, Z.; Spengler, B., Mass spectrometry imaging with high resolution in mass and space (HR(2) MSI) for reliable investigation of drug compound distributions on the cellular level. *Anal Bioanal Chem* **2011,** *401* (1), 65-73.
121. Krasny, L.; Hoffmann, F.; Ernst, G.; Trede, D.; Alexandrov, T.; Havlicek, V.; Guntinas-Lichius, O.; von Eggeling, F.; Crecelius, A. C., Spatial Segmentation of MALDI FT-ICR MSI Data: A Powerful Tool to Explore the Head and Neck Tumor In Situ Lipidome. *J Am Soc Mass Spectr* **2015,** *26* (1), 36-43.
122. Wildburger, N. C.; Wood, P. L.; Gumin, J.; Lichti, C. F.; Emmett, M. R.; Lang, F. F.; Nilsson, C. L., ESI-MS/MS and MALDI-IMS Localization Reveal Alterations in Phosphatidic Acid, Diacylglycerol, and DHA in Glioma Stem Cell Xenografts. *J Proteome Res* **2015,** *14* (6), 2511-9.

123. Prideaux, B.; Dartois, V.; Staab, D.; Weiner, D. M.; Goh, A.; Via, L. E.; Barry, C. E., 3rd; Stoeckli, M., High-sensitivity MALDI-MRM-MS imaging of moxifloxacin distribution in tuberculosis-infected rabbit lungs and granulomatous lesions. *Analytical chemistry* **2011,** *83* (6), 2112-8.
124. Kennedy, J. H.; Aurand, C.; Shirey, R.; Laughlin, B. C.; Wiseman, J. M., Coupling desorption electrospray ionization with solid-phase microextraction for screening and quantitative analysis of drugs in urine. *Analytical chemistry* **2010,** *82* (17), 7502-8.
125. Kennedy, J. H.; Wiseman, J. M., Evaluation and performance of desorption electrospray ionization using a triple quadrupole mass spectrometer for quantitation of pharmaceuticals in plasma. *Rapid Commun Mass Spectrom* **2010,** *24* (3), 309-14.
126. Lamont, L.; Eijkel, G. B.; Jones, E. A.; Flinders, B.; Ellis, S. R.; Porta Siegel, T.; Heeren, R. M. A.; Vreeken, R. J., Targeted Drug and Metabolite Imaging: Desorption Electrospray Ionization Combined with Triple Quadrupole Mass Spectrometry. *Anal Chem* **2018,** *90* (22), 13229-13235.
127. Kallback, P.; Nilsson, A.; Shariatgorji, M.; Andren, P. E., msIQuant--Quantitation Software for Mass Spectrometry Imaging Enabling Fast Access, Visualization, and Analysis of Large Data Sets. *Analytical chemistry* **2016,** *88* (8), 4346-53.
128. Khatib-Shahidi, S.; Andersson, M.; Herman, J. L.; Gillespie, T. A.; Caprioli, R. M., Direct molecular analysis of whole-body animal tissue sections by imaging MALDI mass spectrometry. *Analytical chemistry* **2006,** *78* (18), 6448-56.
129. Patterson, K. B.; Prince, H. A.; Kraft, E.; Jenkins, A. J.; Shaheen, N. J.; Rooney, J. F.; Cohen, M. S.; Kashuba, A. D., Penetration of tenofovir and emtricitabine in mucosal tissues: implications for prevention of HIV-1 transmission. *Sci Transl Med* **2011,** *3* (112), 112re4.
130. Prathipati, P. K.; Mandal, S.; Destache, C. J., Simultaneous quantification of tenofovir, emtricitabine, rilpivirine, elvitegravir and dolutegravir in mouse biological matrices by LC-MS/MS and its application to a pharmacokinetic study. *J Pharm Biomed Anal* **2016,** *129*, 473-481.
131. Gautam, N.; Roy, U.; Balkundi, S.; Puligujja, P.; Guo, D.; Smith, N.; Liu, X. M.; Lamberty, B.; Morsey, B.; Fox, H. S.; McMillan, J.; Gendelman, H. E.; Alnouti, Y., Preclinical pharmacokinetics and tissue distribution of long-acting nanoformulated antiretroviral therapy. *Antimicrob Agents Chemother* **2013,** *57* (7), 3110-20.
132. Kompauer, M.; Heiles, S.; Spengler, B., Atmospheric pressure MALDI mass spectrometry imaging of tissues and cells at 1.4-mum lateral resolution. *Nat Methods* **2017,** *14* (1), 90-96.
133. Kawashima, M.; Iwamoto, N.; Kawaguchi-Sakita, N.; Sugimoto, M.; Ueno, T.; Mikami, Y.; Terasawa, K.; Sato, T. A.; Tanaka, K.; Shimizu, K.; Toi, M., High-resolution imaging mass spectrometry reveals detailed spatial distribution of phosphatidylinositols in human breast cancer. *Cancer Sci* **2013,** *104* (10), 1372-9.
134. Zavalin, A.; Todd, E. M.; Rawhouser, P. D.; Yang, J.; Norris, J. L.; Caprioli, R. M., Direct imaging of single cells and tissue at sub-cellular spatial resolution using transmission geometry MALDI MS. *J Mass Spectrom* **2012,** *47* (11), 1473-81.
135. Vallianatou, T.; Strittmatter, N.; Nilsson, A.; Shariatgorji, M.; Hamm, G.; Pereira, M.; Kallback, P.; Svenningsson, P.; Karlgren, M.; Goodwin, R. J. A.; Andren, P. E., A mass spectrometry imaging approach for investigating how drug-drug interactions influence drug blood-brain barrier permeability. *Neuroimage* **2018,** *172*, 808-816.
136. Nilsson, A.; Peric, A.; Strimfors, M.; Goodwin, R. J. A.; Hayes, M. A.; Andren, P. E.; Hilgendorf, C., Mass Spectrometry Imaging proves differential absorption profiles of well-characterised permeability markers along the crypt-villus axis. *Sci Rep* **2017,** *7* (1), 6352.
137. McEwen, A. B.; Henson, C. M.; Wood, S. G., Quantitative whole-body autoradiography, LC–MS/MS and MALDI for drug-distribution studies in biological samples: the ultimate matrix trilogy. *Bioanalysis* **2014,** *6* (3), 377-391.
138. Wang, L.; He, K.; Maxwell, B.; Grossman, S. J.; Tremaine, L. M.; Humphreys, W. G.; Zhang, D., Tissue Distribution and Elimination of [^{14}C]Apixaban in Rats. *Drug Metabolism and Disposition* **2011,** *39* (2), 256.

139. Panee, J., Potential Medicinal Application and Toxicity Evaluation of Extracts from Bamboo Plants. *J Med Plant Res* **2015,** *9* (23), 681-692.
140. De Campeneere, D.; Baurain, R.; Slachmuylder-Otte, C.; Trouet, A., Immunological evaluation of blood contamination in tissue distribution studies. *Pharmacol Res* **1989,** *21* (1), 19-26.
141. Neubert, H.; Fountain, S.; King, L.; Clark, T.; Weng, Y.; O'Hara, D. M.; Li, W.; Leung, S.; Ray, C.; Palandra, J.; Ocana, M. F.; Chen, J.; Ji, C.; Wang, M.; Long, K.; Gorovits, B.; Fluhler, E., Tissue bioanalysis of biotherapeutics and drug targets to support PK/PD. *Bioanalysis* **2012,** *4* (21), 2589-604.
142. Waterer, G. W.; Wunderink, R. G., Increasing threat of Gram-negative bacteria. *Critical care medicine* **2001,** *29* (4), N75-N81.
143. Hartzell, J. D.; Neff, R.; Ake, J.; Howard, R.; Olson, S.; Paolino, K.; Vishnepolsky, M.; Weintrob, A.; Wortmann, G., Nephrotoxicity associated with intravenous colistin (colistimethate sodium) treatment at a tertiary care medical center. *Clinical infectious diseases* **2009,** *48* (12), 1724-1728.
144. Landman, D.; Georgescu, C.; Martin, D. A.; Quale, J., Polymyxins revisited. *Clinical microbiology reviews* **2008,** *21* (3), 449-465.
145. Bellomo, R.; Ronco, C.; Kellum, J. A.; Mehta, R. L.; Palevsky, P., Acute renal failure–definition, outcome measures, animal models, fluid therapy and information technology needs: the Second International Consensus Conference of the Acute Dialysis Quality Initiative (ADQI) Group. *Critical care* **2004,** *8* (4), R204.
146. Keirstead, N. D.; Wagoner, M. P.; Bentley, P.; Blais, M.; Brown, C.; Cheatham, L.; Ciaccio, P.; Dragan, Y.; Ferguson, D.; Fikes, J.; Galvin, M.; Gupta, A.; Hale, M.; Johnson, N.; Luo, W.; McGrath, F.; Pietras, M.; Price, S.; Sathe, A. G.; Sasaki, J. C.; Snow, D.; Walsky, R. L.; Kern, G., Early Prediction of Polymyxin-Induced Nephrotoxicity With Next-Generation Urinary Kidney Injury Biomarkers. *Toxicological Sciences* **2013,** *137* (2), 278-291.
147. Fuchs, T. C.; Frick, K.; Emde, B.; Czasch, S.; Landenberg, F. v.; Hewitt, P., Evaluation of Novel Acute Urinary Rat Kidney Toxicity Biomarker for Subacute Toxicity Studies in Preclinical Trials. *Toxicologic Pathology* **2012,** *40* (7), 1031-1048.
148. Ichimura, T.; Asseldonk, E. J. P. v.; Humphreys, B. D.; Gunaratnam, L.; Duffield, J. S.; Bonventre, J. V., Kidney injury molecule–1 is a phosphatidylserine receptor that confers a phagocytic phenotype on epithelial cells. *The Journal of Clinical Investigation* **2008,** *118* (5), 1657-1668.
149. Pinches, M. D.; Betts, C. J.; Bickerton, S. J.; Beattie, L.; Burdett, L. D.; Thomas, H. T.; Derbyshire, N. A.; Moores, M.; Price, S. A., Evaluation of Novel Urinary Renal Biomarkers: Biological Variation and Reference Change Values. *Toxicologic Pathology* **2012,** *40* (3), 541-549.
150. Velkov, T.; Thompson, P. E.; Nation, R. L.; Li, J., Structure− activity relationships of polymyxin antibiotics. *Journal of medicinal chemistry* **2009,** *53* (5), 1898-1916.
151. Vaara, M., Novel derivatives of polymyxins. *Journal of Antimicrobial Chemotherapy* **2013,** *68* (6), 1213-1219.
152. Brown, P.; Dawson, M. J., Development of new polymyxin derivatives for multi-drug resistant Gram-negative infections. *The Journal of antibiotics* **2017,** *70* (4), 386.
153. Vaara, M.; Vaara, T.; Tyrrell, J. M., Structure–activity studies on polymyxin derivatives carrying three positive charges only reveal a new class of compounds with strong antibacterial activity. *Peptides* **2017,** *91*, 8-12.
154. Brown, P.; Abbott, E.; Abdulle, O.; Boakes, S.; Coleman, S.; Divall, N.; Duperchy, E.; Moss, S.; Rivers, D.; Simonovic, M.; Singh, J.; Stanway, S.; Wilson, A.; Dawson, M. J., Design of Next Generation Polymyxins with Lower Toxicity: The Discovery of SPR206. *ACS Infect Dis* **2019,** *5* (10), 1645-1656.
155. Danner, R. L.; Joiner, K. A.; Rubin, M.; Patterson, W. H.; Johnson, N.; Ayers, K. M.; Parrillo, J. E., Purification, toxicity, and antiendotoxin activity of polymyxin B nonapeptide. *Antimicrobial Agents and Chemotherapy* **1989,** *33* (9), 1428-1434.
156. Vaara, M.; Siikanen, O.; Apajalahti, J.; Fox, J.; Frimodt-Møller, N.; He, H.; Poudyal, A.; Li, J.; Nation, R. L.; Vaara, T., A novel polymyxin derivative that lacks the fatty acid tail

and carries only three positive charges has strong synergism with agents excluded by the intact outer membrane. *Antimicrobial agents and chemotherapy* **2010,** *54* (8), 3341-3346.
157. Vaara, M., Polymyxin derivatives that sensitize Gram-negative bacteria to other antibiotics. *Molecules* **2019,** *24* (2), 249.
158. Yun, B.; Azad, M. A. K.; Wang, J.; Nation, R. L.; Thompson, P. E.; Roberts, K. D.; Velkov, T.; Li, J., Imaging the distribution of polymyxins in the kidney. *Journal of Antimicrobial Chemotherapy* **2014,** *70* (3), 827-829.
159. Yun, B.; Azad, M. A. K.; Nowell, C. J.; Nation, R. L.; Thompson, P. E.; Roberts, K. D.; Velkov, T.; Li, J., Cellular Uptake and Localization of Polymyxins in Renal Tubular Cells Using Rationally Designed Fluorescent Probes. *Antimicrobial Agents and Chemotherapy* **2015,** *59* (12), 7489.
160. Dai, C.; Li, J.; Tang, S.; Li, J.; Xiao, X., Colistin-Induced Nephrotoxicity in Mice Involves the Mitochondrial, Death Receptor, and Endoplasmic Reticulum Pathways. *Antimicrobial Agents and Chemotherapy* **2014,** *58* (7), 4075.
161. Robichaud, G.; Garrard, K. P.; Barry, J. A.; Muddiman, D. C., MSiReader: an open-source interface to view and analyze high resolving power MS imaging files on Matlab platform. *J Am Soc Mass Spectrom* **2013,** *24* (5), 718-21.
162. Schroit, A. J.; Gallily, R., Macrophage fatty acid composition and phagocytosis: effect of unsaturation on cellular phagocytic activity. *Immunology* **1979,** *36* (2), 199.
163. Ali, M.; Heyob, K.; Rogers, L. K., DHA Suppresses Primary Macrophage Inflammatory Responses via Notch 1/ Jagged 1 Signaling. *Scientific Reports* **2016,** *6* (1), 22276.
164. Lee, J. Y.; Plakidas, A.; Lee, W. H.; Heikkinen, A.; Chanmugam, P.; Bray, G.; Hwang, D. H., Differential modulation of Toll-like receptors by fatty acids: preferential inhibition by n-3 polyunsaturated fatty acids. *Journal of Lipid Research* **2003,** *44* (3), 479-486.
165. Schmitz, G.; Ecker, J., The opposing effects of n-3 and n-6 fatty acids. *Prog Lipid Res* **2008,** *47* (2), 147-55.
166. Zagryagskaya, A. N.; Aleksandrov, D. A.; Pushkareva, M. A.; Galkina, S. I.; Grishina, Z. V.; Sud'ina, G. F., Biosynthesis of leukotriene B4 in human polymorphonuclear leukocytes: regulation by cholesterol and other lipids. *Journal of Immunotoxicology* **2008,** *5* (4), 347-352.
167. Hashidate-Yoshida, T.; Harayama, T.; Hishikawa, D.; Morimoto, R.; Hamano, F.; Tokuoka, S. M.; Eto, M.; Tamura-Nakano, M.; Yanobu-Takanashi, R.; Mukumoto, Y.; Kiyonari, H.; Okamura, T.; Kita, Y.; Shindou, H.; Shimizu, T., Fatty acid remodeling by LPCAT3 enriches arachidonate in phospholipid membranes and regulates triglyceride transport. *Elife* **2015,** *4*.
168. Tengstrand, E. A.; Miwa, G. T.; Hsieh, F. Y., Bis(monoacylglycerol)phosphate as a non-invasive biomarker to monitor the onset and time-course of phospholipidosis with drug-induced toxicities. *Expert Opinion on Drug Metabolism & Toxicology* **2010,** *6* (5), 555-570.
169. Frederick, T. E.; Chebukati, J. N.; Mair, C. E.; Goff, P. C.; Fanucci, G. E., Bis(monoacylglycero)phosphate Forms Stable Small Lamellar Vesicle Structures: Insights into Vesicular Body Formation in Endosomes. *Biophysical Journal* **2009,** *96* (5), 1847-1855.
170. Maunsbach, A. B.; Tripathi, S.; Boulpaep, E. L., Ultrastructural changes in isolated perfused proximal tubules during osmotic water flow. *American Journal of Physiology-Renal Physiology* **1987,** *253* (6), F1091-F1104.
171. Tripathi, S.; Boulpaep, E. L.; Maunsbach, A. B., Isolated perfused Ambystoma proximal tubule: hydrodynamics modulates ultrastructure. *American Journal of Physiology-Renal Physiology* **1987,** *252* (6), F1129-F1147.
172. Manchandani, P.; Zhou, J.; Babic, J. T.; Ledesma, K. R.; Truong, L. D.; Tam, V. H., Role of Renal Drug Exposure in Polymyxin B-Induced Nephrotoxicity. *Antimicrobial agents and chemotherapy* **2017,** *61* (4), e02391-16.

Appendix

Table of content

Table of Figures

Table of Tables

Appendix 1: Supplementary information to Chapter 2

Table A1.1: Annotation details for the heatmap features

Annotation	Adduct	Measured *m/z*	Theoretical *m/z*	Error [ppm]	Molecular formula	MS/MS
Serine	[M-H2O-H]-	86.024	86.025	5	$C_3H_7NO_3$	
Leucine	[M+Cl]-	166.064	166.064	0	$C_6H_{13}NO_2$	
Hydroxyleucine	[M-H]-	146.082	146.082	0	$C_6H_{13}NO_3$	
Methionine	[M-H]-	148.044	148.044	1	$C_5H_{11}NO_2S$	
Acetyl-valine	[M-H]-	158.083	158.082	4	$C_7H_{13}NO_3$	
Phenylalanine	[M-H]-	164.072	164.072	0	$C_9H_{11}NO_2$	
Asparagine	[M+Cl]-	167.024	167.023	4	$C_4H_8N_2O_3$	
N-Acethylhistidine	[M+Na]+	220.070	220.069	2	$C_8H_{11}N_3O_3$	
GABA	[M-H]-	102.056	102.056	2	$C_4H_9NO_2$	
Glutathione	[M-H]-	306.077	306.077	0	$C_{10}H_{17}N_3O_6S$	
Hypoxanthine	[M+K]+	175.002	175.002	1	$C_5H_4N_4O$	
Xanthine	[M-H]-	151.026	151.026	2	$C_5H_4N_4O_2$	
Dimetyluric acid	[M-H]-	195.052	195.052	0	$C_7H_8N_4O_3$	
Dimethylxanthine	[M+Cl]-	215.034	215.034	0	$C_7H_8N_4O_2$	
Methylguanidine	[M-H2O-H]-	146.047	146.047	1	$C_6H_7N_5O$	
Uridine	[M-H]-	243.063	243.062	3	$C_9H_{12}N_2O_6$	
Inosine	[M-H]-	267.072	267.073	5	$C_{10}H_{12}N_4O_5$	
Methyluridine	[M+Cl]-	293.055	293.055	0	$C_{10}H_{14}N_2O_6$	
UMP	[M-H]-	323.029	323.029	2	$C_9H_{13}N_2O_9P$	
AMP	[M-H]-	346.056	346.056	0	$C_{10}H_{14}N_5O_7P$	
FA(16:2)	[M-H]-	251.203	251.202	5	$C_{16}H_{28}O_2$	
FA(18:3)	[M-H]-	277.216	277.217	5	$C_{18}H_{30}O_2$	
FA(20:5)	[M-H]-	301.217	301.217	0	$C_{20}H_{30}O_2$	
FA(20:4)	[M-H]-	303.233	303.233	0	$C_{20}H_{32}O_2$	
FA(22:6)	[M-H]-	327.235	327.233	5	$C_{22}H_{32}O_2$	
FA(22:5)	[M-H]-	329.250	329.249	5	$C_{22}H_{34}O_2$	
FA(22:4)	[M-H]-	331.266	331.264	4	$C_{22}H_{36}O_2$	
FA(12:1(O))	[M+Na]+	235.130	235.130	1	$C_{12}H_{20}O_3$	
FA16:2(OH))	[M-H]-	267.196	267.197	2	$C_{16}H_{28}O_3$	
FA(18:3(OH))	[M-H]-	293.213	293.212	3	$C_{18}H_{30}O_3$	
FA(18:2(OH))	[M-H]-	295.229	295.228	3	$C_{18}H_{32}O_3$	
FA(18:1(OH))	[M-H]-	297.244	297.244	3	$C_{18}H_{34}O_3$	
FA(18:3(OH3)	[M-H]-	325.203	325.202	4	$C_{18}H_{30}O_5$	
FA(18:1(OH3))	[M-H]-	329.235	329.233	4	$C_{18}H_{34}O_5$	
FA(20:2(OH))	[M-H]-	323.258	323.259	5	$C_{20}H_{36}O_3$	
FA(20:4(OH2))	[M-H]-	335.223	335.223	2	$C_{20}H_{32}O_4$	
FA(20:3(OH2))	[M-H]-	337.239	337.238	2	$C_{20}H_{34}O_4$	
FA(20:2(OH2))	[M-H]-	339.255	339.254	2	$C_{20}H_{36}O_4$	
FA(20:5(OH3))	[M+Na]+	373.197	373.198	2	$C_{20}H_{30}O_5$	
FA(20:4(OH3))	[M+Na]+	375.213	375.214	1	$C_{20}H_{32}O_5$	
FA(22:6(OH))	[M-H]-	343.228	343.228	0	$C_{22}H_{32}O_3$	
FA(22:5(OH))	[M-H]-	345.243	345.244	0	$C_{22}H_{34}O_3$	
FA(22:4(OH))	[M-H]-	347.259	347.259	0	$C_{22}H_{36}O_3$	
FA(22:5(OH2))	[M-H]-	361.241	361.238	6	$C_{22}H_{34}O_4$	
Phosphate	[M-H]-	96.970	96.970	3	H_3PO_4	
KCl	[M+Cl]-	108.902	108.903	5	KCl	
KCl	[M+K]+	112.896	112.895	5	KCl	
Lactate	[M-H]-	89.025	89.024	2	$C_3H_6O_3$	
Hydroxymethylbutyric acid	[M-H]-	117.055	117.056	4	$C_5H_{10}O_3$	
Hydroxynonenoic acid	[M+Na]+	195.100	195.099	5	$C_9H_{16}O_3$	
Mevalonolactone	[M-H]-	129.056	129.056	2	$C_6H_{10}O_3$	
Citrate	[M-H2O-H]-	173.008	173.009	4	$C_6H_8O_7$	
Ascorbic acid	[M-H]-	175.024	175.025	5	$C_6H_8O_6$	
Ascorbic acid sulfate	[M-H]-	254.983	254.982	3	$C_6H_8O_9S$	
Pantothenic acid	[M-H]-	218.102	218.103	6	$C_9H_{17}NO_5$	
Taurine	[M-H]-	124.007	124.007	1	$C_2H_7NO_3S$	
Choline	[M+H]+	104.107	104.107	3	$C_5H_{13}NO$	
Phosphocholine	[M+H]+	184.074	184.073	2	$C_5H_{14}NO_4P$	
Betaine	[M+H]+	118.087	118.086	4	$C_5H_{11}NO_2$	

Creatine	[M+H]+	132.077	132.077	1	$C_4H_9N_3O_2$	
Carnitine	[M+K]+	200.069	200.068	1	$C_7H_{15}NO_3$	
Acethylcarnitine	[M+H]+	204.123	204.123	0	$C_9H_{17}NO_4$	
Butyryl-carnitine	[M+H]+	232.154	232.154	2	$C_{11}H_{21}NO_4$	
Deoxyglucose	[M+Cl]-	199.037	199.038	4	$C_6H_{12}O_5$	
Glucosamine	[M+Cl]-	214.048	214.049	5	$C_6H_{13}NO_5$	
Glucose	[M+K]+	219.026	219.027	2	$C_6H_{12}O_6$	
Glucose-phosphate	[M-H]-	259.021	259.022	4	$C_6H_{13}O_9P$	
LPE(18:0)	[M+Na]+	504.305	504.306	1	$C_{23}H_{48}NO_7P$	
LPE(20:1)	[M-H]-	506.325	506.325	1	$C_{25}H_{60}NO_7P$	
LPE(20:0)	[M-H]-	508.340	508.341	1	$C_{25}H_{62}NO_7P$	
PE(36:2)	[M+K]+	782.508	782.509	1	$C_{41}H_{78}NO_8P$	Yes
PE(36:3)	[M-H]-	740.525	740.524	2	$C_{41}H_{76}NO_8P$	Yes
PE(36:4)	[M+K]+	778.476	778.478	2	$C_{41}H_{74}NO_8P$	Yes
PE(38:6)	[M-H]-	762.511	762.508	4	$C_{43}H_{74}NO_8P$	Yes
PE(38:5)	[M-H]-	764.526	764.524	4	$C_{43}H_{76}NO_8P$	Yes
PE(38:4)	[M-H]-	766.542	766.539	3	$C_{43}H_{78}NO_8P$	Yes
PE(38:2)	[M+K]+	810.539	810.540	2	$C_{43}H_{82}NO_8P$	
PE(40:4)	[M+K]+	834.539	834.540	2	$C_{45}H_{82}NO_8P$	
PE(34:0(CH2))	[M+Na]+	754.533	754.535	2	$C_{40}H_{78}NO_8P$	
PE(44:10(OH))	[M-H]-	854.536	854.534	2	$C_{49}H_{78}NO_9P$	
PE(44:9(OH))	[M-H]-	856.551	856.550	2	$C_{49}H_{80}NO_9P$	
LPC(16:1)	[M+Na]+	516.305	516.306	1	$C_{24}H_{48}NO_7P$	
LPC(16:0)	[M+Na]+	518.320	518.321	3	$C_{24}H_{50}NO_7P$	
LPC(18:2)	[M+Na]+	542.320	542.321	3	$C_{26}H_{50}NO_7P$	
LPC(18:1)	[M+Na]+	544.336	544.337	2	$C_{26}H_{52}NO_7P$	
LPC(18:0)	[M+Na]+	546.352	546.352	1	$C_{26}H_{54}NO_7P$	
LPC(20:4)	[M+K]+	582.294	582.295	1	$C_{28}H_{50}NO_7P$	
PC(34:2)	[M+H]+	758.568	758.569	1	$C_{42}H_{80}NO_8P$	Yes
PC(34:4)	[M+K]+	792.491	792.493	3	$C_{42}H_{76}NO_8P$	Yes
PC(34:2)	[M+K]+	796.523	796.525	2	$C_{42}H_{80}NO_8P$	Yes
PC(34:1)	[M+K]+	798.538	798.540	3	$C_{42}H_{82}NO_8P$	Yes
PC(36:2)	[M+K]+	824.554	824.557	3	$C_{44}H_{84}NO_8P$	Yes
PC(38:4)	[M+K]+	848.555	848.556	1	$C_{46}H_{84}NO_8P$	Yes
PC(40:8)	[M+K]+	868.527	868.525	3	$C_{48}H_{80}NO_8P$	Yes
LPC(18:2(OH))	[M+Na]+	558.315	558.316	3	$C_{26}H_{50}NO_8P$	
LPC(20:4(OH)	[M+Na]+	582.314	582.316	3	$C_{28}H_{50}NO_8P$	
PC(25:0(COOH))	[M+Na]+	688.415	688.415	1	$C_{33}H_{64}NO_{10}P$	
PC(34:2(OH))	[M+Na]+	796.544	796.546	3	$C_{42}H_{80}NO_9P$	Yes
PC(36:4(OH))	[M+Na]+	820.544	820.546	2	$C_{44}H_{80}NO_9P$	Yes
PC(36:3(OH))	[M+Na]+	822.560	822.561	2	$C_{44}H_{82}NO_9P$	Yes
PC(36:2(OH))	[M+Na]+	824.575	824.577	3	$C_{44}H_{84}NO_9P$	Yes
PC(38:4(OH))	[M+Na]+	848.576	848.577	1	$C_{46}H_{84}NO_9P$	
LPS(20:0)	[M-H]-	552.332	552.331	1	$C_{26}H_{52}NO_9P$	
PS(36:4)	[M-H]-	782.500	782.498	3	$C_{42}H_{74}NO_{10}P$	Yes
PS(36:2)	[M-H]-	786.532	786.529	3	$C_{42}H_{76}NO_{10}P$	Yes
PS(38:4)	[M-H]-	810.533	810.529	5	$C_{44}H_{78}NO_{10}P$	Yes
PS(40:6)	[M-H]-	834.531	834.529	2	$C_{46}H_{78}NO_{10}P$	Yes
PS(34:0)-Me	[M-H]-	774.531	774.529	2	$C_{41}H_{78}NO_{10}P$	Yes
PS(38:4)-Me	[M-H]-	822.534	822.529	5	$C_{45}H_{78}NO_{10}P$	Yes
LPI((16:0) $[M-H]^-$	[M-H]-	571.288	571.289	1	$C_{25}H_{49}O_{12}P$	
LPI(18:1) $[M-H]^-$	[M-H]-	597.305	597.305	1	$C_{27}H_{51}O_{12}P$	
LPI(18:0) $[M-H]^-$	[M-H]-	599.321	599.320	1	$C_{27}H_{53}O_{12}P$	
PI(36:4) $[M-H]^-$	[M-H]-	857.522	857.519	4	$C_{45}H_{79}O_{13}P$	Yes
PI(38:4) $[M-H]^-$	[M-H]-	885.555	885.550	6	$C_{47}H_{83}O_{13}P$	Yes
Sphingosine (d16:1-P)	[M-H2O-H]-	332.198	332.200	5	$C_{16}H_{34}NO_5P$	
Ceramide (d42:1)	[M+K]+	688.599	688.600	2	$C_{42}H_{83}NO_3$	
SM(d34:1)	[M+K]+	741.529	741.532	4	$C_{39}H_{79}N_2O_6P$	
Cortisol	[M+Cl]-	397.177	397.179	5	$C_{21}H_{30}O_5$	
Dihydrocortisol	[M+Cl]-	399.193	399.194	5	$C_{21}H_{32}O_5$	
Cholesterol sulfate	[M-H]-	465.305	465.304	1	$C_{27}H_{46}O_4S$	
Taurodeoxycholic acid	[M-H]-	498.290	498.289	0	$C_{26}H_{45}NO_6S$	
Taurocholic acid	[M-H]-	514.283	514.284	3	$C_{26}H_{45}NO_7S$	
Hydroxycholecalciferol	[M+Na]+	423.322	423.323	3	$C_{27}H_{44}O_2$	
CE(20:4)	[M+K]+	711.545	711.547	3	$C_{47}H_{76}O_2$	

MG(18:1)	[M+K]+	395.255	395.255	0	$C_{21}H_{40}O_4$
MG(18:0)	[M+K]+	397.270	397.271	2	$C_{21}H_{42}O_4$
DG(32:0)	[M+K]+	607.472	607.469	4	$C_{35}H_{68}O_5$
DG(34:2)	[M+K]+	631.468	631.469	3	$C_{37}H_{68}O_5$
DG(34:1)	[M+K]+	633.485	633.485	0	$C_{37}H_{70}O_5$
DG(36:4)	[M+K]+	655.467	655.469	3	$C_{39}H_{68}O_5$
DG(36:3)	[M+K]+	657.484	657.485	2	$C_{39}H_{70}O_5$
DG(38:4)	[M+K]+	683.499	683.501	2	$C_{41}H_{72}O_5$

Table A1.2: Statistical information for annotated heatmap features

Annotation	Polarity	Median Abundances [*a.u.*]*					Statistical significance P**			
		Fresh-Frozen Kidney	Formal in-Fixed Kidney	Fresh-Frozen Liver	Formal in-Fixed Liver	FFPE liver	Fresh-Frozen v Formal in-Fixed Kidney	Fresh-Frozen v Formal in-Fixed Liver	Fresh-Frozen v FFPE Liver	Formal in-Fixed v FFPE liver
Serine	-	2968	0.000	1445	0.000	0.000	<0.001	<0.001	<0.001	<0.001
Leucine	-	2192	0.000	5368	0.000	0.000	<0.001	<0.001	<0.001	<0.001
Hydroxy-leucine	-	4940	0.000	0.000	0.000	18802	<0.001	<0.001	<0.001	<0.001
Methionine	-	4382	1697	0.000	2938	0.000	<0.001	<0.001	<0.001	<0.001
Acetyl-valine	-	5350	1974	1741	2938	71950	<0.001	<0.001	<0.001	<0.001
Phenylalanine	-	2689	0.000	2528	0.000	0.000	<0.001	<0.001	<0.001	<0.001
Asparagine	-	8127	874.0	20272	0.000	1591	<0.001	<0.001	<0.001	<0.001
Acethyl-histidine	+	0.000	3347	0.000	1603	0.000	<0.001	<0.001	<0.001	<0.001
GABA	-	40195	0.000	3147	0.000	0.000	<0.001	<0.001	<0.001	<0.001
Glutathione	-	14495	0.000	33063	0.000	0.000	<0.001	<0.001	<0.001	ns
Hypoxanthine	+	5631	0.000	1447	0.000	0.000	<0.001	<0.001	<0.001	<0.001
Xanthine	-	86253	20129	42701	2938	0.000	<0.001	<0.001	<0.001	<0.001
Dimetyluric acid	-	38836	18278	232805	0.000	0.000	<0.001	<0.001	<0.001	<0.001
Dimethylxanthine	-	337022	26728	501221	0.000	0.000	<0.001	<0.001	<0.001	<0.001
Methyl-guanidine	-	427032	2636	27990	1741	2093	<0.001	<0.001	<0.001	<0.001
Uridine	-	15874	3755	5165	0.000	0.000	<0.001	<0.001	<0.001	<0.001
Inosine	-	33698	12791	13512	5736	0.000	<0.001	<0.001	<0.001	<0.001
Methyluridine	-	774.4	834.0	5075	1057	2463	<0.001	<0.001	<0.001	<0.001
UMP	-	8795	0.000	10529	0.000	0.000	<0.001	<0.001	<0.001	ns
AMP	-	59441	0.000	14343	0.000	0.000	<0.001	<0.001	<0.001	ns
FA(16:2)	-	7151	4578	6194	3894	0.000	<0.001	<0.001	<0.001	<0.001
FA(18:3)	-	45320	42495	162445	66291	0.000	<0.001	<0.001	<0.001	<0.001
FA(20:5)	-	29111	34088	109682	44199	0.000	<0.001	<0.001	<0.001	<0.001
FA(20:4)	-	422356	1000000	458781	1245220	2480	<0.001	<0.001	<0.001	<0.001
FA(22:6)	-	109054	65832	188029	139123	0.000	<0.001	<0.001	<0.001	<0.001
FA(22:5)	-	47151	27765	131519	54772	0.000	<0.001	<0.001	<0.001	<0.001
FA(22:4)	-	27475	37325	80100	31703	0.000	<0.001	<0.001	<0.001	<0.001
FA(12:1(O))	+	0.000	7757	0.000	18471	281386	<0.001	<0.001	<0.001	<0.001
FA16:2(OH))	-	1575	12791	6185	5736	1056	<0.001	<0.001	<0.001	<0.001
FA(18:3(OH))	-	9043	197702	116059	206160	0.000	<0.001	<0.001	<0.001	<0.001
FA(18:2(OH))	-	11335	283032	87898	309557	1798	<0.001	<0.001	<0.001	<0.001
FA(18:1(OH))	-	8015	174157	26568	162739	2370	<0.001	<0.001	<0.001	<0.001
FA(18:3(OH3)	-	1270	10004	7600	10763	9325	<0.001	<0.001	<0.001	<0.001
FA(18:1(OH3))	-	2738	54362	1776	35624	2481	<0.001	<0.001	0.0339	<0.001
FA(20:2(OH))	-	0.000	8612	2299	12265	0.000	<0.001	<0.001	<0.001	<0.001
FA(20:4(OH2))	-	2554	67268	6589	63020	0.000	<0.001	<0.001	<0.001	<0.001
FA(20:3(OH2))	-	0.000	44502	3647	43371	1978	<0.001	<0.001	<0.001	<0.001
FA(20:2(OH2))	-	0.000	12600	2319	11590	0.000	<0.001	<0.001	<0.001	<0.001
FA(20:5(OH3))	+	0.000	5263	0.000	5122	977.9	<0.001	<0.001	<0.001	<0.001
FA(20:4(OH3))	+	0.000	12986	0.000	13915	1824	<0.001	<0.001	<0.001	<0.001
FA(22:6(OH))	-	1989	16678	9480	22441	9165	<0.001	<0.001	ns	<0.001
FA(22:5(OH))	-	798.8	7505	6577	10046	2270	<0.001	<0.001	<0.001	<0.001
FA(22:4(OH))	-	0.000	4272	2519	4190	0.000	<0.001	<0.001	<0.001	<0.001
FA(22:5(OH2))	-	0.000	7833	3964	8265	0.000	<0.001	<0.001	<0.001	<0.001
Phosphate	-	132675	318868	48681	111410	3935	<0.001	<0.001	<0.001	<0.001
KCL	-	10452	0.000	4815	0.000	0.000	<0.001	<0.001	<0.001	ns
KCl	+	8183	0.000	6827	0.000	0.000	<0.001	<0.001	<0.001	ns
Lactate	-	693776	67077	1445	0.000	101149	<0.001	<0.001	<0.001	<0.001
Hydroxymethyl butyric acid	-	4450	997.3	1549	9037	198339	<0.001	<0.001	<0.001	<0.001

Hydroxy-nonenoic acid	+	38836	18278	232805	0.000	0.000	<0.001	<0.001	<0.001	<0.001
Mevalono-lactone	-	8838	5717	6452	601.1	454411	<0.001	<0.001	<0.001	<0.001
Citrate	-	38616	0.000	24215	0.000	2633	<0.001	<0.001	<0.001	<0.001
Ascorbic acid	-	279919	0.000	181887	0.000	0.000	<0.001	<0.001	<0.001	<0.001
Ascorbic acid sulfate	-	22250	0.000	13496	366720	0.000	<0.001	<0.001	<0.001	<0.001
Pantothenic acid	-	87613	1536	4556	0.000	0.000	<0.001	<0.001	<0.001	<0.001
Taurine	-	337618	849.1	24886	601.1	1018	<0.001	<0.001	<0.001	<0.001
Choline	+	761457	230829	259560	239633	37457	<0.001	<0.001	<0.001	<0.001
Phospho-choline	+	5767	2293	3939	0.000	0.000	<0.001	<0.001	<0.001	<0.001
Betaine	+	95027	34383	162982	18829	0.000	<0.001	<0.001	<0.001	<0.001
Creatine	+	4120	0.000	0.000	0.000	0.000	<0.001	<0.001	<0.001	ns
Carnitine	+	12371	0.000	5185	0.000	0.000	<0.001	<0.001	<0.001	<0.001
Acethyl-carnitine	+	28411	1964	26494	0.000	0.000	<0.001	<0.001	<0.001	<0.001
Butyryl-carnitine	+	4274	0.000	4620	0.000	0.000	<0.001	<0.001	<0.001	<0.001
Deoxyglucose	-	38836	0.000	1833	0.000	0.000	<0.001	<0.001	<0.001	<0.001
Glucosamine	-	39800	521.0	85146	0.000	0.000	<0.001	<0.001	<0.001	<0.001
Glucose	-	18691	3195	45633	1858	795.3	<0.001	<0.001	<0.001	<0.001
Glucose-phosphate	-	22250	1201	12719	366720	0.000	<0.001	<0.001	<0.001	<0.001
LPE(18:0)	+	0.000	4565	0.000	0.000	0.000	<0.001	<0.001	ns	<0.001
LPE(20:1)	-	0.000	2036	0.000	2485	0.000	<0.001	<0.001	ns	<0.001
LPE(20:0)	-	0.000	10506	0.000	1116	0.000	<0.001	<0.001	<0.001	<0.001
PE(36:2)	+	4575	0.000	9697	0.000	0.000	<0.001	<0.001	<0.001	<0.001
PE(36:3)	-	0.000	0.000	2617	0.000	23232	<0.001	<0.001	<0.001	<0.001
PE(36:4)	+	11714	0.000	13751	0.000	0.000	<0.001	<0.001	<0.001	<0.001
PE(38:6)	-	2547	0.000	5732	0.000	0.000	<0.001	<0.001	<0.001	ns
PE(38:5)	-	6734	0.000	5851	0.000	0.000	<0.001	<0.001	<0.001	ns
PE(38:4)	-	24856	0.000	14418	0.000	0.000	<0.001	<0.001	<0.001	ns
PE(38:2)	+	2597	0.000	7455	266048	0.000	<0.001	<0.001	<0.001	<0.001
PE(40:4)	+	0.000	0.000	11536	0.000	0.000	ns	<0.001	<0.001	ns
PE(34:0(CH2))	+	15214	35923	9618	0.000	0.000	<0.001	<0.001	<0.001	<0.001
PE(44:10(OH))	-	0.000	2773	0.000	2330	0.000	<0.001	<0.001	<0.001	<0.001
PE(44:9(OH))	-	0.000	4656	0.000	2330	0.000	<0.001	<0.001	<0.001	<0.001
LPC(16:1)	+	0.000	4616	0.000	5377	0.000	<0.001	<0.001	<0.001	<0.001
LPC(16:0)	+	18841	4616	8692	5377	7647	<0.001	<0.001	<0.001	<0.001
LPC(18:2)	+	3861	35390	18841	4616	18841	<0.001	<0.001	<0.001	<0.001
LPC(18:1)	+	986.7	31479	986.7	31479	2664	<0.001	<0.001	<0.001	<0.001
LPC(18:0)	+	15366	187504	7399	151606	10504	<0.001	<0.001	<0.001	<0.001
LPC(20:4)	+	7049	0.000	39714	5527	0.000	<0.001	<0.001	<0.001	<0.001
PC(34:2)	+	0.000	0.000	12030	0.000	0.000	<0.001	<0.001	<0.001	<0.001
PC(34:4)	+	1910	0.000	7768	3482	0.000	<0.001	<0.001	<0.001	<0.001
PC(34:2)	+	200785	0.000	461328	0.000	0.000	<0.001	<0.001	<0.001	<0.001
PC(34:1)	+	191030	0.000	179388	0.000	1738	<0.001	<0.001	<0.001	<0.001
PC(36:2)	+	117896	0.000	254702	35028	0.000	<0.001	<0.001	<0.001	<0.001
PC(38:4)	+	264530	0.000	411929	0.000	0.000	<0.001	<0.001	<0.001	<0.001
PC(40:8)	+	0.000	9511	0.000	11310	0.000	<0.001	<0.001	<0.001	<0.001
LPC(18:2(OH))	+	0.000	3241	15031	4260	0.000	<0.001	<0.001	<0.001	<0.001
LPC(20:4(OH)	+	0.000	3657	47405	5527	0.000	<0.001	<0.001	<0.001	<0.001
PC(25:0(COOH))	+	4267	14295	0.000	36881	0.000	<0.001	<0.001	<0.001	<0.001
PC(34:2(OH))	+	0.000	17205	0.000	31331	1738	<0.001	<0.001	<0.001	<0.001
PC(36:4(OH))	+	439050	16217	0.000	26043	0.000	<0.001	<0.001	<0.001	<0.001
PC(36:3(OH))	+	0.000	14655	0.000	35028	0.000	<0.001	<0.001	<0.001	<0.001
PC(36:2(OH))	+	0.000	7235	0.000	21394	0.000	<0.001	<0.001	<0.001	<0.001
PC(38:4(OH))	+	0.000	8147	0.000	0.000	0.000	<0.001	<0.001	<0.001	<0.001
LPS(20:0)	-	0.000	2064	0.000	0.000	0.000	<0.001	<0.001	ns	<0.001
PS(36:4)	-	5036	0.000	1936	0.000	0.000	<0.001	<0.001	<0.001	<0.001
PS(36:2)	-	3698	0.000	2155	0.000	0.000	<0.001	<0.001	<0.001	<0.001

PS(38:4)	-	24856	0.000	14418	0.000	0.000	<0.001	<0.001	<0.001	<0.001
PS(40:6)	-	0.000	0.000	4317	550.8	0.000	ns	<0.001	<0.001	<0.001
PS(34:0)-Me	-	0.000	1082	0.000	2284	0.000	<0.001	<0.001	<0.001	<0.001
PS(38:4)-Me	-	0.000	2066	0.000	3126	0.000	<0.001	<0.001	<0.001	<0.001
LPI((16:0)	-	0.000	22761	0.000	10239	1850	<0.001	<0.001	<0.001	<0.001
LPI(18:1)	-	0.000	3894	0.000	10239	0.000	<0.001	<0.001	<0.001	<0.001
LPI(18:0)	-	1900	97652	1082	10239	23232	<0.001	<0.001	<0.001	<0.001
PI(36:4)	-	6808	3104	10013	3065	0.000	<0.001	<0.001	<0.001	<0.001
PI(38:4)	-	49327	25104	59462	18567	3092	<0.001	<0.001	<0.001	<0.001
Sphingosine (d16:1-P)	-	0.000	1990	0.000	1817	0.000	<0.001	<0.001	<0.001	<0.001
Ceramide (d42:1)	+	4371	0.000	0.000	36881	0.000	<0.001	<0.001	<0.001	<0.001
SM(d34:1)	+	65823	2373	18846	0.000	0.000	<0.001	<0.001	<0.001	<0.001
Cortisol	-	0.000	2121	0.000	1388	0.000	<0.001	<0.001	ns	<0.001
Dihydrocortisol	-	0.000	3560	0.000	3424	0.000	<0.001	<0.001	<0.001	<0.001
Cholesterol sulfate	-	46542	64394	4659	1920	0.000	<0.001	<0.001	<0.001	<0.001
Taurodeoxy-cholic acid	-	0.000	3605	3710	2485	0.000	<0.001	<0.001	<0.001	<0.001
Taurocholic acid	-	0.000	3417	10605	2233	0.000	<0.001	<0.001	<0.001	<0.001
Hydroxy-cholecalciferol	+	0.000	18286	0.000	14418	0.000	<0.001	<0.001	<0.001	<0.001
CE(20:4)	+	3893	0.000	2569	0.000	0.000	<0.001	<0.001	<0.001	ns
MG(18:1)	+	11166	0.000	69541	0.000	0.000	<0.001	<0.001	<0.001	<0.001
MG(18:0)	+	31310	3196	23976	2801	0.000	<0.001	<0.001	<0.001	<0.001
DG(32:0)	+	25206	3657	4254	0.000	0.000	<0.001	<0.001	<0.001	ns
DG(34:2)	+	25206	0.000	4254	0.000	0.000	<0.001	<0.001	<0.001	ns
DG(34:1)	+	13657	0.000	11047	0.000	0.000	<0.001	<0.001	<0.001	<0.001
DG(36:4)	+	6643	0.000	6227	0.000	0.000	<0.001	<0.001	<0.001	<0.001
DG(36:3)	+	5526	0.000	12291	0.000	0.000	<0.001	<0.001	<0.001	<0.001
DG(38:4)	+	6654	0.000	12291	0.000	0.000	<0.001	<0.001	<0.001	<0.001

* Median abundances determined from all pixel for each treatment group

** Statistical significance determined using Kruskal-Wallis followed by Dunn's test for multiple comparisons, $\alpha = 0.05$, n = Frozen Kidney 29587, Formalin-Fixed Kidney 22650, Frozen Liver 36374, Formalin-Fixed Liver 55233 and FFPE Liver 35543 considered pixel (Positive ion mode)/ Frozen Kidney 32300, Formalin-Fixed Kidney 25517, Frozen Liver 37022, Formalin-Fixed Liver 60958 and FFPE Liver 38569 considered pixel (Negative ion mode), ns = not significant

Appendix 2: Supplementary information to Chapter 4

Table A2.1: Statistical information for annotated heatmap features

Annotation	Adduct	Average measured *m/z*	Theoretical *m/z*	Error [ppm]	Molecular formula	Statistical significance (P)*		
						Control v UV-C 30 min	Control v UV-C 180 min	UV-C 30 min v UV-C 180 min
Threonate	$[M+K]^+$	175.000	175.000	0	$C_4H_8O_6$	<0.001	<0.001	<0.001
Acetylneuraminic acid	$[M-H]^-$	308.098	308.099	1	$C_{11}H_{19}NO_9$	<0.001	<0.001	<0.001
Acetylmuramic acid	$[M+CL]^-$	328.081	328.080	0	$C_{11}H_{19}NO_8$	<0.001	<0.001	<0.001
Phosphocholine	$[M+Na]^+$	206.055	206.055	0	$C_5H_{14}NO_4P$	<0.001	<0.001	<0.001
Glycerol-phosphate	$[M-H2O-H]^-$	152.995	152.996	5	$C_3H_9O_6P$	<0.001	<0.001	<0.001
Thiamine	$[M+H]^+$	265.111	265.112	2	$C_{12}H_{17}N_4OS$	<0.001	<0.001	<0.001
Cysteine	$[M-H]^-$	120.013	120.012	0	$C_3H_7NO_2S$	<0.001	<0.001	<0.001
Glutamine	$M-H]^-$	145.062	145.062	0	$C_5H_{10}N_2O_3$	<0.001	<0.001	Ns
Glutamate	$[M-H]^-$	146.046	146.046	0	$C_5H_9NO_4$	<0.001	<0.001	<0.001
Tryptophan	$[M-H]^-$	203.083	203.083	0	$C_{11}H_{12}N_2O_2$	<0.001	<0.001	Ns
Ethylguanidine	$[M+H]^+$	88.087	88.086923	4	$C3H9N_3$	<0.001	<0.001	<0.001
Pentose (Ribose)	$[M-H]^-$	149.045	149.046	5	$C_5H_{10}O_5$	<0.001	<0.001	<0.001
Hypoxanthine	$[M+Na]^+$	159.028	159.028	0	$C_5H_4N_4O$	<0.001	<0.001	<0.001
Adenine	$[M+H]^+$	136.062	136.062	0	$C_5H_5N_5$	<0.001	<0.001	<0.001
Thymine	$[M+CL]^-$	161.012	161.012	0	$C_5H_6N_2O_2$	<0.001	<0.001	<0.001
Cytosine	$[M+H]^+$	112.051	112.051	0	$C_4H_5N_3O$	<0.001	<0.001	<0.001
Guanine	$[M-H2O-H]^-$	132.032	132.032	0	$C_5H_5N_5O$	<0.001	<0.001	<0.001
Uracil	$[M-H]^-$	111.020	111.020	0	$C_4H_4N_2O_2$	<0.001	<0.001	<0.001
Adenosine	$[M+H]^+$	268.104	268.104	0	$C_{10}H_{13}N_5O_4$	<0.001	<0.001	<0.001
Methyladenosine	$[M-H]^-$	280.104	280.105	5	$C_{11}H_{15}N_5O_4$	<0.001	<0.001	<0.001
Guanosine	$[M+Na]^+$	306.081	306.081	0	$C_{10}H_{13}N_5O_5$	<0.001	<0.001	<0.001
Uridine	$[M-H]^-$	243.062	243.062	0	$C_9H_{12}N_2O_6$	<0.001	<0.001	<0.001
AMP	$[M-H]^-$	346.056	346.056	0	$C_{10}H_{14}N_5O_7P$	<0.001	<0.001	<0.001
GMP	$[M-H]^-$	362.051	362.051	1	$C_{10}H_{14}N_5O_8P$	<0.001	<0.001	<0.001
UMP	$[M-H]^-$	323.029	323.029	0	$C_9H_{13}N_2O_9P$	<0.001	<0.001	<0.001
IMP	$[M-H]^-$	347.039	347.040	3	$C_{10}H_{13}N_4O_8P$	<0.001	<0.001	<0.001
FA(20:4)	$[M-H2O-H]^-$	285.222	285.222	2	$C_{20}H_{32}O_2$	<0.001	<0.001	<0.001
FA(20:4)	$[M-H]^-$	303.233	303.233	0	$C_{20}H_{32}O_2$	<0.001	<0.001	<0.001
FA(24:5)	$[M-H]^-$	357.280	357.280	1	$C_{24}H_{38}O_2$	<0.001	<0.001	<0.001
FA(24:4)	$[M-H]^-$	359.295	359.296	1	$C_{24}H_{40}O_2$	<0.001	<0.001	<0.001
FA(22:2)	$[M-H]^-$	307.264	307.264	1	$C_{24}H_{44}O_2$	<0.001	<0.001	<0.001
FA(22:6)	$[M-H]^-$	327.232	327.233	2	$C_{22}H_{32}O_2$	<0.001	<0.001	<0.001
FA(22:5)	$[M-H]^-$	329.249	329.249	0	$C_{22}H_{34}O_2$	<0.001	<0.001	<0.001
FA(22:4)	$[M-H]^-$	331.265	331.264	1	$C_{22}H_{36}O_2$	<0.001	<0.001	<0.001
FA(18:3)-ethanolamide	$[M+K]^+$	362.245	362.245	0	$C_{20}H_{37}NO_2$	<0.001	<0.001	<0.001
FA(20:4)-ethanolamide	$[M+Na]^+$	370.271	370.271	1	$C_{22}H_{37}NO_2$	<0.001	<0.001	<0.001
FA(20:4)-ethanolamide	$[M+K]^+$	386.245	386.245	1	$C_{22}H_{37}NO_2$	<0.001	<0.001	<0.001
FA(18:2(OH))	$[M+K]^+$	335.198	335.198	1	$C_{18}H_{32}O_3$	<0.001	<0.001	<0.001
FA(18:2(OH))	$[M+CL]^-$	331.204	331.205	2	$C_{18}H_{32}O_3$	<0.001	<0.001	<0.001
FA(18:2(OH2)	$[M+K]^+$	351.193	351.193	1	$C_{18}H_{32}O_4$	<0.001	<0.001	<0.001
FA(18:2(OH)2)	$[M+CL]^-$	347.199	347.200	2	$C_{18}H_{32}O_4$	<0.001	<0.001	<0.001
FA(18:1(OH)2)	$[M+CL]^-$	349.214	349.216	4	$C_{18}H_{34}O_4$	<0.001	<0.001	<0.001
FA(18:0(OH)3)	$[M-H]^-$	331.248	331.249	2	$C_{18}H_{36}O_5$	<0.001	<0.001	<0.001
FA(18:2(OH)3)	$[M+CL]^-$	363.194	363.195	2	$C_{18}H_{32}O_5$	<0.001	<0.001	<0.001
FA(18:2(OH)3)	$[M+K]^+$	367.188	367.188	0	$C_{18}H_{32}O_5$	<0.001	<0.001	<0.001
FA(18:3(OH)3)	$[M+K]^+$	365.172	365.172	1	$C_{18}H_{30}O_5$	<0.001	<0.001	<0.001
FA(18:1(OH)4)	$[M-H]^-$	345.228	345.228	0	$C_{18}H_{34}O_6$	<0.001	<0.001	<0.001
FA(18:2(OH)4)	$[M-H]^-$	343.212	343.213	1	$C_{18}H_{32}O_6$	<0.001	<0.001	<0.001
FA(20:2(OH))	$[M-H2O-H]^-$	305.248	305.249	3	$C_{20}H_{36}O_3$	<0.001	<0.001	<0.001
FA(20:4(OH))	$[M-H]^-$	319.228	319.228	0	$C_{20}H_{32}O_3$	<0.001	<0.001	<0.001
FA(20:5(OH))	$[M-H]^-$	317.212	317.212	1	$C_{20}H_{30}O_3$	<0.001	<0.001	<0.001
FA(20:2(OH2)	$[M+K]^+$	379.225	379.225	0	$C_{20}H_{36}O_4$	<0.001	<0.001	<0.001
FA(20:0(O))	$[M-H]^-$	325.275	325.275	1	$C_{20}H_{38}O_3$	<0.001	<0.001	<0.001
FA(22:6(OH))	$[M+K]^+$	383.198	383.198	1	$C_{22}H_{32}O_3$	<0.001	<0.001	<0.001
FA(22:6(OH))	$[M-H2O-H]^-$	325.218	325.217	1	$C_{22}H_{32}O_3$	<0.001	<0.001	<0.001
FA(22:5(OH)2)	$[M-H2O-H]^-$	343.227	343.228	2	$C_{22}H_{34}O_4$	<0.001	<0.001	<0.001

FA(20:2(OH)3)	$[M-H]^-$	355.249	355.249	0	$C_{20}H_{36}O_5$	<0.001	<0.001	<0.001
FA(24:1(OH))	$[M+K]^+$	421.308	421.307	1	$C_{24}H_{46}O_3$	<0.001	<0.001	<0.001
LPA(18:3)	$[M-H]^-$	431.220	431.220	0	$C_{21}H_{37}O_7P$	<0.001	<0.001	<0.001
LPG(16:0)	$[M-H]^-$	483.272	483.273	1	$C_{22}H_{45}O_9P$	<0.001	<0.001	<0.001
LPG(18:0)	$[M-H]^-$	511.304	511.304	1	$C_{24}H_{49}O_9P$	<0.001	<0.001	<0.001
LPS(18:1)	$[M-H]^-$	522.284	522.284	0	$C_{24}H_{46}NO_9P$	<0.001	<0.001	<0.001
LPS(18:0)	$[M-H]^-$	524.300	524.299	1	$C_{24}H_{48}NO_9P$	<0.001	<0.001	<0.001
LPI(20:4)	$[M-H]^-$	619.289	619.289	0	$C_{29}H_{49}O_{12}P$	<0.001	<0.001	<0.001
LPE(18:3)	$[M-H]^-$	480.310	480.310	1	$C_{23}H_{48}NO_7P$	<0.001	0.003	<0.001
LPC(20:4)	$[M+K]^+$	582.295	582.296	2	$C_{28}H_{50}NO_7P$	<0.001	<0.001	<0.001
LPC(22:6)	$[M+K]^+$	606.297	606.295	3	$C_{30}H_{50}NO_7P$	<0.001	<0.001	<0.001
PA(P-32:1)	$[M-H]^-$	629.456	629.455	1	$C_{35}H_{37}O_7P$	<0.001	<0.001	<0.001
PA(O-32:0)	$[M-H]^-$	633.486	633.487	1	$C_{35}H_{71}O_7P$	<0.001	<0.001	<0.001
PG(38:4)	$[M-H]^-$	797.534	797.534	0	$C_{44}H_{79}O_{10}P$	<0.001	<0.001	<0.001
PC(32:0)	$[M+H]^+$	734.567	734.569	3	$C_{40}H_{80}NO_8P$	<0.001	<0.001	<0.001
PC(36:4)	$[M+K]^+$	820.525	820.525	0	$C_{44}H_{80}NO_8P$	<0.001	<0.001	<0.001
PC(36:3)	$[M+K]^+$	822.538	822.541	3	$C_{44}H_{82}NO_8P$	<0.001	<0.001	<0.001
PC(36:2)	$[M+K]^+$	824.555	824.557	2	$C_{44}H_{84}NO_8P$	<0.001	<0.001	<0.001
PE(38:6)	$[M+Na]^+$	814.535	814.536	0	$C_{45}H_{78}NO_8P$	<0.001	<0.001	<0.001
PI(38:4)	$[M-H]^-$	885.549	885.550	1	$C_{47}H_{83}O_{13}P$	<0.001	<0.001	<0.001
PC(34:1(OH))	$[M+H]^+$	776.578	776.579	2	$C_{42}H_{83}NO_9P$	<0.001	<0.001	<0.001
PC(36:4(OH))	$[M+K]^+$	836.515	836.520	5	$C_{44}H_{80}NO_9P$	<0.001	<0.001	<0.001
PC(36:3(OH))	$[M+K]^+$	838.531	838.535	5	$C_{44}H_{82}NO_9P$	<0.001	<0.001	<0.001
PC(36:2(OH))	$[M+K]^+$	840.548	840.551	4	$C_{44}H_{84}NO_9P$	<0.001	<0.001	<0.001
PC(36:4(OH)2)	$[M+K]^+$	852.511	852.515	4	$C_{44}H_{80}NO_{10}P$	<0.001	<0.001	<0.001
PC(36:3(OH)2)	$[M+K]^+$	854.528	854.530	3	$C_{44}H_{82}NO_{10}P$	<0.001	<0.001	<0.001
PC(36:2(OH)2)	$[M+K]^+$	856.542	856.546	5	$C_{44}H_{84}NO_{10}P$	<0.001	<0.001	<0.001
PC(36:4(OH)3)	$[M+K]^+$	868.508	868.510	2	$C_{44}H_{80}NO_{11}P$	<0.001	<0.001	<0.001
PC(36:3(OH)3)	$[M+K]^+$	870.522	870.525	4	$C_{44}H_{82}NO_{11}P$	<0.001	<0.001	<0.001
PC(36:2(OH)3)	$[M+K]^+$	872.540	872.541	1	$C_{44}H_{84}NO_{11}P$	<0.001	<0.001	<0.001
PS(24:1(OH))	$[M-H]^-$	664.385	664.383	2	$C_{32}H_{60}NO_{11}P$	<0.001	<0.001	<0.001
PI(38:4(OH))	$[M-H]^-$	901.544	901.545	1	$C_{47}H_{83}O_{14}P$	<0.001	<0.001	<0.001
PI(38:4(OH)2)	$[M-H]^-$	917.541	917.540	1	$C_{47}H_{83}O_{15}P$	<0.001	<0.001	<0.001
PI(38:4(OH)3)	$[M-H]^-$	933.536	933.535	1	$C_{47}H_{83}O_{16}P$	<0.001	<0.001	<0.001
Hydroxycholesterol	$[M+Na]^+$	425.339	425.339	0	$C_{27}H_{46}O_2$	<0.001	<0.001	<0.001
Hydroxycholesterol	$[M+K]^+$	441.311	441.313	4	$C_{27}H_{46}O_2$	<0.001	<0.001	<0.001
Ketocholesterol	$[M+K]^+$	439.297	439.297	0	$C_{27}H_{44}O_2$	<0.001	<0.001	<0.001
Dihydroxycholesterol	$[M+Na]^+$	441.333	441.334	3	$C_{27}H_{46}O_3$	<0.001	<0.001	<0.001
Dihydroxycholesterol	$[M+K]^+$	457.307	457.308	2	$C_{27}H_{46}O_3$	<0.001	<0.001	<0.001
Trihydroxycholesterol	$[M+CL]^-$	469.308	469.309	1	$C_{27}H_{46}O_4$	<0.001	<0.001	<0.001
Hydroxycholestendione	$[M+K]^+$	453.276	453.277	2	$C_{27}H_{42}O_3$	<0.001	<0.001	<0.001
Hydroxycholestdione	$[M+K]^+$	469.271	469.271	1	$C_{27}H_{42}O_4$	<0.001	<0.001	<0.001
Trihydroxycholestenone	$[M+K]^+$	471.287	471.287	0	$C_{27}H_{44}O_4$	<0.001	<0.001	<0.001
Trihydroxycholesterol	$[M+K]^+$	473.303	473.302	1	$C_{27}H_{46}O_4$	<0.001	<0.001	<0.001
Pregnanolone	$[M+K]^+$	357.218	357.219	3	$C_{21}H_{34}O_2$	<0.001	<0.001	<0.001
Tetrahydroxy-cholecalciferol	$[M+K]^+$	487.282	487.282	0	$C_{27}H_{44}O_5$	<0.001	<0.001	<0.001
Calcitriol	$[M+Na]^+$	439.317	439.318	2	$C_{27}H_{44}O_3$	<0.001	<0.001	<0.001
Calcitriol	$[M+K]^+$	455.292	455.292	1	$C_{27}H_44O_3$	<0.001	<0.001	<0.001
Diphenhydramine	$[M+H]^+$	256.169	256.170	3	$C_{17}H_{21}NO$	<0.001	<0.001	<0.001
Dextromethorphan	$[M+H]^+$	272.200	272.201	4	$C_{18}H_{25}NO$	<0.001	<0.001	<0.001
Losartan	$[M-H]^-$	421.155	421.155	1	$C_{22}H_{23}ClN_6O$	<0.001	<0.001	<0.001
Terfenadine	$[M+H]^+$	472.320	472.321	1	$C_{32}H_{41}NO_2$	<0.001	<0.001	<0.001

* Statistical significance determined using Kruskal-Wallis followed by Dunn's test for multiple comparisons, α = 0.05, *n* = considered pixel (Positive ion mode)/ considered pixel (Negative ion mode), ns = not significant

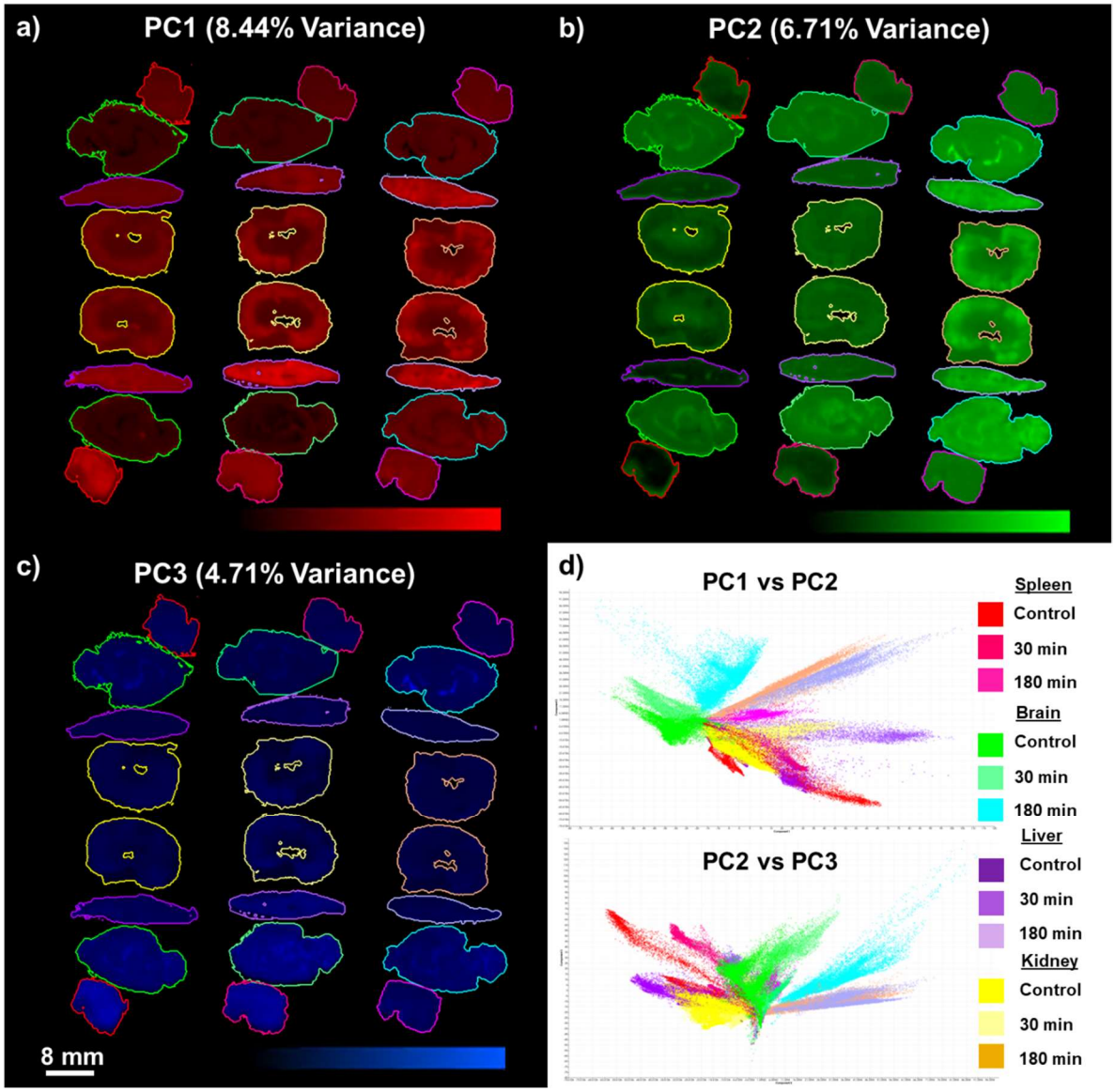

Figure A2.1, Monochromatic images and scoring plots of the pixel-wise PCA: Monochromatic images of a) PC1, b) PC2 and C) PC3 for the pixel-wise PCA of the whole dataset and d) the corresponding scoring plots.

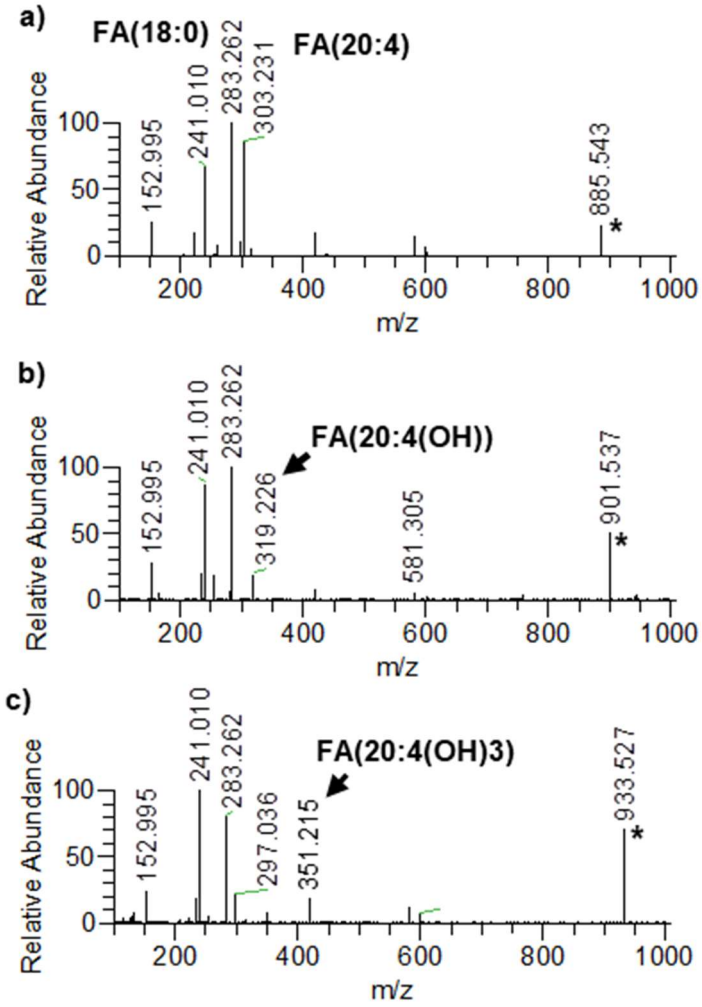

Figure A2.2: Tandem-MS validation of oxy-lipids: In-Situ MS/MS spectra of a) PI(38:4) with the fatty acid chains FA(18:0) at m/z283.262 and FA(20:4) at m/z 303.231, b) PI(38;4(OH)) with the fatty acid chains FA(18:0) and the hydroxy fatty acid FA(20:4((OH)) at m/z 319.226 and c PI(34:4((OH)3) with FA(18:0) and FA(20:4(OH)3) at m/z 351.215 and subsequent product ions due to water loss. * labels the isolated precursor ions.

Table A2.2: Statistical evaluation of samples prepared on glass slides

Annotation	Polarity	Median Abundances*			Statistical significance (P)**		
		Control	UVC	UVC+Argon	Control vs UVC	Control vs UVC+Argon	UVC vs UVC+Argon
FA(20:4)	-	409051	22939	38179	<0.001	<0.001	<0.001
FA(22:2)	-	12797	870.5	1907	<0.001	<0.001	<0.001
FA(22:6)	-	88403	3793	6265	<0.001	<0.001	<0.001
FA(22:5)	-	34106	1527	2593	<0.001	<0.001	<0.001
FA(24:5)	-	2174	0.000	0.000	<0.001	<0.001	<0.001
FA(24:4)	-	1095	0.000	0.000	<0.001	<0.001	<0.001
FA(18:1(OH)4)	-	0.000	2098	1916	<0.001	<0.001	<0.001
FA(18:1(OH)2)	-	0.000	1777	1879	<0.001	<0.001	<0.001
FA(18:2(OH))	+	0.000	6157	5958	<0.001	<0.001	ns
FA(18:2(OH)3)	-	0.000	2015	1952	<0.001	<0.001	ns
FA(18:2(OH2)	+	0.000	10423	10307	<0.001	<0.001	ns
FA(18:3(OH)3)	+	0.000	6024	7205	<0.001	<0.001	<0.001
FA(18:2(OH)3)	+	0.000	4053	4513	<0.001	<0.001	<0.001
FA(20:2(OH2)	+	0.000	1781	1704	<0.001	<0.001	ns
FA(20:2(OH))	-	42615	2425	4204	<0.001	<0.001	<0.001
FA(20:0(O))	-	0.000	1490	1609	<0.001	<0.001	<0.001
FA(18:2(OH))	-	0.000	1591	1898	<0.001	<0.001	<0.001
FA(18:0(OH)3)	-	0.000	1490	1609	<0.001	<0.001	0.0026
FA(18:2(OH)4)	-	2037	6583	6158	<0.001	<0.001	<0.001
FA(20:2(OH)3)	-	0.000	2767	2568	<0.001	<0.001	<0.001
PA(P-32:1)	-	0.000	0.000	0.000	<0.001	<0.001	ns
PA(P-32:1)	-	0.000	0.000	0.000	<0.001	<0.001	ns
PE(38:6)	+	0.000	5732	5857	<0.001	<0.001	0.0004
PC(36:4)	+	106085	7096	4266	<0.001	<0.001	<0.001
PC(36:3)	+	27734	0.000	0.000	<0.001	<0.001	<0.001
PC(36:2)	+	36112	8258	6299	<0.001	<0.001	<0.001
PG(38:4)	-	0.000	0.000	0.000	<0.001	<0.001	ns
PI(38:4)	-	39709	5114	9825	<0.001	<0.001	<0.001
PC(34:1(OH))	+	0.000	0.000	0.000	<0.001	<0.001	<0.001
PC(36:3(OH))	+	0.000	0.000	0.000	<0.001	<0.001	ns
PC(36:2(OH))	+	0.000	0.000	0.000	<0.001	<0.001	<0.001
PC(36:4(OH)2)	+	0.000	0.000	0.000	<0.001	<0.001	ns
PC(36:3(OH)2)	+	0.000	0.000	0.000	<0.001	<0.001	ns
PC(36:2(OH)2)	+	0.000	3510	3534	<0.001	<0.001	0.0017
PS(24:1(OH))	-	0.000	3078	3043	<0.001	<0.001	ns
PI(38:4(OH))	-	0.000	0.000	0.000	ns	<0.001	<0.001
PI(38:4(OH)2)	-	0.000	0.000	0.000	<0.001	<0.001	<0.001
PI(38:4(OH)3)	-	979.4	0.000	1349	<0.001	<0.001	<0.001

* Median abundances determined from all pixel for each treatment group

** Statistical significance determined using Kruskal-Wallis followed by Dunn's test for multiple comparisons, $\alpha = 0.05$, $n = 19007$ (Control), 18723 (UVC) and 17965 (UVC+Argon) considered pixel (Positive ion mode), $n = 20490$ (control), 19135 (UVC) and 19812 (UVC+Argon) considered pixel (Negative ion mode), ns = not significant

Table A2.3: Statistical evaluation of samples prepared on PP wafers

Annotation	Polarity	Median Abundances*			Statistical significance (P)**		
		Control	UVC	UVC+Argon	Control vs UVC	Control vs UVC+Argon	UVC vs UVC+Argon
FA(20:4)	-	205743	7855	9780	<0.0001	<0.0001	<0.0001
FA(22:2)	-	8820	0.000	0.000	<0.0001	<0.0001	<0.0001
FA(22:6)	-	61211	1291	1787	<0.0001	<0.0001	<0.0001
FA(22:5)	-	25320	0.000	517.1	<0.0001	<0.0001	<0.0001
FA(24:5)	-	0.000	0.000	0.000	<0.0001	<0.0001	<0.0001
FA(24:4)	-	0.000	0.000	0.000	0.0015	0.00003	ns
FA(18:1(OH)4)	-	0.000	0.000	0.000	ns	ns	ns
FA(18:1(OH)2)	-	0.000	994.1	915.8	<0.0001	<0.0001	<0.0001
FA(18:2(OH))	+	0.000	5357	5155	<0.0001	<0.0001	0.0002
FA(18:2(OH)3)	-	0.000	622.4	508.0	<0.0001	<0.0001	<0.0001
FA(18:2(OH2)	+	0.000	7044	6735	<0.0001	<0.0001	<0.0001
FA(18:3(OH)3)	+	0.000	5084	4710	<0.0001	<0.0001	<0.0001
FA(18:2(OH)3)	+	0.000	3559	3373	<0.0001	<0.0001	<0.0001
FA(20:2(OH2)	+	0.000	1607	2195	<0.0001	<0.0001	<0.0001
FA(20:2(OH))	-	0.000	1607	2195	<0.0001	<0.0001	<0.0001
FA(20:0(O))	-	0.000	6099	5129	<0.0001	<0.0001	<0.0001
FA(18:2(OH))	-	0.000	1485	1416	<0.0001	<0.0001	ns
FA(18:0(OH)3)	-	0.000	0.000	0.000	<0.0001	<0.0001	ns
FA(18:2(OH)4)	-	0.000	0.000	0.000	<0.0001	<0.0001	<0.0001
FA(20:2(OH)3)	-	0.000	0.000	0.000	<0.0001	<0.0001	<0.0001
PA(P-32:1)	-	0.000	0.000	0.000	0.0097	ns	ns
PA(P-32:1)	-	0.000	0.000	0.000	<0.0001	<0.0001	ns
PE(38:6)	+	0.000	5164	4435	<0.0001	<0.0001	<0.0001
PC(36:4)	+	151839	4128	12137	<0.0001	<0.0001	<0.0001
PC(36:3)	+	41787	0.000	2364	<0.0001	<0.0001	<0.0001
PC(36:2)	+	54424	5091	7983	<0.0001	<0.0001	<0.0001
PG(38:4)	-	0.000	0.000	0.000	<0.0001	<0.0001	ns
PI(38:4)	-	75096	3354	6389	<0.0001	<0.0001	<0.0001
PC(34:1(OH))	+	0.000	0.000	0.000	<0.0001	ns	<0.0001
PC(36:3(OH))	+	0.000	0.000	0.000	<0.0001	<0.0001	<0.0001
PC(36:2(OH))	+	0.000	0.000	0.000	<0.0001	<0.0001	<0.0001
PC(36:4(OH)2)	+	0.000	0.000	0.000	<0.0001	<0.0001	<0.0001
PC(36:3(OH)2)	+	0.000	1322	0.000	<0.0001	<0.0001	<0.0001
PC(36:2(OH)2)	+	0.000	3157	2770	<0.0001	<0.0001	<0.0001
PS(24:1(OH))	-	0.000	2929	2561	<0.0001	<0.0001	<0.0001
PI(38:4(OH))	-	0.000	0.000	0.000	<0.0001	<0.0001	<0.0001
PI(38:4(OH)2)	-	0.000	0.000	0.000	<0.0001	<0.0001	<0.0001
PI(38:4(OH)3)	-	2002	0.000	824.6	<0.0001	<0.0001	<0.0001

* Median abundances determined from all pixel for each treatment group

** Statistical significance determined using Kruskal-Wallis followed by Dunn's test for multiple comparisons, $\alpha = 0.05$, n = 18181 (Control), 18965 (UVC) and 18734 (UVC+Argon) considered pixel (Positive ion mode), n = 19435 (control), 19431 (UVC) and 19562 (UVC+Argon) considered pixel (Negative ion mode), ns = not significant

Table A2.4: Statistical evaluation of samples prepared on glass compared to samples prepared on PP wafers

Annotation	Polarity	Median Abundances*				Statistical significance (P)**	
		Glass		PP		Glass vs PP Kidney	Glass vs PP Liver
		Kidney	Liver	Kidney	Liver		
FA(20:4)	-	29034	17138	9931	7973	<0.0001	<0.0001
FA(22:2)	-	0	1482	0	0	<0.0001	<0.0001
FA(22:6)	-	3010	5010	1033	2444	<0.0001	<0.0001
FA(22:5)	-	0	2287	0	1065	<0.0001	<0.0001
FA(24:5)	-	0	0	0	0	<0.0001	ns
FA(24:4)	-	0	0	0	0	<0.0001	ns
FA(18:1(OH)4)	-	1671	4662	0	1529	<0.0001	<0.0001
FA(18:1(OH)2)	-	1791	2640	0	1042	<0.0001	<0.0001
FA(18:2(OH))	+	6075	11370	3938	8617	<0.0001	<0.0001
FA(18:2(OH)3)	-	1945	3391	0	1242	<0.0001	<0.0001
FA(18:2(OH2)	+	8588	20385	5613	15267	<0.0001	<0.0001
FA(18:3(OH)3)	+	7911	13353	4813	9752	<0.0001	<0.0001
FA(18:2(OH)3)	+	3700	7439	2912	6175	<0.0001	<0.0001
FA(20:2(OH2)	+	0	2585	0	1867	<0.0001	<0.0001
FA(20:2(OH))	-	2773	2670	786.8	1065	<0.0001	<0.0001
FA(20:0(O))	-	1636	3592	0	1586	<0.0001	<0.0001
FA(18:2(OH))	-	1164	2561	0	0	<0.0001	<0.0001
FA(18:0(OH)3)	-	0	0	0	0	<0.0001	<0.0001
FA(18:2(OH)4)	-	5630	16702	2644	6199	<0.0001	<0.0001
FA(20:2(OH)3)	-	3734	9385	1336	3570	<0.0001	<0.0001
PA(P-32:1)	-	0	0	0	0	ns	ns
PA(P-32:1)	-	0	0	0	0	ns	ns
PE(38:6)	+	11162	15776	7802	13838	<0.0001	<0.0001
PC(36:4)	+	5021	7756	2812	4698	<0.0001	<0.0001
PC(36:3)	+	0	0	0	0	<0.0001	<0.0001
PC(36:2)	+	6100	18004	3515	11466	<0.0001	<0.0001
PG(38:4)	-	0	0	0	0	<0.0001	0.0032
PI(38:4)	-	5006	14679	3034	10599	<0.0001	<0.0001
PC(34:1(OH))	+	0	0	0	1741	<0.0001	<0.0001
PC(36:3(OH))	+	0	6062	0	4489	<0.0001	<0.0001
PC(36:2(OH))	+	0	6220	0	5283	<0.0001	<0.0001
PC(36:4(OH)2)	+	0	2793	0	1768	<0.0001	<0.0001
PC(36:3(OH)2)	+	2015	9088	0	6753	<0.0001	<0.0001
PC(36:2(OH)2)	+	5127	18049	3043	14140	<0.0001	<0.0001
PS(24:1(OH))	-	9560	14629	2215	4237	<0.0001	<0.0001
PI(38:4(OH))	-	0	0	0	0	0.0002	ns
PI(38:4(OH)2)	-	0	0	0	0	<0.0001	<0.0001
PI(38:4(OH)3)	-	0	0	0	0	<0.0001	<0.0001

* Median abundances determined from all pixel for each treatment group

** Statistical significance determined using Kruskal-Wallis followed by Dunn's test for multiple comparisons, $\alpha = 0.05$, n = 11543 (Glass - Kidney), 11640 (PP - Kidney), 9378 (Glass – Liver) and 9601 (PP – Liver) considered pixel, n = 11389 (Glass - Kidney), 11209 (PP - Kidney), 8638 (Glass – Liver) and 9647 (PP – Liver) considered pixel (Negative ion mode)
ns = not significant

Appendix 3: Supplementary information to Chapter 5

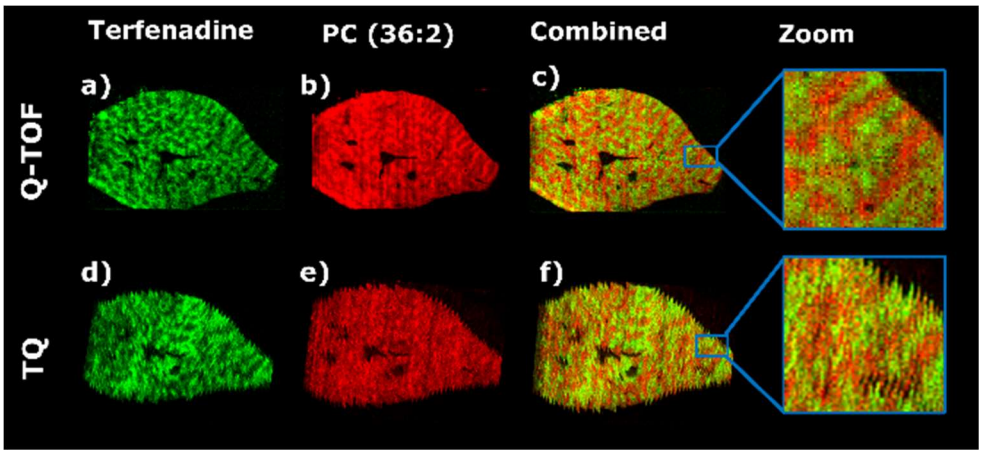

Figure A3.1, Comparison of the image quality before re-alignment: Ion images for terfenadine (a,d) and endogenous lipid PC (36:2) (b,e) obtained by DESI-MSI performed on a Xevo G2-XS or a Xevo TQ-S. Figures c and f show the combined ion images of the drug and the endogenous lipid. The zoomed view displays the tissue edges. Images d-f are the original images prior re-alignment of the individual line scans.

Appendix 4: Supplementary information to Chapter 6

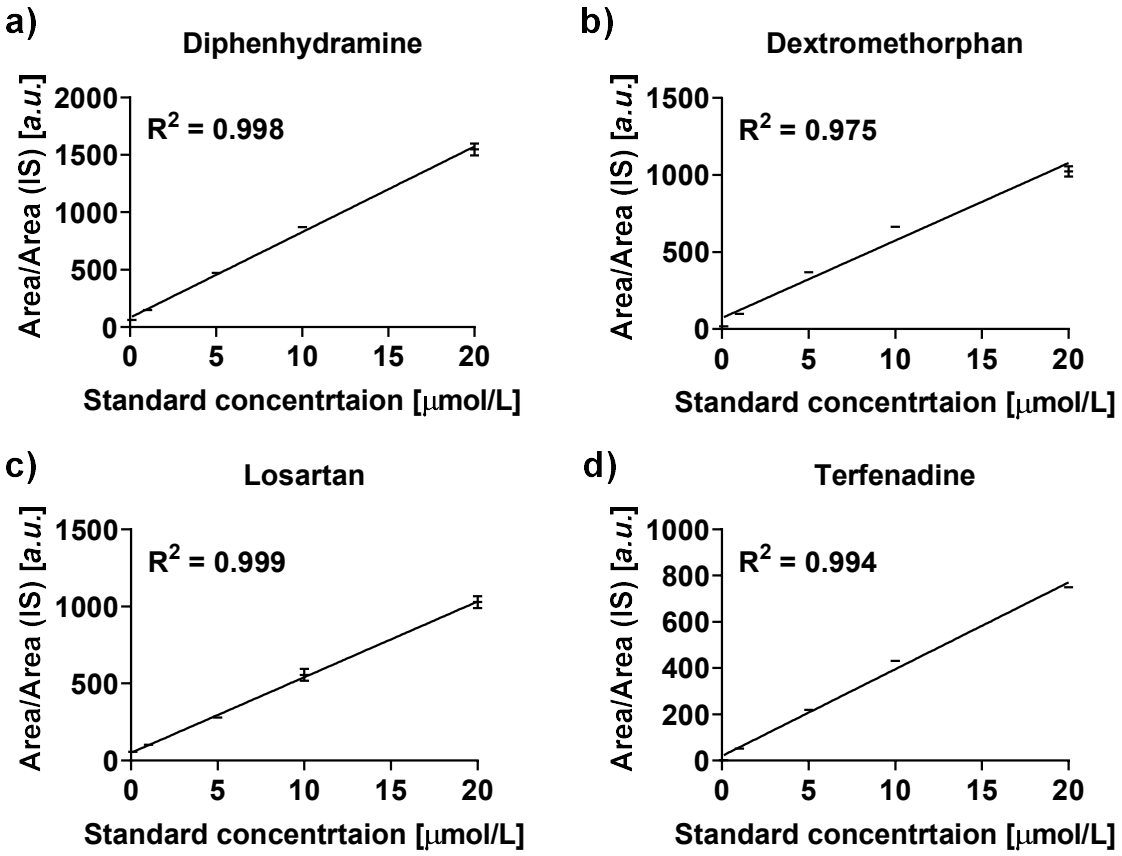

Figure A4.1, Calibration lines for the drug quantification by LC-MS/MS analysis: Linear regressions for the internal standard (IS) normalized peak areas over the standard concentration for (a) diphenhydramine, (b) dextromethorphan, (c) losartan and (d) terfenadine. Data is presented as mean ± SD, *n* = 4 replicates pear measurement

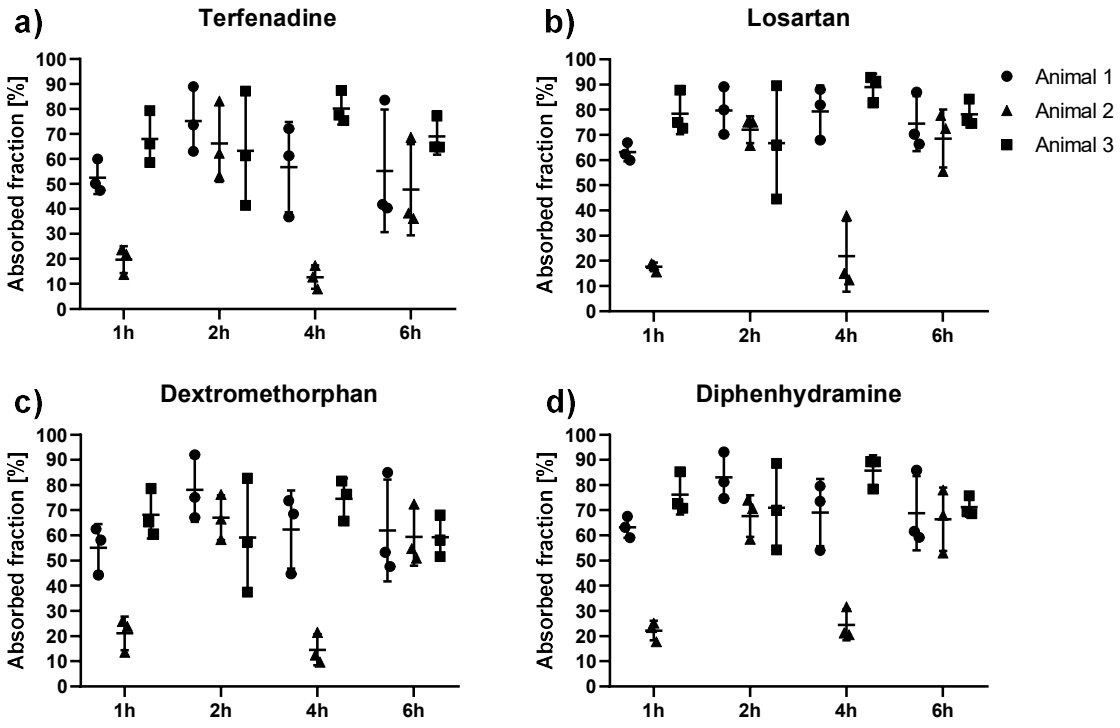

Figure A4.2, Estimation of the absorbed drug fractions: for a) terfenadine, b) Losartan, c) Dextromethorphan and d) diphenhydramine. As the sample collection was terminal, animals 1-3 represent different animals for each timepoint. The assignment of the symbols is identical with the assignment in Figure 6.2.

Appendix 5: Supplementary information to Chapter 7

Table A5.1: Accurate masses of the features identified from the exploratory full scan experiments performed on the DESI-Q-Exactive setup and the resulting precursor and product ions chosen for the MRM transition on the DESI-TQ setup

Compound	Adduct	*m/z* bin	Measured mass [*m/z*]	Accurate mass [*m/z*]	Error [ppm]	Precursor ion [*m/z*]	Product ion [*m/z*]
FA(20:4)	$[M-H]^-$	303.25	303.232	303.233	-3	303.23	285.22
FA(22:6)	$[M-H]^-$	327.25	327.232	327.233	-3	327.23	283.24
Ascorbic acid	$[M-H]^-$	175.05	175.024	175.025	-6	175.02	115.002
Cholesterol-sulfate	$[M-H]^-$	465.35	465.304	465.303	2	465.3	96.96
PC(32:0)	$[M+K]^+$	772.55	772.525	772.525	0	772.53	162.96
PC(34:1)	$[M+K]^+$	798.55	798.540	798.541	-1	798.54	739.47
PC(36:2)	$[M+K]^+$	824.55	824.557	824.557	0	822.54	763.46
PC(38:4)	$[M+K]^+$	848.55	848.556	848.557	-1	848.53	789.48
PE(18:0_20:4)	$[M-H]^-$	766.55	766.537	766.539	-3	766.54	303.23
PE(16:0_22:4)	$[M-H]^-$	766.55	766.537	766.539	-3	766.54	255.23
PS(38:4)	$[M-H]^-$	810.55	810.526	810.529	-4	810.53	283.26
PS(18:0_18:2)	$[M-H]^-$	786.55	786.527	786.527	0	786.53	283.26
BMP(20:4_20:4)	$[M-H]^-$	817.55	817.501	817.501	0	817.5	767.54
BMP(20:4_22_6)	$[M-H]^-$	841.55	841.502	841.503	-1	841.5	327.23
BMP(22:6_22:6)	$[M-H]^-$	865.55	865.501	865.503	-2	865.5	327.23
PI(18:0_20:4)	$[M-H]^-$	885.55	885.548	885.550	-2	885.55	303.23